Research and development of silicon photomultipliers with bulk-integrated quench resistors for future particle tracking and astroparticle physics applications

PhD Thesis

by

Stefan Petrovics

Semiconductor Laboratory
of the Max-Planck Society

and

Department of Physics
Ludwig-Maximilians-Universität München

May 19th 2022

Research and development of silicon photomultipliers with bulk-integrated quench resistors for future particle tracking and astroparticle physics applications

Dissertation
an der Fakultät für Physik
Ludwig–Maximilians–Universität München
und am
Halbleiterlabor der Max-Planck Gesellschaft

vorgelegt von

Stefan Petrovics
geboren in Vukovar

München, 19. Mai 2022

Erstgutachter: Prof. Dr. Christian Kiesling

Zweitgutachter: Prof. Dr. Jochen Schieck

Tag der mündlichen Prüfung: 23. September 2022

たったひとりの人間には世界を変えることは難しいが、世界を傾けるくらいなら、できなくはないのかもしれんのう。

– 忍野 忍

Zusammenfassung

Das Hauptaugenmerk dieser Arbeit richtet sich auf die Forschung und Entwicklung neuartiger Silizium-Photomultiplier (SiPM), mit dem späteren Ziel der Anwendung im Bereich der Hochenergie-Teilchenphysik (Tracking Detektor und Kalorimeterauslese) und Astro-Teilchenphysik (Cherenkov-Teleskop-Kamera). In den letzten Jahren haben sich SiPMs aufgrund ihrer stetigen Entwicklungen und technischen Verbesserungen immer mehr als vielversprechende Nachfolger für Photomultiplier-Röhren bewiesen. Konventionelle SiPMs sind üblicherweise als eine Matrix von Lawinenphotodioden aufgebaut, welche jeweils im Geiger-Modus betrieben werden und parallel verbunden sind und somit die Möglichkeit für die Detektion von einzelnen Photonen bieten. Das Signal wird dabei aus der Summe aller ausgelöster Zellen zusammengesetzt. Um der Ladungslawine entgegenzuwirken und das Wiederaufladen der Zelle zu ermöglichen, wird ein hochohmiger Löschwiderstand benötigt, der normalerweise auf der Oberfläche der Bauteile platziert wird und damit ein Hindernis für einfallendes Licht darstellt. Das Konzept, welches am Halbleiterlabor der Max-Planck Gesellschaft entwickelt wird und Silicon Multipixel Light Detector (SiMPl) genannt wird, versucht, diesen Nachteil (und viele daraus folgende) zu umgehen, indem es den Löschwiderstand in den Silizium-Bulk des Sensors integriert. Dies hat ein freies Eintrittsfenster für Licht zur Folge und erlaubt damit, eine höhere Photonendetektionseffizienz zu erhalten. Desweiteren wird dadurch die Anzahl der benötigten Prozessschritte während der Herstellung verringert, was wiederum die Kosten für eine Massenproduktion senkt.

Erste Prototypen von SiMPl waren in der Lage, sowohl einen Konzeptnachweis, als auch erste Charakterisierungsmessungen zu ermöglichen, welche vielversprechende Resultate geliefert haben, die das allgemeine Potential von zukünftigen Chargen unterstreichen. Allerdings waren die ersten Prototypen auch von technischen Mängeln betroffen. Das Ziel dieser Dissertation war es dementsprechend, die Erkenntnisse der ersten Prototypen in die Weiterentwicklung des SiMPl-Projektes zu integrieren, um so die Qualität der Bauteile weiter zu verbessern und zusätzlich neuartige Konzepte zu verwirklichen. Im Rahmen dieses Bestrebens, fiel der Fokus auf zwei separate Anwendungsschwerpunkte. Diese waren zum Einen, ein Sensor für die Detektion von optischen Lichtquellen geringer Intensität, welcher zum Beispiel im Auslesesystem eines Cherenkov-Teleskopes genutzt werden kann und zum Anderen, ein Sensor mit geringer Dicke und schnellen Timing für die Anwendung als Tracking-Detektor in der Linearbeschleunigerphysik.

Simulationsstudien mit dedizierten TCAD-Simulationsanwendungen wurden durchgeführt, um die Reinraumprozessierung zu optimieren und die Umsetzbarkeit der geplanten Adaptionen zu untersuchen. Diese Studien beinhalten Prozess- und Bauteilsimulationen, deren Ergebnisse später mit den Messungen abgeglichen werden können und führten zu vielversprechenden Resultaten. Die Simulationsergebnisse konnten damit als Basis für die Entwicklung neuer Prototypen dienen.

Hinsichtlich der Sensoren für geringe Lichtintensitäten, wurde das Ziel gesetzt, die charakteristischen Parameter von SiPMs zu verbessern, um so die generelle Leistung der SiMPl-Sensoren zu optimieren und letztendlich einen konkurrenzfähigen Stand gegenüber kommerzieller Bauteile zu erreichen. Während den Messungen sind jedoch unerwartete Komplikationen aufgetreten, welche zu erheblichen Einbußen in der Qualität der SiMPl-Bauteile führten. Zu diesem Zeitpunkt lag die Vermutung nahe, dass die Komplikationen aufgrund von problembehafteten Prozessschritten hervorgerufen wurden. Infolgedessen wurde beschlossen, mehr Zeit in die Untersuchung dieser Problematik zu investieren, damit diese nicht erneut in späteren Chargen auftreten und diese damit unbrauchbar machen können. Da es sich hierbei jedoch um eine neuartige Problemstellung handelte,

waren zahlreiche investigative Messverfahren notwendig.

Detailierte Untersuchungen bezüglich der Anwendung von SiMPl als Tracking Detektoren wurden durchgeführt. Eine solche beinhaltete die Messung der Elektronendetektionseffizienz mithilfe eines neuentwickelten Messaufbaus. Die Ergebnisse stimmen dabei sehr gut mit den Simulationsstudien überein und bestätigen damit die Realisierbarkeit des Konzepts. Dieses basiert wiederum auf der zugrundelegenden höheren Detektionseffizienz bei geladenen Teilchen im Vergleich zu Photonen und erlaubt somit das Betreiben der Sensoren bei weniger ausgeprägten Störsignalen. Die erste Prototype-Charge wurde erfolgreich hergestellt und technologisch an die Anforderungen der Ausleseelektronik angepasst. Desweiteren war eine erste Montage von Sensor-Interposern auf Auslesechips erfolgreich und dient damit als Basis für die nächsten Schritte. Charakterisierungsmessungen mit den ersten Prototypen waren zwar möglich, jedoch sind diese ebenfalls von den oben aufgeführten Komplikationen betroffen, was die Ergebnisse nur eingeschränkt nutzbar macht.

Beide Anwendungschargen wurden zusätzlich noch durch Bestrahlungskampagnen und Simulationen auf ihre Strahlentoleranz geprüft. Dies war notwendig, da Sensoren für beide Anwendungsgebiete innerhalb strahlungsreicher Umgebungen prolongiert zum Einsatz kommen können. Dabei wurden der allgemeine Einfluss auf das Sensormaterial und die Auswirkungen auf die Leistung der Sensoren untersucht und im Anschluss mit den Ergebnissen der Simulationen verglichen. Die Ergebnisse wiesen selbst nach verlängerten Bestrahlungen eine mehr als zufriedenstellende Strahlentoleranz auf.

Abstract

The main focus of this thesis is the research and development of novel silicon photomultipliers (SiPMs) with the goal of utilization in high energy particle physics (tracking and calorimeter readout) as well as astroparticle physics (Cherenkov telescope camera). In recent years, SiPMs have been a very promising candidate for replacing conventional photomultiplier tubes in many applications due to the ongoing development and technological improvements. Conventional SiPMs are usually realized as an array of avalanche photodiodes, operated in Geiger mode and connected in parallel, providing single photon counting capabilities with the signal being the sum of all fired cells. In order to stop the avalanche process passively and enable cell recharge, a high ohmic quench resistor is necessary, generally located on the surface of the device, thus limiting its fill factor to a certain degree. The concept developed at the Semiconductor Laboratory of the Max-Planck Society, called Silicon Multipixel Light Detector (SiMPl) attempts to circumvent these (and resulting) drawbacks by incorporating the quench resistor in the silicon bulk material of the sensor. This results in a free entrance window for light and hence higher photon detection efficiencies, while also allowing the reduction of necessary processing steps during production, thus reducing the cost for mass production.

First prototype iterations of SiMPl have provided a proof-of-concept as well as the possibility for first characterization measurements, yielding promising results outlining the potential of future batches, while also dealing with technological issues. The main goal of this thesis was therefore to build upon the previous discoveries in order to improve the device performance and include novel designs for future SiMPl batches. In this context, enhancements towards two distinct fields of applications were prioritized, namely low light level photon detection for e.g. the readout systems of Cherenkov telescopes (classic SiMPl approach) and low material budget fast timing tracking applications for e.g. linear collider particle physics (novel approach).

Simulation studies with dedicated TCAD simulation tools were carried out in order to improve the technological processing procedure and to investigate the feasibility of the planned adaptations made to the design. These studies include processing and device simulations, which can be further utilized for comparison with later measurements. The results showed promise and provided the basis new prototype productions.

In regards to low light level detection applications, an optimization of the characteristic SiPM parameters and thereby overall performance of SiMPl devices was attempted, in order to achieve results competitive with current commercially available devices. During characterizations a potential technological issue was encountered, resulting in a degradation of the affected batches. Hence, focus was later shifted towards the investigation of said issue such that a reoccurence in later batches would not take place. Due to the issue being of a novel nature, various attempts at characterization needed to be carried out.

In depth investigation towards the tracking application of SiMPl was carried via a sophisticated experimental setup, design to determine the electron detection efficiency of devices. Results have shown very good agreement with simulated predictions, confirming the concepts feasibility based on increased efficiency rates compared to light detection, which in turn allows operation with lower noise contribution. A first batch of prototypes was developed, adapted to fulfill the requirements of the sophisticated readout electronics. First assembly procedures of sensors interposers and readout ASICs yielded satisfying results, enabling the next development steps. First sensor characterizations were carried out as well.

Both batches were additionally investigated in terms of their radiation hardness via

simulations and actual irradiation procedures, as the majority of the possible applications will require prolonged operations in a radiation-rich environment. The general impact on the material, as well as on the device performance was analyzed and compared to simulations. The results proved promising results, suggesting no major drawbacks even after extensive exposure to radiation.

Contents

1 Introduction

In the environment of experimental physics of a multitude of different branches, the development and enhancement of the experimental equipment, i.e. the detector systems, plays a crucial role at enabling new discoveries and breakthroughs in mankind's understanding of the building blocks of our universe. As theoretical concepts and models predict certain quantities and mechanisms, experimental validation is required to prove said theories and establish them as commonly accepted models. These validations, in turn, call for or greatly benefit from technological improvements, since, for example, the detection of certain events requires improved signal-to-noise ratios in the detector systems. A fairly current example pertaining to this necessity, can be found in the confirmation of the existence of the Higgs boson in 2012, which was proposed back in 1964 and heavily relied - amongst other criteria - on the ever improving detector technology in order to enable its detection in background-dominated decay channels.

This thesis did therefore focus on the technological research and development of such novel detector concepts in the shape of a silicon photomultiplier, developed at the Max-Planck Semiconductor Laboratory. Chapter 2 will introduce various physics experiments in which these novel devices could be incorporated. This will include high energy particle physics found at i.e. linear colliders as well as gamma-ray astronomy, since these device could allow implementation in a wide range of applications.

However, in order to understand the working principle and potential challenges of novel detector devices, their underlying physics characteristics need to be known, which is going to be the subject of Chapter 3. A brief summary of the necessary properties of semiconductors will be presented, as these devices are based on semiconductor material, followed by an introduction to the basic interaction of light and particles with matter. Afterwards, a step-by-step approach from simple *pn*-junctions to silicon photomultipliers will be elaborated, establishing the knowledge needed to understand the novel detector approach of this thesis.

Since many environments of the experimental applications presented in Chapter 2 feature high levels of radiation exposure in different shapes, it is crucial to a have strong grasp on the potential adverse effects on detectors stemming from radiation damage. This will be the focus of Chapter 4, dealing with both non-ionizing and ionizing radiation damage. In both cases, the damage mechanisms as well as the potential impact on the detector performance and ways to alleviate these a negative effects will be discussed in detail, since part of the development procedure of the novel detector concept presented in this study also attempted to suppress these adverse effects.

Knowledge of the above chapters will then allow for the introduction of the experimental setups for the characterization of the various parameters of silicon photomultipliers in Chapter 5. During this introduction, an in-depth discussion of these parameters will be given as they are required for a thorough understanding and assessment of the quality and performance of the devices. Detailed explanations pertaining to the specific static and dynamic experimental methods to determine these parameters will also be elaborated.

After all necessary information was presented, the novel detector concept will be introduced in Chapter 6, discussing its advantages and drawbacks compared to conventional silicon photomultipliers for low level light detection and furthermore, a new approach aiming at utilization in particle tracking will be elaborated upon and the necessary steps towards its realization. This will also include are brief summary of the expected impact of radiation damage on these devices specifically, as the previous chapter was focusing on the general aspects.

The development of novel detector devices entails thorough simulation studies, which are going to be the topic of Chapter 7. The procedure of technology and device simulations will be explained including the simulation tools utilized for these studies. Technology simulations reenact the manufacturing process of the devices and allow analysis of the impact of certain technological parameters, while device simulations aim to mirror device operation and the different static measurements. These mark an essential step during detector production as they can drastically cut down time and cost and offer better understanding of the devices at hand.

All devices utilized within this study will be presented in Chapter 8, introducing the various test structures and photomultiplier arrays available. In addition, since radiation hardness of the novel devices will be a topic of discussion, details on the irradiation of the test devices will be given here as well.

Chapter 9 will feature a detailed discussion of all simulation and experimental results with the new batches of the novel detector concept of this thesis. The discussion will be structured into the different prototype batches developed in the course of this study and each one will deal with the respective challenges, simulation and experimental approaches and a final conclusion, summarizing the outcome and determining if the batch was able to achieve its initial goal and what insights can be learned. Afterwards, the impact of radiation damage on the novel devices will be analyzed by means of simulations and experimental studies, again divided by batches, as both are conceived for different applications. Due to the aforementioned notion of utilization in high energy physics, a first proof of concept measurement will be discussed, including an introduction of the experimental setup and underlying simulation study, providing evidence of the feasibility of the novel detector approach as potential tracking detector. While the focus of the first result section was initial placed on the detailed characterization of the device properties presented in Chapter 5, certain technological difficulties were experienced in the course of this study, making this task increasingly difficult and unfeasible. Thus, it was decided to dedicate additional resources to investigate this issue, as it may impact future iterations and therefore needs to be understood and avoided. This investigation will also be presented here, including an analysis of its potential origin as well as possible solutions for future productions.

At last, a short summary of the goals and concepts of this thesis will be given in Chapter 10, summarizing the results of the simulation and experimental studies, as well as the other issues mentioned above. This will also include a discussion regarding the feasibility of the novel concept according to the obtained results and conclude in a outlook in terms of future iterations.

2 Detectors for physics at the high energy collider and cosmic frontier

The devices researched within this study can be utilized within scientific experiments located on both ends of the size spectrum. On one end, high energy collider experiments allow the analysis of the structure of the fundamental building blocks of matter, their interactions and most recently the acquisition of mass, all culminating in the formulation of the Standard Model. This theoretical model aims to provide an overall theory for elementary particles and all fundamental forces. It is, however, incomplete, as certain aspects like the gravitational force and dark matter can currently not be described by the Standard Model. Thus, novel collider experiments with improved instruments for detection are required to shed light on these unresolved issues, by, for example, finding evidence of potential particles constituting dark matter.

More insight on the topic of dark matter can also be gained from shifting towards the other end of the size spectrum, namely to the cosmic frontier. Furthermore, measurements performed by telescopes or satellite based experiments allowed for investigation of cosmic objects like supernova remnants and in recent years even black holes, thereby enabling a better understanding of the evolution of the universe. Similar to particle physics, improved observation of the known and the potential for new discoveries will hinge on novel detection methods and consequently on the detector instruments within these novel experiments.

The following chapter aims to give a brief introduction on these two major scientific topics and the important role that devices like the ones studied within this thesis can play in their instrumentation and potential for new discoveries.

2.1 Future linear colliders

The latest achievements of the LHC and its experiments like ATLAS and CMS have proven the discovery potential for fundamental mechanisms of the Standard Model at the high energy frontier. A detailed characterization of the acquired data pertaining to the newfound boson as well as potentially reaching the territory of new physics thus mark two of the top priorities going forward. This, in turn, can be achieved by reaching even higher energies, while simultaneously reducing the amount of background events for a cleaner experimental environment. The latter can be accomplished by utilizing e.g. electrons and positrons instead of hadrons for collision. Due to the parton structure of hadrons, the actual collisions take place between constituents carrying only a fraction of the proton energy, whereas the center-of-mass energy is equal to the sum of the two colliding particles energies in the case of electrons and positrons. However, their energy gain within a circular trajectory is limited by synchrotron radiation. Hence, a linear acceleration scheme at energies beyond the LHC will be required.

The following section will introduce the physics case of such linear colliders, with an emphasis on their advantages in the Higgs sector and new physics. Afterwards, a brief overview of the two major proposed collider concepts will be presented. Finally, two specific subsystems of the potential detector systems will be discussed, which would enable the utilization of the devices studied within this thesis.

2.1.1 Physics cases at linear colliders

Compared to hadron collider experiments and their pronounced QCD background, linear electron-positron colliders are capable of providing a clean experimental environment by virtue of their colliding elementary (structureless) particles and the orders of magnitude lower backgrounds pertaining to said collisions. As a result, trigger-free readout becomes feasible and full event reconstruction a possibility. In addition, the recent discovery of a light Higgs boson, achieved by the Large Hadron Collider (LHC) and its ATLAS and CMS experiments, has further cemented the linear collider (LC) physics case as "Higgs factories" and its prospects of new discoveries.

The main topics of the LC physics program can be summarized in the following categories [1]:

- precise measurements of the Higgs sector properties,
- precise characterization of the interactions of top quarks, gauge bosons and new particles, and
- search for physics beyond the Standard Model (SM).

Thus, the findings of future LCs, complementary to the studies performed at the LHC, will be able to deepen the understanding of known physics as well as unraveling the underlying structure of potential new physics. In the following, a brief summary regarding the Higgs physics and physics beyond the SM will be elaborated, while a more detailed discussion on the entirety of the physics case at LCs can be found in [1–3].

Higgs physics

In the SM, the Higgs mechanism, as predicted by Peter Higgs in 1964 [4], plays a pivotal role as it is the reason for electroweak symmetry breaking and the underlying mechanism for the generation of the masses of all other elementary particles. After its experimental discovery at the LHC in 2012 [5], it is now essential to precisely analyze its properties and coupling to gauge bosons, fermions and itself.

Two channels dominate Higgs production at a LC, depending on the center-of-mass energy $\sqrt{s}$ and can be seen in Fig. 2.1. In an initial low-energy phase ($\sqrt{s} \approx (250- -500)$ GeV) the main process is given by Higgs-strahlung (Fig. 2.1 left) via $e^+e^- \rightarrow ZH$. Later stages during the LC runs will feature higher energies ($\sqrt{s} > 500$ GeV),

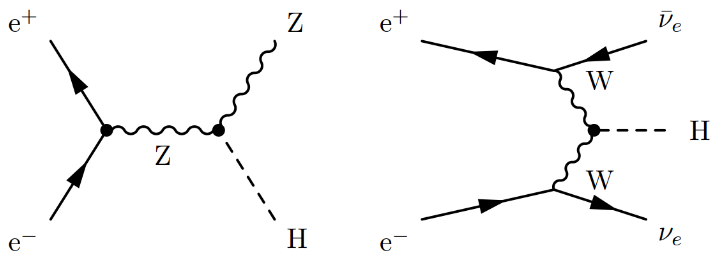

Figure 2.1: Feynman diagrams of the two main production processes for Higgs bosons at linear colliders. At lower center-of-mass energies Higgs-strahlung is the dominant process (left), while increased energies make vectorboson fusion (right) prevalent.

making vectorboson fusion with W-bosons $e^+e^- \rightarrow H\nu_e\bar{\nu_e}$ the dominant process for Higgs production (Fig. 2.1 right). Sufficient statistics for Higgs events can be expected even for low-energy phases in LC and additional rare processes like $e^+e^- \rightarrow t\bar{t}H$, $e^+e^- \rightarrow ZHH$ and $e^+e^- \rightarrow HH\nu_e\bar{\nu_e}$ provide further data and allow access to the Higgs self-coupling and top quark Yukawa coupling [1].

At $\sqrt{s} < 500$ GeV events can be selected based on a final state with two oppositely charged leptons with an invariant mass of m_Z. Unique to a LC is the fact that the Higgs decay is not required in the event selection, thus also allowing evaluation of events even with invisible final Higgs-states. Hence, thanks to the low SM-cross-section for background processes in a LC, a model-independent measurement of the Higgs-coupling constant g_{HZZ} is possible. In addition, absolute measurements of the Higgs branching fractions can be performed by identification of the individual final states the various Higgs and Z decay modes. Furthermore, the Higgs-coupling to b-quarks and c-quarks becomes feasible via $H \rightarrow b\bar{b}$ and $H \rightarrow c\bar{c}$ due to the reduced QCD background.

On the other hand, at higher energy the focus shifts towards analysis of the coupling of the Higgs boson to the W- and Z-bosons, allowing the verification of SM predictions such as $g_{\mathrm{HWW}}/g_{\mathrm{HZZ}} = \cos^2\Theta_W$, with Θ_W being the weak mixing angle. In both energetic cases, another important aspect of the Higgs sector is the Higgs self-coupling, which is crucial for the proper establishment of the Higgs mechanism. The overall results, in turn, can then be compared to the predictions of the SM enabling identification of potential new physics in the case of deviations from the expected outcomes.

Finally, while LHC experiments provided the groundwork for the discovery of the Higgs boson, LCs will enable a more thorough and precise characterization of its properties. The Higgs mass, for example, should be measurable with a precision of 50 MeV, further improving the results of the LHC data. In addition, the spin of the Higgs boson can be determined via the angular distribution of the Z boson and its decay products from a Higgs-strahlung process. At higher luminosities, precision measurements of the CP of the Higgs boson via the process $e^+e^- \rightarrow t\bar{t}H$ become possible, also enabling the determination of potential CP-mixing.

New physics

In regards to the search for new physics at the LC, the manifestations of physics beyond the SM (BSM) can be summarized in three different points of interest [1]:

- confirmation and refinement of previous LHC discoveries with higher precision due to the cleaner experimental environment,
- a potential for direct discoveries of new physics, in particular in terms of the search for color-neutral states and within the Higgs sector, and
- new discoveries through high precision, due to the increased sensitivity in tiny deviations from the SM, linking to new physics.

One example for the above mentioned aspects is the discovery of neutrino oscillations, as well as the need for additional sources of CP-violation in order to explain the asymmetry in the baryonic sector, as both effects cannot be explained solely with the SM. Even the Higgs boson offers room for BSM physics via the existence of additional Higgs bosons which mix with the SM-type Higgs boson. This would result in a Higgs-quintuplet, consisting of four additional Higgs-states in addition the SM one. One possible way of measuring multiple Higgs bosons lies in e.g. gauge boson couplings, namely the scattering of WW/ZZ and WW final state processes. Since these processes are investigated by analyzing the decay products of both gauge bosons into final quark states, an improved jet-energy resolution and decreased QCD background will be required and are considered achievable by future LC experiments.

The basis of the concept of multiple Higgs bosons lies in the possible existence of new electroweak matter states, which is another important aspect of the search for BSM physics. LCs should allow a more thorough analysis of their potential existence due to the increased event rate compared to the reduced strongly interacting background. The most well-known concept of new electroweak matter states is the theory of Supersymmetry (SUSY), as it provides a calculable and complete framework. Apart from the introduction of additional Higgs bosons, new scalars, different gauge charges and additional fermions are introduced to the existing SM counterparts. Thanks to the cleaner experimental environment of a LC, it is possible to produce these new states directly, improving the chances for a discovery and determination of their properties with a discovery reach of roughly $\sqrt{s}/2$.

A final example of BSM physics is given in the form of the search for dark matter. It is a well-established fact that the universe must contain a certain fraction (27%) of matter, which is practically not detectable by conventional means, thus labeled dark matter. These dark matter particles are certainly not part of SM particles but instead consist of a chargeless massive state χ that interacts with approximately weak gauge force strength [1], labeled WIMP (weakly interacting massive particle). SUSY provides a potential candidate for χ in the form of the lightest neutralino, as it shares its predicted properties. The potential for direct dark matter production at the LC is given by the process $\mathrm{e^+e^-} \rightarrow \chi\chi\gamma$, utilizing the initial-state radiated photon or gluon for event-tagging and providing information on the WIMP interaction with electrons. Thus it becomes possible to determine the WIMP mass as well as the strength and chiral structure of the $\mathrm{e^+e^-}\chi\chi$-interaction.

2.1.2 Proposed collider concepts

Currently, two different approaches for a future $\mathrm{e^+e^-}$ machine have been proposed and developed, namely the International Linear Collider (ILC) and the Compact Linear Collider (CLIC). While the technology for the ILC is generally better understood and realizable on a shorter time scale, CLIC offers the potential for higher center-of-mass energies at the cost of additional development time. Both concepts differ in their main linac acceleration scheme with the ILC utilizing superconducting RF in contrast to the separate drive beam of CLIC. A short overview of both systems will be given below. In both cases, a detailed description of the accelerators and their parameters can be found in the respective technical design reports [3, 6, 7].

The International Linear Collider

The ILC is a high-luminosity linear electron-positron collider utilizing 1.3 GHz superconducting radio-frequency (SCRF) acceleration technology with an approximate length of 31 km as depicted in its schematic in Fig. 2.2. An overview of the key parameters is listed in Table 2.1. In the initial stages, the center-of-mass energy $\sqrt{s}$ will ramp through roughly 200 GeV up to 500 GeV, while later stages will see it extended to 1 TeV.

Electrons and positrons will be injected from their respective sources and subsequently accelerated to roughly 5 GeV before entering the damping ring with a circumference of 3.2 km. The particles are then condensed into compact bunches, necessary for the final collisions, by circling the damping rings roughly 10000 times. The beams are then transported through an additional amplification stage (up to 15 GeV) into the

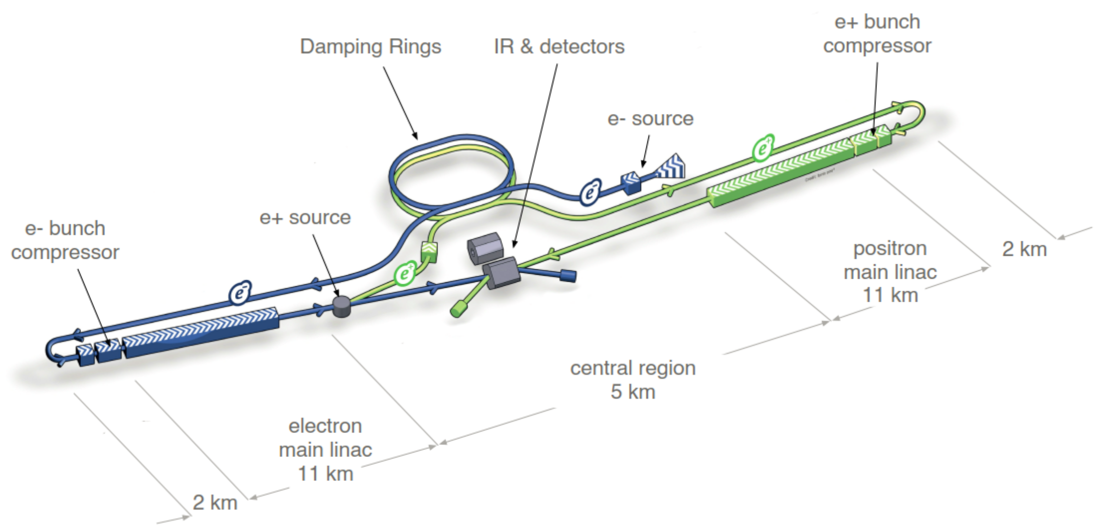

Figure 2.2: Schematic layout of the International Linear Collider (ILC) and its major subsystems. A total length of 31 km can be expected. Image taken from [8].

Table 2.1: Key parameters of the ILC design. The beam sizes are assumed at the interaction point and depict the root mean square. Taken from [8].

Parameter			Unit
$\sqrt{s}$	0.5	1	TeV
Peak luminosity	1.8	4.9	10^{34} cm^{-2}s^{-1}
Main linac average gradient	31.5	39.2	MVm^{-1}
Collision rate	5	4	Hz
Bunches per pulse	1312	2450	
Bunch population	2.0	1.74	10^{10}
Bunch separation	554	366	ns
Horizontal beam size	474	335	nm
Vertical beam size	5.9	2.7	nm

main linear accelerators, each with a length of 11 km using SCRF cavities made of pure niobium with an average gradient of 31.5 MV/m. Their operation requires cooling via liquid helium down to 2 K. It is crucial during this step to preserve the small bunch emittance established in the damping rings in order to allow for a high luminosity. Finally, two beam delivery systems, each 2.2 km long, will bring the now fully accelerated beams into collision at a single interaction point with a 14 mrad crossing angle, where the events can be analyzed with a sophisticated detector system. This step will also include additional monitoring of the key physics parameters before the collision, which also allows a refined selection of particles and removal of cases with energies and amplitudes outside the acceptable range (beam-halo), thus minimizing the background.

At $\sqrt{s} = 500$ GeV (1 TeV), the system will feature a collision rate of 5 (4) Hz with approximately 1312 (2450) bunches per collision, each containing $2 \cdot 10^{10}$ $(1.74 \cdot 10^{10})$ particles with a bunch separation time of 554 (366) ns. As a result, a peak luminosity of $1.8 \cdot 10^{34}$ $(4.9 \cdot 10^{34})$ cm^{-2}s^{-1} can be expected allowing for the realization of a top quark and Higgs factory at already early stages of operation.

The Compact Linear Collider

Compared to the ILC, CLIC aims to achieve even higher center-of-mass energies up to 3 TeV and a luminosity of $5.9 \cdot 10^{34}$ cm^{-2}s^{-1}. Its main difference to the ILC design is the main linac concept which is based on a two-beam scheme. A schematic layout of CLIC is depicted in Fig. 2.3, featuring a total length of approximately 48 km. Key parameters are listed in Table 2.2.

Similar to ILC, the electrons and positrons are injected at 2.86 GeV into the main acceleration line after passing through a two-stage damping ring and a bunch compressor for purposes of emittance reduction. Afterwards, they reach the main linear accelerator (each with a length of 21 km) which makes use of a second "Drive Beam" and its compression and reconversion into RF power, which is then being fed into the main beam. In contrast to the conventional approach found in the ILC, utilizing klystron powering, the two-beam concept is capable of achieving accelerating gradients up 100 MV/m in order to enable higher $\sqrt{s}$. The drive beam is running parallel to the main beam and consists of electrons with energies of about 2.4 GeV and a 100 A current. It then enters one

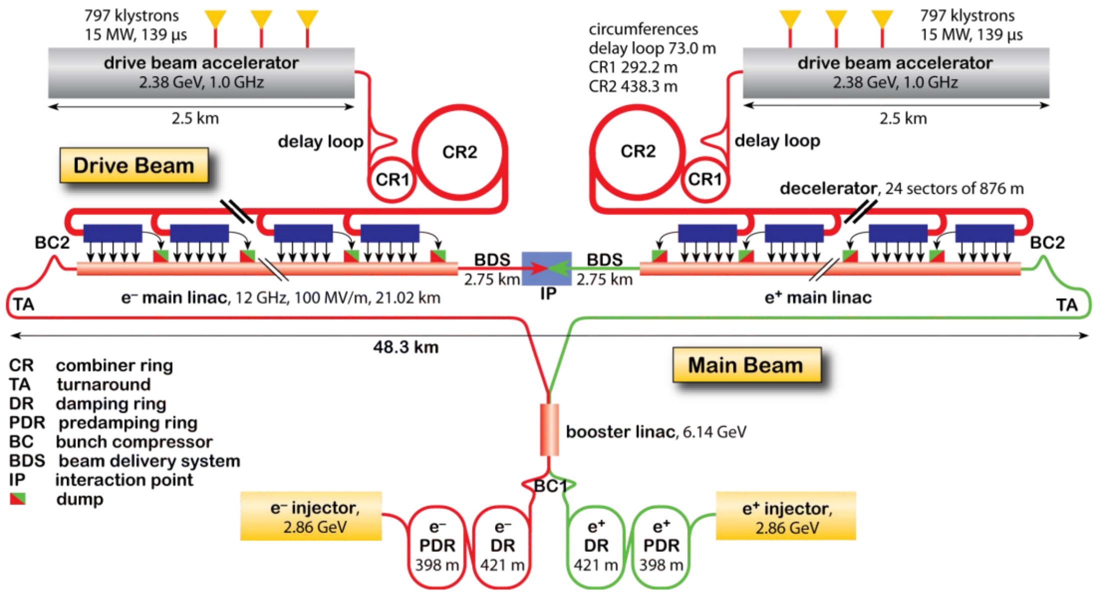

Figure 2.3: Schematic layout of the Compact Linear Collider (CLIC) and its major subsystems. Contrary to the ILC, CLIC utilizes a two-beam acceleration scheme with a drive beam (see text). Image taken from [3].

Table 2.2: Key parameters of the CLIC design. The beam sizes are assumed at the interaction point. Taken from [3].

Parameter			Unit
$\sqrt{s}$	0.5	3	TeV
Peak luminosity	2.3	5.9	10^{34} cm^{-2}s^{-1}
Main linac average gradient	80	100	MVm^{-1}
Collision rate	50	50	Hz
Bunches per pulse	312	312	
Bunch population	6.8	3.72	10^9
Bunch separation	0.5	0.5	ns
IP horizontal beam size RMS	202	40	nm
IP vertical beam size RMS	2.3	1.0	nm

of 24 sectors of decelerators, labeled power extraction and transfer structures (PETS), which convert the electron energy loss into RF power which, in turn, is collected and transferred to the main beam. Afterwards the particles enter the final beam delivery system, where the collision will take place within a dedicated detector system.

In early stages $\sqrt{s}$ can be expected to be roughly 500 GeV with a final design of 3 TeV. At peak energy, a collision rate of 50 Hz could be achieved with roughly 312 bunches per train, assuming $3.72 \cdot 10^9$ particles per bunch and a bunch separation time of 0.5 ns. This is expected to culminate in a peak luminosity of $5.9 \cdot 10^{34}$ cm^{-2}s^{-1}.

However, due to the proposed design being highly ambitious in terms of technology and requirements, certain trade-offs need to be made and are reflected in the choice of specific parameters. The main trade-off is a balance between a high luminosity and lowest possible cost. A different example is given by the high accelerating fields limiting the RF-to-beam transfer efficiency due to the creation of wakefields. Hence, a constant balance has to be aimed for during the design, as discussed in more detail in [3].

2.1.3 Examples for detector systems

In order to meet the requirements of the physics cases discussed in Sec. 2.1.1, two different detector concepts have been proposed and validated for the ILC, namely the International Large Detector (ILD) and the Silicon Detector (SiD) [9]. Both concepts are depicted in Fig. 2.4 and share the same established detector structure ("onion structure"), also found in other experiments like ATLAS, but utilize different approaches for certain subsystems. They are expected to be interchangeable during operation by means of a push-and-pull approach. In the case of CLIC, modified designs of both ILD and SiD have been proposed, as the more demanding experimental environment requires certain adaptations.

The common design consists of multiple layers surrounding the beam line and interaction point. The innermost layer is made up of the vertex detector which utilizes a multi-layer barrel layout combined with endcaps in the forward and backward regions. Its main purpose is the vertex reconstruction of primary, secondary and tertiary vertices for e.g. heavy flavor identification and it forms the first step of the tracking system. The next layers make up the main tracker, measuring the tracks of charged particles within a strong magnetic field in order to determine their momentum. While both proposals utilize silicon detectors for the vertex layers, the main tracker is being handled differently depending on the design. In the case of the SiD, the use of silicon micro-strip sensors in an all-silicon approach (as the name implies) is proposed, while the ILD utilizes a two-macro-layer approach consisting of an inner gaseous-based Time Projection Chamber (TPC) layer surrounded by an outer silicon based strip detector casing. The main tracker is then followed by the calorimeter systems, made up of an electromagnetic and a hadronic calorimenter, measuring the energy of charged and neutral particles by means of full absorption. The outermost layer in both cases entails a muon detector system, as only muons will be able to reach this layer, and can also be used for muon track-reconstructions.

In the following, a brief overview of two subsystems which offer a possible utilization of the devices investigated within this study will be presented, discussing their particular challenges and requirements for the respective detector devices.

Vertex-tracking detector

As mentioned above, one of the main aspects of the vertex detector system is the spacial reconstruction of individual vertices in order to identify the corresponding flavor parti-

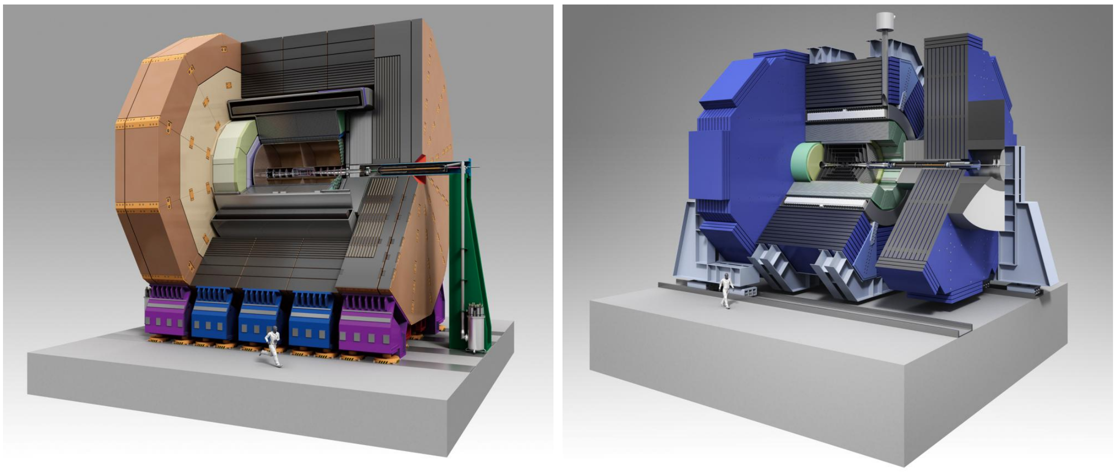

Figure 2.4: Rendered illustration of the ILD (left) and SiD (right) detector concepts. While the main structure is similar in both cases, the individual subsystems are realized in a different fashion (see text). Images taken from [10].

cles. A key component of this procedure also lies in the track reconstruction of the decay products, thus imposing the necessity for an advanced vertex tracking detector system which can fulfill the requirements set by the experimental environment of a LC. Another driving factor are Higgs studies via Higgs-strahlung and the track reconstruction of the Z boson decay products.

The case of the SiD can be taken as an example. Due to the location of the inner layers within the 5 Tesla magnetic field, a device insensitive to magnetic fields is crucial. General spatial constraints and the need for a reduction of multiple Coulomb scattering result in the requirement of a very low material budget of approximately 0.3% X_0 per layer, with X_0 being the radiation length. This would drastically improve the track reconstruction capabilities and thereby the three dimensional vertex resolution for heavy quarks. As a direct consequence, operation of the detector has to be feasible with basic air cooling as even sophisticated cooling systems with liquids would strongly increase the material budget. Hence, a low average power consumption in the order of 100 µW/mm^2 within the barrel is desirable.

A high fill factor and low occupancy are generally preferred in order to avoid a loss of space points. In addition, a hit resolution σ_{hit} in the barrel better than 5 µm is needed, implying a pixel size of approximately 17 µm according to the binary hit precision of $\sigma_{hit} = (\text{Pixel size})/\sqrt{12}$ [11]. Finally, a fast readout system will be needed since a single bunch time resolution has to be achieved which amounts to 366 ns in the case of the ILC. As is the case for the majority of high energy physics experiments, the radiation hardness of the detector devices also play a central role in the choice of material and detector systems. Even though the experienced radiation background can be expected to be much less compared to the LHC, care needs to be taken to ensure acceptable device performance even after multiple years of operation during radiation exposure.

Currently, a number of possible choices of different technologies are being considered for this purpose. Some examples include the Monolithic Active Pixel Sensor (MAPS), the CMOS Pixel Sensor (CPS) and the Depleted Field Effect Transistor (DEPFET). However, in recent years, the utilization of Geiger-mode avalanche photodiode arrays as tracking pixel detectors was suggested [12]. Their main advantages in this regard stem from their fast timing and readout in the sub ns range, low power consumption and high sensitivity towards charged particles.

Calorimeter readout

The calorimeter system consists of two subsections, namely the electromagnetic and the hadron calorimeter. While photons and electrons will get absorbed in the former, charged and neutral hadrons will traverse this first layer and start interacting in the latter. The absorption of the subsequently generated particle jets allows for determination of the primary particles properties. However, the current low-granularity calorimeter technologies do not offer sufficiently high resolution jet energy reconstruction and di-jet mass performances, thus a novel approach was developed for high-granularity calorimeter systems, named the Particle Flow Algorithm (PFA). This technique utilizes the fact that a large fraction of energy deposits in the calorimeter originate from charged tracks which can be previously measured by the tracking system. Thus, combining the tracking data with the calorimeter measurements, offers a suitable solution, further underlining the importance of an adequate tracking system.

A common approach for the design of calorimeters is a sandwich structure, alternating between a passive absorber material like steel and an active material like plastic scintillators. Traversal of particles through these scintillators will cause light emission, which requires a dedicated readout system. In order to achieve the high granularity requirements, a compact photodetector, unaffected by magnetic fields is needed. Furthermore, and similar to the previous section, a low power consumption and fast timing will be required.

The CALICE (Calorimeter for the Linear Collider Experiment) collaboration was able to obtain promising results with the Analogue Hadron Calorimeter (AHCAL) prototype by implementing Silicon Photomultipliers (SiPM) for the scintillator readout in a test beam environment [13]. While the first prototype required wavelength shifting fibers in order to accommodate the sensitivity peak of the deployed device, the next generation of AHCAL aims to utilize new SiPM technology, which offers peak sensitivity within the characteristic wavelength of the scintillating material, thus omitting the need for wavelength shifting fibers.

The technology of the devices of this study can also be adapted towards the same ends, thus making them a possible candidate for future prototype runs of similar experiments as will be investigated later.

2.2 Astroparticle physics with Cherenkov telescopes

Shifting from the small scale events taking place at high energy collider experiments to the other end of the scale-spectrum leads to cosmic ray observation within astroparticle physics. As an example, cosmic gamma-rays in the energy range of GeV to TeV cannot be generated by thermal emission from hot celestial bodies. Hence, mechanisms other than thermally based ones, are required to explain the observed existence of the latter. The investigation of high energy gamma-rays and the determination of their origin can thereby offer insight on topics such as dark matter annihilation as well as the evolution of our own and other galaxies. A sky map projection, produced by summarizing the data of nine years of operation of the Large Area Telescope on board of the Fermi Gamma-ray Space Telescope, seen in Fig. 2.5, reveals a high density of gamma-ray sources within our galaxy.

The observation of gamma-rays is a comparatively young field of science due to its dependency on technological developments, i.e. the necessity for space-based instrumentation, since terrestrial surface detection is difficult, especially for the low end of the gamma-ray spectrum because of absorption within the earths atmosphere. On the

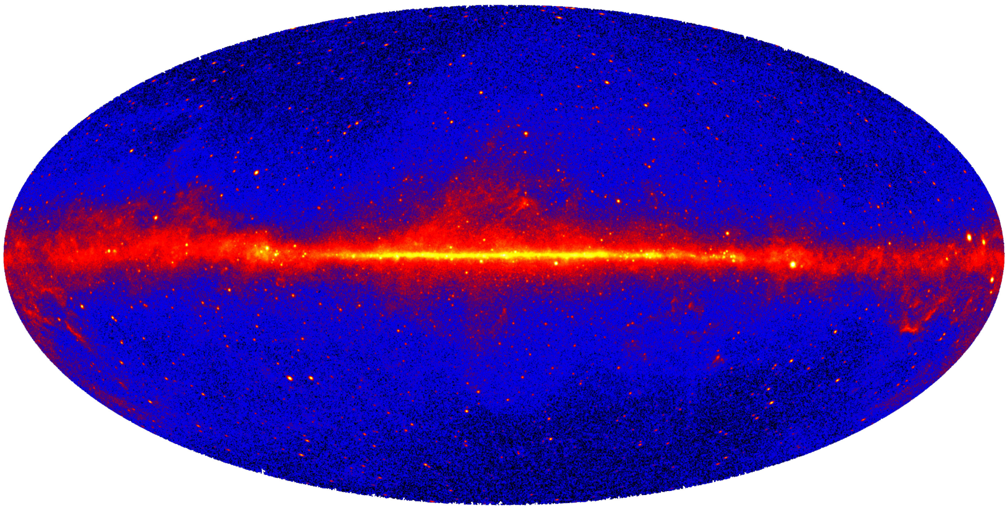

Figure 2.5: Hammer-Aitoff projection of the nine year data map of the Large Area Telescope on board of the Fermi Gamma-ray Space Telescope. Brighter colors indicate a higher number of gamma-ray sources. Image taken from [14].

other hand, even satellite-based detection displays clear limitations, as high-energy photon absorption imposes certain requirements on the size and weight of the calorimeter system to be launched by a rocket. In addition, the scarcity of such events ($\mathcal{O}(10^{-11})$ photons/(cm^{2}s) [15]) also complicates their observation compared to the existing background events. However, high energy gamma-rays will interact within the atmosphere, namely with atmospheric nuclei via pair-production and subsequent bremsstrahlung and generate a shower of secondary particles (electron, positrons, photons), which, in turn, will traverse the upper atmosphere with velocities v higher than the speed of light in air c'. They will consequently start emitting Cherenkov light, which can then be detected by ground-based Cherenkov telescopes. This method is called Imaging Atmospheric Cherenkov Technique (IACT) and is summarized in Fig. 2.6.

The Cherenkov angle Θ describes the emittance angle of the Cherenkov light with respect to the propagation direction of the particles and is given by

$$\cos(\Theta) = \frac{c'}{v} = \frac{1}{\beta n} \,, \tag{2.1}$$

where n is the refractive index of the medium, $c' = c/n$ and $\beta = v/c$. The intensity and the geometrical extension of the Cherenkov light cone can be used to determine the energy of the primary high energy gamma-ray. For initial energies in the TeV range, the maximum shower development takes place at roughly 10 km above sea level, leading to $\Theta < 0.7°$ and resulting in a ground coverage within a light cone of approximately 100 m to 150 m size, depending on the height above sea level of the detector system [15]. By reconstructing the shower axis, the primary gamma-ray can be traced back to its origin, in both spatial location and potentially type of phenomenon.

Due to the IACT utilizing the entire atmosphere, the effective area and hence coverage is significantly larger ($\mathcal{O}(10^5)$ m^2) compared to conventional satellite based instruments. However, as mentioned above, the rarity of the events in question requires the use of large optical reflectors (parabolic mirrors) in order to collect enough light, which then can be detected by the dedicated detector systems. Since the Cherenkov light emission is in the optical spectrum, operation of such ground-based telescopes can

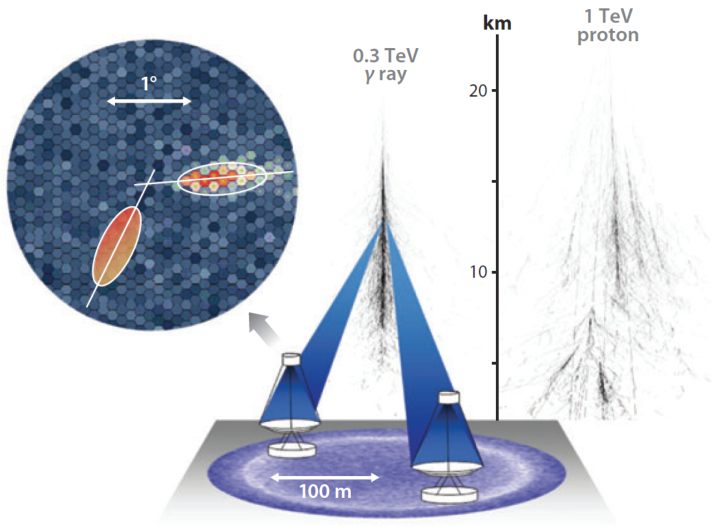

Figure 2.6: Illustration of the Imaging Atmospheric Cherenkov Technique (IACT). The formation of an electromagnetic shower for a 300 GeV gamma-ray is depicted and the resulting Cherenkov radiation as blue cones. The resulting image within the detection camera can also be seen. For comparison, a cascade created by a hadron (here: 1 TeV proton) is given, leading to a much broader and extended shower. Image taken from [15].

only be carried out in dark nights at clear skies. Regardless of the implementation of the aforementioned light collection, the overall light levels are still exceedingly low and occur only in short pulses in the range of a few ns, thus a fast and low light level sensitive imaging system for detection will be required.

The following will give a brief overview of the physics program of gamma-ray astronomy and will be followed by examples of said imaging systems for Cherenkov telescopes.

2.2.1 Physics cases for gamma-ray astronomy

In astrophysical research it is of general interest to identify the sources of cosmic rays. However, interstellar and intergalactic magnetic fields will bend the electrically charged component of the cosmic spectrum, therefore all information regarding direction and origin is lost for these rays from distant sources. One major exception to this, however, are the gamma-rays which carry no electric charge and are therefore unaffected by the interstellar/intergalactic magnetic fields.

The creation of highly energetic gamma-rays can stem from a multitude of fundamental processes, based on the interaction of charged particles (electrons/positrons or nuclei) with magnetic fields or ambient matter [15]. The primary goal of gamma-ray physics is then to establish in which cosmic sources or events such particle acceleration takes place. Even though the basic acceleration mechanisms are known, the exact origin or process behind it, is not fully understood up to now.

Gamma-rays will be created in a secondary process from highly energetic charged particles, by e.g. synchrotron radiation in a magnetic field or by emission of bremsstrahlung in the electric field of a nucleus in the interstellar medium. Furthermore, relativistic electrons are capable of transferring their energy to photons via inverse Compton scattering. In addition, collision of hadrons with other hadrons can result in the creation of neutral pions, which will decay into a pair of gamma-rays. Finally, gamma-ray generation via matter-antimatter annihilation makes up another possible origin.

Taking this into account, the goals of a gamma-ray astronomy project can then be summarized into three main topics, serving as the key science drivers [16]:

- understanding of the origin of high-energy cosmic rays and their impact on the universe,
- investigation of the nature and different types of acceleration processes around black holes, and other celestial objects and
- search for physics beyond the SM with the main focus on dark matter.

The first issue generally deals with the process of galactic particle accelerators and the impact of the accelerated particles on the environment. Current astroparticle physics instruments have proven particle acceleration to energies up to 10^{14} eV. While it is commonly accepted that supernovae remnants are responsible for a certain percentage of cosmic rays (CRs), it cannot be proven that they accelerate the bulk of all detected CRs.

An alternative is given by pulsars, which are rotating neutron stars, emitting electromagnetic radiation. These objects are also acting as efficient accelerators, however, up to this date, no complete and accepted model for the acceleration mechanism has been established. The process involves electrodynamics at very high magnetic fields in addition to effects of general relativity, thus measurements at extreme energies are required. A direct result of pulsars, are pulsar wind nebulae, an example being the crab nebula, which in turn are believed to make up the most populous class of identified gamma-ray sources.

Binary systems, consisting of a very compact object, like a neutron star or black hole (microquasar), orbited by a massive star are also known to act as gamma-ray emitters. These system still offer many unanswered questions since in some cases the direct energy source for the acceleration mechanism cannot be identified and could be attributed to either the accretion disk surrounding a black hole or a pulsar-driven nebula around the neutron star.

As already mentioned, the study of black holes is of major importance in the context of gamma-ray physics. The previous point mentioned binary systems with microquasars, but even standalone, these small scale black holes with radiation emitting accretion disks can offer new insights. Many physics aspects of microquasar within the Milky Way resemble processes of super-massive black holes of distant active galaxies. However, due to the reduced time scale, insight in the evolution and characteristics of super-massive black holes can be obtained within a reasonable time frame.

Super-massive black holes, commonly expected in the center of galaxies, also offer a means to study gamma-rays due to their highly energetic accretion disks. The closest example and one of the prime candidates for future gamma-ray astronomy is the Milky Ways galactic center, Sagittarius A*. Due to the increased observation resolution and sensitivity, a variety of results on particle acceleration and gamma-ray production near black holes can be expected. Furthermore, extragalactic Active Galactic Nuclei (AGN) have historically been some of the earliest discoveries by the IACT [15]. Due to AGNs being among the most energetic objects in the known cosmos, they also offer an excellent source of gamma-rays. Initial observations showed a fast oscillating gamma-ray flux, indicating their production close to the black hole, opening up the possibility of new discoveries. In addition to the accretion disk, AGNs exhibit particle radiation at their poles in a cone-shaped manner, called jets. If an AGN is oriented in a fashion that these jets are directed towards the earth, it is labeled a blazar and produces very high energy gamma-rays which can be observed via IACT. Since both the emission of the gamma-rays of black holes and the composition and origin of their jets is still not fully understood, the investigation of said topics will be one of the major focuses of future Cherenkov telescopes.

Further increasing the scale, galaxy clusters, the largest gravitationally bound objects, are considered a "storehouse" of CRs, because all CRs produced in their galaxies since the beginning of the universe are expected to be stored within [16]. Probing of their CR via the generated gamma-rays might therefore give insights on the early stages of galaxies and their non-thermal output. Estimates predict levels below the current level of instrument sensitivity, thus future IACT-based applications aim at improvements towards this goal.

Gamma-ray bursts are considered to be the most powerful explosion in the known universe, resulting in the most luminous light sources, which can be detected up to very high redshifts. They should thereby contain information about the history of star formations and the reionization of the universe. In addition, a thorough investigation of their intrinsic spectrum and acceleration mechanism will be required in order to determine if they are responsible for the highest energy particles detected in the universe.

Finally, mechanism beyond the SM might also play a pivotal role in the creation of gamma-rays, thus potentially allowing the determination of complementary data to the results obtained from high energy physics experiments like the LHC or the future LC discussed above. According to certain BSM physics models, dark matter particles are capable of annihilation processes, leading to the creation of gamma-rays. Assuming increased densities of dark matter close to gravitational wells like black holes, a detectable flux of gamma-ray creation can be expected, since the annihilation rate is proportional to the square of the density [16]. Furthermore, said dark matter particle annihilations are also expected to result in an almost mono-energetic photon emission and hence, spectral line. Future IACT based applications like the CTA (see below) aim to improve their sensitivities and angular resolution in order to allow detection of such fluctuations and spectral lines, thereby attempting to find conclusive evidence for dark matter.

A more in-depth discussion regarding the astroparticle physics case for gamma-ray astronomy with IACT based applications can be found in [15–17].

2.2.2 Low light level detector systems for future Cherenkov telescopes

Since the implementation and evolution of IACT telescopes, major astrophysical discoveries via the observation of over 150 gamma-ray sources was achieved [17], demonstrating the physics potential and reliability of the measurement method. Three of the major arrays are the High Energy Stereoscopic System (H.E.S.S.), located in Namibia [18], the Major Atmospheric Gamma-Ray Imaging Cherenkov Telescopes (MAGIC), located in La Palma (Canary Islands) [19] and the Very Energetic Radiation Imaging Telescope Array System (VERITAS), located in Arizona (USA) [20] and were decisive in this endeavor. However, if a survey of the complete visible night sky would be attempted with these array systems, the duration would expand over a decade, which is considered unfeasible.

The present telescope arrays can reach sensitivities of roughly 1% of the flux of the Crab nebula in an energy range of 100 GeV up to 1 TeV with a quickly degrading sensitivity towards lower and higher energies due to threshold effects and a limited detection area, respectively. For comparison, the detection of gamma-rays above 10 TeV within an observation cycle of 50 hours would require several square km detection area. Hence, the next generation of IACT based telescope arrays aims to build upon the discoveries of the previous arrays in order to improve the sensitivity by a factor of 10 [16]. This will be achieved by, among other things, increasing the detection area, thus also

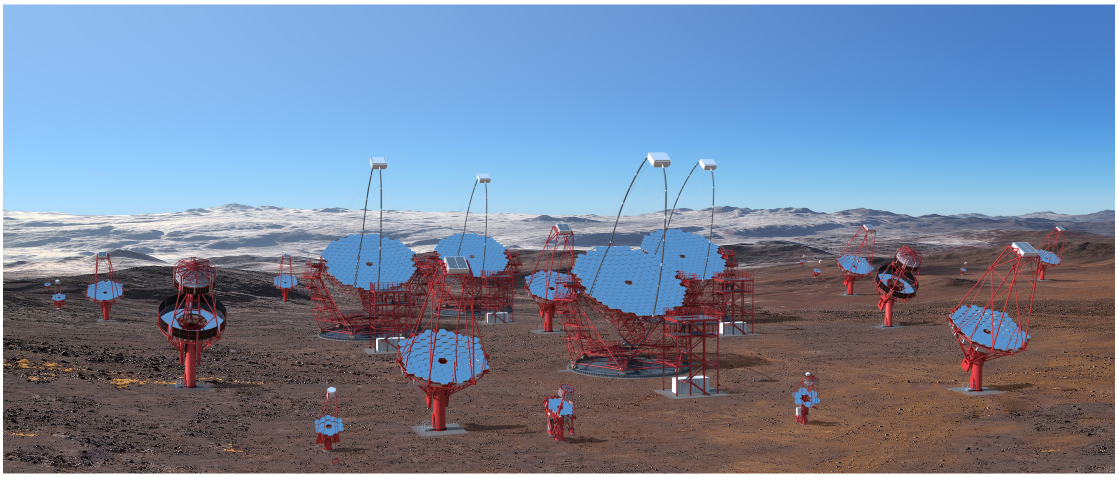

Figure 2.7: Rendered image of a possible layout for the Cherenkov Telescope Array (CTA) on the southern hemisphere location. The three different telescope sizes (small (SST) with 4 m diameter, medium (MST/SCT) with 12 m diameter, large (LST) with 23 m diameter) can be seen. Image taken from [21].

enabling detection of shorter timescale phenomena. Furthermore, by implementing an additional site at the other hemisphere, access to the entire night sky can be provided.

This new generation will be realized in the form of the Cherenkov Telescope Array (CTA), featuring arrays in La Palma (northern hemisphere) and in the Atacama Desert (Chile, southern hemisphere). Three different sizes of telescopes will be deployed at the CTA, namely the Small-Sized Telescopes (SSTs), the Medium-Sized Telescope (MST) with a dual-mirror variation called the Schwarzschild-Couder Telescope (SCT) and finally the Large-Sized Telescope (LST). A rendered impression of a possible layout including all aforementioned telescope types is depicted in Fig. 2.7. The main focus of the northern CTA will be low- and mid-energy ranges from 20 GeV up to 20 TeV, thus resulting in a smaller array size without deployment of any SSTs, as they are utilized for the highest energy gamma-rays, while the LSTs are used for the lowest-energy spectrum, respectively. In contrast, the southern CTA will cover energies up to 300 TeV and feature all telescope variations with a total number of 99 telescopes covering an area of 4 km^2. However, with the increased array size also comes the need for a large amount of photon detectors able to fulfill the technical requirements imposed by the application.

As already mentioned in the previous section, gamma-ray signals can be highly red-shifted, leading to small cascades and thereby low light levels. Hence detectors sensitive to only low amounts of light are required. In addition, gamma-ray signals are found to appear in short burst, thus fast timings in the range of a few ns in detectors will be preferred. The energy threshold for the minimum detectable energy can be reduced by increasing the photon detection efficiency of the devices, or by an increase of the maximum mirror size and thereby light collection.

Due to the gamma-ray showers being detected via Cherenkov radiation, the intensity spectrum can be derived and is generally proportional to $1/\lambda^2$, with λ being the wavelength, resulting in increased intensities towards the ultraviolet and blue regime [22]. However, shorter wavelengths are absorbed by the atmospheric ozone, which will lead to an abrupt drop-off below $\lambda = 300$ nm. The Cherenkov spectrum is given in Fig. 2.8 (red line), depicting this drop-off and a peak intensity at $\lambda \approx 350$ nm with a steady decrease for increasing wavelengths. The green line illustrates the night sky background spectrum, featuring distinct peaks in the regime $\lambda > 550$ nm. Hence, a photon detector

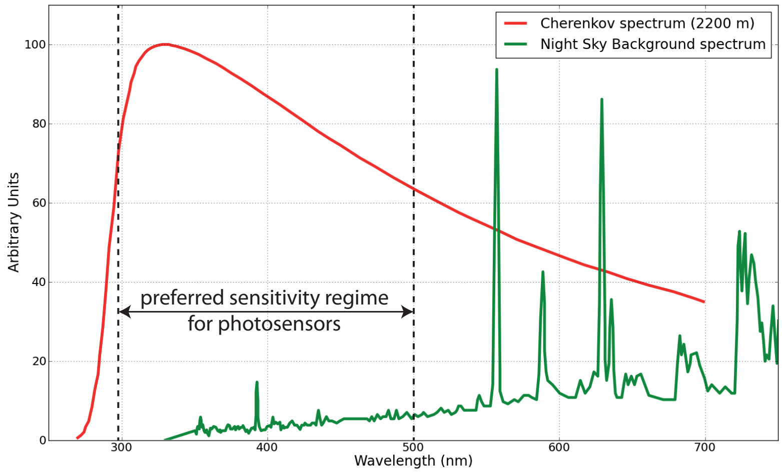

Figure 2.8: Cherenkov emission spectrum for a wide range of wavelengths (red line). Peak intensities can be found at lower wavelengths with a sharp cut-off at $\lambda \approx 300$ nm due to absorptions in the atmospheric ozone. An overall peak can be seen at $\lambda \approx 350$ nm. For comparison, the spectrum of the night sky background (green line) is included, showing distinct peaks at longer wavelengths. Hence, the preferred sensitivity regime is illustrated. Image adapted from [23].

sensitive to wavelength in the range of 300 nm $< \lambda <$ 500 nm with a preferred peak at $\lambda \approx 350$ nm and insensitivity for $\lambda > 500$ nm is desirable for the deployment at the CTA, in order to minimize noise contribution from the night sky background. This can be achieved by optical filters and surface coating.

An additional prerequisite is given by the desired durability of the detectors in regards to high light level exposure, since observations during bright moonlight phases are a necessity for long-term observation cycles. Detectors with noticeable aging effects are therefore sub-optimal as they will likely not be able to survive such prolonged high-level exposures over multiple years of operations. Furthermore, due to the increased coverage and amount of telescopes, devices with reduced cost are preferred. A low power consumption and small dimension are generally advantageous, as additional cooling can be omitted and potentially higher pixel counts can be achieved, respectively.

The current generation of telescope arrays has been utilizing matrices of roughly 500 to 2000 Photomultiplier Tubes (PMTs) as the photon sensor. However, one of the main drawbacks of PMTs are the prevalent aging effects limiting prolonged high-light level exposure and general life time. In recent years, on the other hand, SiPMs have solidified their place as a promising alternate technology, since they are able to meet the above mentioned requirements while also avoiding the drawbacks of PMTs. This was further cemented by the results of the First G-APD Cherenkov Telescope (FACT), which, as the name suggests, utilized Geiger-mode avalanche photo diodes to confirm their performance in IACT based applications.

Studies like [24] have shown the possibility of measurements during bright moon light under stable trigger conditions, while maintaining voltage and gain stability on the level of a few percent. In addition, Monte Carlo simulations of the dark count spectrum showed matching results with actual measurements, allowing for proper detector simulations offline. Nevertheless, novel improvements of SiPM devices will have the capability of further enhancing the camera performance at the deployed telescope arrays, be it by increasing the photon detection efficiency or reducing the pixel size in order to improve their resolution and dynamic range. Thus, dedicated technological development, as was one of the major goals of this study, will always be of utmost importance.

3 Physics of semiconductor detectors and light detection

Light detection with semiconductor based detectors requires understanding of not only the fundamental processes of photon interaction with matter, but also of the general working principle of the detector itself. This, in turn, can be achieved by investigation of the basic semiconductor properties, leading towards the more sophisticated discussion of avalanche based semiconductor photon detectors. Furthermore, by understanding the underlying processes of photon-matter and particle-matter interactions, adaptation of the detectors towards the necessities of specific applications becomes possible.

Hence, this chapter will provide a discussion to the above mentioned topics in order to enable a better understanding of the studies and investigations of this thesis. First, basic semiconductor properties like the *pn*-junction, charge generation and recombination as well as impact ionization will be elucidated. This will be followed by an introduction to the basic methods of interaction between photons and matter, as well as between charged particles and matter, since these very interactions allow detection of said sources within detectors. Finally, the basic working principle of a silicon photomultiplier detector will be explained by deriving its properties from basic avalanche photo diodes and Geiger-mode avalanche photo diodes.

The majority of the information listed in this chapter is readily available in textbooks dealing with these topics, such as [22, 25–32] and was obtained from these if not stated otherwise.

3.1 Semiconductor properties

The properties of semiconductors are the basis for understanding the working principles of a semiconductor based detector. In the case of avalanche photon detectors, the properties of the *pn*-junction play an important role as many of their characteristics can be derived from said properties. Generation and recombination of charge carriers also needs to be considered as it has a crucial impact on the dynamic of many sensor types and represents part of the basis for the discussion of radiation damages in semiconductors. Finally, since this study will focus on detectors utilizing internal charge multiplication to create an avalanche, the process of impact ionization leading towards an avalanche breakdown needs to be discussed in detail.

This section will focus on the above topics, while assuming a general knowledge of basic semiconductor properties like doping of semiconductors and the band model, easily found in many textbooks (see above).

3.1.1 The pn-junction

Bringing two extrinsic semiconductors of opposite doping types, meaning a n-type and a p-type respectively into contact, a p-n junction will be established at the contact area. Without any external excitations impacting the structure, a state of thermal equilibrium can be assumed. This, in turn, postulates a uniform Fermi level within both sections of

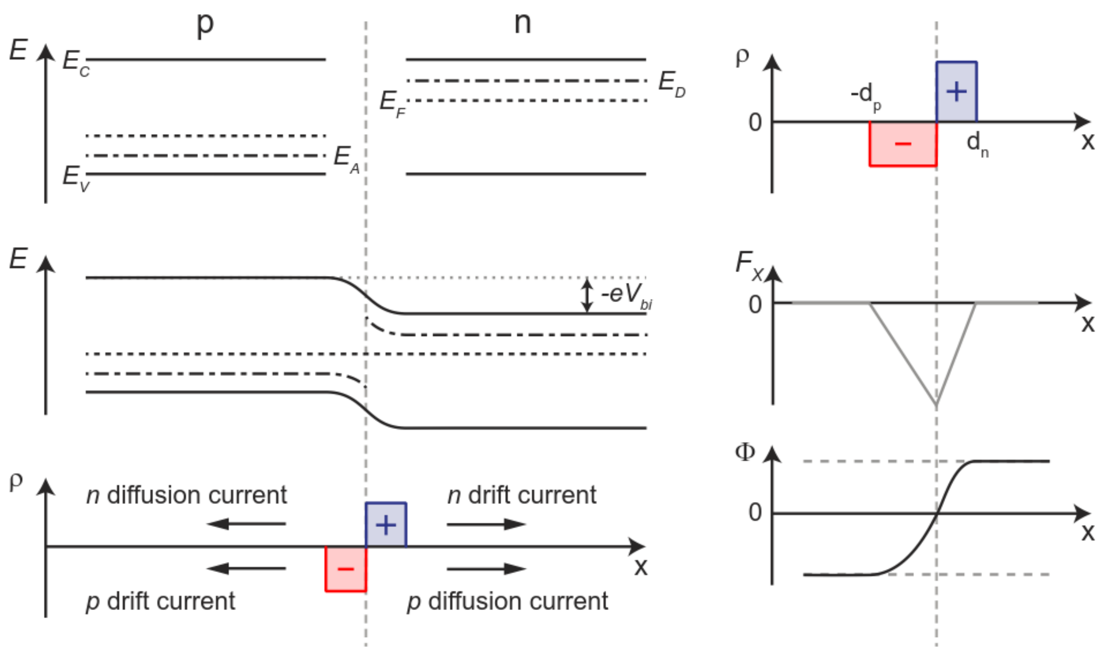

Figure 3.1: Schematic overview of an abrupt p-n junction. The energy band diagrams for n and p material and the subsequent band bending when both come into contact is depicted on the left. The resulting drift and diffusion currents for electrons and holes are shown below. The width of the depletion region can be seen to consist of d_n and d_p and features the maximum electric field at the junction line (see right hand side). Picture taken from [33].

the p-n junction, leading to a bending of the conduction and valence band at the junction region as seen in Fig. 3.1. Due to the high mobility of the electrons in the n-type and holes in the p-type semiconductor as well as the opposite charges in both areas of the junction, a diffusion of charge carriers will take place. The diffusion of electrons into the p-area and of the holes into the n-area will leave behind positively charged donor atoms and negatively charged acceptor atoms, creating an electric field counteracting the diffusion current, until an equilibrium state is reached. Afterwards, this junction area, also called space charge region or depletion region, will be void of free charge carriers and will extend with d_n into the n-side and d_p into the p-side.

The total electrostatic potential difference between the n-side and p-side in thermal equilibrium is called the built-in voltage V_{bi}. It can be derived by utilizing the Poisson equation

$$\frac{\mathrm{d}^2\Psi}{\mathrm{d}x^2} = -\frac{\rho_s}{\epsilon_0\epsilon_r} = -\frac{q_0}{\epsilon_0\epsilon_r}\,(N_D - N_A + p - n)\ , \tag{3.1}$$

with Ψ being the electrostatic potential, ρ_s the charge density, q_0 the elementary charge, ϵ_0 the vacuum permittivity, ϵ_r the relative permittivity, N_D and N_A the doping densities of donors and acceptors and n and p the electron and hole densities. Since there are no free charge carriers in the depletion region, $n = p = 0$ can be assumed and by taking into account the boundary condition of charge neutrality

$$N_D - N_A = 0\ , \tag{3.2}$$

the term for the built-in voltage results in

$$V_{bi} = \frac{kT}{q_0} \ln\left(\frac{N_D N_A}{n_i^2}\right) , \tag{3.3}$$

where k denotes the Boltzmann constant, T the temperature and n_i the intrinsic carrier concentration of silicon. The latter is given by

$$n_i = \sqrt{N_C N_V}\, e^{-\frac{E_g}{2kT}} \tag{3.4}$$

and N_C and N_V represent the effective densities of states in the conduction and valence band, respectively. The commonly accepted value for the intrinsic carrier concentration of silicon at 300 K is $n_i = 9.65 \cdot 10^9\ \mathrm{cm}^{-3}$ [25].

As mentioned above, the depletion region will extend in both the n and p-sides of the junction with a total width of the depletion region of $d_{bi} = d_n + d_p$. Making use of Eq. (3.1) and of the overall space charge neutrality within the depletion region

$$N_D d_n = N_A d_p , \tag{3.5}$$

an expression for d_{bi} in thermal equilibrium can be obtained:

$$d_{bi} = \sqrt{\frac{2\epsilon_0\epsilon_r}{q_0}\, V_{bi} \left(\frac{N_D + N_A}{N_D N_A}\right)} . \tag{3.6}$$

The last term can be defined as an effective doping concentration

$$N_{\mathrm{eff}} = \frac{N_D N_A}{N_D + N_A}. \tag{3.7}$$

If the doping concentration on one side of a p-n junction is much higher than that of the other side, the junction is referred to as an one-side abrupt junction. As an example, such a p^+-n junction can be achieved by having a highly doped p^+-side compared to the n-side. Equation (3.5) then dictates that the resulting space charge region will mainly expand into the n-type material, hence one can speak of a n-type bulk. In this case the effective doping concentration for the depletion region can be simplified to $N_{\mathrm{eff}} \approx N_D$. The opposite case with a p-type bulk can be derived accordingly.

Considering an one-side abrupt junction, the relation between N_{eff} and the resistivity ϱ of the bulk material is given via

$$\varrho = \frac{1}{q_0 \mu_x |N_{\mathrm{eff}}|} , \tag{3.8}$$

where μ_x is the respective mobility of the charge carriers depending on the type of bulk, meaning electron mobility μ_n in the case of a n-type bulk and hole mobility μ_p in case of a p-type bulk.

If an external voltage V is applied across the junction the equilibrium state is no longer present and d_{bi} becomes dependent of the applied voltage:

$$d(V) = \sqrt{\frac{2\epsilon_0\epsilon_r}{q_0 |N_{\mathrm{eff}}|}\, (V_{bi} - V)} . \tag{3.9}$$

Applying a positive voltage to the p-side with respect to the n-side results in a forward bias of the junction, in which case the total electrostatic potential of the junction is reduced by $V > 0$ and $d(V)$ decreases accordingly. On the other hand, the case inverts for a positive voltage on the n-side with respect to the p-side, resulting in a reverse biased junction with an increased potential by $V < 0$ and therefore a higher $d(V)$.

From Eq. (3.9), it can be seen that continued increase of the reverse bias voltage will also lead to a continued increase in depletion depth $d(V)$. However, a limit is set upon reaching the surfaces of the depleted material in question or other highly doped regions with orders of magnitude higher doping concentrations that the depleted bulk. In such a case the device (or the specific part of it) will be in full depletion with d_{depl} and the corresponding external voltage required for this state is called full depletion voltage

$$V_{depl} = \frac{q_0}{2\epsilon_0\epsilon_r} \, |N_{\text{eff}}| \, d_{depl}^2 - V_{bi} \; . \tag{3.10}$$

A fully depleted p-n junction with area A can be interpreted as a parallel plate capacitor with a plate distance of d_{depl}. Hence the common capacitance formula can be applied to obtain the capacitance of the full depletion layer of the junction

$$C_D = \frac{dQ}{dV} = \epsilon_0\epsilon_r \frac{A}{d_{depl}} \; , \tag{3.11}$$

where dQ represents the change of the depleted charge over an incremental voltage step dV. By combining Eq. (3.9) and (3.11) the following term can be derived:

$$\frac{1}{C_D^2} = \frac{2(V_{bi} - V)}{q_0\epsilon_0\epsilon_r|N_{\text{eff}}|A^2} \; . \tag{3.12}$$

This states that plotting $1/C_D^2$ versus V will produce a straight line with a slope given by N_{eff} until full depletion is reached, whereafter $1/C_D^2$ will plateau at a nearly constant value even after increasing the external voltage.

In addition to altering the depletion depth, breaking of the thermal equilibrium via an external voltage will also impact the current dynamics within the device as the counterbalance between drift and diffusion will be disturbed. Under idealized assumptions, no current will be generated withing the depletion region. Currents will only be flowing from the neutral boundary regions due to the external voltage. Utilizing the steady-state continuity equation, a expression for the characterization of the current dynamics can be calculated:

$$I(V) = I_s \left(e^{\frac{q_0 V}{kT}} - 1 \right) \; . \tag{3.13}$$

This is called the ideal diode equation or Shockley diode equation with I_s being the saturation current

$$I_s = \frac{q_0 D_n n_{p0}}{L_n} + \frac{q_0 D_p p_{n0}}{L_p} \; . \tag{3.14}$$

Here $D_{n,p}$ represent the diffusion coefficients of electrons and holes, n_{p0} and p_{n0} the equilibrium electron density in the p-side and the equilibrium hole density in the n-side, respectively. The diffusion length for electrons is defined as $L_n = \sqrt{D_n \tau_n}$, where τ_n is the recombination lifetime of electrons in the p-side and vice versa for L_p.

3.1.2 Generation-Recombination and Shockley-Read-Hall statistics

As established in the previous section, applying an external voltage across a p-n junction will disturb its thermal equilibrium condition $pn = n_i^2$. However, there are processes in place to restore this condition: recombination and thermal generation. On one hand, for a forward biased junction $pn \gg n_i^2$ holds true and recombination becomes the dominant process. Examples for this are band-to-band electron-hole recombinations by emission

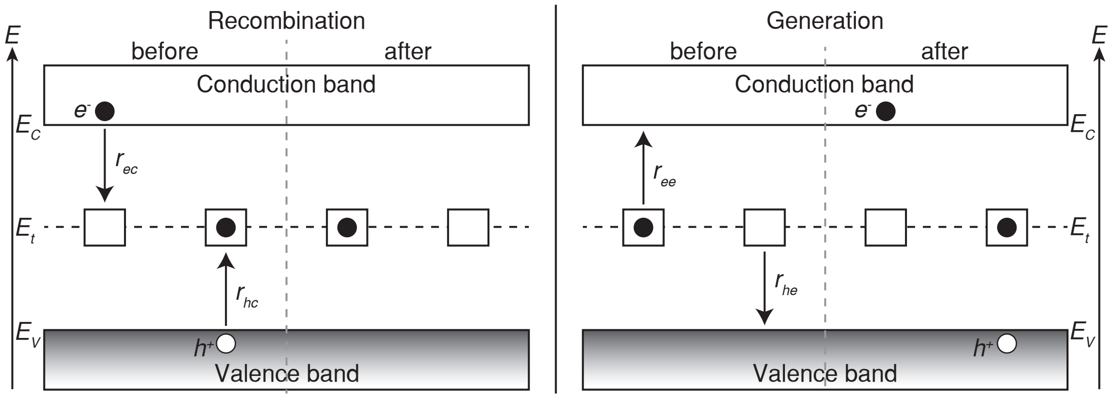

Figure 3.2: Illustration of the processes involved in the Shockley-Read-Hall statistics with reaction rates r_{ec}, r_{hc}, r_{ee} and r_{he} (inspired by [25]). The two recombination processes are shown on the left, while the generation processes can be seen on the right. In all cases, the situation before and after the transition of the involved charge carrier (electron e^- or hole h^+) is displayed. The trap shown is located at E_t withing the bandgap and neutral when not occupied by an electron and exhibits a negative charge if occupied by an electron. The processes are namely a) electron capture, b) hole capture, c) electron emission and d) hole emission (see text).

of a photon by the electron in the conduction band in order transition into the valence band, or the Auger process, in which the energy of the electron or hole is transferred to another electron or hole in the respective energy band. On the other hand, $pn \ll n_i^2$ becomes true for the reverse bias scenario, where generation is the leading process.

For indirect bandgap semiconductors like silicon however, those direct recombination processes are very unlikely, because additional lattice interactions would be required. In their cases similar processes can be achieved via impurities that produce energy states located in the forbidden bandgap. These impurities may stem from native defects such as vacancies in the lattice or even chemical impurities and are always present in a real semiconductor. With these additional energy states present, generation and recombination becomes dominated by indirect transitions. Considering only single-level defects or trap states, the occupation of the trap states as well as the transition of charge carriers from and into the energy bands are described by Shockley-Read-Hall statistics [34, 35]. According to Shockley-Read-Hall (SRH), the dynamic of the problem can be expressed in four statistical processes that can be described with different reaction rates. Those processes are depicted in Fig. 3.2 and can be summarized to the following:

a) Recombination via an electron from the conduction band being captured by a trap state (electron capture) with a rate

$$r_{ec} = c_n n p_t \tag{3.15}$$

b) Recombination via a hole from the valence band being captured by a trap state (hole capture) with a rate

$$r_{hc} = c_p p n_t \tag{3.16}$$

c) Generation via an electron being emitted by a trap state into the conduction band (electron emission) with a rate

$$r_{ee} = \epsilon_n n_t \tag{3.17}$$

d) Generation via a hole being emitted by a trap state into the valence band (hole emission) with a rate

$$r_{he} = \epsilon_p p_t \tag{3.18}$$

Here n_t and p_t denote the fraction of trap states occupied by electrons and holes respectively. The emission probability for electrons (holes) is given by ϵ_n (ϵ_p) and the capture coefficient by c_n (c_p).

After lengthy calculations the net transition rate U_{SRH} for charges taking all four processes into account can be obtained:

$$U_{\mathrm{SRH}} = \frac{\sigma_n\ \sigma_p\ \nu_{th}\ N_t\ (pn - n_i^2)}{\sigma_n\ \left(n + n_i\ e^{\frac{E_t - E_i}{kT}}\right) + \sigma_p\ \left(p + n_i\ e^{\frac{E_i - E_t}{kT}}\right)}\ , \tag{3.19}$$

where σ_n and σ_p are the electron and hole capture cross sections, respectively, N_t the trap level density and E_t its energy level and ν_{th} the thermal velocity. Considering the situation of the reverse biased junction, generation via electron and hole emission processes is dominant and recombination can be neglected since number of free charge carriers is negligibly small $pn \ll n_i^2$. Furthermore, it can be seen from Eq. (3.19) that U_{SRH} peaks for energy levels of the trap states close to mid-gap $E_t = E_i$. Consequently only such trap states will contribute to the generation current present in a reverse bias *p*-*n* junction. This reverse current is generally referred to as leakage current and can for example be found in every silicon diode under reverse bias.

This observation is of great importance when discussing major aspects of the experimental results shown in later chapters. More often than not, a as small as possible leakage current is desired in order to improve device performance. For one, in the case of silicon based avalanche photodetectors the devices are commonly operated in reverse bias mode, therefore increased generation currents can lead to higher noise levels which one usually tends to avoid as will be explained in Sec. 3.4 and Sec. 5. In addition, this will also be of utmost interest when discussing radiation damage in semiconductor devices since various different trap states will be introduced and depending on their charge dynamics, they will have different impacts on device performance which will be discussed in Sec. 4.

3.1.3 Impact ionisation and avalanche breakdown

Providing sufficiently large electric fields to a reversed biased *p*-*n* junction can enable charge multiplication via impact ionization within the depleted volume. If a charge carrier is located within a high-field region, it will become accelerated due to the electric field. If the gained kinetic energy surpasses the respective threshold, the charge carrier is then able to create an additional electron-hole pair based on impact ionization of the lattice atoms. The secondary charges are then also capable of repeating this process, thus resulting in a charge multiplication procedure. In case of very high electric fields, the gain of both electrons and holes between subsequent collisions can be high enough to create new charge carriers. If this requirement is met, an avalanche breakdown can be achieved.

The process of impact ionization and the subsequent multiplication process is commonly characterized by ionization rates for electrons α_i and holes β_i. They are defined as the probabilities of ionization per unit length and are highly dependent on the electric field F [27]. This dependency can in good approximation be expressed for electrons and holes by the following empirical equations:

$$\alpha_i = \alpha_\infty\ e^{-\frac{b_n}{F}} \tag{3.20}$$

$$\beta_i = \beta_\infty\ e^{-\frac{b_p}{F}}\ . \tag{3.21}$$

Here α_∞, β_∞ and $b_{n,p}$ denote the ionization coefficients for electrons and holes, respectively. For calculation of the ionization rates, it is commonly accepted to utilize the ionization coefficients provided in the model by Van Overstraeten [36].

When describing the process of charge multiplication electrons and holes traversing a high-field region with width W can be considered. For every incremental path element $\mathrm{d}x$ an electron will create an average of $\alpha_i \mathrm{d}x$ new electron-hole pairs, thus increasing the electron current density j_n due to electron multiplication by

$$\left.\frac{\mathrm{d}j_n}{\mathrm{d}x}\right|_n = \alpha_i j_n \mathrm{d}x\ . \tag{3.22}$$

However, j_n will additionally increase due to hole multiplication via

$$\left.\frac{\mathrm{d}j_n}{\mathrm{d}x}\right|_p = \beta_i j_p \mathrm{d}x\ , \tag{3.23}$$

leading to

$$\frac{\mathrm{d}j_n}{\mathrm{d}x} = \alpha_i j_n + \beta_i j_p. \tag{3.24}$$

The analogous statements hold true for the case of holes:

$$\frac{\mathrm{d}j_p}{\mathrm{d}x} = -\beta_i j_p - \alpha_i j_n, \tag{3.25}$$

with

$$\frac{\mathrm{d}j_n}{\mathrm{d}x} = -\frac{\mathrm{d}j_p}{\mathrm{d}x}. \tag{3.26}$$

Considering both electron and hole multiplication, a multiplication factor $M_{n,p}$ describing the ratio between initial and final amount of charge carriers can be obtained for electrons M_n and hole M_p, resulting in

$$M_n = \left(1 - \int_0^W \alpha_i e^{-\int_0^x (\alpha_i - \beta_i)\mathrm{d}x'} \mathrm{d}x\right)^{-1} \tag{3.27}$$

$$M_p = \left(1 - \int_0^W \beta_i e^{-\int_0^x (\alpha_i - \beta_i)\mathrm{d}x'} \mathrm{d}x\right)^{-1} \tag{3.28}$$

for an assumed electron injection ($j_p(0) = 0$) and hole injection ($j_n(W) = 0$), respectively.

An avalanche breakdown can only occur for a sufficiently high electric field and thereby external bias voltage and corresponds to $M \to \infty$. This breakdown condition is given by the ionization integral, leading to

$$\int_0^W ...\ \mathrm{d}x = 1\ . \tag{3.29}$$

Once this condition is fulfilled the avalanche itself becomes self-sustaining due to the positive feedback of constant charge generation within the high-field region, thus requiring no additional external carrier injection. The phenomenon of the avalanche breakdown is being utilized in avalanche photo detectors, which will be discussed in more detail in Sec. 3.4.

3.2 Light-matter interaction

The interaction of photons with matter is quite limited compared to charged particles (see Sec. 3.3) due to their lack of an electric charge, thus nullifying the potential for charge dependent scattering processes. This also results in photons, or more specific γ-rays and x-rays, having significantly higher penetration depths into matter, as the possible interaction (see below) yield overall smaller cross-section.

Considering a photon beam, linear propagation through matter will not lead to a degradation of the photon energy but rather in an attenuation of the intensity. Since all possible interaction result in a loss of the photon from the initial beam, either via absorption or elastic scattering, the total number will be reduced by the amount of interacting photons. This attenuation of a photon beam with initial intensity I_0 within a distance x can be described by

$$I(x) = I_0 e^{-\mu x} , \tag{3.30}$$

with μ being the material specific absorption coefficient, directly related to the interaction cross-section [28]. The cross-section heavily depends on the type of interaction taking place, which, in turn, hinges on the energy of the photon beam.

Since electromagnetic waves cover a large spectrum of energies over many orders of magnitude from γ-rays to radio waves, different interactions will be dominant for different energies and wavelengths. The main interactions can be summed up to the photoelectric effect, Compton scattering and pair production. The effective absorption coefficient is a sum of the absorption coefficient of the interaction possible for a specific

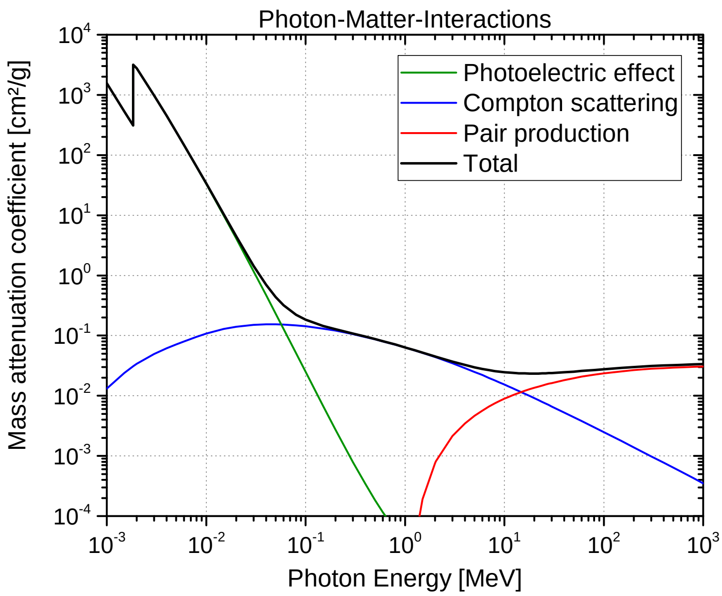

Figure 3.3: Mass attenuation coefficient of the different interaction methods of light with matter for a wide range of photon energies. The three main interactions, namely the photoelectric effect, Compton scattering and pair production can be seen to be dominant for different energy ranges. Lower energies up to tens of keV mainly feature the photoelectric effect while mid-range energies between roughly 50 keV and 20 MeV are dominated by Compton scattering. For energies surpassing $2m_ec^2 \approx 1.02$ MeV pair production can occur and will be predominant for higher energies. Data obtained from [37].

energy. Figure 3.3 depicts the mass attenuation coefficient for a wide range of photon energies. The contribution of the above interactions can be seen, as well as the total resulting coefficient.

All three cases result in free charge carriers, forming a potential signal within a detector, thus allowing the detection of the incident photons. The individual processes and their respective energies will be discussed in the following.

3.2.1 Photoelectric effect

During the photoelectric effect (photoeffect), the incident photon gets completely absorbed within the material, resulting in the emission of an electron, often referred to as photoelectron (phe). The absorption cannot take place with free electrons and always requires a nucleus due to momentum conservation. Two different types of subcategories of the photoelectric effect can be distinguished, depending on the emission of the electron, which are also closely tied to the absorber material. The external photo effect describes the emission of the phe from the surface of the material into the vacuum and mainly occurs in metals, while the internal photoeffect is common for semiconductors, in which an electron from the valence band is excited into the conduction band.

In order to enable the photoelectric effect, the energy of the incident photons is required to surpass a certain threshold energy E_{thr}. In the case of the external photoeffect, this threshold is represent by a material specific work function of the metal necessary to excite the surface electron into the vacuum and was found to be in the range of several eV. For semiconductors E_{thr} is given by the band gap energy E_g and thus also depends on the material used.

Following the absorption of the incident photon, the kinetic energy of the emitted phe is given by

$$E = h\nu - E_{thr} \; , \tag{3.31}$$

with ν being the frequency of the incident photon and h the Planck constant. For $h\nu \gg E_{thr}$ the emitted electron will carry the majority of the initial photons energy, thereby being capable of creating secondary charge carries via impact ionization (see Sec. 3.1.3). As shown in Fig. 3.3, the photoelectric effect is the dominant process for photon energies up to the order of tens of keV. Examples for this energy interval are visible light from i.e. scintillating materials (ca. 380 nm–750 nm) or ultraviolet light from i.e. Cherenkov radiation (ca. 50 nm–350 nm), making the photoelectric effect the dominant interaction mechanism for the semiconductor photon detectors of this study.

The cross-section of the photoeffect is heavily dependent on the atomic number Z of the absorber material and partially on the photon energy, leading to a dependence to the 4th or 5th power of Z [28]. This severe dependence is the main reason for the utilization of high-Z material like lead as γ-ray absorber and shielding material.

3.2.2 Compton scattering

Compton scattering describes the inelastic scattering process between the initial photon and an electron of the absorbing material. The bound electron however, can be considered quasi-free if the photon energy is high compared to the bounding energy of the absorber material.

The incoming photon is scattered in an angle Θ with respect to its initial orientation, transferring a portion of its energy to the electron in the process. Applying energy and momentum conservation the energy of the photon after scattering E'_γ and as well as the energy of the recoil electron E'_e can be derived, leading to

$$E'_\gamma = h\nu' = \frac{h\nu}{1 + \frac{h\nu}{m_e c^2}(1 - \cos\Theta)} \tag{3.32}$$

and

$$E'_e = E_\gamma - E'_\gamma \; . \tag{3.33}$$

Here $m_e c^2 = 0.511$ MeV denotes the rest-mass energy of an electron and nu' the photon frequency after scattering. From these equation it becomes apparent that the maximum energy transfer will be achieved at $\Theta = \pi$, while small scatter angles lead to only minimal transfers.

From Fig. 3.3, the process of Compton scattering can be found to be dominant for photon energies between roughly 50 keV and 20 MeV, thus being negligible for this study.

Utilizing the Klein-Nishina formula, the differential cross-section for Compton scattering can be calculated, revealing a linear dependence on Z.

3.2.3 Pair production

If the photon energy surpasses twice the rest-mass energy of the electron ($E_\gamma > 2m_e c^2 \approx$ 1.02 MeV) the transformation of the photon energy into matter via the generation of a electron-positron pair becomes energetically possible:

$$\gamma \rightarrow e^- + e^+$$

Again, this procedure can only occur in the presence of a nucleus, in order to satisfy momentum conservation. The entire excess energy above the required threshold is afterwards distributed to the electron-positron pair in the form of kinetic energy. Even though photon energies of roughly 1 MeV are required for the above process, the method of interaction only becomes dominant for energies beyond tens of MeV (see Fig. 3.3), thus limiting pair production to high energy γ-rays, thereby making this process, like Compton scattering, negligible for this study.

The probability of pair production per nucleus was found to be dependent on the square of Z [22].

3.3 Particle-matter interaction

Contrary to photons, charged particles carry an electric charge enabling additional electromagnetic interactions with the absorber material. In general, these particles will lose part of their energy and potential undergo a change of their incident direction as a result from either inelastic collisions with atomic electrons or elastic scattering with nuclei. The first theory for this process was developed by Bohr using classical arguments [28] and later improved by Bethe [38], Bloch [39] and Landau [40] by tackling the issue in a quantum mechanical way.

The average rate of ionization loss by a charged particle in matter is described by the Bethe-Bloch formula [28]:

$$-\frac{\mathrm{d}E}{\mathrm{d}x} = 2\pi N_a r_e^2 m_e c^2 \rho \frac{Z}{A}\frac{z^2}{\beta^2}\left[\ln\left(\frac{2m_e\gamma^2 v^2 W_{max}}{I^2}\right) - 2\beta^2 - \delta - 2\frac{C}{Z}\right] \; , \tag{3.34}$$

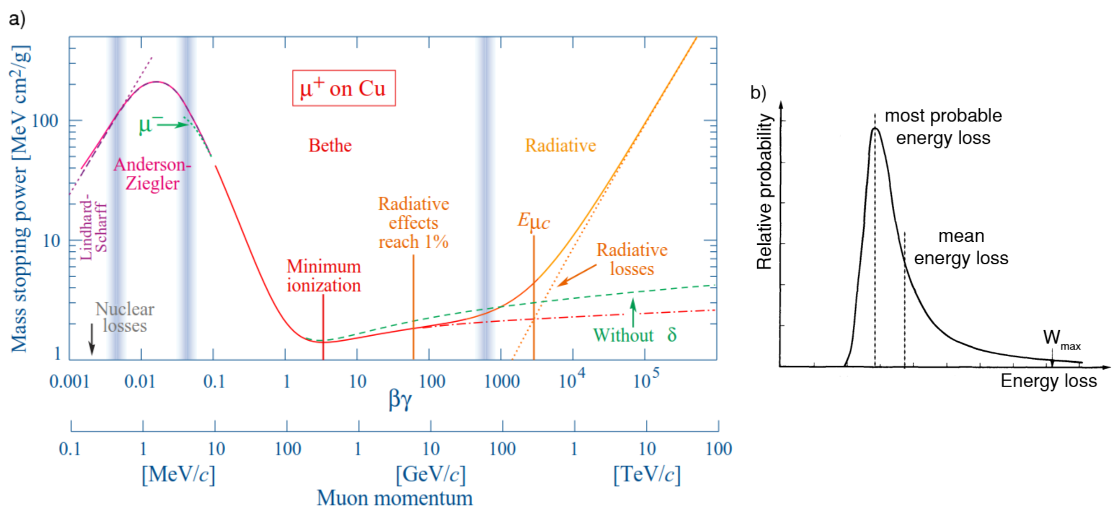

Figure 3.4: Mass stopping power according to the Bethe-Bloch equation a) and typical Landau distribution b). The mass stopping power $\mathrm{d}E/\mathrm{d}x$ is given for a wide range of energies of positive muons in copper. The muon energy is also listed in units of $\beta\gamma$. A minimum energy deposition can be found at $\beta\gamma \approx 3$ representing the case of minimum ionizing particles (MIPs). The solid curve describes the total stopping power, while the dashed and dotted lines represent cases without specific corrections or contributions from certain effects. Taken from [41]. A typical Landau distribution for energy loss in thin absorbers can be seen in b). Its asymmetry with a long tail results in a higher mean energy loss than the most probable one. Adapted from [28].

with

$$
\begin{aligned}
N_a &= \text{Avogadro's number} = 6.022 \cdot 10^{23}\text{mol}^{-1} \\
r_e &= \text{classical electron radius} = 2.817 \cdot 10^{-13}\text{cm} \\
m_e c^2 &= \text{rest-mass energy of an electron} = 0.511 \text{ MeV} \\
\rho &= \text{density of absorbing material} \\
Z &= \text{atomic number of absorbing material} \\
A &= \text{atomic weight of absorbing material} \\
z &= \text{charge of incident particle in units of} e \\
\beta &= v/c \ \text{ of the incident particle} \\
\gamma &= 1/\sqrt{1-\beta^2} \\
W_{max} &= \text{maximum energy transfer in a single collision} \\
I &= \text{mean excitation potential} \\
\delta &= \text{density correction} \\
C &= \text{shell correction}
\end{aligned}
$$

The average energy loss per unit path length or mass stopping power $\mathrm{d}E/\mathrm{d}x$ of a charged particle, dependent on its energy is shown in Fig. 3.4a) depicting the case of muons traversing copper. The shell and density corrections are included, affecting low and high energy ranges, respectively. A minimum of $\mathrm{d}E/\mathrm{d}x$ can be found for $\beta\gamma \approx 3$ representing the range of minimum energy deposition in the medium. Particles at this point are commonly referred to as minimum ionizing particles (MIPs). It is interesting to note that the energy deposit for MIPs is almost identical for particles of the same charge. For that reason, MIPs serve as a good benchmark for particle detectors, as they define a threshold for the signal-to-noise ratio.

The lower energy regime can be utilized for particle identification as $\mathrm{d}E/\mathrm{d}x$ is dominated by the $1/\beta^2$ factor with this region being distinct for each particle. Increased particle energies beyond the MIP regime lead to an increase in $\mathrm{d}E/\mathrm{d}x$ due to radiative losses.

The majority of the energy loss of charged particles in matter is caused by the inelastic collision component. During these collisions, energy of the impinging particle is transferred to the absorber medium resulting in ionization of the latter. The number of collision as well as the respective energy transfer, however, can vary, due to statistical fluctuations. In rare instances, also referred to as δ-rays, the transferred energy is much higher than the average one. While these events are rare, their energy discrepancy is large enough to distort the distribution of the energy transfer, leading to the most probable value being roughly 30% lower than the average one [29] for thin absorbers. This effect can be identified by the asymmetric long tail towards higher energy deposits in the resulting distribution, also called Landau distribution, depicted in Fig. 3.4b).

Even though the band gap energy of silicon is 1.12 eV, the average energy required for the creation of an electron-hole pair is 3.6 eV due to it being an indirect semiconductor. Part of the energy is required for the creation of phonons which, in turn, are needed for passing of the band gap. Thus considering MIPs and their energy deposition in matter, the most probable number of electron-hole pairs generated per μm in silicon amounts to roughly 76, while the average one is 108. The commonly applied rule-of-thumb is the creation of roughly 80 electron-hole pairs per μm.

Unfortunately, the above discussion can only be applied to electrons in a limited degree, since electrons suffer from additional energy loss due to emission of electromagnetic radiation stemming from scattering in the electric field of a nucleus. This is referred to as bremsstrahlung and is caused by their small mass being identical to the hull electrons of the absorbing material. The total energy loss of electrons (and positrons) can therefore be written as a combination of collision and radiative loss

$$\left(\frac{\mathrm{d}E}{\mathrm{d}x}\right)_{tot} = \left(\frac{\mathrm{d}E}{\mathrm{d}x}\right)_{rad} + \left(\frac{\mathrm{d}E}{\mathrm{d}x}\right)_{coll} . \tag{3.35}$$

While the basic mechanism of the energy loss due to collision is identical to Eq. (3.34), certain corrections need to be applied due to the low mass of the electron as mentioned above. A detailed discussion of these corrections is beyond the scope of this thesis and can be found in [30]. Bremsstrahlung becomes dominant for higher energy electrons ($\sim$ tens of MeV), surpassing the energy loss due to collision thanks to its Z^2-dependence in contrast to the linear dependence Z exhibited by the collision component.

The electrons in this study are obtained from a radioactive source (Strontium 90) and thus feature energies below the bremsstrahlungs-threshold. Therefore, a description via the adjusted Bethe-Bloch formula is acceptable, making the use of the above mentioned rule-of-thumb valid. Breamsstrahlung can thereby be neglected for the measurements of this study.

3.4 Semiconductor photon detectors

The detection of photons within a silicon detector is based on the measurement of the created charges by means of the interaction methods described in Sec. 3.2. Hence, a basic *pn*-junction can already act as a photon detector in the shape of a photon cell.

Charges generated in the depleted volume will drift to the p and n side respectively due to the inherent electric field (see Sec. 3.1.1). The resulting change in voltage can then be externally measured.

The depletion width can, as previously explained, be enhanced by application of a reverse bias voltage to the junction, thus further increasing the sensitive area. However, in doing so the reverse bias leakage current stemming from thermal generation will also increase, making low light level detection difficult, as the device will be dominated by the leakage current rather than the photocurrent. This, in turn, lowers the overall signal-to-noise ratio (SNR) drastically, making low light level detection practically unfeasible.

Fortunately, as explained in more detail in Sec. 3.1.3, the process of charge multiplication via impact ionization can be utilized in order to increase the internal gain of a detector, thereby potentially improving its SNR. The following section will discuss different approaches utilizing impact ionization in silicon detectors for the development for low light level photon detectors.

3.4.1 Avalanche photo diodes

Section 3.1.3 already discussed that the process of impact ionization depends on the electric field within the depletion or high-field region and thus on the external bias voltage of the device. In the early stages of charge multiplication, the enhanced signal will still be proportional to the incident amount of photons, thus being labeled the proportional or linear mode operation. This can also be seen in Fig. 3.5a). Operation in the proportional mode thus leads to a gain $1 < M_{n,p} < \infty$, increasing the SNR with increasing gain as a result. Such devices are commonly referred to as avalanche photo diodes (APDs) and feature a higher detection efficiency and dynamic range compared to photon cells.

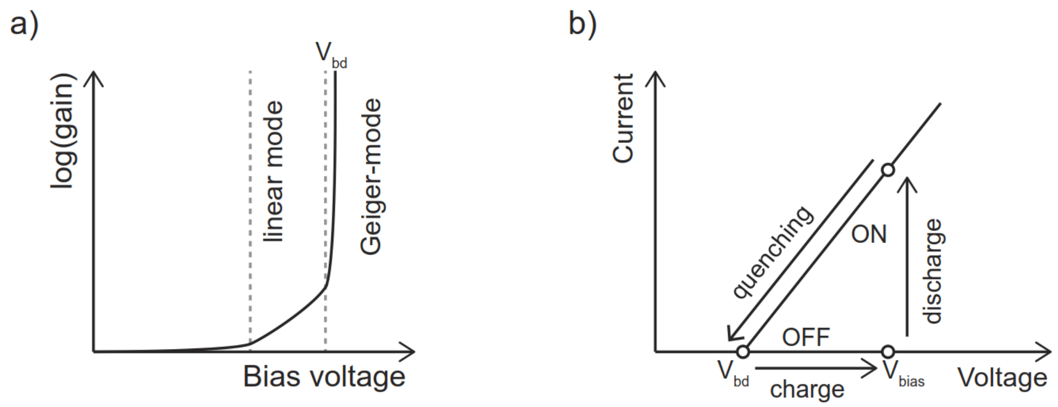

Figure 3.5: Operational modes of photo diodes based on their reverse bias voltage (a)) and G-APD operational cycle (b)). The gain of the photo diode in a) depends on the reverse bias voltage. For sufficient voltages, the device enters the linear or proportional mode, while still operating below V_{bd}. This marks the operation mode of APDs and features a gain proportional to the incident light. Beyond V_{bd}, the device enters the Geiger-mode, which is characterized by a gain obtained via an avalanche breakdown ($\mathcal{O}(10^6)$). See text for more details. The basic operational loop of an G-APD is shown in b). The device cycles between an avalanche discharge, a quenching process (passive or active) and the recharge or recovery of the cell back to its initial state. During quenching, the avalanche is stopped, reducing the current to zero and allowing the device to increase the voltage $V_{bd} \rightarrow V_{bias}$. Picture taken from [33]

As already mentioned, APDs are operated at voltages below the breakdown voltage V_{bd}, which means that charge multiplication is generally carried by the electron contribution as the ionization rates of holes are significantly smaller for the respective electric fields. In order to maximize the potential gain while still remaining in the proportional mode, operation at higher voltages is preferred, however, voltages close to V_{bd} can already result in breakdowns, as the process itself is of statistical nature. Hence smaller bias voltages are necessary, limiting the gain to a level at which thermal generation can still degrade the overall SNR significantly, depending on the quality of the technological procedures. In addition, inhomogeneities in the doping profiles of the high-field region combined with the statistical nature of the multiplication process can result in distinct fluctuations of the avalanche gain, thereby preventing a clear separation of individual photoelectron peaks during readout.

3.4.2 Geiger-mode avalanche photo diodes

Further increase of the bias voltage beyond V_{bd} will result in the device reaching the Geiger mode operation (see Fig. 3.5a)). This mode is characterized by its high internal gain ($\mathcal{O}(10^6)$) and can be translates to an impact ionization gain $M_{n,p} \to \infty$ in a first order approximation. Such a devices is labeled Geiger-mode avalanche photo diode (G-APD) or single photon avalanche diode (SPAD). The increased gain now offers the possibility for a high SNR making low light level detection feasible.

A device operated above V_{bd} will now be able to initiate an avalanche breakdown via a generated electron-hole pair after absorption of a photon. The gain is defined by the capacitance of the depletion layer or high-field region of the device (C_D) as a breakdown amounts to a full Geiger discharge of C_D.

However, when considering the avalnche breakdown for application in photon (or particle) detection due to its inherent amplification capabilities, the self sustaining feature of an avalanche breakdown needs to be taken into account. A continuous flow of charge carriers after the initial breakdown would result in one-time-use device or require a perpetual adaptation of the bias voltage. Thus a concept was developed to passively limit or quench the current flow via external means. This can be realized by implementation of a high-impedance series resistor, also called quench resistor R_Q, as shown in Fig. 3.6. The avalanche current causes a voltage drop at R_Q effectively reducing V_{bias} of the cell to roughly V_{bd}, thus drastically reducing the possibility of charge carriers to initiate more multiplication processes and thereby quenching the avalanche.

Following the quenching procedure, the cell requires a characteristic amount of time

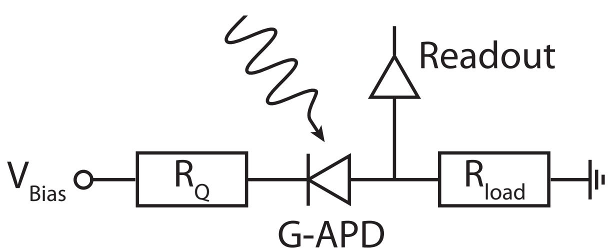

Figure 3.6: Circuit diagram of a G-APD with passive quenching. The avalanche is suppressed via the quench resistor R_Q resulting in a voltage drop $V_{bias} \to V_{bd}$ and a subsequent recharge process. The signal of the G-APD is commonly read out at front-end electronics, with an input resistance R_{load}, usually in the order of 50 Ω. Picture adapted from [42].

to recharge via R_Q until $V_{bias} > V_{bd}$ is reached again. This time is called the recovery time τ and will be discussed in more detail in Sec. 3.4.3 and Sec. 5.3.4. Afterwards, the cell is ready to initiate a new avalanche after absorption of photon and the subsequent charge creation. This cycle of discharge, quenching and recovery is illustrated in Fig. 3.5b) and constitutes the main operation cycle of G-APDs.

The above procedure describes the case of passive quenching via R_Q, however it is also possible to quench the avalanche breakdown in an active fashion by means of dedicated electronics (active quenching). In this scenario, the breakdown current triggers the electronics to reduce V_{bias} until the current is completely quenched. Afterwards the voltage can be increased again, similar to the recovery procedure above. In contrast to the passive case, active quenching in general allows for much faster recovery times, only limited by the electronics in use [42].

As mentioned above, G-APDs allow low light level detection due to their inherently high internal amplification. Even single photon detection is possible after implementation of a simple external amplifier (see Fig. 3.6). However, therein lies a significant issue, as this leads to G-APDs also being sensitive to thermally generated electron-hole pairs. The resulting signal will be identical to one of an absorbed photon, thereby making the identification of the cause of the Geiger discharge impossible. No information regarding the energy of the initiator of the avalanche is stored within the signal due to the nature of the avalanche multiplication, resulting in a quasi-digital output of G-APD devices. Therefore, G-APDs are severely limited by the quality of their material and fabrication steps, as low levels of thermal generation are required, making large area G-APDs without cooling unfeasible.

In addition, any information pertaining to the amount of incident light is also lost, as the resulting breakdown will always be identical (see left hand side of Fig. 3.7). Furthermore, due to the required recovery time of the G-APD, there will always be a dead time between two consecutive measurements, as the cell will not be able to initiate a new discharge. Partial discharges are possible and make up one the parasitic aspects of such devices as will be discussed in Sec. 5.3.7.

3.4.3 Silicon Photomultiplier

The drawbacks of G-APDs discussed in the previous section can be circumvented by segmentation of a large single G-APD cell into an array of multiple smaller ones, connected in parallel (see Fig. 3.7). The signal of a single G-APD cell does not carry any information regarding the number of incident photons due to its quasi-digital output. By utilizing an array, however, the resulting signal becomes the sum of all simultaneously firing cells, thus making photon counting possible. For N detected photons, the peak height of the output signal equals N times the single photon peak.

In recent years, multiple commercial companies as well as scientific groups have developed their own type of G-APD matrix, resulting in various different device with differing names such as the Solid State Photomultiplier (SSPM) or the Multi Pixel Photon Counter (MPPC) developed by Hamamatsu Photonics[1]. The most commonly accepted term for such device, however is the Silicon Photomultiplier (SiPM), which will also be applied throughout this study. SiPMs have become feasible replacements for vacuum photomultiplier tubes in many applications due to their numerous advantages [43]. Their insensitivity to magnetic fields as well as compact size make them prime candidates for e.g. scintillator readout in high energy physics or general medical applications. In addition, the required bias voltage and overall energy consumption also enable easier

[1] `https://www.hamamatsu.com/jp/en/index.html`

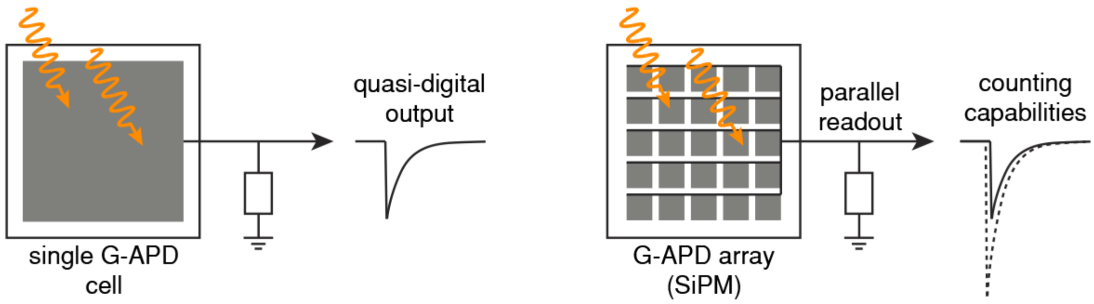

Figure 3.7: Juxtaposition of the output of an G-APD and SiPM for a multiple incident photon event. Due to the quasi-digital (binary) signal output of the G-APD, events with more than one simultaneous incident photons cannot be registered as such, as it will always result in a single avalanche. By combining multiple G-APDs into an array structure (SiPM) seen on the right, all cells are being read out in parallel leading to the signal being sum of all fired cells (dashed line). Thus, photon counting becomes possible. Picture adapted from [33].

implementation in multiple applications.

The operation cycle of a single G-APD shown in Fig. 3.5 is also applicable for a SiPM. The equivalent circuit diagram, however, has to be adapted, by taking the entirety of the array into account. This can be seen in Fig. 3.8, which depicts the case of a passively quenched SiPM. The respective circuit of a single G-APD cell is shown within the dashed square consisting of a cell capacitance C_D as well as a cell resistor R_D. Passive quenching is achieved by the quench resistor R_Q, located underneath and in parallel to its stray quench capacitance C_Q. Considering an array of N cells, it can be divided into the fraction of cells initiating an avalanche N_f (active) and the remaining passive part $N_p = N - N_f$. While the passive cells will not directly contribute to the signal formation, their electric components will still have an measurable impact on the shape of the device output and thus need to be considered. Furthermore, an additional parasitic capacitance C_g originates from the metal grid required for contacting of the individual cells and their respective quench resistors. With this information, the remaining parameters listed on the right hand side of Fig. 3.8 can be obtained.

For the discussion of the created signal, as well as the quenching and recovery behavior, the case of only one active cell is going to be considered for simplicity. Before a cell can initiate an avalanche discharge, a sufficiently large electric field which supports the impact ionization procedure is required. For this purpose, the depletion or high-field region of the cell can be approximated to a common capacitance C_D with a width of W. The application of an external bias voltage V_{bias} then results in an electric field of

$$F \approx \frac{V_{bias}}{W} \; . \tag{3.36}$$

For $V_{bias} > V_{bd}$ the electric field is large enough to support the formation of an avalanche. The strength of the discharge depends on V_{bias}, or more precisely, on the overbias voltage $V_{ob} = V_{bias} - V_{bd}$, as the current is given by

$$I = \frac{V_{ob}}{R_Q + R_D} \approx \frac{V_{ob}}{R_Q} \; . \tag{3.37}$$

The approximation in the second step is valid since usually $R_D \ll R_Q$. This discharge of the capacitance over R_Q is represented in the circuit diagram by the closing of a switch,

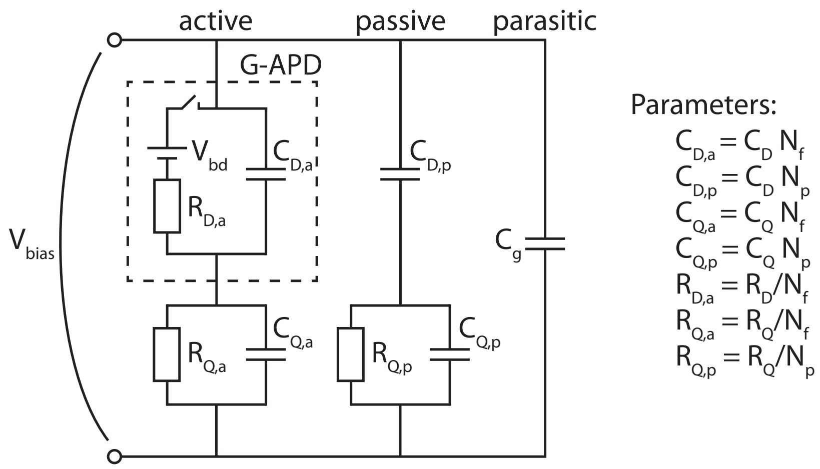

Figure 3.8: Equivalent circuit diagram of a SiPM. The SiPM consists of an array of G-APD cells (dashed square) connected in parallel. Each cell has a cell capacitance C_D parallel to a the cell resistance R_D and requires a quench resistor R_Q with its own quench capacitance C_Q in parallel. The overall parameters of the entire array can be obtained by taking the number of fired cell N_f into account. The fact that passive cells (not firing), labeled by a "p" index, as well as the parasitic grid capacitance C_g of metal contacting grid also contribute needs to be taken into account. The resulting parameters are shown on the right. The avalanche discharge in SPICE simulations is implemented via a voltage switch, effectively reducing the operational voltage $V_{bias} \to V_{bd}$. Picture adapted from [44].

resulting in a voltage drop over R_Q leading to $V_{bias} \to V_{bd}$. This transient voltage and current behavior can be obtained via SPICE simulation[2] and are depicted in Fig. 3.9. The voltage and its corresponding scale (left) are colored blue, while the current and its scale (right) are given in red. The parameters utilized for the simulation are listed in a). The explained drop in voltage can be seen followed by a increase back to the initial value. In the case of the current, only a short burst at the time of the avalanche creation at $t = 50$ ns can be seen. A zoom-in, focusing on the time interval close to the discharge is shown in b). If the current falls below a certain threshold, the possibility that the avalanche is quenched arises. Otherwise the avalanche would remain intact as the process is self-sustaining as previously explained. A commonly accepted rule-of-thumb for this quenching condition is a threshold current of roughly 20 µA as suggested by Cova [42]. If the current falls below this threshold, quenching occurs via the switch opening again and the cell can start the recharge process. This can be seen in Fig. 3.9b) as the current drops to zero after reaching the threshold, resulting in the voltage to start increasing again towards V_{bias}.

This recharge of the cell capacitance C_D via R_Q is also called recovery and is defined by a characteristic recovery time

$$\tau_{rec} = R_Q C_D \ . \tag{3.38}$$

During recovery, it is possible to reach voltage values which are sufficient to initiate a second avalanche breakdown after a certain time Δt. The amount of charge generated in

[2]Performed with LTspice,
`https://www.analog.com/en/design-center/design-tools-and-calculators/ltspice-simulator.html`

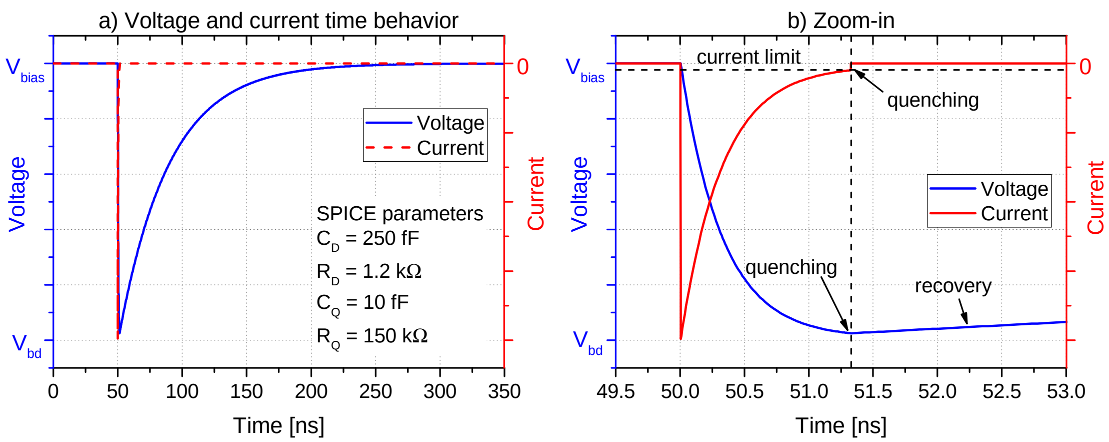

Figure 3.9: Transient behavior of the cell current and voltage of a SiPM in Geiger mode obtained via SPICE simulations. b) features a zoom-in to the time of the avalanche creation at $t = 50$ ns. When the breakdown occurs, the voltage can be seen to drop $V_{bias} \rightarrow V_{bd}$ (blue line and scale (left)), due to a short current pulse (red line and scale (right)). After the current reached the threshold (20 µA) it is quenched, leading to a sudden drop off to zero and initiating the recovery process of the cell. Thus the voltage recharges again towards V_{bias}. The parameters for the SPICE simulation are listed in a). See text for more details.

this second avalanche $Q(\Delta t)$ then depends on the current overbias bias voltage $V_{ob}(\Delta t)$ applied to the cell:

$$Q(\Delta t) = C_D V_{ob}(\Delta t) = C_D V_{ob} \left(1 - e^{-\frac{\Delta t}{\tau_{rec}}}\right) . \tag{3.39}$$

Utilizing this equation, it is possible to define different levels of recovery and consequently their respective recovery times, as will be shown in more detail in Sec. 5.3.4.

From Eq. (3.38), one major design trade-off of SiPMs can be identified. It becomes apparent that fast recovery times can be achieved for small values of both R_Q and C_D in order to enable higher currents which are capable of reloading the cell quicker. This, however, is in direct opposition to the quench condition if applied to Eq. (3.37), as this would lead to only small possible values of V_{ob}, limiting the operational range of the device. Thus, either a balance between both aspects has to be achieved or the design needs to be adjusted for a specific application, favoring one of the two aspects while being lenient on the other.

In addition, the trigger probability or efficiency for an avalanche increases with higher V_{ob}. It is defined as the likelihood of the generated charges to trigger an avalanche breakdown while drifting through the high-field region. Since this parameter is a function of the electric field, it is directly dependent on the applied voltage. Furthermore, the profile of the electric field is of importance as an homogeneous field distribution is preferred for high trigger efficiency. As the distance over which generated charge carriers can gain kinetic energy is limited, the position of the initial charge absorption also plays a major role as does the type accelerated charge. As was already discussed, electrons have generally higher ionization coefficients, making them the preferred charge carrier for avalanche initiation. Therefore, in order to maximize the trigger probability, the design and thus the technological parameters of the SiPM need to be adapted, since different wavelengths have varying penetration depths, as seen in Sec. 3.2.

Even though SiPMs offer the possible of detecting multiple incident photons simultaneously, the counting capability is nonetheless limited, since two photons impinging on the same cell within the array will still net only one effective signal. In turn, the amount of incident light has to be kept below a certain threshold as the response of the device will depend heavily on the total number of cell within the array. This refers to the dynamic range of a SiPM and will be discussed in more detail in Sec. 5.3.9.

Similar to G-APDs, the most crucial limiting factor of SiPMs is the thermally generated current, resulting in thermal discharges or dark counts. The rate of these dark counts can vary from tens of kHz up to several MHz per square millimeter. The issue, again, is that these thermal pulses cannot be distinguished from those initiated by absorbed photons. However, the possibility of two dark counts taking place simultaneously can be considered negligible [45], thus voltage thresholds for triggering of the output signal of a SiPM can be applied to reduce the impact of thermal generation. In addition cooling of the devices can further reduce the amount of thermally generated charge carriers.

Apart from the recovery time and the dark counts, there are various other parameters and negative effects characteristic of SiPMs which will be investigated in more detail during Sec. 5.2 and Sec. 5.3. In the majority of the cases, an improvement of the overall SiPM performance can be achieved via technological optimization of the fabrication process, as well as novel approaches of existing concepts. One such approach is the main focus of this study, which incorporates the quench resistor into the bulk material of the SiPM, resulting in several advantages but also drawbacks compared to conventional SiPMs. This novel concept will be introduced in Chapter 6.

4 Radiation damage in semiconductor detectors

During its lifetime, a radiation detector will more often than not inevitably be exposed to radiation damage, caused by the very particles it is design to detect. The radiation damage can roughly be categorized in non-ionizing and ionizing damage. The former describes the impact of lattice damages caused within the bulk, while the latter can be found mainly in surface layers like the silicon oxide. Both will be discussed in the following chapter, although the primary focus of this study in regards to radiation damage lies in the impact of bulk damage on the detector performance, hence greater emphasis will be put on its explanation.

In both cases, the underlying mechanism which causes the damage will be explained, as well as the general impact on the device properties. However, the more specific effect on SiPMs and especially on the novel SiPM devices which are the focus of this study will be presented in Sec. 6.5 after the individual properties of said device were explained.

The topics discussed in this chapter can, for the most part, be found in recognized standard reference works, including published books and dissertations, as well as specialized peer-reviewed journal publications. If not specifically stated otherwise, the scientific basis of this chapter can be found in [29, 31, 46–67][1].

4.1 Non-ionizing radiation damage

This section will start with an explanation of the basic damage mechanisms caused by the interaction of high energy particles with the detector bulk. In this context, a method for comparing the damage produced by different particles with different energies will be introduced. Afterwards, the damage states will be classified in the context of their electrical properties. In addition, the concept of defect annealing will be discussed and finally an overview of the different impacts of defects on the detector performance will be presented.

4.1.1 Damage mechanism

The main cause for radiation damage in the silicon bulk originates from interactions with the silicon lattice. Interplay with the electron cloud are possible, but they will not or only negligibly contribute to bulk damage.

While nuclear interactions like neutron capture and transmutations will have an impact, the majority of the observable damage arises from high energy particles like neutrons, protons, pions, electrons and others displacing a silicon atom out of its initial lattice site, thereby creating a silicon interstitial, also called the Primary Knock-on Atom (PKA) and a leftover vacancy in the lattice, which are classified as a Frenkel pair or Frenkel defect. The condition for generating a PKA and its subsequent impact on the lattice is given by two different variables: First the imparted energy E_R on the initially

[1]This chapter has been structured in resemblance to a topically similar section of one of the authors previous studies [68]

displaced atom by an external particle, which can be calculated via the non-relativistic scattering approach and second, its relation to the displacement threshold energy $E_{R,thr}$. However, this threshold is not well defined, since it depends heavily on the direction of the recoil. Thus, the common practice is to use a displacement threshold energy at which the displacement probability is roughly 50%, amounting to $E_{R,thr} \approx 25$ eV for silicon [46].

With this, three different scenarios are possible: In the case of $E_R < E_{R,thr}$, it is very likely that only lattice vibrations will occur, while for $E_R > E_{R,thr}$ a Frenkel pair will be created in addition. The resulting PKA and vacancy can afterwards traverse through the lattice and perform further important interactions within the lattice, which will be discussed in Sec. 4.1.3.1. Should the imparted energy greatly exceed the threshold ($E_R \gg E_{R,thr}$), the recoiling silicon atom of the resulting Frenkel pair will be able to loose energy in the form of ionization and thereby create secondary Frenkel pairs. Depending on the energy, either only isolated point defects (see Sec. 4.1.3.1) or multiple defect clusters can be formed, as the end of the recoil is dominated by non-ionizing interactions.

4.1.2 NIEL scaling hypothesis

Considering the previous section, it can be seen that the probability of creating a PKA is heavily dependent on the type and energy of the impinging radiation. Since the majority of the kinematics and energy transfer is governed by the non-relativistic scattering approach, the mass of the radiation particles can have a huge impact. Also, charged and neutral particles will have different elastic cross-sections for scattering, since electrostatic interactions are not possible for neutral particles like neutron. A brief overview of a few important characteristics regarding primary interactions of different particles is given in Table 4.1. It is important to note that the secondary interactions of the created PKA are only dependent of the energy of said atom and are in fact independent of the type of the primary interaction.

With this in mind, a common scaling with respect to the radiation induced changes observed in the detector material for a more streamlined description is highly desirably. This scaling is achieved by the so-called Non-Ionizing Energy Loss (NIEL) hypothesis. It is based on the assumption that any displacement damage induced change of the material properties scales linearly with the total energy transfered in displacement collisions,

Table 4.1: Characteristics of primary interactions of radiation with silicon (taken from [31]). The type of interaction, the maximum kinetically possible recoil energy T_{max}, the average recoil energy T_{av} and the minimum radiation energy E_{min} required for the creation of a point defect and a defect cluster are given for various radiation particles with an energy of 1 MeV.

Radiation	Electrons	Protons	Neutrons	Si^+
Interaction	Coulomb scattering	Coulomb and nuclear scattering	Elastic nuclear scattering	Coulomb scattering
T_{max} [eV]	155	133700	133900	1000000
T_{av} [eV]	46	210	50000	265
E_{min} [eV]				
point defect	260000	190	190	25
defect cluster	4600000	15000	15000	2000

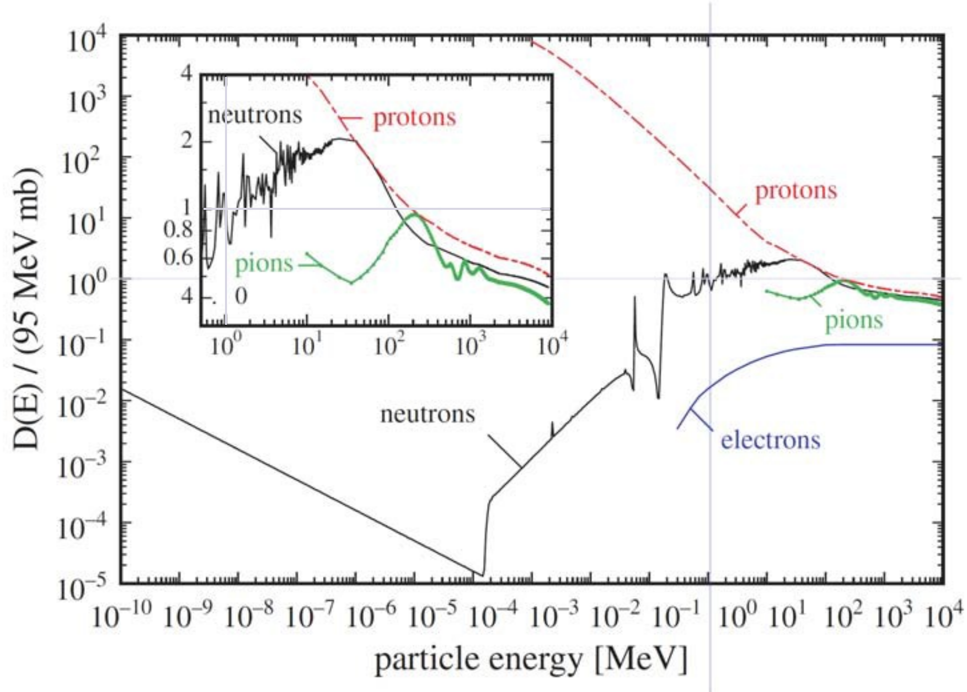

Figure 4.1: Displacement damage function $D(E)$ for neutrons, protons, pions and electrons of different particle energies (taken from [49]). $D(E)$ is normalized to 95 MeV mb, which corresponds to the value of 1 MeV neutrons. The gray lines mark the position of 1 MeV and $D(E)_{\text{norm}} = 1$ on the x and y axes respectively. The insert displays a zoomed-in part of the figure. The values for electrons are obtained by theoretical approaches and are (mostly) not validated by experimental data.

regardless of the spatial distribution of the introduced displacement defects in one PKA cluster and regardless of any annealing scenario taking place after the initial damage event [47]. The NIEL can be expressed by the displacement damage cross-section

$$D(E) = \sum_i \sigma_i(E) \cdot \int_0^{E_R^{max}} f_i(E, E_R) P(E_R) \mathrm{d}E_R \; . \tag{4.1}$$

Here the index i denotes all possible interactions of lattice atoms and incoming particles with energy E, which lead to displacement damages, σ_i the cross-section of the respective reaction and $f_i(E, E_R)$ the probability for the generation of a PKA with recoil energy E_R by a particle with energy E in the reaction i. $P(E_R)$ is the so-called Lindhard partition function [48], which takes into consideration that only a fraction of the recoil energy is imparted in form of displacement damage and that this fraction also depends on the recoil energy itself. Equation (4.1) has to be summed up over all possible interactions and the integration is done over all possible recoil energies. Energies below the threshold energy are excluded by setting the partition function to zero $P(E_R < E_{R,thr}) = 0$.

The displacement damage induced by neutrons with an energy of 1 MeV was chosen and defined as a reference value for $D(E)$. Furthermore, a hardness factor κ was introduced as means to compare the damage produced by different particles with individual energy spectra $\phi(E)$ to the damage which would result from monoenergetic neutrons of

1 MeV and the same irradiation fluence Φ:

$$\kappa = \frac{\int D(E)\phi(E)\mathrm{d}E}{D(E_n = 1\,\mathrm{MeV}) \cdot \int \phi(E)\mathrm{d}E} \,. \tag{4.2}$$

The reference value of the displacement damage function for 1 MeV neutrons is set to $D(E_n = 1\,\mathrm{MeV}) = 95$ MeV mb. Thus, it is possible to determine the equivalent 1 MeV neutron fluence Φ_{neq} that will create the same damage as an irradiation with a specific particle with different energies E and fluence Φ:

$$\Phi_{neq} = \kappa\,\Phi = \kappa \int \phi(E)\mathrm{d}E \,. \tag{4.3}$$

The unit for irradiation fluences is then given in terms of 1 MeV neutron equivalent per square centimeter, which will be abbreviated to [neq/cm^2].

The displacement damage function, normalized to 95 MeV mb, for neutrons, protons, pions and electrons as a function of particle energy is shown in Fig. 4.1. It should be noted that, even though, a minimum kinetic energy of $\approx$ 185 eV is required [47] for neutrons to impart enough energy in order to create displacements by elastic scattering, an increase of $D(E)$ for neutrons of smaller energies can be seen. This effect is caused by neutron capture processes, which emit gamma rays leading to a recoil energy much higher than the threshold energy. For neutrons in the MeV range the displacement damage function increases, since additional nuclear reaction become available. In the case of protons Coulomb interactions have a major impact on $D(E)$ at low energies, whereas for higher energies in the GeV range $D(E)$ becomes almost identical to that of neutrons, because of the dominant contributions of nuclear reactions.

4.1.3 Classification of point defects

The following section will treat the properties and formation of point defects in more detail. First, a summary of different types of point defects and their characteristics are presented. Afterwards, their electrical properties for specific biasing scenarios will be discussed.

4.1.3.1 Formation and characterization of stable defects

Section 4.1.1 briefly touched upon the possibility of Frenkel pairs forming different types of point defects. This can occur due to the fact that the formed vacancy-interstitial pair is not stable, meaning that both parties are mobile at room temperature. Hence, part of those pairs will inevitably recombine again or diffuse out of the surface, having negligible net influence on the bulk. Another part, however, has the capability to interact with other defects or impurities, thus forming a new type of defect, which will be stable at room temperature. These are referred to as point defects and are responsible for the actual change of electrical properties of the bulk material. Figure 4.2 illustrates some of the possible point defects formed within the silicon lattice.

One example of a point defect is a complex formed by an oxygen interstitial and a vacancy, called an A-center. Oxygen is usually present within the silicon lattice but the amount depends mainly on the particular crystal growth process. In itself, oxygen interstitials are electrically inactive, but by forming an A-center, the new defect will be able to act as a trapping center for electrons. Another example is the formation of a vacancy right next to a phosphorus atom, thus creating an E-center. Phosphorus

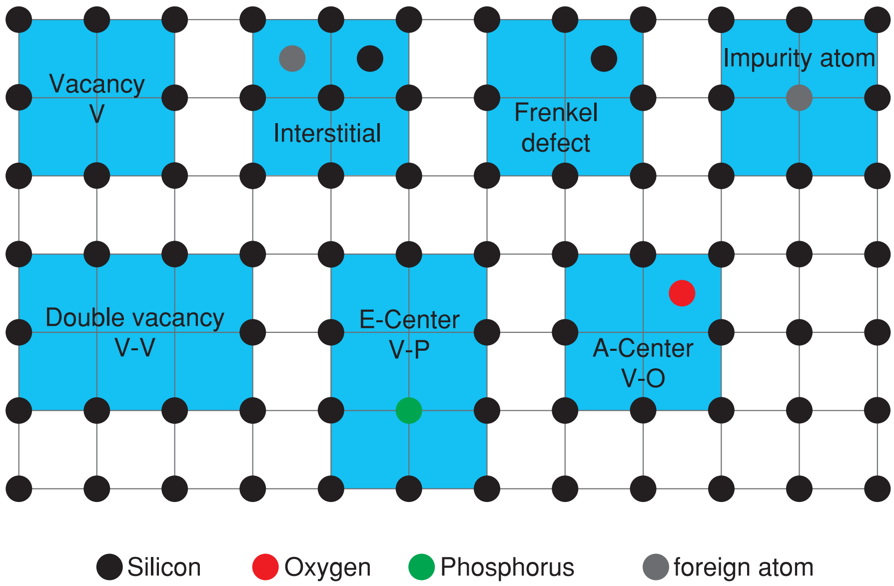

Figure 4.2: Exemplary illustration of various important point defects in the silicon lattice (inspired by [29]). Atoms are represented by colored circles, where silicon is black, oxygen red and phosphorus green. Gray atoms represent the general case of non-specified foreign atoms. The vacancy, interstitial and Frenkel defect are not considered point defects by definition of being stable but are included for illustrative purposes.

is generally used as a standard dopant for n-type silicon, however after forming the E-center its electrical properties change and it is longer able to act as a donor.

Note that the previous two examples of stable defects were explained as two-step processes. In reality these processes are very complicated and can contain multiple steps, where not only the radiation generated primary defects play an important role but also the already present defects introduced during the crystal growing. Unfortunately, the formation of stable defects in semiconductors is still only partially understood and requires additional experimental validation [31].

Point defects can be classified as donors, acceptors and amphoteric defects. A donor is defined as a defect that can be neutral or positively charged depending on its energy E_t relative to the Fermi level E_F. Should the Fermi level be located above the defect level ($E_t < E_F$), the donor will be populated with an electron and thereby neutral, while a Fermi level lower than the defect level ($E_t > E_F$) will see the donor in its positive charge state. The most common representative of a donor is phosphorus found in n-type silicon. Acceptors, like boron utilized for p-type doping on the other hand can be found in either a negative or neutral charge state. Again, the charge state is dictated by the Fermi level with $E_t < E_F$ resulting in a negative and $E_t > E_F$ in a neutral state. Defects like divacancies are called amphoteric, because they can have multiple energy levels and be donors and acceptors.

In the case of a space charge region the charge state will no longer be ruled by the Fermi level, since this scenario does not describe a thermal equilibrium. Therefore the electron and hole emission and capture probabilities will be responsible for the charge state of a defect, which will be explained in the next section. Regardless of type, every defect can act as trap for electrons and holes, however certain processes involving certain charge carriers are more likely than others, as will be explained below.

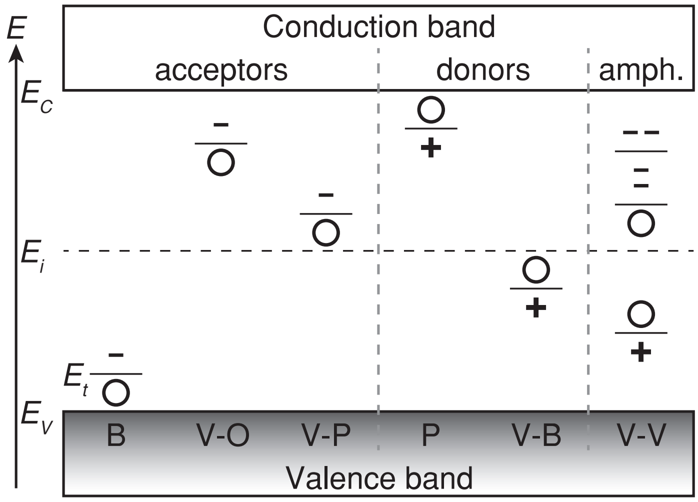

Figure 4.3: Schematic of defect classifications by their possible charge states in the band gap (inspired by [47]). Acceptors, donors and amphoteric levels of different energies E_t are indicated as small solid lines. Their possible charges in respect to the Fermi level are given by the symbols (+ / - / ∘) (see text). The example shown are boron (B), vacancy-oxide (V-O), vacancy-phosphorus (V-P), phosphorus, vacancy-boron (V-B) and a divacancy (V-V).

Another naming convention that should be elaborated is the labeling of defects as deep or shallow. Usually a defect state is defined as deep in the context of the bandgap, meaning that if it is located quite close to the middle of the bandgap one speaks of a deep level. On the contrary, shallow levels can be found close to either conduction or valence band. Unfortunately, the line at which a defect stops being considered deep and becomes shallow is never clearly defined, thus, in order to avoid confusion, the energy levels should always be attached in discussions.

A summary of the main classification for defect complexes in the band gap and their charge states can be seen in Fig. 4.3 and Table 4.2. The defect or trap levels with energy E_t are indicated as small solid lines while their possible charge states are depicted as symbols with (+ / - / ∘), meaning positive, negative or neutral respectively. Table 4.2 also contains their respective energy levels relative to the conduction and valence band, as well as their annealing temperature (see Sec. 4.1.4.2).

4.1.3.2 Electrical properties

As mentioned above, the formation of point defects does not only lead to the defects becoming stable at room temperature, but also to a change in their electrical properties. The type of defect alone is not sufficient to explain the macroscopic impact it will have on the device. Another important quality is its energy level within the bandgap, as will be shown in the following.

In order to understand the electrical properties of energy states in the bandgap their charge exchange with the energy bands is essential. This dynamic is explained by SRH statistics as discussed in Sec. 3.1.2. Considering all four interactions (electron capture, hole capture, electron emission, hole emission) and their respective rates (r_{ec}, r_{hc}, r_{ee}, r_{he}) given by Eq. (3.15)-(3.18), a differential equation describing the occupation of a

Table 4.2: Characteristics of several important defects in silicon (taken from [31]). Their different charge states and energy levels with respect to the conduction band E_C and valence band E_V are displayed (see also Fig. 4.3). In addition, the annealing temperature is given (see Sec. 4.1.4.2). From this, it is easy to see that vacancies and some of the interstitials are not stable at room temperature due to their low annealing temperature. The last two entries are possible candidates for deep acceptor levels, according to [50].

Impurity	Charge state	Energy level	
phosphorus	P^0 P^+	$E_C - 0.045$	
boron	B^- B^0	$E_V + 0.045$	

Defect	Charge state	Energy level	Annealing temperature [K]
interstitial	I^- I^0 I^+	$E_C - 0.39$ $E_V + 0.4$	140–180 540–600 370–420
vacancy	V^{--} V^- V^0 V^+ V^{++}	$E_C - 0.09$ $E_C - 0.4$ $E_V + 0.05$ $E_V + 0.13$	≈ 90 150
divacancy	V_2^{--} V_2^- V_2^0 V_2^+	$E_C - 0.23$ $E_C - 0.39$ $E_V + 0.21$	≈ 570 ≈ 570 ≈ 140 ≈ 570
A-center	$(V\text{–}O)^-$ $(V\text{–}O)^0$	$E_C - 0.18$	≈ 600
E-center	$(V\text{–}P)^-$ $(V\text{–}P)^0$	$E_C - 0.44$	≈ 420
boron interstitial	B_I^- B_I^0 B_I^+	$E_C - 0.45$ $E_C - 0.12$	420
vacancy boron	$(V\text{–}B)^0$ $(V\text{–}B)^+$	$E_V + 0.45$	≈ 300
divacancy oxygen complex	$(V_2\text{–}O)^-$ $(V_2\text{–}O)^0$	$E_C - 0.50$	?
trivacancy oxygen complex	$(V_3\text{–}O)^-$ $(V_3\text{–}O)^0$	$E_V + 0.40$	?

defect state in the bandgap with an electron can be formulated:

$$\begin{aligned}\frac{\mathrm{d}n_t}{\mathrm{d}t} &= r_{ec} + r_{he} - r_{ee} - r_{hc} \\ &= c_n n p_t + \epsilon_p p_t - \epsilon_n n_t - c_p p n_t \ . \end{aligned} \tag{4.4}$$

The probability that an electron occupies an electronic state with energy E is given by the Fermi-Dirac distribution

$$F(E) = \frac{1}{1 + e^{\frac{E-E_F}{kT}}} \ . \tag{4.5}$$

With this, the densities n and p of free electrons in the conduction band and holes in the valence band, respectively, can be calculated by taking all possible energy states within both energy bands into account, leading to

$$n = \int_{E_C}^{E_{\mathrm{top}}} e_C(E)\ F(E)\ \mathrm{d}E \qquad \text{and} \tag{4.6}$$

$$p = \int_{E_{\mathrm{bottom}}}^{E_V} e_V(E)\ F(E)\ \mathrm{d}E \ , \tag{4.7}$$

where $e_C(E)$ and $e_V(E)$ denote the energy density of levels in the conduction and valence band, respectively. Equations (4.6) and (4.7) are valid for intrinsic semiconductors as well as ones with doping impurities, since these only affect n and p by varying the Fermi level. Assuming energy levels that are $3kT$ above or below the Fermi level, Eq. (4.5) can be simplified due to the exponential term and if $|E_{C,V} - E_F| > 3kT$ is true, Eq. (4.6) and (4.7) can be approximated to

$$n, p = N_{C,V}\ e^{\pm\frac{E_F - E_{C,V}}{kT}} \ . \tag{4.8}$$

Equation (4.8) can be expressed in terms of the intrinsic carrier density with the help of Eq. (3.4):

$$n, p = n_i\ e^{\pm\frac{E_F - E_i}{kT}} \ . \tag{4.9}$$

With Eq. (4.9) and SRH statistics (Eq.(4.4)) it is now possible to calculate the occupation statistics for trapping centers under different conditions, as will be shown in the following.

Occupation statistics for traps under thermal equilibrium

In thermal equilibrium condition, there is no net flow of electrons $\mathrm{d}n_t/\mathrm{d}t = 0$, which, in consequence, means that the rates for electron emission and electron capture must be equal $r_{ee} = r_{ec}$, such as the rates for hole emission and hole capture $r_{he} = r_{hc}$. The fraction of a trap state with concentration N_t and energy E_t within the bandgap occupied by electrons n_t or holes p_t, respectively, is given by Fermi-Dirac statistics:

$$n_t = N_t\ F(E_t) \tag{4.10}$$

$$p_t = N_t\ (1 - F(E_t)) \ , \tag{4.11}$$

with $N_t = n_t + p_t$. Note that traps which are not occupied by an electron are automatically regarded as occupied by a hole and vice versa.

For the calculation of the emission probability of electrons ϵ_n and holes ϵ_p of the trap levels, the above established equality of emission and capture rates can be utilized together with Eq. (4.9)-(4.11), arriving at

$$\epsilon_{n,p} = c_{n,p}\ n_i\ \frac{1 - F(E_t)}{F(E_t)}\ e^{\frac{E_F - E_i}{kT}} \ . \tag{4.12}$$

Finally, with

$$\frac{1 - F(E_d)}{F(E_d)} = e^{\frac{E_d - E_F}{k_B T}} \tag{4.13}$$

and expressing the capture coefficients $c_{n,p}$ in terms of capture cross-sections $\sigma_{n,p}$ and thermal velocity $\nu_{th;n,p}$ of electrons and holes, respectively

$$c_{n,p} = \sigma_{n,p}\, \nu_{th;n,p} \ , \tag{4.14}$$

one obtains

$$\epsilon_{n,p} = \sigma_{n,p}\, \nu_{th;n,p}\, n_i\, e^{\pm \frac{E_t - E_i}{kT}} \ . \tag{4.15}$$

This expression is independent of E_F thereby giving it the advantage that it is also valid under non-equilibrium conditions, which will become of interest in the following scenario.

Occupation statistics for traps the space charge region

In many applications of semiconductor detectors, the device is operated in reverse bias thus creating a space charge region and sensitive volume within its detector bulk. This in turn also means that the system is now placed in a non-equilibrium state, making Eq. (4.10) and (4.11) no longer valid.

As established in Sec. 3.1.2, in the case of a space charge region the electron and hole capture rates can be omitted $r_{ec} \approx r_{hc} \approx 0$ since the density of free charge carriers is negligibly small ($n \approx p \approx 0$). Generation of charges will be dominant and this reduces Eq. (4.4) to

$$\frac{\mathrm{d}n_t}{\mathrm{d}t} = \epsilon_p p_t - \epsilon_n n_t \ . \tag{4.16}$$

Considering a steady state with no net flow ($r_{ee} = r_{he}$),

$$n_t, p_t = N_t\, \frac{\epsilon_{p,n}}{\epsilon_n + \epsilon_p} \tag{4.17}$$

can be derived for the occupation of traps in the space charge region. This can further be modified by utilizing the previously found expressions for ϵ_n and ϵ_p yielding

$$n_t, p_t = \frac{N_t}{1 + \left(\frac{\sigma_n\, \nu_{th,n}}{\sigma_p\, \nu_{th,p}}\right)^{\pm 1} e^{\pm 2 \frac{E_t - E_i}{kT}}} \ . \tag{4.18}$$

The ratio of electron and hole emission probabilities, obtained from Eq. (4.15)

$$\frac{\epsilon_n}{\epsilon_p} = \frac{\sigma_n\, \nu_{th,n}}{\sigma_p\, \nu_{th,p}}\, e^{2 \frac{E_t - E_i}{kT}} \tag{4.19}$$

together with Eq. (4.18) already contain most of the important information regarding the charge dynamics of trap levels withing the bandgap.

In both cases, the energy level of said defect is essential, since absorption cross-sections and thermal velocities for electrons and holes are of similar magnitude. Thus, it can be deduced that defects located above E_i are much more likely to emit electrons than holes and defects located below E_i, respectively, show higher probabilities for hole emission than electron emission. Hence, trap states above the center of the band gap will mainly be found in a more positive charge state, while the ones below are predominantly in a more negative one. In addition, the closer the state is located to the conduction band the higher ϵ_n will become and the fraction of those trap states occupied by electrons n_t

will become negligibly small while $p_t \approx N_t$. Accordingly the opposite holds true for trap levels found closer to the valence band.

For a trap level close to midgap $E_t \approx E_i$, Eq. (4.18) and (4.19) show that the result mainly depends on the absorption cross-sections and thermal velocities for electrons and holes, but it was already established that those will be in a similar order of magnitude. It can further be assumed that those states will be found in both occupation states with very similar likelihoods and that the emission rates for electrons and holes will also be close to equal. This becomes even more evident when considering the generation rate for electron-hole pairs of a trap state in the space charge region:

$$\begin{aligned} G_t &= \epsilon_n\, n_d = \epsilon_p\, p_d \\ &= N_t n_i \, \frac{\sigma_n\, \nu_{th;n}\, \sigma_p\, \nu_{th;p}}{\sigma_n\, \nu_{th;n}\, e^{\frac{E_t - E_i}{kT}} + \sigma_p\, \nu_{th;p}\, e^{-\frac{E_t - E_i}{kT}}} \;. \end{aligned} \tag{4.20}$$

This expression shows a clear maximum of G_t for energy level close to midgap, while the rate is minimized for traps located close to the energy bands. Thereby, only traps with $E_t \approx E_i$ will have a significant contribution on the overall generation rate of electrons and holes and consequently on the leakage current of the detector bulk with bulk generation current density

$$j_{BGC} = \sum_{\text{traps}} q_0\, G_t \;. \tag{4.21}$$

Finally, the effective doping concentration in the detector bulk can be derived by taking all occupied trap states into account as well as the charge dynamics previously discussed which reveals

$$N_{\text{eff}} = \sum_{\substack{\text{donors} \\ \text{in SCR}}} p_t - \sum_{\substack{\text{acceptors} \\ \text{in SCR}}} n_t \;. \tag{4.22}$$

The above derivations are true under the assumption of a low to moderate amount of leakage current in the bulk. However, the situation changes if the leakage current becomes too high. Then the capture rates for electrons and holes (r_{ec} and r_{hc}) cannot be neglected any longer. Therefore, all four components of Eq. (4.4) now have to be taken into account, resulting in a fraction of traps occupied by electrons of

$$\begin{aligned} n_t &= N_t\, \frac{\sigma_n\, \nu_{th;n}\, n + \epsilon_p}{\epsilon_n + \sigma_p\, \nu_{th;p}\, p + \sigma_n\, \nu_{th;n}\, n + \epsilon_p} \\ &= N_t \frac{\sigma_n\, \nu_{th;n}\, n + \sigma_p\, \nu_{th;p}\, n_i\, e^{-\frac{E_t - E_i}{kT}}}{\sigma_n\, \nu_{th;n} \left(n + n_i\, e^{\frac{E_t - E_i}{kT}} \right) + \sigma_p\, \nu_{th;p} \left(p + n_i\, e^{-\frac{E_t - E_i}{kT}} \right)} \;. \end{aligned} \tag{4.23}$$

This can have an influence on the amount of change of the total doping concentration due to certain deep acceptor states being filled with electrons and starting to contribute to N_{eff} (see Sec. 4.1.5.2). Overall, an increased leakage current will have negative effects on a SiPM with additional contributions of charge capture and release potentially leading to increased contributions of afterpulsing, as will be discussed in Sec. 5.3.7.

4.1.4 Annealing of radiation damage

Annealing generally refers to the semi-disappearance of radiation induced crystal defects after the exposure to a temperature treatment.

A short overview of the basic annealing mechanisms as well as its dependence on temperature will be given in the following section. Furthermore, a brief insight on reverse annealing will follow.

4.1.4.1 Annealing mechanisms

On first glance, one would assume that annealing can be described by the recombination of interstitials and vacancies in the detector bulk. Since certain defects like the Frenkel pairs are mobile at room temperature, a migration of said defects through the lattice is possible. Subsequently, they are able to come across their counterpart and finally recombine, leaving no net influence on the detector behind. Even though this is one of the major underlying mechanism for annealing, it is incorrect to assume that after a long enough period of time, the crystal will become perfect again, e.g. that all interstitials will have recombined with vacancies.

Another major aspect of annealing is the formation of new stable complexes, which will not have the same adversary effects as the previous defects. This way, the lattice remains imperfect but the net effect of the initial defect might vanish. However it is also possible, that neutral and initially stable defects might become mobile and create defects with adversary impacts, which can be refereed to as reverse annealing (see below). In addition, given enough vibrational lattice energy, complex defects are able to dissociate into their respective components, resulting in the components being able to undergo the aforementioned processes.

In order to achieve this dissociation and annealing of not only the defects that are mobile at room temperature but also of additional ones that have negative impacts on the performance of the detector, the ambient temperature can be increased as explained below.

4.1.4.2 Annealing temperature

Each mechanism involved in annealing requires a sufficiently large amount of activation energy E_A in order to occur. It can differ vastly for the three processes explained above, depending on the specific defect states involved. In general the required energy is most commonly provided via an increase in ambient temperature which makes the annealing process itself and the rate in which it occurs highly dependent on the temperature at which the device is kept during the waiting period after irradiation.

Every trap state or complex has a specific annealing temperature in order to provide E_A (as was already briefly shown in Table 4.2) and remove a certain percentage of the present trap concentration. According to [47], the annealing temperature can be defined as the temperature at which the defect concentration drops below the (1/e)-th part of the initial concentration $N_{t,0}$ for a certain time interval Δt, which is chosen in the order of $\Delta t \approx 20$ min. The annealing temperature T_{ann} can then be derived to be

$$T_{ann} = \frac{E_A}{k \ \ln\left(k_0 \Delta t\right)} \ , \tag{4.24}$$

where k_0 is called a frequency factor which depends linearly on the temperature. It is important to note that T_{ann} is not a precise limit, since the same amount of annealing may also occur at smaller temperatures, due to statistical fluctuations of the kinetic energies of lattice atoms.

In summary, a greater temperature and exposure time to said temperature will increase the overall impact the annealing procedure will have on the device as higher activation energies can be accessed and more time for statistical processes will be provided.

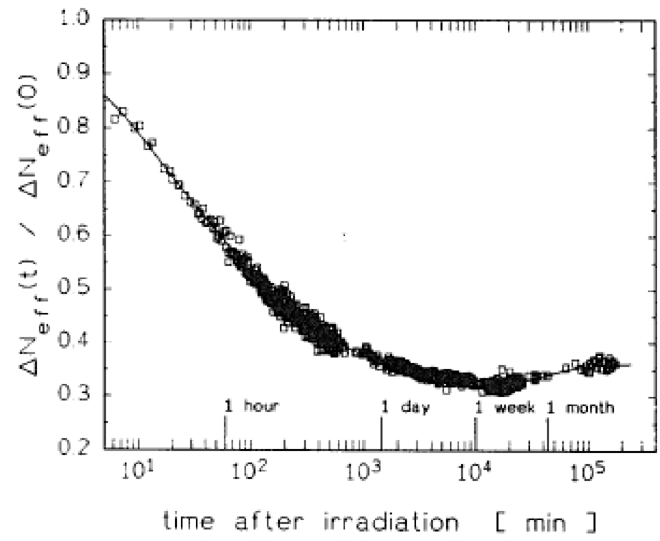

Figure 4.4: Relative change of effective impurity concentration as function of time for room temperature annealing (taken from [51]). The initial trend of the decreasing change of effective doping concentration stops after approximately one week and an increase can be observed afterwards.

4.1.4.3 Reverse annealing

As one of the possible annealing mechanism involves the formation of new complexes, the effect of annealing may not always be beneficial for the device performance. Measurements of the effective doping concentration of irradiated samples by Wunstorf [51,52] have shown that after a sufficiently long annealing period, the change in effective doping concentration started behaving contrary to expectations. Not only did it cease to decrease, but it started to increase as well (see Fig. 4.4). Due to its contra-beneficial nature, this effect is usually referred to as reverse annealing. As already mentioned above, it can be explained, when considering the presence of electrically inactive defects, initially formed by irradiation. If these defects are involved in an annealing process, it is possible that new, electrically active defects are created, which can have an impact on the overall detector performance. Analytical models for the description of this effect by defect interaction rates exist [31], but will not be discussed here, since the impact of reverse annealing on the measurements performed in this study should be negligible.

4.1.4.4 The importance of controlled annealing

It was previously established in Sec. 4.1.4.2 that the annealing process is strongly dependent on the annealing Temperature T_{ann} as well as the annealing time. An example of this dependence can be witnessed in Fig. 4.5 which illustrates the impact on the current related damage rate α for different annealing scenarios. This parameter and its importance will be explained in Sec. 4.1.5.1, but for the current discussion, it is sufficient to say that it is directly related to the increase in leakage current caused by radiation damage.

From Fig. 4.5 it is easy to see that measurements of α performed right after irradiation at room temperature can have significantly varying results if the time at which the measurement was done differs only slightly (order of minutes). Like α, many other parameters depend on the defect concentration and are thereby affected in the same manner. Hence, in order to properly compare such results, knowledge of the exact annealing history of the device is necessary, which, however, might be complicated due to various measuring circumstances when considering the time scale in question.

A more reliable approach is to store the irradiated samples at lower temperatures (e.g. below 273 K) before exposing them to a controlled annealing procedure for them

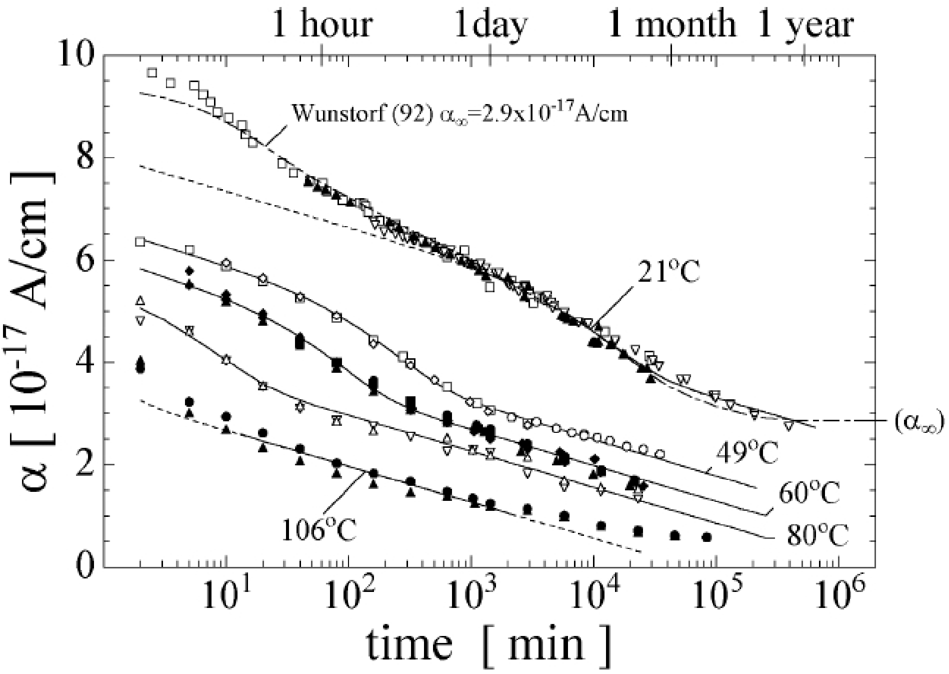

Figure 4.5: Current related damage rate α as a function of annealing time at different temperatures (taken from [47]). The impact of annealing on the defect concentration and therefore on α can be seen to be very critical for small annealing times. Thus a heat treatment is commonly used to achieve a stable (in terms of measurement time) situation, where changes are only noticeable after time differences in the order of weeks or months.

to reach a situation where room temperature annealing has no longer a considerable impact on the defect concentration of the samples in terms of the measuring time. Such a situation can for example be found after approximately one month of room temperature annealing (see Fig. 4.5). By taking full advantage of the temperature dependence of the annealing process, the same state can already be achieved after a smaller amount of time but at higher temperatures.

A commonly accepted annealing scenario for reaching such a (quasi-) stable state is an 80 minute annealing at a temperature of 60°C (80min, 60°C). This roughly corresponds to 20 days of room temperature annealing and provides a state in which prolonged measurement at room temperature (in the order of days) will not have a significant impact any longer. It is important to keep in mind that such studies can only be compared if they used the same annealing scenario or if their individual annealing scenario is known, so that the results can be scaled accordingly.

4.1.5 Impact on detector performance

After the detailed discussions of the previous sections, the macroscopic change in the detector properties due to the electrical properties of the defects can now be reviewed. Radiation induced crystal defects will have various impacts on the overall device performance, mainly being an increase in leakage current, a change in effective doping concentration and consequently in full depletion voltage and finally a change in charge collection efficiency.

Depending on the detector or device type, other implications are possible like an increase in $1/f$ noise but this section will focus on the impact one can expect on parts of the device utilized in this study, which amount to silicon diodes and a unique type of test measurement device, developed in the curse of this study. The impact on the performance of a novel type of SiPM (see Chapter 6) is likewise of great importance, however, this discussion will take place after the characteristics of said devices were explained in more detail (see Sec. 6.5).

The following section will deal with those effects with the assumption of pure bulk damage induced by neutrons[2] on a n-type silicon bulk. Furthermore, for some cases the influence of annealing on the macroscopic behavior of the detector will be shown. It is of importance to note, that the following review will only give a short summary of a vast amount of extensive studies performed on this field. More in depth discussions can be found in e.g. [47, 51–59].

4.1.5.1 Leakage current

With the help of Eq. (4.18) and (4.19) it was established that defects located close to the middle of the bandgap will predominantly contribute to an increase in leakage current. Thus, an increased number of defects due to prolonged irradiation will also increase the volume-generated leakage current in the bulk. The difference in leakage current before and after irradiation ΔI for a volume V in dependence of the equivalent 1 MeV neutron fluence Φ_{neq} can be expressed by

$$\frac{\Delta I}{V} = \alpha\ \Phi_{neq}\ , \tag{4.25}$$

where α is the aforementioned current related damage rate. This linear relation was confirmed by multiple studies already, e.g. performed by Moll [47] or Wunstorf [51] and can be seen in a measurement by Moll [47], shown in Fig. 4.6. An independence of $\Delta I/V$ on the different bulk material (n or p-type) and thus on the respective resistivity can be observed. Therefore all measurements resulted in the same constant slope of the curve which is represented by the current related damage rate $\alpha(80\text{min}, 60°\text{C}) = (3.99 \pm 0.03) \cdot 10^{-17}$ A/cm, utilizing the annealing scenario introduced in Sec. 4.1.4.4. Since this value for α will be obtained regardless of detector material if the irradiation was scaled according to the NIEL hypothesis, it can be used as a tool for confirmation of the quality of the irradiation procedure.

However, it has to be taken into account that the leakage current shows a strong temperature dependence. For proper comparison of measured data, it is thereby advised to scale I_{leak} to a reference temperature T_R:

$$I_{leak}(T) = R(T)\ I_{leak}(T_R) \qquad \text{with} \qquad R(T) = \left(\frac{T}{T_R}\right)^2 e^{\frac{E_{\text{eff}}}{2k}\left(\frac{1}{T_R} - \frac{1}{T}\right)}\ . \tag{4.26}$$

Instead of the normal bandgap energy E_g, an effective bandgap energy $E_{\text{eff}} = 1.21$ eV was chosen in order to incorporate the temperature dependence of $E_g(T)$, as was recommended by the RD50 collaboration [60].

The impact of annealing on I_{leak} was already illustrated in Fig. 4.5. A long high-temperature annealing is desirable as the leakage current can be decreased by almost half of an order of magnitude in certain cases, as more and more defects will be restored.

---

[2]Considering protons or other charged particles would result in additional radiation damage in oxide surfaces, which will be discussed in Sec. 4.2

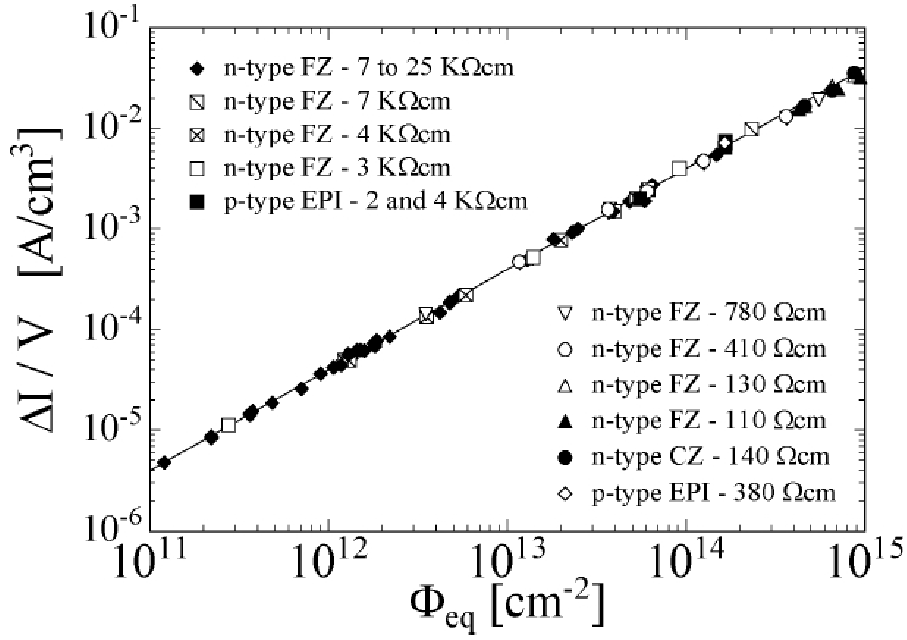

Figure 4.6: Fluence dependence of the leakage current increase per volume (taken from [47]). Different types of silicon material show all the same result, which is a slope of $\alpha(80\text{min}, 60°\text{C}) = (3.99 \pm 0.03) \cdot 10^{-17}$ A/cm. The expression in the brackets states that the current was measured after a heat treatment for 80 min at 60°C for annealing.

4.1.5.2 Effective doping concentration

Introducing defect states into the detector material via irradiation will lead to a change of the effective doping concentration N_{eff} which is also in direct correlation with the depletion voltage, as was shown in Eq. (3.10).

The reason for this change can, again, be explained when taking Eq. (4.18) and (4.19) into account. It was already established that the occupational probabilities for the defect states n_t and p_t reach higher values the closer the energy level is located to one the energy bands (see Sec. 4.1.3.2). Acceptors close to the conduction band and donors close to the valence band will therefore very likely be found in a neutral charge state (see Fig. 4.3). However, when considering a acceptor near the valence band and donor near the conduction band instead, the case changes drastically. They will predominantly be found in a non-neutral charge state, resulting in a negatively charged acceptor and a positively charged donor, respectively.

Assuming those defect states to be stable, they will then have an impact on N_{eff} by contribution of their charge state. According to [61], it is also possible that acceptors located close to midgap can contribute to the change in N_{eff}. Within this deep acceptor model, it is suggested that a high leakage current will provide enough electrons to keep said defects consistently occupied despite their increased emission rates, thus resulting to a net effect on the effective doping.

This, however is not the only method in which radiation damage can cause a change in N_{eff}. As was shown in Sec. 4.1.3.1, the formation of an E-center requires a vacancy and a phosphorus atom present in the lattice. Since phosphorus is utilized as a donor for n-type silicon, this effectively results in the removal of donor state in favor of the creation of an acceptor, thereby doubly impacting N_{eff}. In addition, the formation of other defects which will not contribute to N_{eff} but will still infer the removal of a donor atom are also possible. Vice versa, respective processes involving initial acceptor atoms will take place due to irradiations as well.

In summary, one can name the following four processes to be responsible for the overall change in effective doping concentration:

- **donor removal** due to the formation of defect complexes including donors (e.g. E-centers)
- **acceptor removal** due to the formation of defect complexes including acceptors (e.g. vacancy-boron defects)
- **donor creation** due to the creation of defects which assume a positive space charge (effective donors)
- **acceptor creation** due to the creation of defects which assume a negative space charge (effective acceptors)

Under the assumption of an independent occurrence of those processes, a fluence dependent expression for N_{eff} can be expected and is given by

$$N_{\text{eff}}(\Phi) = N_{D,0}\, e^{-c_D \Phi} - N_{A,0}\, e^{-c_A \Phi} + b_D\, \Phi - b_A\, \Phi\ , \tag{4.27}$$

where $N_{D,0}$ and $N_{A,0}$ denote the initial donor and acceptor concentrations, respectively and c_D, c_A, b_D and b_A the different reactions constants for the individual processes listed above. Assuming an n-type detector bulk, acceptor removal and donor creation will either not occur or only to a negligibly small degree ($c_A \approx b_D \approx 0$) (as stated by [31]), so that Eq.(4.27) can be simplified to

$$N_{eff}(\Phi) = N_{D,0}\, e^{-c\Phi} - N_{A,0} - b\, \Phi\ , \tag{4.28}$$

where $c_D = c$ and $b_A = b$ was used. According to [53], c can be interpreted as the donor removal cross-section while b represents the probability to create an acceptor state by a hadron per unit path length in silicon. Values for c and b have to be determined experimentally by fitting the measured results to Eq.(4.28).

The result of such a measurement is displayed in Fig. 4.7, where the impact of increasing radiation fluence on the effective doping concentration and thus depletion voltage for an initially n-type material is shown. A decrease of the effective doping with irradiation is clearly visible until the material becomes intrinsic, leading to $U_{depl} \approx 0$. At this threshold the initially n-doped bulk effectively becomes p-type, which is why this effect is referred to as type inversion. Above that, a linear increase of N_{eff} is visible as the formation of new acceptor states continues. Note, however, that the determination of the full depletion voltage will only provide information on the effective difference of donors and acceptors in the bulk, but not yield any information on the separate contributions.

The effects of annealing on N_{eff} were already briefly shown in Fig. 4.4. Since some newly formed defect complexes are not stable at room temperature, dissociation and the formation of new, more stable defects which will have the opposite impact on the effective doping are possible. In contrast to the leakage current (see Fig. 4.5), reverse annealing can have a negative impact on the overall detector performance as the change in space charge continues to increase after a certain amount of time of room temperature annealing. This has to be taken into account when considering long term operation of the detector after irradiation.

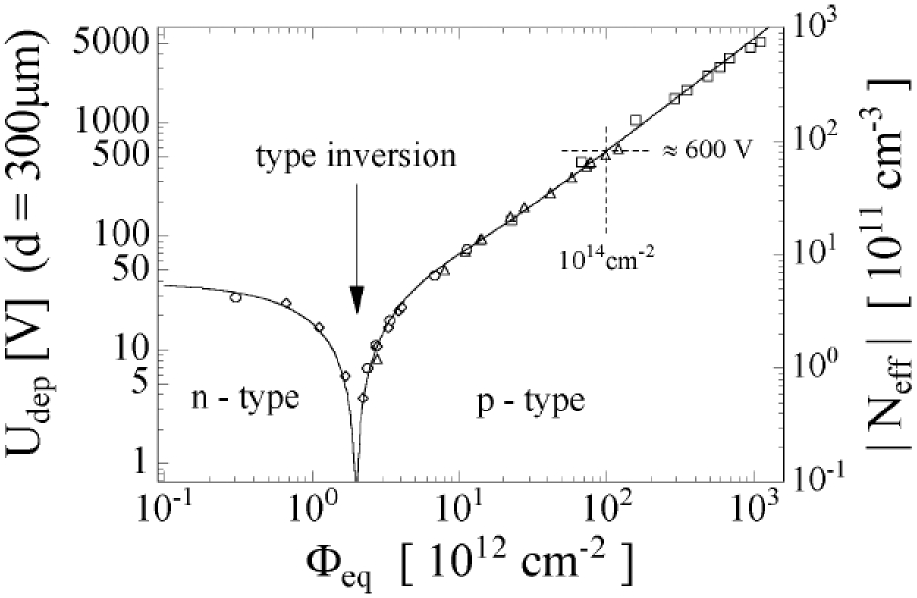

Figure 4.7: Change in effective doping concentration and depletion voltage (taken from [47]). The values were measured immediately after irradiation. A change of the space charge sign can be experienced for a certain neutron fluence. At this point type inversion occurs, i.e. the initially n-type silicon bulk effectively gets converted into a p-type.

4.1.5.3 Charge collection efficiency

Signal charges created in the detector bulk, can be trapped by defect states within the bandgap. The trapping dynamics can be described by the emission probabilities $\epsilon_{n,p}$ and capture coefficients $c_{n,p}$ for electrons and holes. Taking the case of a space charge region with low leakage current, one can assume that the majority of traps will not be occupied by free charges. In addition, the trapping probability can be expected to be proportional to the effective trap concentration N_t. Hence, the capture probability per unit time for electrons and holes can be written as

$$\frac{1}{\tau_{t,n}} = \sum_t \sigma_n \, \nu_{th,n} \, p_t = \sum_t \sigma_n \, \nu_{th,n} \, N_t \frac{\epsilon_{n,t}}{\epsilon_{n,t} + \epsilon_{p,t}} \tag{4.29}$$

and

$$\frac{1}{\tau_{t,p}} = \sum_t \sigma_p \, \nu_{th,p} \, n_t = \sum_t \sigma_p \, \nu_{th,p} \, N_t \frac{\epsilon_{p,t}}{\epsilon_{n,t} + \epsilon_{p,t}} \, , \tag{4.30}$$

with $\tau_{t,n}$ and $\tau_{t,p}$ being the trapping time constants for electrons and holes, respectively. The total probability is a summation of all individual traps within the bulk. From Sec. 4.1.3.2 it is easy to see that trap levels below E_i will predominantly act as traps for holes, since they will most likely be found in a more negative charge state. Accordingly, the trap levels above E_i will then predominantly be electron traps. Re-emission of charges will occur after a specific amount of time, which is strongly dependent on the energy level and consequently characteristic for every trap.

Electrons or holes, which are trapped by a defect and not re-emitted before the end of a readout period of the detector system will not be accounted for in the measured signal, thus falsifying the results. An increased number of traps in the bulk can therefore lead to a decrease in charge collection efficiency. While traps, located close to the energy bands, may release trapped charges fast enough to still fall within one readout cycle, the opposite is also possible for traps deep within the bandgap. Hence, an adaptation of the readout time (if feasible) can to a certain degree diminish the impact of the reduced charge collection efficiency.

4.2 Ionizing radiation damage

In the previous section, the damage induced to the bulk of the detector material, based on destruction of the perfect crystal lattice was discussed. However, it is also possible for the device to experience damages caused by ionizing radiation damage. These are most of the time referred to as surface damages, as ionizing radiation mainly induces damages in surface layers of the devices, i.e. the SiO_2 layer and the SiO_2-Si interface.

First a quick overview of the damage mechanism at work will be given and afterwards the general effects on the device performance will be explained. Note, however, that due to the nature of the devices under test in this study, the experiments will mainly focus on the impact of bulk damage, as its effect is expected to be more prevalent than that of surface damage. Thus, the discussion below is going to be kept brief and concise and focus on the facts relevant for understanding the expected implications on the novel SiPM devices of this experimental study[3].

4.2.1 Damage mechanism

In the case of NIEL, the damage to the detector bulk was caused due to interactions with the (semi-) perfect lattice, leading to the introduction of defects with different electrical properties. This however is not an issue for surface layers of silicon devices like the aforementioned SiO_2, since its crystal structure is already highly irregular.

Silicon and silicon dioxide have different lattice structures which leads to the existence of interface traps caused by unsaturated bindings of $[sp^3]$-orbitals, called dangling bonds. The presence of dangling bonds, together with lattice mismatches increases the amount of defects located at the interface drastically.

Additional damages in these layers are caused by ionizing radiation (e.g. photons, x-rays and charged particles), more specifically due to the generation of electron-hole pairs. While immediate recombination of those pairs is possible, it strongly depends on the quality of the oxide, ranging between several percent and 100% [29]. Due to several orders of magnitude difference in mobility, the pairs will separate almost instantly and electrons will swiftly diffuse out of the surface layer, whereas the holes will require significantly more time for their transition. However, defect states can also be found within the surface layer, making hole capture one of the dominant processes. This can be attributed to the higher bandgap energy in insulators ($E_g(SiO_2) = 8.8$ eV and $E_g(Si_3N_4) = 5$ eV) and thereby, if a trap is located deep enough within the forbidden gap, hole emission becomes virtually impossible.

Even though the holes will become trapped, their drift towards the SiO_2-Si interface can still continue thanks to a hopping mechanism, displayed in Fig. 4.8, in which the holes jump from one localized defect to another until they reach the interface. The motion of the charges can also be enhanced by the application of an positive voltage on the metal side of the oxide, which corresponds to the common operation mode of a transistor.

[3]More detailed explanations and discussions of ionizing radiation damage and its impact on different detector performances can be found in various of the many literature sources listed in the beginning of this chapter

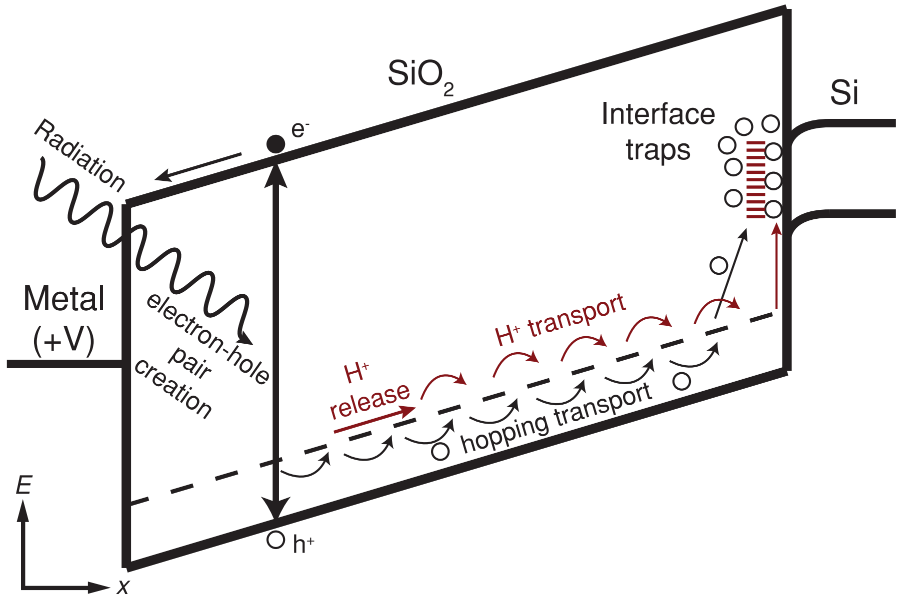

Figure 4.8: Schematic illustration of the surface damage creation in a MOS structure after irradiation (inspired by [63]).Ionizing radiation creates electron-hole pairs, and the holes in turn can release hydrogen ions from within defects. Both hydrogen and holes are able to traverse the oxide towards the SiO_2-Si interface via a hopping process where they will support the creation of additional interface traps or lead to a build up of positive charges, respectively (see text).

Depending on the material quality, but unavoidable in general, hydrogen will also be present within the oxide layer (oxide defects containing hydrogen), which can be released by the hopping holes. After mimicking the hopping process of the holes, the hydrogen will eventually reach the interface region, leading to the creation of even more dangling bonds and therefore more defects by depassivating a previously passivated dangling bond[4].

Due to trapping being more likely in regions with a higher defect density, the positively charged holes will be accumulated at the SiO_2-Si interface. As stated in [29, 31], the static positive charge will saturate at about $N_{ox} \approx 3 \cdot 10^{12}\mathrm{cm}^{-2}$, because of the limited number of semi-permanent defects within the oxide - given a sufficiently large irradiation dose was provided. This will, in turn, lead to an accumulation of negative charges from the silicon at the interface, which can have an impact on the device in question.

It should be noted that various circumstances like the biasing condition during irradiation as well as the oxide thickness and the oxide annealing scenario can have drastic effects on the formation of surface defects, but will not be elaborated on here.

4.2.2 Impact on detector performance

The creation of positive oxide charges and subsequent accumulation of negative charges in the silicon close to the interface will have various effects, depending on the type of device one is considering.

[4]This is a very simplified depiction of the various mechanism involved in the creation of interface traps. See e.g. [62] for a more detailed and thorough discussion.

When, for example, looking at a device like a silicon strip detector with an oxide on top of the area between the individual strips, the following effects can be expected. First, the positive oxide charges will naturally influence the flat-band voltage causing it to increase. One can make use of this fact though, by utilizing it as a diagnostic tool for investigation of surface damages. Furthermore, additional effects can be contributed to the accumulated negative charges in the silicon. They will decrease the inter-strip resistance, thus increasing the cross-talk between individual strips, as well as increase the inter-strip capacitance, leading to increased noise contributions.

On the other hand, in the case of electronic circuit devices like a NMOS or PMOS, additional effects will have to be considered. The main issue arises from the shift in the threshold voltage of the device, as it may at some point require bias voltages for proper operation beyond what can be provided by the integrated electronics. Defects close to the interface are capable of interacting with the accumulated holes, thus forming new defects close to midgap, which in turn will result in an increased leakage current. Finally, a decrease of the signal-to-noise ratio can be expected, because of the positive oxide charges via the formation of parasitic charge transfer paths in the substrate.

While the above effects on the properties of MOS-based devices should by no means be taken lightly, as they can have devastating consequences on the performance of the detector systems, the case for the SiPM devices utilized in this study is different. Many of these mechanisms will not be present or not directly impact the performance, making surface damages less problematic, as will be explained in Sec. 6.5.

5 Experimental setups and characterizations of SiPMs

In order to determine the various characteristic parameters of SiPMs, different experimental setups or devices are necessary. The following section will introduce the setups and experimental instruments utilized in this study in addition to the dedicated readout board for SiPMs. In the course of this endeavor, the various characteristic SiPM parameters will be explained as well as the experimental methods for obtaining the respective parameters. First, the static types of measurements will be discussed, followed by the more sophisticated dynamic measurements. Finally, the photon emission microscopy method will be introduced.

5.1 Dedicated SiPM readout board

The signal of a SiPM is made up of the sum of all simultaneously firing pixels within its array, due to all individual cells being connected in parallel. Since in most cases this signal does not amount to a feasibly detectable signal, in particular for a small number of fired cells, an additional external amplification will be required.

Therefore, a custom-made readout board equipped with a pre-amplifier was utilized for the majority of the measurements on chip level. Figure 5.1 depicts a photograph (left) of said readout board and its circuit diagram (right). The SiPMs can be mounted in a socket designated for a 44-pin ceramic on the topside or via a smaller 2-pin mount on the backside of the board. The signal is then amplified via a dedicated pre-amplifier. Voltage for the SiPM and the amplifier is supplied by the respective connections on the side of the board.

Two different amplifiers were utilized in this study, namely the MiniCircuits MAR8-ASM+ and the Infineon BGA 614. Their effective amplification while mounted on the readout board, taking into account all additional electronics components was measured with a Rhode & Schwarz ZVA8 frequency analyzer for a frequency range between 300 kHz and 4 GHz and the results are shown in Fig. 5.2. Overall the MAR8-ASM+ exhibits a higher and more constant amplification of roughly 29.8 dB up to a frequency of 100 MHz, after which it begins to decrease. Its -3 dB bandwidth limit can be found at a frequency of roughly 480 MHz. In comparison, the BGA 614 provides a peak amplification of roughly 19.3 dB for frequencies between 80 MHz and 300 MHz, with its -3 dB bandwidth limit being at approximately 1.3 GHz.

If not stated otherwise, a readout board with a MAR8-ASM+ amplifier was utilized for measurements performed on chip level within this study, as it provides an overall more stable amplification over a wider frequency range.

5.2 Static measurements

Static or stationary measurements comprise current-voltage (I-V) and capacitance-voltage (C-V) measurements. These are, if not mentioned otherwise, performed with the setup illustrated in Fig. 5.3. The DUTs are placed within a light tight box of a

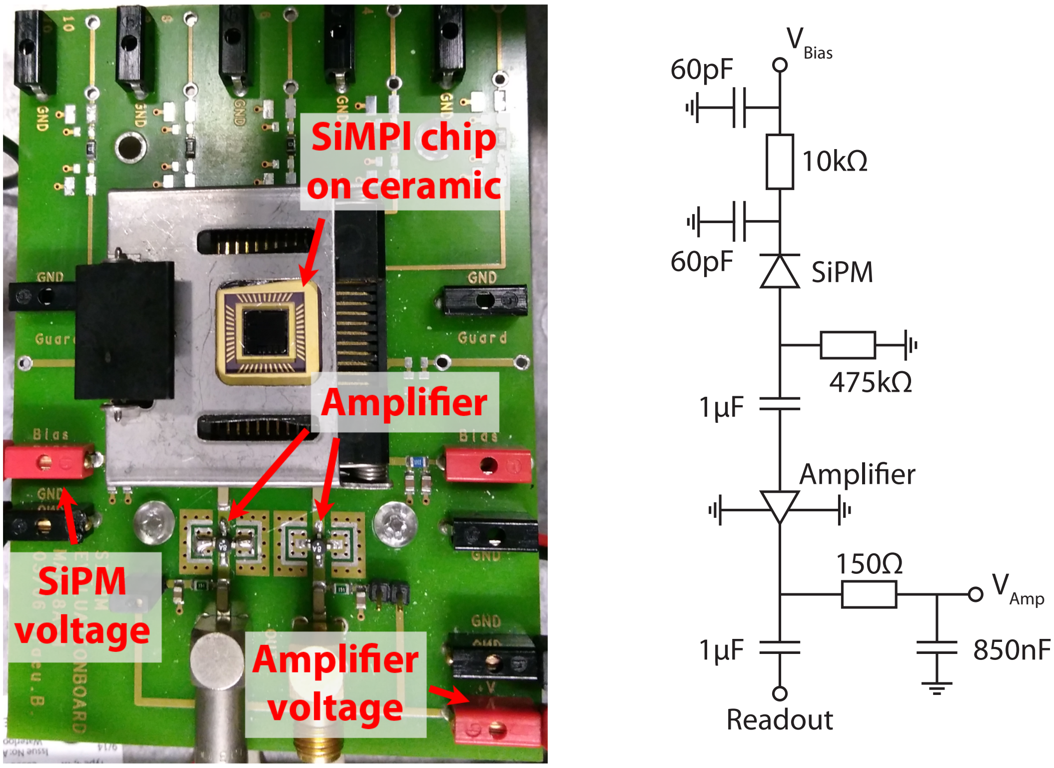

Figure 5.1: Photograph and circuit diagram of the custom-made SiPM readout board with mounted pre-amplifier. The SiPM can either be mounted within a socket for a 44-pin ceramic or via a 2-pin socket on the backside (not shown). Either a MAR8-ASM+ or BGA 614 amplifier are utilized. Bias voltage for the SiPM and the amplifier is supplied via the connections on the side. The additional electronic components are chosen according to the requirements of the amplifiers and a fast signal output.

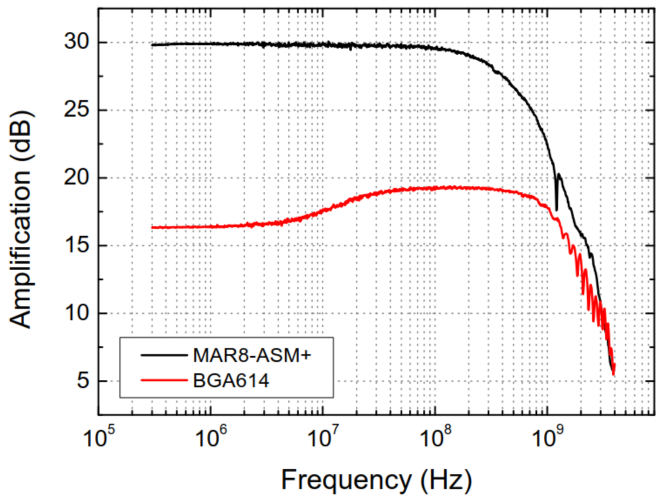

Figure 5.2: Measured amplification for the MAR8-ASM+ and BGA 614 amplifiers mounted on the SiPM readout board. The BGA 614 exhibits a peak amplification of roughly 19.3 dB for frequencies between 80 MHz and 300 MHz. On the other hand, the MAR8-ASM+ can provide a constant 29.8 dB amplification for frequencies up to roughly 100 MHz, afterwards decreasing to 25 dB at $f \approx 700$ MHz. Plot taken from [33]

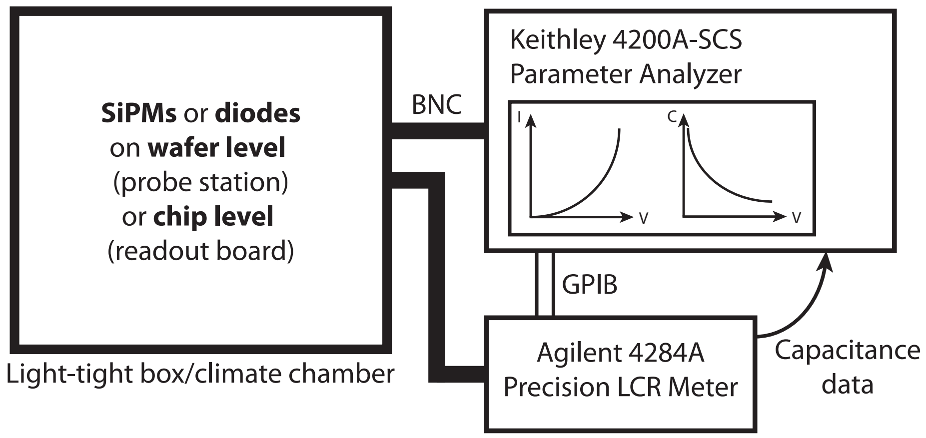

Figure 5.3: Schematic of the experimental setup for static characterizations. The DUTs are either located in a light tight box and contacted via probes of a probe station if the measurements are performed on wafer level, or placed in a light tight climate chamber while being mounted on the dedicated readout board. The I-V characteristics are directly obtained via a Keithley 4200A-SCS Parameter Analyzer and can further be connected to an Agilent 4284A Precision LCR Meter, which provides capacitance data for the C-V measurements.

probe station for measurements on wafer level or a light tight climate chamber in the case of chip level measurements. The wafer can then be contacted via multiple needles of the probe station, which are connected to the readout devices, while single chips are usually mounted on the dedicated readout board introduced above, which, in turn, can also be connected to the readout devices. The I-V-characteristics are determined by a Keithley 4200A-SCS Parameter Analyzer, which is furthermore connected to an Agilent 4284A Precision LCR Meter, additionally enabling C-V-measurements.

5.2.1 Current-voltage measurements

Static I-V-characterizations of SiPMs can provide information on the leakage current before breakdown, as well as the breakdown behavior of the devices. An example of such measurement in shown in Fig. 5.4a), where the full I-V-curve in reverse bias conditions for a Hamamatsu MPPC S10362-11-100C with a cell size of 100 µm and total area of 1 mm^2 can be seen. The leakage current below the breakdown voltage V_{bd} is caused by thermal generation in the high-field region and additional surface contributions. At V_{bd} and a dark current of roughly $I_D \approx 1$ nA the device is considered to be entering the Geiger-mode operation, enabling avalanche multiplication and resulting in a drastic increase of the current. V_{bd} is strongly dependent on technological parameters impacting the high-field region and is thus specific for each set of devices as will be seen later.

Changing the temperature during measurement, changes in the dark current according to Eq. (5.4) can be observed, as well as an impact in the breakdown voltage. Overall, a decrease in V_{bd} can be seen with decreasing temperature. The reason for this observation lies in the reduction of phonons with decreasing temperature, thus leading to less electron-phonon scattering within silicon. As a result, the mean free path of the accelerated charge carriers becomes longer, further increasing their ionization rate and thereby lowering the required voltage for a Geiger breakdown to occur [69]. The rate at which V_{bd} changes with different temperatures $\partial V_{bd}/\partial T$, again, varies on a device basis. As an example, the Hamamatsu MPPCs utilized within this thesis exhibit an average

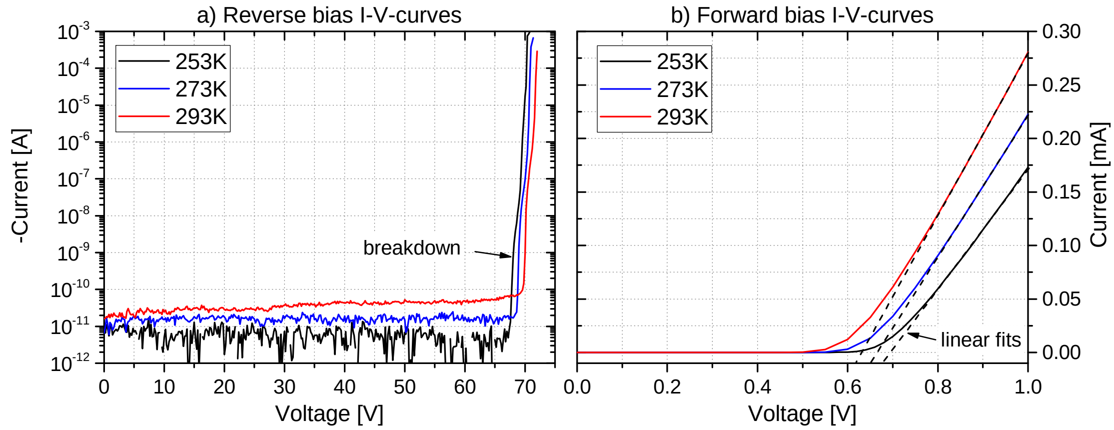

Figure 5.4: Static I-V-measurements of a Hamamatsu MPPC with 100 µm pixel size in a) reverse and b) forward bias. The dark current before breakdown (V_{bd}) in a) can be seen to vary with the temperature T (different colored lines) according to Eq. (5.4). At a certain voltage V_{bd}, breakdown occurs, enabling charge multiplication and thus increasing the current. This breakdown voltage can also be observed to depend on T and decreases with smaller temperatures (see text). The forward bias case, seen in b), can be utilized to determine R_Q by applying a linear fit (dashed line) to the linear section of the I-V-curve. The resistance of the polysilicon quench resistor can be observed to decrease with increasing temperature.

temperature coefficient of $\partial V_{bd}/\partial T = 56\text{mV/K}$.

By applying a forward bias to a conventional SiPM device, like a Hamamatsu MPPC, a curve similar to the one seen in Fig. 5.4b) can be observed. After a certain voltage, the entire characteristic becomes dominated by the quench resistor. Now a linear fit can be applied to the curve, as depicted, allowing the extraction of the quench resistor R_Q, which also exhibits a temperature dependence, depending on the material.

5.2.2 Capacitance-voltage measurements

The capacitance of a SiPM device or diode can be determined with a LCR meter. It makes use of a capacitance bridge in serial mode and measures the impedance of a device. By superimposing a small-amplitude AC signal to the biasing DC signal, the serial capacitance component C_s can be obtained [70]. As will be discussed in Sec. 9.4.1.1, an AC signal frequency of 50 kHz with a 200 mV signal amplitude was found to yield the most reliable results.

A common result of C-V-measurement is shown in Fig. 5.5 (blue line and scale), however a $1/C^2$-V-curve (black line and scale) usually allows for a more accessible analysis of the data. A decrease of the capacitance C can be witnessed up to a certain voltage, when the bulk becomes presumably fully depleted. In the depicted example this results in a diode capacitance of roughly 185 fF. This behavior is easier to extrapolate when looking at the $1/C^2$-V curve as a minute change in C is much more prominent in this case. The curve behaves according to Eq. (3.12) and increases linearly with V until full depletion of the diode or high-field region is reached, afterwards the value for $1/C^2$ saturates in a plateau.

Within this plateau, the measured capacitance can be attributed to the entire depleted volume of the diode or high-field region. One has to keep in mind that slight discrepancies from the nominal value can be expected, because of the measurement pro-

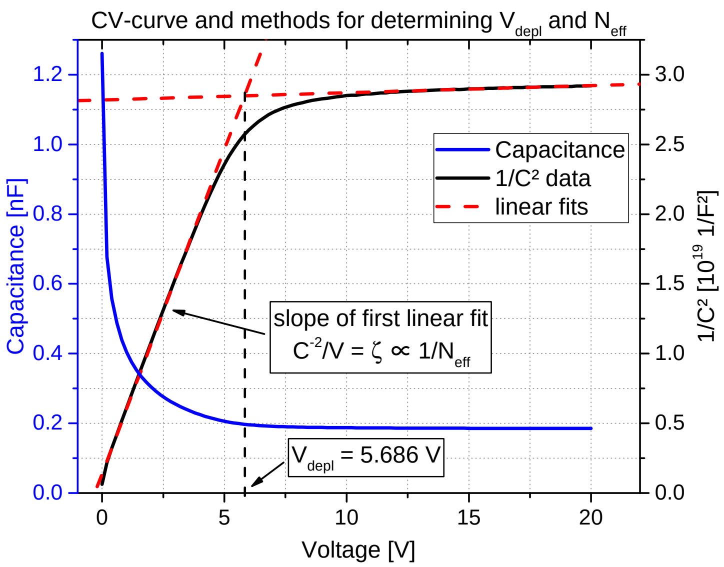

Figure 5.5: Illustration of a common C-V-curve of a diode and the methods for obtaining V_{depl} and N_{eff}. The capacitance measurement is represented by the blue line and scale (left) while the derived $1/C^2$-curve is shown in black and corresponds to the black scale (right). At full depletion the diode reaches a capacitance of roughly 185 fF. Two linear fits (dashed red lines) can be applied to the $1/C^2$-curve within the region of constant increase and the plateau region, respectively. The slope ζ of the fist linear fit enables evaluation of N_{eff} by merit of $\zeta \propto 1/N_{\text{eff}}$ (slope method). For the second method (double linear fit method) the intersection of both linear fits can be utilized to extrapolate V_{depl}.

cedure itself. The LCR meter only measures either the serial or parallel component of the capacitance, C_s and C_p, respectively, which never perfectly fit the total nominal capacitance expected by Eq. (3.11).

The main purpose of C-V-measurements in this study will be applied in the characterization of diodes via the determination of the full depletion voltage V_{depl} and consequently the effective doping concentration N_{eff}, as derived in Eq. (3.10). There are two different methods which allow this determination as illustrated in Fig. 5.5 and will be explained in the following.

The first method, which will be referred to as "slope method", makes use of Eq. (3.12), namely the fact that the slope of the $1/C^2$-V-curve ζ is proportional to $1/N_{\text{eff}}$. ζ can be determined by applying a linear fit on the section during the initial decrease of C of the $1/C^2$-curve, as shown by the first red dashed line of Fig. 5.5. After N_{eff} was derived, Eq. (3.10) can be used to obtain V_{depl}, thus providing both variables needed for further investigations of the change in effective doping concentration after e.g. irradiation. However, this method quickly runs into issues if the shape of the $1/C^2$-curve starts to deviate from the optimal one, which usually starts happening due to the impact of radiation damage.

The approach of the second method is similar to the first, since the linear fit in the first linear section is required. Now, a second fit is applied to the linear section after the $1/C^2$-curve has reached the plateau region, as demonstrated in Fig. 5.5. The intersection of both linear fits then reveals V_{depl}. Afterwards, this can be used to derive N_{eff} via Eq. (3.10). This method will be called "double linear fit method" in the following. As it relies on the quality of linear fits, much like the slope method, it also bears the same disadvantages. Although, manually adjusting the linear fits in cases where the linear sections are not well defined can alleviate some of the issue to still yield viable results.

5.3 Dynamic measurements

Contrary to the static measurements, dynamic characterizations of SiPMs are performed by analyzing the signal shape and similar parameters during the device's normal operation. The following methods require the SiPM device being mounted on the dedicated readout board. For the majority of the cases the signal output is then connected to either a LeCroy WaveRunner 610Zi digital oscilloscope with a 1GHz bandwidth at 20GS/s or an Agilent 53131A Frequency Counter. If there is a deviation from this common setup, a more detailed explanation will be given in the respective section.

The methods and effects introduced in this section can, for the majority, be found in studies like [33, 45, 71–76].

5.3.1 Amplitude and charge spectra

Two significantly important tools for evaluation of SiPM performance are the amplitude and charge spectra, as they allow the determination of various other parameters. The amplitude spectrum can be obtained by recording the peak-to-peak amplitude of the SiPM signal with a digital oscilloscope within a defined measurement window with respect to the initial trigger event. One such spectrum can be seen in Fig. 5.6a) with each peak representing a certain number of fired cells within the array. The 1 photon equivalent (1 p.e.) peak dominates the result, however, events with more than one fired cell can occur due to optical cross-talk, explained in Sec. 5.3.6.

The charge spectrum, on the other hand, can be derived by integration of the pulse shape with an sufficient integration window. It is common practice to chose a window of roughly 7 τ_{rec} to allow a 99.9% recovery of the cell (see Eq. (3.38)).

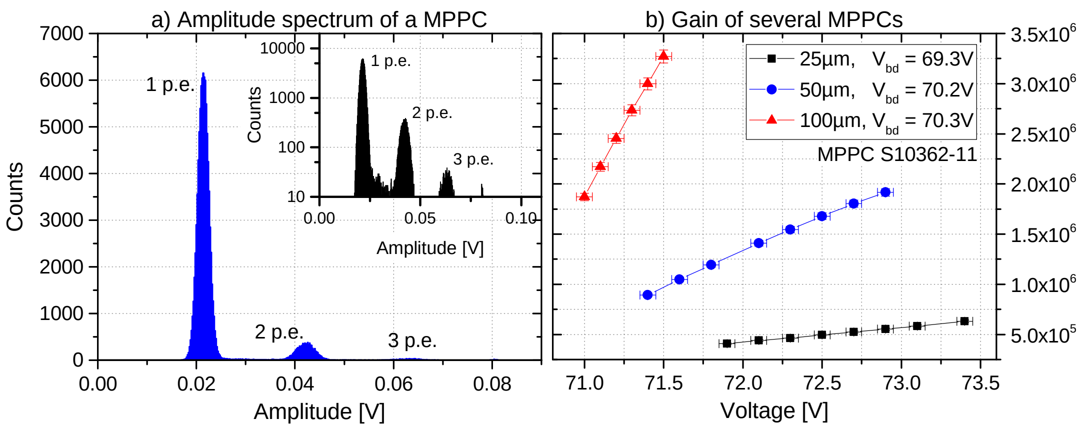

Figure 5.6: Amplitude spectrum (inlet in semi-logarithmic scale) (a)) and gain (b)) of a Hamamatsu MPPC. In a) clearly separated peaks corresponding to different amounts of p.e. can be seen and directly translate to the number of simultaneously fired cells. This amplitude spectrum can be utilized to determine the gain of the device at different overbias voltages as seen in b), by measuring the distance between two p.e. peaks. A linear increase of the gain with increasing V_{ob} according to Eq. (5.1) is visible, while the difference in absolute levels between the different cell sizes can be explained by the difference in C_{cell}.

5.3.2 Gain

The gain of a SiPM is equivalent to its internal amplification and thus determined by the charge Q generated during a single avalanche breakdown. It depends, in good approximation, linearly on the pixel or cell capacitance C_{cell}, as well as the applied overbias voltage V_{ob}, which is defined as the difference between the applied voltage V_{bias} and the breakdown voltage V_{bd}, leading to the gain G:

$$G = \frac{Q}{q_0} = \frac{C_{cell}}{q_0}(V_{bias} - V_{bd}) = \frac{C_{cell}V_{ob}}{q_0} \ . \tag{5.1}$$

By utilizing the charge or amplitude spectrum, the gain is then equivalent to the distance between two p.e. peaks. Determined gains for Hamamatsu MPPCs with three different pitch sizes can be seen in Fig. 5.6b) for an increasing bias voltage. The linear increase can be explained by taking Eq. (5.1) into account: Since C_{cell} can be considered constant after reaching the Geiger-operation, the gain will only depend linearly on the applied V_{ob}. The impact of C_{cell} is directly observable by the difference in absolute levels of G for the different cell sizes.

5.3.3 Noise

Several noise contributions within a SiPM can be accounted for. Considering a measured charge spectrum with an external trigger condition, opposite to the trigger condition of at least one fired cell, a zero-hit-peak or pedestal peak can be observed. The corresponding pedestal noise σ_{ped} stems mainly from electronics noise and is reflected in the width of said pedestal peak.

In a similar fashion, a pixel-to-pixel gain variation σ_{gain} due to imperfection in the fabrication process pertaining to the high-field region can be defined. It can be minimized, however, by ensuring a uniform pixel capacitance within the arrays. Since peaks higher than the 1 p.e. peak all entail an avalanche process in multiple cells, the resolution for the n-th p.e. peak thus becomes

$$\sigma^2(n) = \sigma^2_{ped} + n \cdot \sigma^2_{gain} \ . \tag{5.2}$$

Finally the Excess Noise Factor (ENF) can be defined by

$$ENF = 1 + \frac{\sigma_{gain}}{G} \ . \tag{5.3}$$

The ENF of SiPMs is usually rather small compared to the APDs operated in the proportional mode, due to the high intrinsic amplification based on a Geiger discharge.

5.3.4 Recovery time

The general recovery time of a SiPM was already introduced in Sec. 3.4.3 by the time constant $\tau_{rec} = R_Q C_D$ (see Eq. (3.38)). Taking Eq. (3.39) into consideration, the required recovery time of the SiPM circuit to recharge the bias voltage to the high-field region to 99.9% of the initial voltage is then given by $\Delta t \approx 7\ \tau_{rec}$. However for purposes of measurement, a more feasible parameter is provided by the required recovery time to 90% $\tau_{90\%}$, amounting to $\tau_{90\%} = \Delta t \approx 2.3\ \tau_{rec}$. This will, in most cases, provide a scenario in which a close-to full signal height of the SiPM cell can be achieved, while simultaneously omitting the longest components of the recovery procedure. Making use of this definition, it can be seen that τ_{rec} will result in a recovery state of roughly $63\% \approx (1 - 1/e) \equiv \tau_{1/e}$, leading to $\tau_{rec} = \tau_{1/e}$.

Table 5.1: Various recovery times for a Hamamatsu MPPC with 50 µm cell size. The data is shown for different temperatures T. $\tau_{1/e}$ and $\tau_{90\%}$ were determined via Eq. (3.38), while τ_{rec} was obtained by applying a exponential fit function on measured waveforms of MPPC signals. A very good agreement between $\tau_{1/e}$ and τ_{rec} can be observed. An increase of the recovery times with decreasing temperature can be attributed to the change in R_Q.

T [K]	C_D [fF]	R_Q [kΩ]	$\tau_{1/e}$ [ns]	$\tau_{90\%}$ [ns]	τ_{rec} [ns]
253	85.7 ± 5	183.5 ± 0.8	15.7 ± 0.9	36.2 ± 2.1	15.8 ± 0.8
273	85.7 ± 5	175.4 ± 0.7	15.0 ± 0.9	34.6 ± 2.0	14.5 ± 0.6
293	85.7 ± 5	168.6 ± 0.8	14.4 ± 0.8	33.2 ± 1.9	13.0 ± 0.5

In the case of conventional SiPMs, the recovery time can either be calculated by making use of Eq. (3.38) or directly extrapolated from the pulse shape. The first method utilized the fact that the quench resistor R_Q can be obtained by applying a forward bias to the SiPM. After determining the diode capacitance C_D from either a C-V-measurement or the gain, τ_{rec} can be calculated. For the second method the pulse shape is recorded and a fit with an exponential function ($\propto \exp(-t/\tau_{rec})$) is applied to the slow part of the signal in order to extract the recovery time and time constant τ_{rec}. An example of the recovery times of a Hamamatsu MPPC obtained at different temperatures with both methods is listed in Table 5.1. Here, a good agreement between the values determined via Eq. (3.38) ($\tau_{1/e}$) and the one derived from fitting the signal curves (τ_{rec}) can be observed.

5.3.5 Dark counts

Due to the high-field region of a SiPM being a depleted volume, thermal generation in compliance with SRH will inevitably occur. These thermally generated charges, however, will also be capable of triggering an avalanche process, thus resulting in a SiPM signal occurring without impinging light, therefore labeled as dark count. It is not possible to distinguish between the origin of the signal, as the shape will be identical, making the dark counts one of the most limiting factors of SiPMs.

The corresponding dark count rate (DCR) can be measured with a frequency counter connected to the signal output of the SiPM device, mounted on the readout board and is usually recorded at a counter trigger threshold level of 0.5 p.e.. An example of a DCR measurement of a Hamamatsu MPPC at different bias voltages is shown in Fig. 5.7. A clear dependence on V_{bias} as well as T can be observed. The former can be expected due to the dependence of the Geiger efficiency on the overbias voltage, while the latter can be explained by taking SRH into account. The resulting temperature scaling for the dark current, which indirectly translates to the dark counts is given by [60]

$$I \propto T^2 e^{-\frac{E_{\text{eff}}}{2k_B T}} , \tag{5.4}$$

with the effective gap energy $E_{\text{eff}} = 1.21$ eV. This illustrates the heavy temperature dependence of the dark current and the possibility of its reduction by decreasing the temperature, resulting in an approximate reduction of the current by a factor of two for every 7 K. If room temperature is considered for the final application of the devices, optimization of technological aspects will be required in order to reduce the inherent defect density.

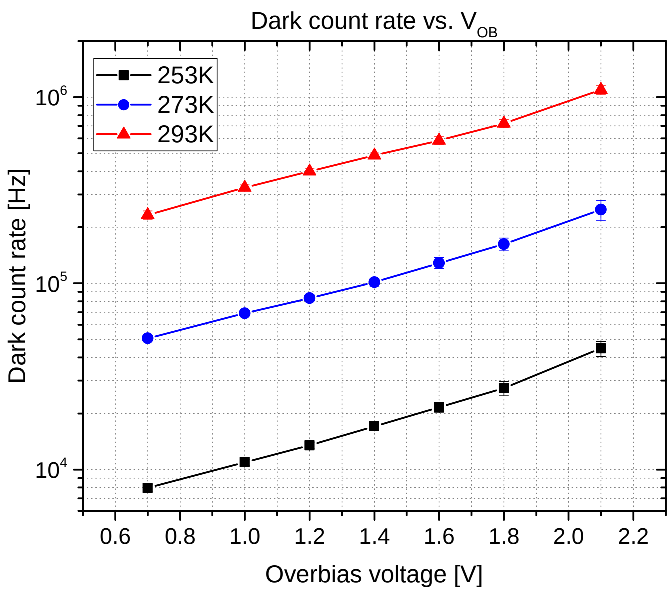

Figure 5.7: Dark count rate (DCR) of a Hamamatsu MPPC with 50 µm cell size for different V_{ob} and T. An increase of the DCR with increasing V_{ob} can be observed due to the higher Geiger efficiency at higher V_{ob}. Due to the majority of the dark counts stemming from thermally generated charge carriers, the temperature scaling can be expected to behave according to SRH statistics. Additional contributions from e.g. trap assisted tunneling at higher electric fields will distort this trend depending on the defect concentration (see text).

It needs to be noted that not all contributions from the dark current before breakdown seen in static I-V-measurements will become dark counts at sufficient voltages, as e.g. surface contributions will not be amplified. In addition, increased dark currents will result in a saturation of the SiPM array caused by the limited dynamic range (see above) and will thus also not lead to a 100% carryover to the DCR.

Furthermore, trap-assisted tunneling can occur in regions with high defect density which does not abide by SRH statistics, as it requires increased electric fields to take place, making this effect only relevant after breakdown is achieved. The tunneled charge carriers can then also be accelerated and initiate an avalanche breakdown, contributing to the overall DCR. This will lead to additional deviations from the expected temperature behavior and can already be witnessed in Fig. 5.7.

The dark current alone, however, is not the sole cause for the final DCR, since secondary pulses by effects like optical cross-talk and afterpulsing additionally contribute to the overall DCR.

5.3.6 Optical cross talk

Various studies have reported the emission of visible light due to charge carriers crossing a p-n-junction with reverse bias beyond V_{bd} [77–80]. The light emission is based on hot-carrier-luminescence, in which hot carriers can lose energy by means of direct and indirect transitions within the conduction band, as suggested by [79]. The resulting spectrum was measured by Mirzoyan [80] and exhibited a broad energy range between 0.5 eV and 3 eV. In terms of the amount of emitted photons during an avalanche, Lacaita [81] has shown that the probability for a photon with sufficient energy to create an additional electron-hole-pair ($E \geq 1.14$ eV) is roughly $3 \cdot 10^{-5}$ per charge carrier crossing. Assuming

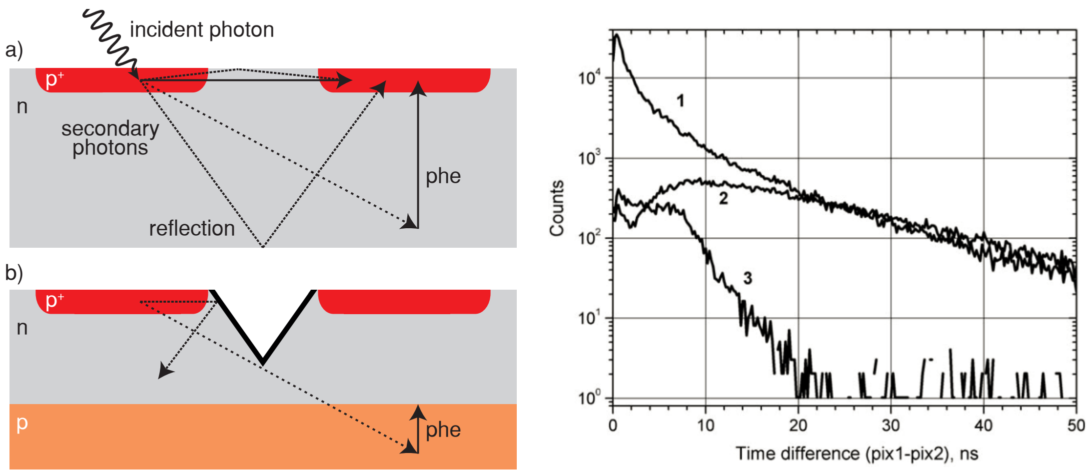

Figure 5.8: Illustration of the process of optical cross-talk (a)) and possible methods of its suppression (b)). Hot-carrier photons generated during an avalanche can reach the neighboring cell by different means (see text). Suppression of this mechanism can be achieved by different means (b)). The fast components can be efficiently suppressed by introducing optical trenches, covered in opaque material, in the gap regions. Adding an additional *pn*-junction to the bulk prevents the photo electron (phe) from traversing to the sensitive region. A proof of concept of this suppression is shown in the right hand side plot, which depicts event for a time difference between two neighboring cells. The data of (1) represents the situation of a) (no suppression), (2) with trenches and (3) with trenches and second junction. A successful suppression of the OCT is easily visible. Adapted from [33] and data taken from [71].

a typical SiPM gain in the range of 10^6, one can expect approximately 30 of such photons during a single avalanche.

These photons are able to propagate in all directions and due to their sufficiently large energy to create additional charge carriers, they are capable of reaching a neighboring pixel, where they will create charge carriers, which in turn are able to initiate a new avalanche breakdown event. This effect is referred to as Optical Cross-Talk (OCT) and cannot be distinguished from a real second signal photon being detected, as the device output will simply display two simultaneous hits, observed as a signal pulse with double pulse height. This has obvious negative implications on the performance of the SiPM, since the single photon-counting resolution will degrade and, furthermore, the increased pixel occupancy will also reduce the dynamic range. Reducing the OCT is thereby a major aspect of ensuring improved SiPM performance.

The different probable ways in which a hot-carrier photon can traverse to a neighboring pixel are illustrated in Fig. 5.8. Depending on the method, two different components of the OCT can be identified according to Buzhan [71]. First, a fast component can be observed, caused by direct transitions to the next pixel or via reflections on the top and backside surfaces, thus allowing the photons to the reach the sensitive area. Second, an indirect and slower component was also detected, which can be explained by the photons traversing to the bulk area of the neighboring pixel and being absorbed. The created photoelectron can then migrate towards the high-field region of said pixel and is now capable of initiating a new avalanche process. This is also shown in the right hand side plot, which depicts the two components and the total resulting OCT in the shape of the measured time difference between the initial and secondary pulse.

By adapting certain technological aspects, the OCT can be drastically reduced as

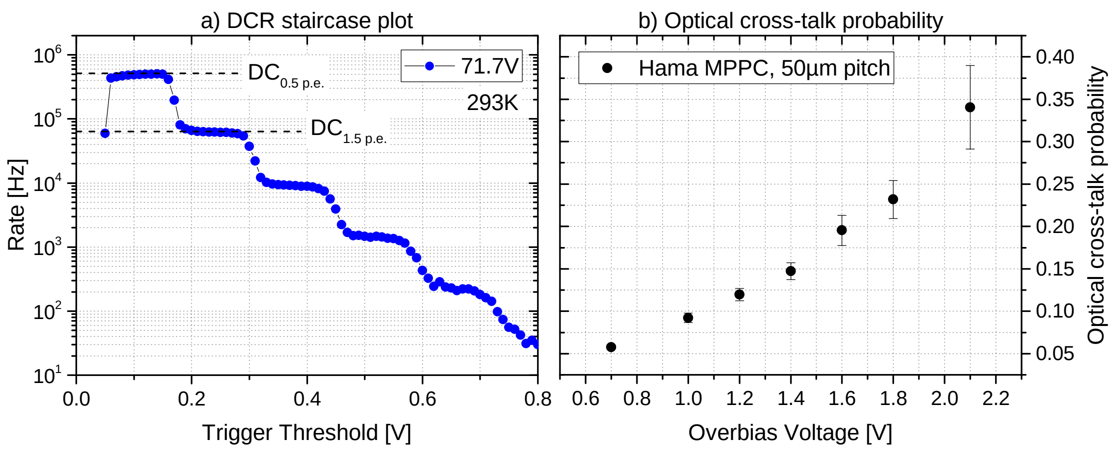

Figure 5.9: Measured DCR for different trigger thresholds (a)) and optical cross-talk (OCT) probability for a Hamamatsu MPPC with 50 µm cell size (b)). Due to the Gaussian distribution of the p.e. signals, a clear staircase shape can be observed in a). The OCT probability can then be derived via Eq. (5.6) by determining the ratio of dark counts on a 1.5 p.e. and 0.5 p.e. threshold. The result is shown in b) for various V_{ob}. A non-linear behavior can be observed, originating from an increased gain and Geiger efficiency with increased V_{ob} (see text).

illustrated in Fig. 5.8 lower left. Introducing optical trenches between the avalanche regions can suppress the fast component as it blocks a direct transition. Adding an additional p-n-junction underneath the sensitive area will inhibit the traversal of created electron towards the avalanche region and thereby potentially suppress the slow component.

The probability for OCT of an SiPM can be determined in different ways. The first makes use of the amplitude spectrum, measured in complete darkness. Considering an ideal detector, the probability of two or more simultaneous thermal events can be considered negligible [45]. Thus, all events exhibiting signals larger than the 1 p.e. peak should be attributed to OCT. Hence the OCT probability can be obtained by calculating the ratio of event entries larger than 1.5 p.e. $N_{1.5p.e.}$ to all entries N_{all}:

$$OCT = \frac{N_{1.5p.e.}}{N_{all}} \ . \tag{5.5}$$

Another approach utilized the SiPM being connected to a frequency counter, measuring the DCR of the device, while incrementally increasing the counter trigger threshold. The resulting staircase plot seen in Fig. 5.9a) stems from the Gaussian distribution of the p.e. signals and will exhibit the stair-shaped trend whenever a p.e. peak threshold is surpassed. Similar to the first method, the OCT probability can hence be derived by comparing the dark counts of the 0.5 p.e. and 1.5 p.e. trigger threshold levels:

$$OCT = \frac{DC_{1.5p.e.}}{DC_{0.5p.e.}} \ . \tag{5.6}$$

Determined cross-talk probabilities of Hamamatsu MPPCs for different bias voltages can be seen in Fig. 5.9b). An increased gap size will reduce the OCT due to the photons being required to pass more material in order to reach the adjacent cell. The dependence on the overbias voltage can also be observed to be non-linear. This originates from the fact that the gain and Geiger efficiency both increase with increasing V_{ob}. An increased gain leads to a higher number of potential photons being able to initiate an avalanche in a neighboring cell while the increased trigger probability for such an event additionally enhances the OCT.

If the device exhibits clearly separated p.e. peaks, the plateaus between decreases in the staircase plot should be on almost constant dark count levels, however, if devices feature a very inhomogeneous gain or suffer from other issues related to high dark count rates, the staircase shape will slowly shift towards a negative linear slope. These issues can be circumvented to a certain degree by utilizing the first method, as it benefits from digital noise filters of the oscilloscope thus increasing the signal-to-noise ratio.

5.3.7 Afterpulsing

Charge trapping in a depleted volume can occur due to defects present in the silicon lattice, as discussed in Sec. 4.1.3 and Sec. 4.1.5.3. If such trapping takes place during an avalanche process, the trapped charge can afterwards be released again after a trapping time τ_i, specific to the individual type of defect and its energy. The released charge is then capable of initiating a new avalanche breakdown, resulting in a slightly delayed fake signal, deteriorating the photon-counting resolution. This effect is referred to as afterpulsing.

Studies [45, 73] have found evidence for afterpulsing mainly being caused by two specific defects resulting in a fast τ_f and slow τ_s trapping time constant. Knowing the respective time constant the probability of an afterpulse taking place at time t after the primary breakdown can be described as

$$P(t) \propto e^{-\frac{t}{\tau_i}} \ . \tag{5.7}$$

In order to determine the afterpulsing probability of a SiPM, the dedicated readout board was connected to an Acqiris AP235 digitizer board with a 500 MHz bandwidth and 8bit resolution. The goal of the measurement is to determine the time difference Δt between two consecutive signals. Due to the secondary avalanche occurring during the recovery process, it is possible for its signal amplitude to not be detected, as it will

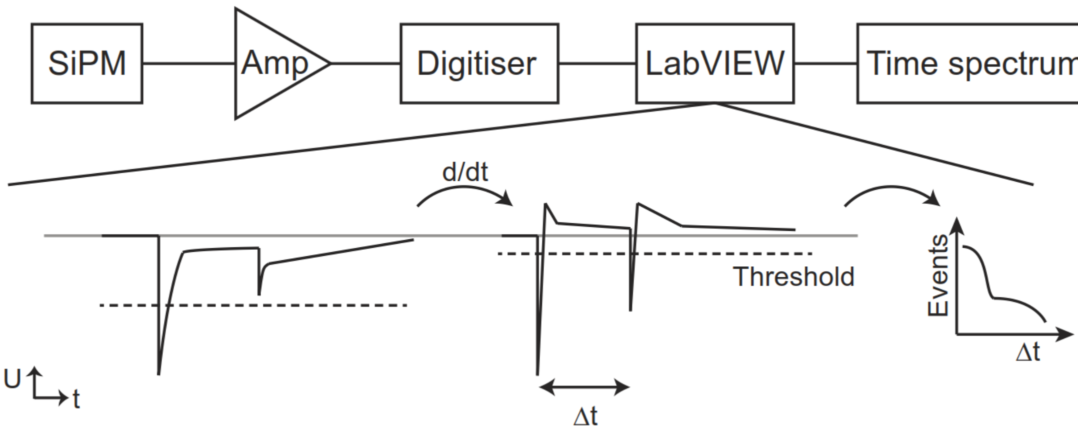

Figure 5.10: Illustration of the measurement procedure for the determination of the afterpulsing probability. The SiPM signal is recorded with a digitizer board and imported into a LabVIEW evaluation program. Here the time derivative is determined which allows easier distinction of signals via a threshold level. The time difference Δt between two consecutive signals is then recorded providing the final event histogram for further analysis. Taken from [33].

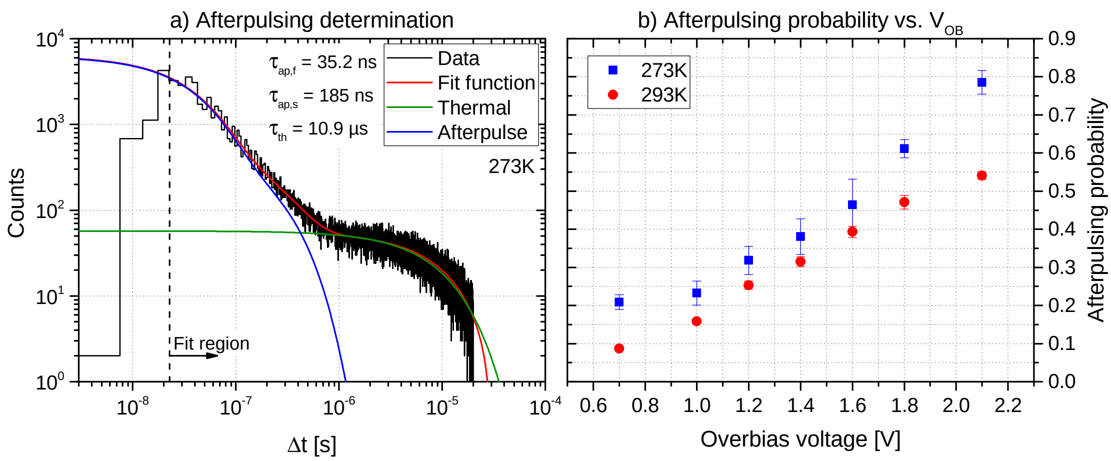

Figure 5.11: Illustration of the determination of the afterpulsing probability (a)) and measured afterpulsing probability for different temperatures (b)). A triple exponential decay fitting function (red) can be applied to the data (black) in a), allowing extraction of the fit parameters necessary for determining P_{ap}. The afterpulsing and thermal components are also plotted separately as blue and green lines, respectively, showing dominance of the afterpulse signals for smaller time differences Δt. The resulting P_{ap} for different V_{ob} and T is depicted in b). The increase with increasing voltage can be explained by an increased trigger probability. The inverse temperature scaling stems from decreased emission rate allowing for a more recovered cell state and less signal loss (see text).

not be sufficiently large for the trigger threshold. Therefore, to minimize this issue, the signal pulses were differentiated with respect to t, resulting in clearly distinguishable peaks for the signals due to their fast rise times. Hence a trigger threshold can be placed on the derivatives above the noise level.

This procedure is illustrated in Fig. 5.10 and overall realized by a custom made LabVIEW routine, providing the desired Δt time spectrum by the end. This spectrum contains a superposition of the probability densities for an event being caused by either thermal pulses

$$n_t = \frac{N_t}{\tau_t}\, e^{-\frac{t}{\tau_t}} \tag{5.8}$$

or by fast or slow afterpulsing events

$$n_{ap} = \frac{N_{ap}}{\tau_{ap}}\, e^{-\frac{t}{\tau_{ap}}}\ , \tag{5.9}$$

as described in [45], with N_t and N_{ap} denoting the integrated numbers of thermal or afterpulsing events, respectively. This leads to a afterpulsing probability given by

$$P_{ap} = \frac{\int_0^\infty (n_s + n_f)\, \mathrm{d}t}{\int_0^\infty (n_t + n_s + n_f)\, \mathrm{d}t} = \frac{N_s + N_f}{N_t + N_s + N_f}\ , \tag{5.10}$$

where n_f and n_s denote the probability densities and N_f and N_s the integrated number of signals for fast and slow afterpulsing events, respectively.

One such Δt spectrum measured for a Hamamatsu MPPC is shown in Fig. 5.11a). The data was taken at $V_{ob} = 1.4$ V and $T = 273$ K. The lower limit of the spectrum is mainly defined by the utilized devices in the setup, as well as the signals themselves, since the issue of very fast afterpulses being lost due to their limited amplitude can still occur. In the measurement presented it was found to be $\Delta t \approx 21$ ns, which was also chosen as the lower limit of the fitting range. The upper limit on the other hand can be defined by time differences long enough to no longer enable a clear distinction between afterpulsing and thermal signals.

By fitting this spectrum (black line) with a superposition of three exponential decay functions (red line), the specific trapping time constants for all three components can be extracted via the fit parameters. The fit data can be seen to be in very good agreement with the measured data and the thermal (green) and afterpulsing (blue) components of the function are plotted separately to illustrate their respective contributions to the overall spectrum. Furthermore, these individual components allow extraction of the parameters τ_t, N_t, τ_f, N_f and τ_s, N_s, respectively, enabling the determination of P_{ap}. The extracted time constants for this measurement are also listed in Fig. 5.11a).

Performing the previous measurement at various overbias voltages and different temperatures yields Fig. 5.11b). An increase of P_{ap} with increasing V_{ob} can be expected, since the trigger probability and thus the chance to initiate an afterpulsing event becomes larger for higher overbias voltages. In addition, based on the gain scaling with V_{ob}, a higher amount of created charge carriers also leads to a higher probability of trapping taking place. The enhanced probability for afterpulsing at lower temperatures can be explained by taking Eq. (4.15) into account. Reducing the temperature will also reduce the emission rates, allowing the cells to reach a more advanced state of recovery, thus resulting in a higher and easier to detect signal peak. This would reduce the probability of the afterpulsing event taking place too quickly after the initial pulse being cut off.

5.3.8 Photon detection efficiency

Arguably the most important parameter of any SiPM is its Photon Detection Efficiency (PDE), describing the probability to detect a single impinging photon. It is commonly a function of the wavelength of the incident light λ, the geometrical Fill Factor FF as well as the overbias voltage V_{ob} and given by

$$PDE(\lambda, V_{ob}) = QE(\lambda) \cdot FF \cdot \epsilon_G(V_{ob}) \,. \tag{5.11}$$

It is easy to see that the PDE depends on three major quantities of a SiPM. The internal Quantum Efficiency $QE(\lambda)$ denotes the probability of a photon with wavelength λ being absorbed within the sensitive region and creating an electron-hole pair. The dependency on λ can be understood by taking Sec. 3.2.1 into account, as the absorption depth plays an integral role.

Due to the sensitive region of the SiPM having a finite extent, located within a certain depth, it is for example possible for blue or near-UV light to be absorbed to close to the surface and outside the depleted volume. This, in turn, will most likely result in immediate recombination of the charge carriers, thus "loosing" the initial photon. On the other hand, increasingly long wavelengths would lead to absorption beyond the active area or even a complete pass-through of the photon, again resulting in no detection. In addition, optical effects like reflection on the surface of the device need to be taken into account and also depend heavily on the wavelength of the incident light. It is, however, possible to minimize this issue by adapting the composition of the surface layers of the device.

The geometrical Fill Factor FF represents the percentage of the active area within a SiPM array compared to the total area. Inactive or dead areas are commonly required for structuring of the individual pixels (gap area) and, in the case of conventional SiPMs, for integration of R_Q and the respective means of contacting. As previously seen, increasing the gap size can lead to OCT suppression at the cost of the fill factor. Most recent SiPM device include optical trenches in the gap regions, which allow minimization of the required dead area, while still offering improved cross-talk suppression.

Finally, the Geiger or Trigger efficiency $\epsilon_G(V_{ob})$ describes the probability of the created charge pair to initiate an avalanche breakdown in the device, while drifting through the high-field region. This parameter depends on the electric field, making it a function of the applied overbias voltage V_{ob} and, in addition, also on the position of the photon absorption, as was already discussed in detail in Sec. 3.4.3.

The most reliable method of determining the PDE entails illuminating the SiPM and a reference PIN-diode, both placed within a dark box, with a pulsed laser source to enable knowledge of the amount of light impinging on both devices. The simultaneous illumination can be achieved by several diffuse reflector materials. By utilizing the fact that the mean number of photons measured by the SiPM is defined by Poisson distribution, the zero-peak of the measured data, meaning all instances in which the laser trigger initiated a measurement but no light was detected, can be taken advantage of. This method allows the determination of the mean number of detected photons without the impact of OCT or afterpulsing.

Knowledge of additional parameters, such as the measured photo current and quantum efficiency of the reference photo diode, as well as the active areas of both devices finally allows the determination of the absolute PDE of the SiPM for specific wavelengths. This procedure can afterwards be combined with a measurement performed with a continuous light source, which only provides relative PDE levels in regards to λ. However, by superimposing the obtained relative values with the absolute ones, the PDE for a wide range of wavelengths can be obtained.

An experimental setup for both procedures was developed during the course of this thesis.

5.3.9 Dynamic range

The amount of photons that can be detected simultaneously by a SiPM array is intrinsically limited by its finite number of pixels. Consequently, the dynamic range and as well as the single photon counting capability become limited due to the device entering saturation for high light levels. The response of a SiPM array with a finite number of cells N_{cell} and thereby this behavior can be expressed by

$$N_{fired} = N_{cell} \left(1 - e^{-\frac{PDE \cdot N_\gamma}{N_{cell}}}\right) , \tag{5.12}$$

where N_{fired}, denotes the number of fired cells, N_γ the number of incident photons and PDE the photon detection efficiency. The equation considers a infinitely fast light pulse in addition to an infinitely fast cell recovery, since the finite recovery time of a SiPM can further influence the signal response.

The direct impact of Eq. (5.12) is displayed in Fig. 5.12, in which N_{fired} is shown depending on N_γ for various N_{cell}, assuming a PDE of 1. An increased number of incident photons can lead to severe deviations from the linear response in the case of a low N_{cell}. This stems from the increased probability of two or more photons impinging on the same cell. As an example, for N_γ exceeding 50% of N_{cell}, a discrepancy from the linear behavior of more than 20% can be observed.

Hence the dynamic range of the SiPM is inherently limited by N_{cell}. Possible adaptations of the design therefore depend on the individual applications. If devices with high detection sensitivity of large amounts of photons are desired, an increase of N_{cell}

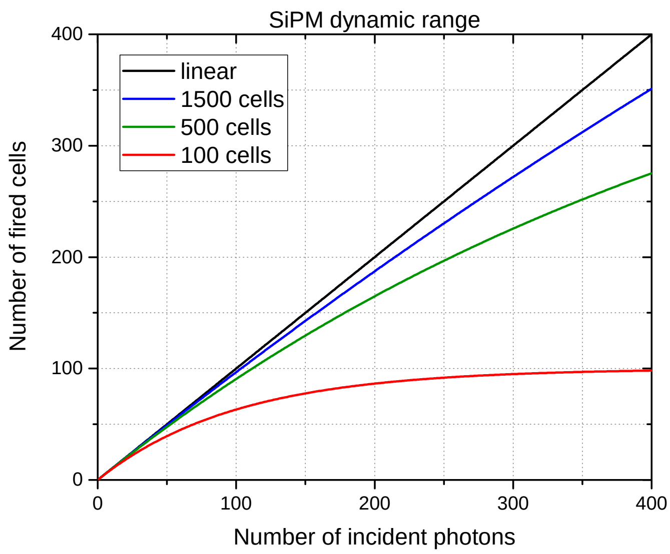

Figure 5.12: Number of fired cells of SiPM arrays of varying sizes in dependence of the number of incident photons. The curves were calculated according to Eq. (5.12), assuming $PDE = 1$. A clear deviation from the linear response behavior (shown for comparison) can be seen and becomes more apparent for smaller array sizes. A saturation of the SiPM response can be observed with increasing numbers of incident photons (see text).

can lead to a better dynamic range while simultaneously limiting the fill factor as more inactive regions for cross-talk suppression and circuitry will be required. On the other hand, applications demanding high detection efficiencies for low light levels will profit from increased cell sizes and fill factors, without the need for a high dynamic range.

5.4 Photon emission microscopy

The light emission emerging from the avalanche process can also be utilized in a beneficial fashion. It was shown in [80] that photons with a broad range of wavelengths are emitted in all directions during an avalanche, which then can be detected for further characterization purposes.

One such purpose is the photon emission microscopy allowing homogeneity and failure analysis of SiPMs and other devices. The measurements are realized by a Hamamatsu PHEMOS-1000 Emission Microscope. The apparatus is located in a light tight box and offers four different magnifications for microscopy, namely 5x, 20x and 100x, as well as a macro-lens with 0.75x. The light emission is measured with a cooled SiCCD or InGaAs-camera by collecting all light emissions over a pre-defined integration time window. This window depends on the magnification and has to be chosen accordingly.

The devices are placed under the microscope while mounted on the dedicated readout board or on wafer level, and the required operational voltages are supplied by a Keithley 4200A-SCS Parameter Analyzer. In order to account for thermal contributions from the individual cameras over the time frame of the integration, a thermal noise correction can be performed with an unbiased condition. The obtained emission picture can afterwards be superimposed with a high-definition pattern microscopy photograph to allow for local identifications.

An example of the resulting emission pictures can be seen in Fig. 5.13. The amount

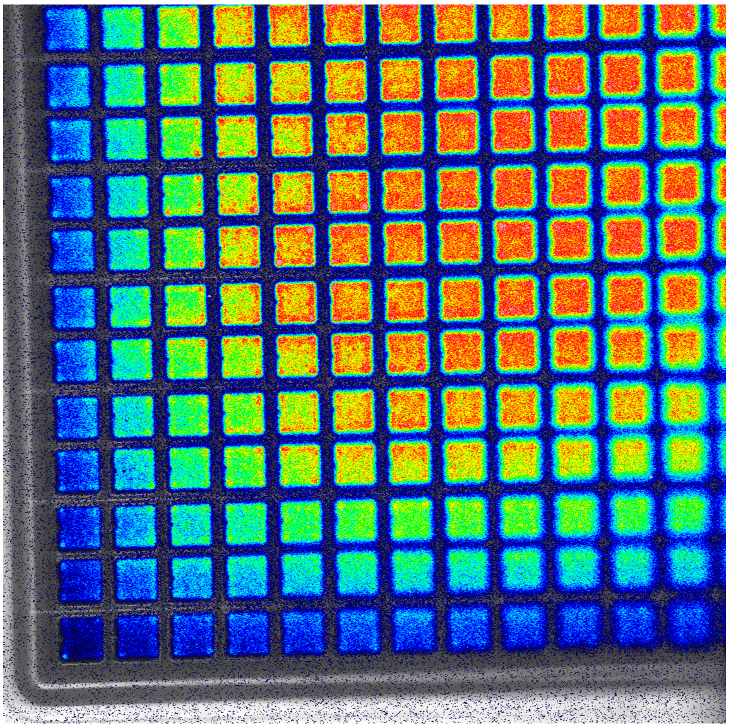

Figure 5.13: Photo emission microscopy photograph of a Hamamatsu MPPC. The amount of light emitted by the device operated above breakdown voltage is given by the color coding. Warmer colors correspond to higher amounts of light detected. A clear separation of the individual pixel of the array can be observed, as well as their respective homogeneity. Increased amounts of light in the center originate from OCT.

of detected light is reflected by the color coding of the emission picture, with increased light intensity being represented by warmer red colors. Depending on the magnification, the homogeneity (or inhomogeneity) within a single cell or the entire array can become visible. One major purposes of these measurements in this study is to identify the issue of early edge breakdowns within the investigated devices. This issue is characterized by the edges of the pixels exhibiting a far higher amount of light emission compared to the rest of the cell at operation above V_{bd}. An easy way to detect such early breakdown issues is to operate the device below the nominal breakdown voltage and perform the emission measurement. Affected regions will then produce light while the unaffected ones will remain dark.

Several limiting factors of this measurement method need to be taken into account. First, the resulting emission photographs only allow for a qualitative comparison within the same photograph as the results only depict the relative light levels instead of an absolute value. This also leads to cases where hot-spots with significantly higher amounts of light emission might indicate that the rest of the cell or array is completely inactive, while this not actually being the case, as the emission measurement is dominated by the hot-spot. Furthermore, this method is not capable of resolving the spatial distribution of individual avalanche processes since the measurement is being integrated over prolonged time windows. The small inhomogeneities found in single pixels are a consequence of the statistical nature and the finite spacial expansion of the avalanche process.

6 SiPM with bulk-integrated quench resistor

A SiPM requires either a passive or active quenching mechanism in order to stop the avalanche breakdown and allow cell recovery for a new avalanche. The passive quenching in conventional devices is commonly achieved by implementation of a high-ohmic polysilicon or metal-composite quench resistor deposited on the top side of the devices, as shown in Fig. 6.1 (gray line). Integration of such resistors requires additional fabrication steps during wafer processing, namely lithography, doping and deposition, which consequently result in higher time consumption and cost. Furthermore, the required value of the resistor ($\sim 10^5\Omega$) for fulfilling the quench condition also depends on the shape and size of the resistor material. Hence, this can limit the yield of the production, since the reproducibility might be affected.

In addition to the resistor, a grid of metal lines for contacting will be required on the topside as well (see Fig. 6.1). Both the resistor and metal grid, therefore, serve as an obstacle for incident light, thus limiting the fill factor and thereby also the photon detection efficiency of the devices.

In order to circumvent these drawbacks, a novel approach for SiPMs is being developed at the Semiconductor Laboratory of the Max-Planck Society (HLL). This novel concept aims to integrate the quench resistor into the silicon bulk of the detector, thereby removing the need for any external resistor and the drawbacks involved. This concept is called the Silicon MultiPixel light (SiMPl) detector and will be discussed in more detail in the following chapter. First the basic concept of SiMPl will be introduced followed by a discussion of its advantages and drawbacks. Afterwards, the latest concept involving

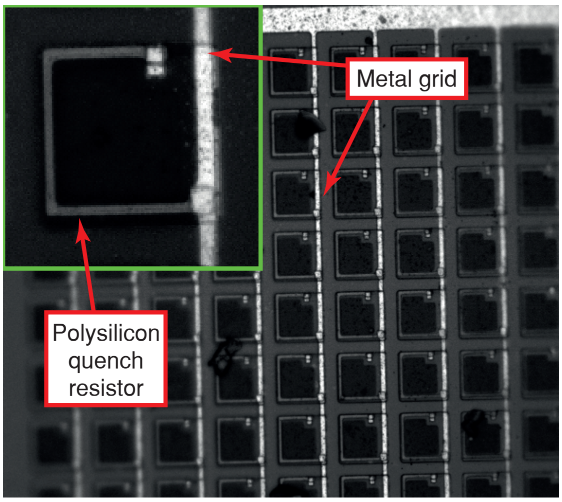

Figure 6.1: Microscope photograph of a conventional SiPM with polysilicon quench resistors (gray). In addition, a grid of metal lines for contacting is required. The depicted device is from the Moscow Engineering Physics Institute (MEPhI) and has a 42 µm pitch size.

the utilization of modified SiMPl devices for particle tracking in high energy physics will be elucidated, followed by discussion regarding the expected radiation damages in SiMPl devices from different sources.

The majority of the information provided in this chapter can be found in [33, 82–85].

6.1 The SiMPl concept

The approach of the SiMPl concept is to integrate the individual quench resistors of the cells into the silicon bulk of the detector material in order to be able to forgo the necessary processing steps pertaining to the external resistor. The equivalent circuit diagram as well as the schematic cross-section can be seen in Fig.6.2. The circuit diagram of one cell, illustrated by the gray rectangle, can be considered identical to that of a conventional SiPM cell in terms of components and structure (see Sec. 3.4.3).

SiMPl devices are based on p-on-n structures, having a lowly doped n-type bulk material, thus increasing the sensitivity of the devices towards shorter wavelength visible light (blue). The two contact planes, connected to external contact pads are given by the highly doped n^+ backside and p^+ topside implants, the former usually being biased at V_{bias} and the latter at 0 V. Here the p^+ is referred to as cathode and is common for the entire cell array, while the n^+ is labeled anode. This is inverted compared to the usual nomenclature of diodes, due to the collection of electrons being associated with anodes.

The high-field or avalanche region is formed between the topside p^+ implant and an additional deep n layer underneath, which is segmented, thus making up the individual pixel areas. One such pixel or cell is represented by the gray rectangle in the cross-section of Fig. 6.2. By applying a potential difference between top and bottom, two different depletion regions within the bulk will be formed. Due to the segmentation of the deep n implant, the depletion will start forming from the topside implant and reach into the bulk area of the device, thus forming a depleted region between two individual cells, also called gap region. This depletion towards the high-field area is stopped by the deep n

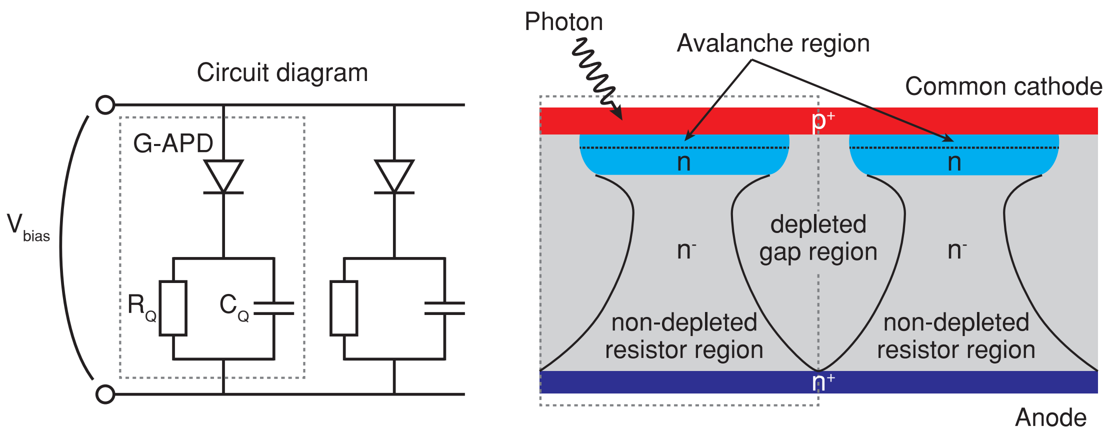

Figure 6.2: Equivalent circuit diagram (left) and cross-section (right) of for SiMPl devices. The circuit diagram for one cell is given by the gray rectangle, with the same rectangle representing a single SiMPl cell on the right. The avalanche region is located between the deep n and p^+-implants on the top. The quench resistor is now integrated into the silicon bulk and formed by the non-depleted volume underneath the avalanche region towards the backside. It is defined by the depletion in the gap area (see text). Picture after [33].

implant, therefore not affecting the spacial extension of the high-field region itself.

In the intended operation mode, this depletion region will only partially extend towards the area underneath the active area of pixel in a lateral fashion, leaving parts of it non-depleted. This vertical non-depleted region now forms the bulk-integrated quench resistor R_Q with a parallel quench capacitance C_Q, which is responsible for the fast signal component of the output signal. The gap between two pixel is then defined as the distance between two adjacent deep n implants, while the cell pitch is given by the distance between two pixel centers or the centers of two adjacent gap areas. A combination of a certain pitch and gap size (usually given in µm) will in most cases be written as pitch/gap in this study.

Since R_Q is formed within the bulk, the bulk parameters will have a direct impact on the resulting value of the quench resistor. Taking Eq. (3.8) as well as the common resistor equation

$$R = \varrho \, \frac{l}{A} \tag{6.1}$$

into account, a dependence on the following parameters becomes apparent:

- bulk resistivity ϱ or effective doping concentration N_{eff} and coupled to those, the temperature dependent charge carrier mobility
- device thickness, which directly translates to the resistor length l
- pitch/gap combination and thus cell size as it directly influences the area A of R_Q
- the geometrical shape of the cells
- V_{bias} due to its direct impact on the amount of the depletion taking place.

As a result, these parameters need to be chosen carefully to obtain a quench resistor in accordance to the quench condition.

Due to the fact that the partial depletion of the bulk occurs laterally, it can already be deduced that the shape of R_Q will not be linear. In fact, the depletion region is more akin to that of a junction field effect transistor (JFET) in source follower mode, with the gate being represented by the p^+ segment in the gap region, while the deep n and backside n^+ implants make up the source and drain contacts, respectively [83]. Thus, approximating the shape of R_Q with that of a cylinder is not valid, as A is a function of the depth within the bulk y. Hence, R_Q can be written as

$$R_Q = \varrho \, \frac{l}{A(l)} = \varrho \int_0^l \frac{1}{r^2(y)\pi} \mathrm{d}y \, , \tag{6.2}$$

where $r(y)$ is the radius of the non-depleted area at a specific depth y. Since V_{bias} impacts the depletion region in the bulk, the above equation is only valid for a chosen biasing voltage. In addition, V_{bias} changes during the operational cycle of a SiPM (see Fig. 3.5b)), which is also true for SiMPl device. Therefore, R_Q can be expected to vary during said cycle resulting in a direct impact on the recovery time of the device and leading to non-linear I-V-curves for R_Q. The possible repercussions of this JFET-like behavior will be discussed in the next section.

Apart from affecting the resulting quench resistor, the choice of the above technological and device parameters also needs to entail avoiding extreme cases in terms of bulk depletion shown in Fig. 6.3. If certain parameters are chosen poorly, i.e. too large gap size or resistivity, a case of pinch-off can occur within the bulk. This can be seen in Fig. 6.3a), characterized by the depletion region reaching fully underneath the active

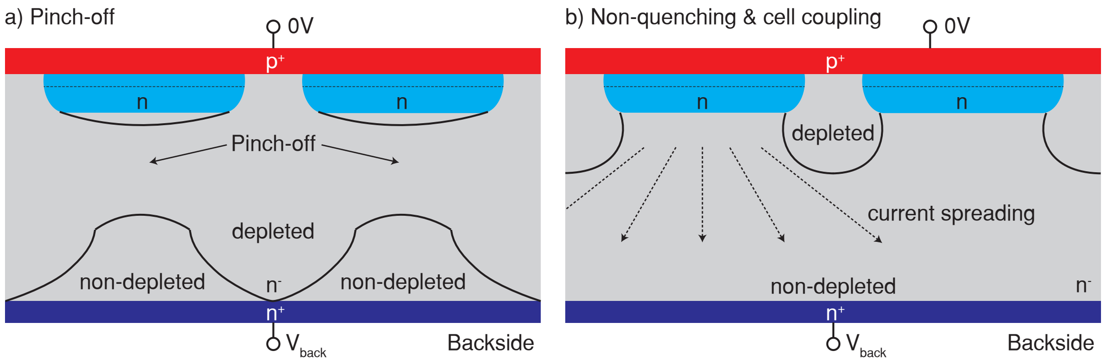

Figure 6.3: Exemplification of pinch-off (a)) as well as non-quenching and cell coupling (b)). Pinch-off describes the effect of the depleted gap region reaching completely underneath the active pixel area and merging with the neighboring one. This leads to a potential drop between backside and high-field region, thus prevent the recovery of the cell (a)). Overly thick wafer material can lead to the situation depicted in b), where the depleted region only extends to a small fraction of the bulk volume. As consequence R_Q decreases drastically, leading to non-quenching in the cell and, in addition, cell coupling due to a strong current spread can take place. See text for details.

area of the cell. As a consequence, R_Q will increase drastically and a voltage drop at the depleted region will take place. This, in turn, will lead to a reduced bias voltage reaching the internal anode and only small currents being possible during the recharge process, resulting in increasingly long recovery times.

On the other hand, choosing i.e. small gap sizes and low resistivity material, the case seen in Fig. 6.3b) can be expected. Here the formation of the depletion region is very limited. It is preferable if the depletion region is able to reach the backside implant in order to enable optimal cell decoupling. If this cannot be achieved, the current created during an avalanche would then spread to the neighboring cells, directly affecting their bias voltage. This is often accompanied by operation of the cell in the non-quenching regime, which is characterized by an insufficiently small R_Q, leading to high currents which cannot fulfill the quenching condition by Cova [42]. Reaching the non-quenching regime is not necessarily tied to the current spreading and cell coupling as it can also take place with normal depletion regions under the "correct" choice of the above mentioned parameters.

Overall, parameters for R_Q must be chosen in order to find a balance in the necessary trade-off between fast recovery times and high potential overbias voltages, as was already seen in conventional SiPMs. The effects of pinch-off and non-quenching/cell coupling make up the extreme scenarios in cases of poor parameter choices for SiMPl devices.

Even though many manufacturers of conventional SiPMs include a guard ring structure in their design in order to allow for a more homogeneous electric field in the high-field region and to prevent edge effects, the SiMPl approach does not include any such structure. The aim of SiMPl was the reduction of technological processing steps and overall simplification of the manufacturing procedure.

6.2 Advantages and drawbacks

When comparing SiMPl devices to conventional SiPMs, several advantages can be derived, but also drawbacks stemming from the novel approach need to be taken into account.

Advantages

One of the major aspects of the SiMPl detectors is to be able to omit the necessity of an external quench resistor, which is usually deposited on the topside of the device. In doing so, the overall technological processing becomes simplified which results in faster production cycles as well as more cost efficient devices, since several fabrication steps can now be skipped. In addition, the unstructured common p^+ implant negates the need for a grid of metal lines for contacting as the entire array can be contacted by a single small metal pad outside of the sensitive area. This further reduces the amount of fabrication steps needed and also minimizes the parasitic stray capacitance C_g.

By removing the need for the external resistor and the metal grid, another advantage becomes apparent. Since no components are deposited on the topside any longer, no obstacles for incident light are present. This will greatly increase the fill factor of SiMPl devices as the entrance window is now completely free, which, in turn, results in higher photon detection efficiencies. The only imposed limitation on the photon detection efficiency now stems from the requirement for optical cross-talk suppression by increased gap sizes between the individual pixels.

Furthermore, SiMPl devices feature a topologically flat surface due to the absence of the external resistor. This allows easier manufacturing of an optimized entrance window via anti-reflection coatings, which also lead to an increase in the overall photon detection efficiency for specific wavelengths. All in all, a maximum efficiency of roughly 60% - 80% was estimated for SiMPl. The flat surface also holds the advantage of making coupling of the device to readout electronics much easier. This can be achieved via bump-bonding and creates hybrid devices which can be utilized for certain applications, as will be discussed in Sec. 6.4.

An additional advantage can be found in the internal anode or deep n implant, making up half of the high-field region of the device. This implant simultaneously acts as an inherent diffusion barrier against minority charge carriers in the bulk, effectively blocking them from reaching the avalanche region and potentially contributing to the dark counts. The potential barrier at the internal anode automatically guides holes towards the p^+ implant in the gap region, resulting in less than one hole per 1000 electron-hole pairs created reaching the high-field region according to simulations [33]. This fact is also beneficial for the suppression of optical cross-talk as its slow component relies on the charge carriers converted from hot-carrier photons to initiate avalanche breakdowns in neighboring cells by means of reaching the high-field region through the bulk. Furthermore, future addition of optical trenches poses no principle problem within the SiMPl approach and was only omitted in the first prototype batches in order to simplify the processing at first.

Finally, by featuring a common p^+-implant instead of a structured topside implant, the radiation hardness of the devices can potentially be increased. As seen in Sec. 4.2, ionizing radiation damage will lead to the creation of positive charges in the surface interface region of the device. These, in turn, will lead to an accumulation of negative charge in the depleted areas underneath and can thereby cause lateral breakdown between individual cells or strips in the case of segmented devices. In the case of SiMPl this cannot occur and the negative impact of the interface charges can also be counteracted by proper choice of the technological parameters for the p^+-implant.

Drawbacks

The first major drawback can be deduced by taking into account the fact that R_Q depends on a variety of parameters related to the bulk material. In order to achieve

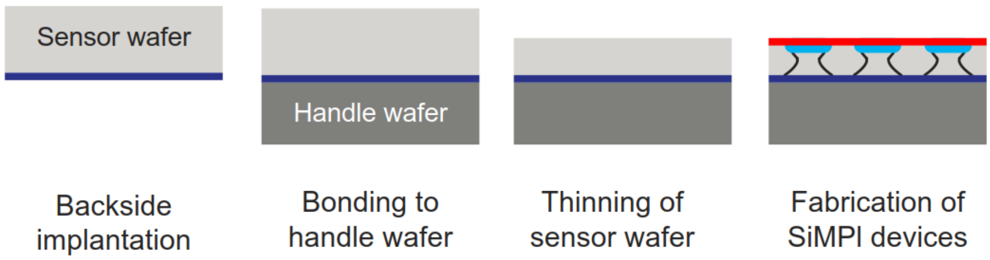

Figure 6.4: Illustration of the individual steps of the fabrication of SOI material for SiMPl. In the first step, the sensor wafer receives its backside implant, followed by the waferbonding procedure in the second step. Afterwards the sensor wafer is thinned down to the desired thickness, while the handle wafer remains fully intact for stability. Finally, the necessary fabrication steps for the actual sensor devices can be carried out. Picture taken from [33].

resistance values, which satisfy the quenching condition, it is not possible to utilize standard wafer material with roughly 450 µm thickness. Instead, thinned material is required, making a different technological approach necessary. This can be achieved by methods like the epitaxial growth, which became a well established technology in the semiconductor industry in recent years.

For the fabrication of SiMPl wafers, however, a different method, namely wafer-bonding was chosen, due to the availability from the laboratory supplier. This method provides the basic Silicon-on-Insulator (SOI) raw material which features a thinned down sensor wafer, which will be used for further processing of the device. It is easy to see, however, that a specific wafer thickness is only valid for a limited range of cell sizes (pitch/gap combination) due to the above dependences of R_Q. Therefore, attempting to significantly change the cell size will inadvertently require an additional adaptation of the bulk material, meaning new SOI material with the respective thickness. Combining drastically different cell sizes on the same wafer is thereby not possible.

The general fabrication procedure for SOI material is shown in Fig. 6.4. Both the sensor and handle wafer are standard thickness material. Before the waferbonding takes place, the backside doping is implanted into the sensor wafer. The heat of the waferbonding procedure is simultaneously used for annealing of said implant. Afterwards the sensor wafer is thinned down to the desired thickness, followed by the necessary fabrication steps for the devices themselves.

The second drawback of SiMPl is the JFET-like behavior mentioned in the previous section. Since the shape of the non-depleted bulk region directly affects R_Q, the resistance value becomes a function of V_{bias}. As already seen in Fig. 3.5b), V_{bias} will vary during the operational cycle of G-APD cell thus making the quench resistor a function of time $R_Q(t)$ as well. The value of R_Q responsible for quenching is given for the case of the largest area of R_Q and thereby smallest resistance. The recovery, on the other hand, takes place while the voltage is recharging, thus steadily increasing the value of R_Q. The former is negative in terms of the quenching conditions as the currents will generally be higher, thus limiting the maximum overbias voltage of the device and the latter will result in prolonged recovery times due the increasing resistance.

Furthermore, the recovery time τ_{rec} itself will become a function of time, making an analytical description of it not feasible. It can be observed (as will be shown later) that the negative impact of the JFET-like behavior increases with increasing relative gap size compared to the pixel pitch, while small relative gap sizes lead to cases closer to the conventional RC element.

For most of the possible and planned applications of SiMPl devices however, this drawback can be considered to be of only small importance, as it only affects the recovery of a single cell.

6.3 First feasibility studies and 2nd prototype

Extensive simulation studies were performed with the simulation tools introduced in Sec. 7, in order to investigate the feasibility of the SiMPl concept. A summary of their results can be found in [83]. These results showed the overall expected formation of a homogeneous high-field region, as well as the distinct depletion region in the bulk, thus providing theoretical evidence for the formation of the quench resistor. In addition, simulations pertaining to a first estimate of the expected range of operation were carried out, suggesting feasible results in regards to the maximum potential overbias voltage. They also showed elongated recovery time estimates, roughly a factor 3 times larger than for conventional SiPMs.

Measurements of the first prototype devices afterwards, carried out by Ninković, were able to provide first proof-of-concept results, successfully demonstrating the avalanche breakdown and subsequent quenching and recovery of the prototype devices [84, 85]. Due to unforeseen technological difficulties concerning surface contaminations and the implantation procedures, the yield of the prototype batch was very low. Hence, no detailed investigation regarding various pitch/gap combinations could be carried out.

The first in-depth analysis was later performed with the second prototype batch, called SiMPl2. This batch also featured a limited yield, again caused by technological difficulties, however, it was significantly higher, allowing detailed characterization measurements and comparisons to the simulation studies. These investigations were carried out by Jendrysik and can be found in [33].

The focus of this study will be the continuation of the development of new SiMPl batches by execution of simulation studies in regards to possible technological improvements and the subsequent characterizations and comparisons to said simulations. The main results in this endeavor will be presented in Chapter 9. However, an additional novel concept has been established which suggests the utilization of SiMPl devices outside of low level light detection application and will be introduced in the next section.

6.4 The Digital-SiMPl concept

When considering the performance requirements of for particle tracking detectors in high energy physics, it becomes apparent that SiPMs are capable of accomplishing many of them. An insensitivity to magnetic fields, as well as a high gain and thereby high SNR are already inherent characteristics of conventional SiPMs and SiMPl devices. A potential high spatial resolution via small pixel sizes was already demonstrated by commercially available SiPMs with pitch sizes of 25 µm (e.g. Hamamatsu MPPCs, KETEK SiPMs), and multiple layers of high fill factor devices could be utilized in applications with more lenient requirements in terms of resolution, while still maintaining a large active area. An extremely fast response time in the sub-nanosecond range can be expected for SiPMs due to the inherently fast nature of the avalanche creation process itself.

Finally, the requirement for a low mass detector can be achieved when taking the necessity of a reduced wafer thickness for SiMPl devices into account. This thickness can be reduced even further by additional adaptation of the sensor material as will be

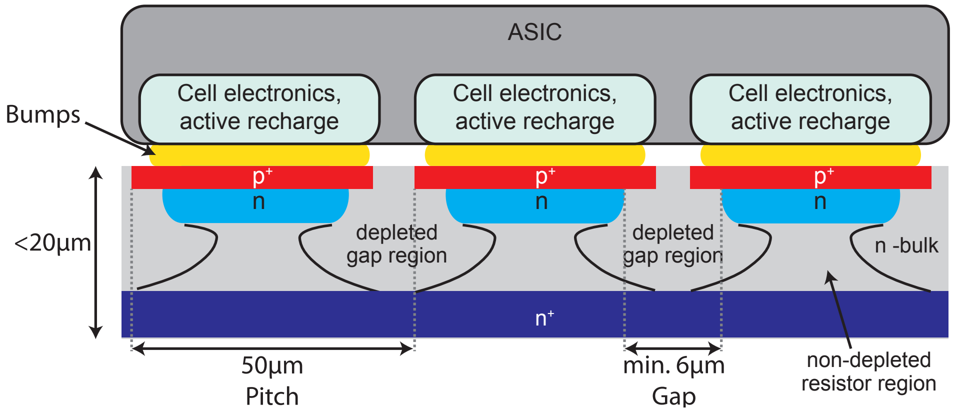

Figure 6.5: Schematic cross-section of the DSiMPl design for potential particle tracking. The already discussed SiMPl design is utilized with slight alterations to meet certain requirements for tracking applications. The thickness is drastically reduced to $d < 20$ µm to allow for a low mass detector. Only one reduced pitch size of 50 µm is featured with varying gap sizes ≥ 6 µm. In order to allow single cell readout, the common p^+ is now segmented. By taking advantage of the topologically flat surface of the SiMPl design, dedicated electronics incorporating active quenching and readout mechanisms can be directly connected to the chips via bump-bonding.

shown below, thus aiming towards even lower material budgets.

To this end, a novel hybrid tracking detector prototype was designed in collaboration with DESY[1], incorporating the SiMPl sensor design. This concept is called Digital SiMPl (DSiMPl) and will be introduced in the following section.

6.4.1 Sensor concept

A schematic cross-section of the DSiMPl design is illustrated in Fig. 6.5. In order to utilize SiMPl devices for particle tracking, a single pixel readout will be required. Hence a structuring of the topside p^+-implant was performed, while the backside anode is still common for the entire array. To realize the single pixel readout, the sensor is going to be connected with sophisticated readout electronics. For this purpose, the previously mentioned advantage of SiMPl featuring a topologically flat surface can be taken advantage of. Since no external resistor or metal lines are present on SiMPl devices, the connection to electronics via methods like bump-bonding (also referred to as flip-chipping) is drastically simplified.

The size of the individual cells and thereby the fill factor are mostly limited by the size of the bumps deposited on the now segmented topside implant. For the first prototype of this concept a pitch size of 50 µm was chosen, mainly due to the technical limitations and availability regarding smaller bump bonds. The gap sizes also vary with a minimum of 6 µm between two adjacent deep n implants.

Making use of the easy access to flip-chipping due to the topologically flat surface allows for the integration of sophisticated readout electronics in the detector design. In addition to providing the bias voltage to the arrays, the electronics will also feature an active quenching mechanism (see next section). In doing so, the requirements on the detector bulk will be less demanding, because quenching and recovery are now no longer being carried out passively by the bulk material. Consequently, the thickness of

[1]Deutsches Elektronen-Synchrotron, Hamburg

the sensor can now be adapted to further suit the requirement of trackers for a very low mass detector. Hence, the sensor wafer thickness for the design of the first DSiMPl prototype was chosen to be < 20 µm. For the first prototype, the handle wafer will still be present in its total thickness. Future iterations of the DSiMPl sensor will need to make use of partial backside etching procedures in order to thin down the material in the sensitive area, while keeping the edges and dead areas in between at full thickness to ensure structural integrity.

Another major advantage of applying a SiPM device for the detection of particles, namely MIPs, is the resulting inherently high trigger efficiency allowing operation at lower overbias voltages. This aspect will be discussed in detail in Sec. 9.5.

The main goal of the first DSiMPl prototype production is threefold. First, the overall functionality of the devices in terms of homogeneous breakdown behavior with the adapted thickness and segmented topside implant needs to be confirmed, as e.g. simulations suggest potential issue in the pixel edge region.

The next major goal is the investigation of the radiation hardness of the sensor material in terms of both ionizing and non-ionizing radiation damage. One example is the aforementioned issue with segmented topside implants which is now a potential problem, in addition to the impact of the change in bulk parameters on the coupling to the electronics.

Finally, the interaction of the electronics and the sensor as well as their feasibility regarding the potential application as tracker requires thorough investigation. This includes the execution of the bump bonding procedure itself and preliminary tests with the electronics coupled to different types of sensors for first studies.

6.4.2 Active quenching readout electronics

The design of DSiMPl incorporates the use of hybrid device, meaning sensors coupled to sophisticated readout electronics which will also provide active quenching circuitry for the sensors. A brief overview of the electronics developed at DESY will be given in the following, but more detailed information can be found in [86].

The ASIC uses a 32x32 pixel matrix with matching 50 µm pitch to the sensors. The electronics will be able to provide individual pixel readout, which also supports cell masking in case of hot pixels, in addition to featuring dedicated trigger logic for event selection, thus potentially lowering parasitic contributions like dark counts or optical cross-talk. Low power consumption can be assumed, since the front-end circuitry will be operating at 3.3 V, which is made possible by the need for only low overbias voltages, while the data processing operates at 1.2 V.

The main benefit of the implementation of active quenching will be the possibility to overcome the inherently slower recovery times of SiMPl devices due to the JFET-like nature of the internal quench resistor. As a result, quenching times < 1 ns can be expected and a cell recovery in the range of 20 ns, which is roughly a factor 10 faster than the recovery time for passively quenched SiMPl2 devices. The trigger timing for events is also expected to be in the sub-nanosecond range, thereby matching the time scale of the creation of the avalanche process itself as well as the requirements for tracking detectors.

The first prototypes of the readout electronics are currently being tested in conjunction with the first batch of the respective SiMPl batch. However, the connection between both is currently established by means of wire bonds as the bump-bonding procedure still requires additional experimental exercise to ensure feasible results. This study will be mainly focusing on sensor aspect of this novel design, thus, the electronics will not be discussed in more detail.

6.5 Expected impact of radiation damage on SiMPl performance

A detailed explanation containing the two different types of radiation damage, namely ionizing and non-ionizing, as well as their underlying damage mechanism, defect classifications and their impact on the overall detector performance of common silicon detectors, was given in Chapter 4. While the phenomena presented also hold true for SiPMs, the following section will discuss how these effects translate to changes in the operation of SiMPl devices, since their basic structures is quite different to that of a conventional SiPM. Several studies like [87–96] have already dealt with the impact of different types of radiation damage on conventional SiPMs manufactured by e.g. Hamamatsu or KETEK and the following discussion will briefly summarize how those findings will impact the special case of SiMPl.

6.5.1 Ionizing radiation damage

In terms of surface damages caused by ionizing radiation damage, two main ramifications on the overall detector performance can be expected. First, due to the creation of additional interface defects, an increased surface-generation current can be observed. This will manifest in higher dark currents over the complete voltage range but will not necessarily translate into a higher DCR, since it is possible that said currents will not be amplified within the high-field region. This, in turn, depends on the shallowness of the avalanche region with respect to the SiO_2-Si interface and can be avoided by adapting the parameters of the high-field implants.

The second repercussion is limited to the novel approach of DSiMPl, as it features a single-pixel readout, thus introducing a segmented p^+ topside implant. As stated above, additional fixed positive oxide charges will be created with increasing dose, leading to the accumulation of negative charges in the gap area between two pixels devoid of any boron implant. This, in turn, can cause the formation of lateral electric field peaks which may result in lateral breakdowns between the p^+ implant and the bulk gap area. In order to prevent said breakdowns, an aluminum grid was deposited on top of the gap areas, allowing accumulation of negative charges to be counteracted by adapting the potential of the aluminum grid.

Various studies like [87, 92] have shown that parameters like the breakdown voltage V_{bd}, pixel capacitance C_D and the quench resistor R_Q were unaffected in conventional SiPMs. For SiMPl the same can be expected in regards to ionizing damages, thus leaving the recovery time $\tau_{rec} = C_D R_Q$ unaffected, as well. In addition, the quench capacitance C_Q for SiMPl devices should also not change in face of ionizing radiation damage, as the quench resistor is located within the bulk and not perturbed by changes in the surface structures.

6.5.2 Non-ionizing radiation damage

The main detrimental effect caused by non-ionizing radiation damage is the increase of the dark current and subsequent dark count rate of the SiPM devices. Due to the creation of additional defect states close to mid-gap, thermal generation will increase proportional to the experienced fluence and if these new defects are located close or within the avalanche region, the generated charges will likely be able to undergo charge multiplication. It is, as of yet, unknown what impact different types (particles) of radiation have on the increase of the dark current and DCR. This issue can be alleviated by cooling the devices down, as this will decrease the overall thermal generation within the detector.

While some parameters will not be directly affected by radiation damage, the increased DCR, in turn, will be able to have a negative impact. One example is the loss of the single photoncounting resolution due to the subsequent noise increase. The constant occupation of the single pixels as well as the following baseline jumping will further deteriorate the single photon counting ability. Even though this aspect can be reversed by, again, decreasing the temperature, depending on the total fluence, certain cases have shown that temperatures down to 84 K might be necessary [91]. Another example for the negative influence of the increased DCR is the subsequent potential self-heating taking place in certain pixels or even arrays. This can lead to a shift in the breakdown voltage $V_{bd}(T)$ and thereby impact the gain of the devices.

The generation of additional defects also causes an increase of the afterpulsing probability, since more trapping centers will be present within the high-field area. This, combined with the already increased DCR, will lead to significant reduction of the photon detection efficiency on account of the severely high pixel occupancy within the array. Given sufficient DCR levels, it is possible to reach complete saturation of larger arrays solely due to increased thermal generation. In addition, a higher DCR will also enable an increased probability for optical cross-talk within the arrays.

The creation of more shallow defects poses another threat to the nominal operation of SiMPl device. Contrary to conventional SiPMs, changes of the effective doping concentration N_{eff} within the non-depleted regions of the bulk underneath the pixels will directly affect the quench resistor R_Q and consequently also the quench capacitance C_Q. Small fluences are expected to have only a very negligible impact, followed by a decrease in N_{eff} and therefore increase of the depletion region stemming from the gap area. This, in turn, should increase R_Q with the extreme scenario close to type inversion leading to complete pinch-off, in which case also V_{bd} will be affected, since there will be a voltage drop within the depleted area in the bulk. Afterwards, a steady increase of N_{eff} can be expected (see Fig. 4.7).

One expected outcome of type inversion will be a shift of V_{bd} to higher voltages. By transitioning from n to p-type, the area forming the quench resistor underneath the deep n implant will now potentially form another junction with either the deep n or the n^+ backside. Hence, it is most likely that said area will become more depleted with increasing bias voltage, thus increasing R_Q as well as the voltage drop to the high-field region. This will consequently result in a smaller supplied voltage to the avalanche region and a higher bias voltage will be required to achieve Geiger breakdown, henceforth artificially increasing V_{bd}. Should no formation of this additional junction take place, the additional accteptor states would be present in a non-depleted region. This, in turn, would lead to an increase in the bulk resistance and thereby affect V_{bd} in a similar fashion. It is however unclear, how exactly type inversion will affect the performance of SiMPl devices, i.e. if proper quenching and recovery will still occur and how the related parameters will change.

As a result of the changes in R_Q and $\tau_{rec} = R_Q C_D$, the recovery time of the cells can also be expected to be affected, namely to increase up to the fluence of type inversion. Afterwards, if a second junction within the bulk is formed, recovery could only occur via punch-through, thus increasing the recovery times exponentially. Previous studies for conventional SiPMs have not shown any signs of C_D being negatively impacted by radiation damage and the same is expected for SiMPl.

Studies like [88], [89] and [90] have reported a shift of V_{bd} for neutron fluences above $\Phi_{neq} = 6 \cdot 10^{12}$ neq/cm^2 with the shift appearing to be dependent on the multiplication layer width and thinner avalanche regions seeming to be less susceptible to shifts in V_{bd}. This is assumed to be linked to the acceptor creation within the high-field region. Due to SiMPl devices featuring a thin avalanche region comparable to the thin one mentioned in the studies above, only a small shift in this regard can be expected.

7 Simulation methods and tools

Simulation studies offer the means to perform pre-selections in terms of certain technological parameters before wafer fabrication. By carrying out technology (process) and device simulations, problematic aspects regarding the devices can be identified and adapted without the need to run into issues after production has finished. This, in turn can help reduce the time and cost of the development procedure. Thus conducting thorough simulation studies before device production can be crucial for the success of a project. Even afterwards, comparisons to experimental data can offer a better understanding of possible issues at hand and is also of great importance.

The following section will first introduce the various Technology Computer Aided Design (TCAD) tools utilized for technology and device simulations of SiMPl devices within this study. In doing so, the different types of device simulations will be elaborated upon in terms of procedure and the desired information from said simulations. In addition, Monte Carlo methods for more sophisticated simulation studies will be discussed.

7.1 Technology simulation

The individual fabrication steps during semiconductor processing can be simulated by utilizing TCAD tools. This allows the investigation of processing steps like ion implantation, annealing, oxidation or etching and their respective parameters. In the case of the ion beam for implantation, the ion energy, dose and implant angle play an important role, while annealing requires detailed information on specific temperatures and durations, as well as atmospheric conditions. Another important aspect that will be discussed below, is given by the photoresist which is used to structure certain implants. The final goal is the determination of the implanted profile, obtained via the finite element method, which can then be either cross-checked with actual measurements or further utilized in device simulations.

Two different TCAD tools were used within this study, however, the majority of the simulated data was obtained with a component of the SYNOPSYS TCAD[1] simulation framework, namely Sentaurus Process (SProcess). While initial process simulations were also carried out with the ISE-TCAD process simulator DIOS[2], the tool is no longer supported by its developers. In addition, DIOS bases the profiles for ion implantation on analytical tables, obtained from experimental data. These, however do not take the effects of channeling within silicon into account, which can occur for certain implant angles, as will be explained in detail in Sec. 9.1.1.1. SProcess on the other hand also offers the additional possibility of calculating said implant profiles via Monte Carlo methods which use a statistical approach to the calculation of the penetration of implanted ions into the target and accumulation of crystal damage based on the binary collision approximation [97] and include effects like channeling. Furthermore, specific diffusion models can be chosen, which allows fine tuning of the annealing procedures during the wafer fabrication.

[1] `https://www.synopsys.com/silicon/tcad.html`
[2] Integrated Systems Engineering AG

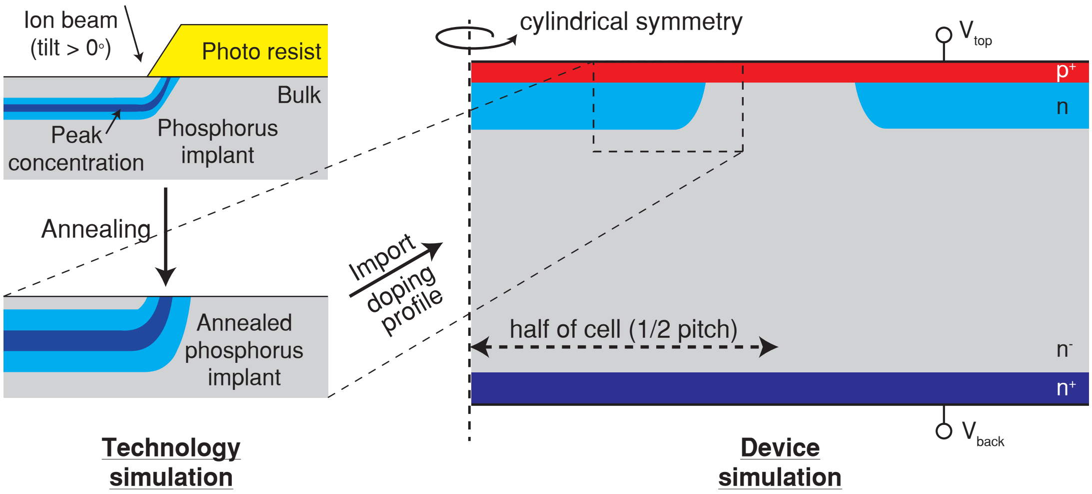

Figure 7.1: Illustration of the technology (left) and device simulation (right) procedure. In the case of technology simulations, the implantation process is simulated via an ion beam being aimed at the bulk at a specific tilt angle. Segmentation of individual implants is achieved via photo resist barriers for the ion beam. The depth of the peak concentration of the implant depends in the energy of the ion beam and can lead to shallow or deep implants. After removal of the photo resist, the structure undergoes a controlled annealing process which leads to diffusion and electrical activation of the initial implant. The resulting doping profile can then be analyzed and imported into the device simulation tool in order to construct the final simulation region (right hand side). Areas featuring homogeneous profiles are obtained via extrapolation of the small region obtained from technology simulations. Only half of the investigated cell is constructed, in addition to half of a neighboring cell, as the device simulator will apply cylindrical symmetry in order to obtain quasi-3D results. The device simulations allow the application of external voltages in order analyze the operational behavior of the final device. See text for more details.

The common process simulation procedure is illustrated in the left hand side of Fig. 7.1. In order to allow for a finer grid resolution and smaller computing times, only a small fraction of the entire device processing is simulated. The first steps can be summarized as the simulation of the ion implantation in the edge area with the specific parameters mentioned above. Afterwards the photoresist is stripped from the region and a predefined annealing scenario takes place, resulting in the diffusion of the doping profile. This final region can then be utilized to construct the entire device within a different tool of the Synopsys framework. Usually regions including transitions in the doping profile or changes in the topology, such as the area surrounding the photoresist edge are focused upon, as the homogeneous regions can be extrapolated from the edges of the region of interest. In the case of one dimensional doping profiles, like the backside n^+-implant, measured profiles obtained from Secondary Ion Mass Spectroscopy (SIMS) or Spreading Resistance Profiling (SRP) measurements can be imported into the framework.

A potential drawback of the SProcess simulation tool lies in its optimization of the parameter space for certain applications within the semiconductor industries. If parameters deviating from the optimized regime are chosen, significant discrepancies between reality and simulation can arise. This can be investigated by performing SIMS or SRP measurements and comparing the data, allowing for further fine-tuning of the simulation.

7.2 Device simulation

The device simulations attempt to describe and simulate the working principle and operation under biasing conditions of the structure constructed within the framework. The basic approach is to numerically solve the equations for the electrostatics and, in the case of applied voltage on pre-defined contacts, the resulting charge carrier transport in the device.

Electrostatics are described by the electrostatic potential Ψ which is the solution for the Poisson equation, given by

$$\nabla(\epsilon_0 \epsilon_r \nabla \Psi + \mathcal{P}) = -q_0(N_D - N_A + p - n) - \rho_t \ , \tag{7.1}$$

which is comparable to Eq. (3.1) but takes the ferroelectric polarization $\mathcal{P}$ and the charge density contributed by traps and fixed charges ρ_t into account [98]. If all contacts of the device are biased to the same voltage, the system can be described by an equilibrium and thereby by a quasi-Fermi potential. However, if different voltages are applied, the equilibrium state is not valid any longer. In this case, the carrier transport can be described by the continuity equations, which describe charge conservation:

$$\nabla \mathcal{J}_n = q_0(R_{net} + \frac{\partial n}{\partial t}) \qquad \text{and} \qquad \nabla \mathcal{J}_p = q_0(R_{net} + \frac{\partial p}{\partial t}) \ . \tag{7.2}$$

Here $\mathcal{J}_n$ and $\mathcal{J}_p$ denote the electron and hole current densities, respectively and R_{net} the net recombination rate. Depending on the simulation framework, several carrier transport models can be chosen, changing the expressions for $\mathcal{J}_n$ and $\mathcal{J}_p$. R_{net} takes various recombination and generation mechanism, like SRH, Auger, optical and surface recombination as well as avalanche generation into account if the specific effects are turned on during the simulation.

However, not all device simulation tools have access to the same amount of physical effects and parameters, making some preferable compared to others. Similar to the process simulations, initially two device simulators were utilized during this study. The first is called WIAS-TeSCA[3], while the second is another component of the Synopsys TCAD framework, namely Sentaurus Device (SDevice). Compared to SDevice, TeSCA is less resource demanding and provides faster results. However, SDevice offers overall more benefits, as it allows a more detailed fine-tuning of physical effects and parameters as well as a more reliable access to a heavily modifiable simulation grid. After initial cross-checks between both simulation tools Synopsys SDevice was chosen as the main tool for device simulations due to its overall advantages.

After technology simulations, the individual obtained implants are arranged according to the device layout to construct the final device, as illustrated in the right hand side of Fig. 7.1. This is achieved via an additional component of Synopsys TCAD, the Sentaurus Structure Editor (SDE) [99].

In order to obtain quasi-3D results, half of one pixel of the device that is simulated is constructed on a 2D-plane, including half of the neighboring pixel. SDevice then solves the problem in cylindrical symmetry with the central pixel being investigated. A detailed study by Jendrysik [33] has shown, that approximation of the hexagonal shape of the devices investigated in this thesis with a cylindrical in-circle approach leads to the most reliable results in terms of the behavior of the bulk integrated quench resistor and the obtained current-voltage characteristics. The comparison was carried out by performing full 3D simulations within SDevice.

[3] Weierstraß Institut für angewandte Analysis und Stochastik, Berlin: *Two-Dimensional Semi-Conductor Analysis Package*

Cells in various shapes, namely hexagonal, cylindrical in-circle, cylindrical equal-area and square, were simulated and the extracted I-V-curves investigated. The approach with an equal area cylinder resulted in higher deviations in terms said characteristics compared to the hexagonal shape and the same could be observed for the square approach. The in-circle approach slightly underestimates the total area of the cell and thus the cell capacitance C_D, but applying a correction factor to the extracted values of C_D can easily alleviate the issue. Furthermore, a comparison of the quasi-3D in-circle approach with the 3D hexagonal case showed deviations in the range of roughly 1% in regards to the I-V-characteristics. Real 3D simulations are exceptionally time consuming and require a great deal of computational resources, thus making them not suitable for an extensive and detailed parameter study. By confirming the accuracy of the quasi-3D simulations, however, it is possible to omit the necessity of performing real 3D simulations and focus on the quasi-3D approach instead, as the approximation was shown to be in very good agreement.

Two different types of device simulations were carried out within this study, namely static or stationary and transient simulations. Both variants will be discussed in the following. Afterwards, a possible implementation of radiation damages within the simulation framework will be introduced.

7.2.1 Stationary simulations

The stationary or static simulations describe a non-time-dependent simulation of the device. The main goal is the investigation of the bulk-integrated quench resistor R_Q and by evaluating its I-V-characteristics the determination of the quench and recovery behavior of the simulated device. These characteristics have - in a first order approximate - a strong dependence on the pitch/gap combination of the cells as well as the applied voltages on the different contacts. This dependence originates from the shape of the non-depleted region making up R_Q being heavily influenced by said parameters. Considering further parameters like temperature dependence, bulk doping variations and the resulting change in charge carrier mobility can lead to additional influences on the

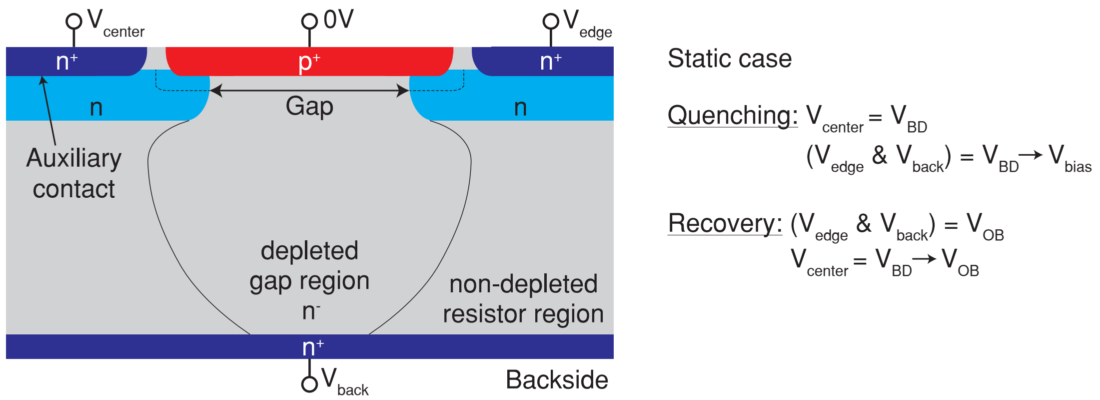

Figure 7.2: Schematic cross-section of the process sequence of static TCAD simulations for SiMPl devices. The voltage settings are listed on the right. The static (or stationary) simulations allow an estimate of the maximum overbias voltage $V_{ob,max}$ and recovery times $\tau_{90\%}$ and $\tau_{1/e}$ by investigating the I-V-behavior between the "Center" and "Back". For $V_{ob,max}$ the quenching condition by Cova [42] is utilized while biasing "Edge" and "Back" beyond V_{bd}. Afterwards, the recovery times can be extracted by increasing the potential at "Center" to a specific overbias voltage V_{ob} (see text).

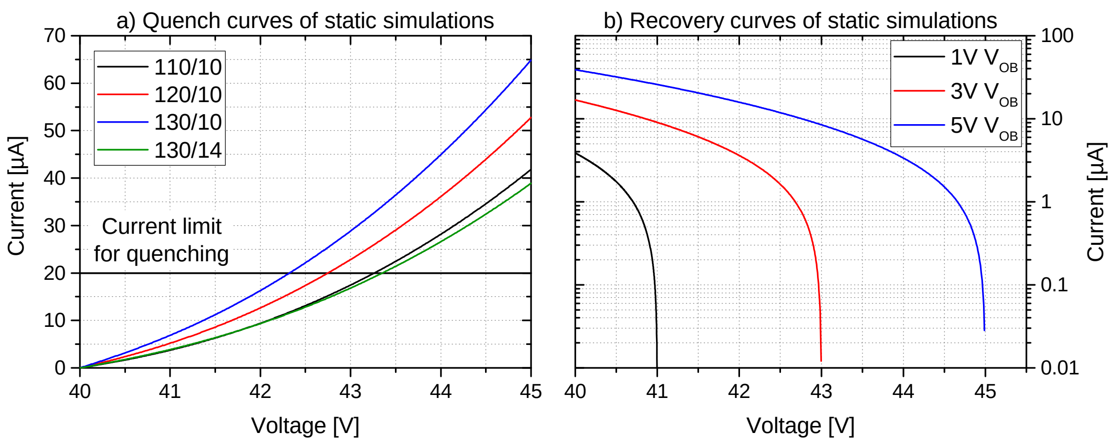

Figure 7.3: Examples of a) quench and b) recovery curves of SiMPl devices obtained from static device simulations. The I-V-curves for evaluation of the quench behavior (a)) are shown for various pitch/gap combinations. $V_{ob,max}$ is given by the voltage at a current limit of 20 µA (see text). A non-linear characteristic caused by the JFET-like behavior is visible. The recovery curves are presented in b) for three different V_{ob}. Applying Eq. (7.5) on these curves allows the extraction of the specific recovery times (see text).

characteristics of R_Q.

In order to access the quench resistor directly, the structure illustrated in Fig. 7.2 was designed, depicting half of the investigated cell and half of a neighboring one, before cylindrical symmetry is applied to achieve a quasi-3D result. Implementation of auxiliary contacts with n^+-doping, labeled "Center" and "Edge" on the topside, while limiting the size of the p^+-implant to the gap region, enables the measurement of the resistor specific I-V-curves between Center and Back. In a preparatory step, all contacts are initially biased with 0 V before the starting conditions for the individual simulation steps.

The quenching behavior can be extracted by analyzing the current at the moment of the breakdown. This is achieved by setting the initial contact voltages to the situation of a cell initiating the avalanche breakdown. The p^+ contact is kept at 0 V while the remaining three are set to the breakdown voltage V_{bd}. To simulate the breakdown at multiple overbias voltages, the Back and Edge contact are then increased to V_{bias} (see the right side of Fig. 7.2) and the current between Center and Back $I_q(V_{bias})$ is recorded. An example of the non-linear JFET-like behavior of the SiMPl R_Q is depicted in Fig. 7.3a) by way of the measured $I_q(V_{bias})$-curve for different bias voltages. In contrast to the conventional SiPM, the non-linearity as well as the dependence on the pitch/gap variations and external voltages shaping the bulk resistor are clearly visible. By utilizing the quenching condition suggested by Cova [42], the potential maximum overbias voltage $V_{ob,max}$ is given via the applied voltage at a current level of 20 µA. Generally, a higher value of $V_{ob,max}$ results in a larger window of operation regarding the voltage and is usually desirable.

In regards to the recovery time, the methods for determination introduced in Sec. 5.3.4 cannot be applied to SiMPl devices because of their inherent characteristics. Direct measurement of R_Q was up to this point not possible, as the quench resistor is only defined within the bulk under reverse bias conditions. Even if such measurement would be possible, it was already discussed in Sec. 6.2 that due to the JFET-like behavior of R_Q, the value of the quench resistor becomes a function of the applied bias voltage $V_{bias}(t)$ and thereby a function of time t. As this also applies to the process of recovery,

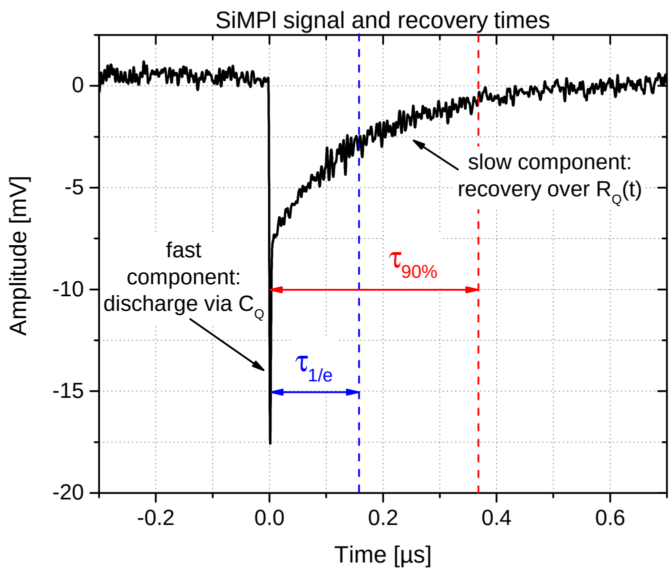

Figure 7.4: Illustration of the determination of the recovery times of SiMPl devices. A SiMPl signal usually consists of two components, namely the fast discharge via C_Q and the slow recovery part of C_D over $R_Q(t)$. The recovery times $\tau_{90\%}$ and $\tau_{1/e}$ can then be determined by deriving the time needed to reach 10% or (1 − 1/e)-th of the slow signal amplitude, respectively. The fast component is not relevant for the recovery analysis.

the time constant τ_{rec} cannot be defined as it would not be constant but also a function of time $\tau_{rec}(t) = R_Q(V_{bias}(t))C_D$. In addition, fitting the slow part of the signal pulse with an exponential decay also becomes inaccurate and not applicable, since $\tau_{rec}(t)$ is not constant.

Considering these methodological limitations, a different approach will be required to determine the recovery times of SiMPl devices. The experimental method is illustrated in Fig. 7.4 and utilizes the pulse shape of a SiMPl signal. This signal generally consists of two different components. The first is a fast contribution to the signal, defined by the discharge over the coupling capacitance C_Q, as well as the grid capacitance C_g and the load resistor R_{load} as previously depicted in Fig. 3.8. This part is not relevant for the recovery analysis and will therefore not be considered. The following slow contribution, however, is directly associated with the recovery of C_D over $R_Q(t)$ and will be utilized. Here, $\tau_{90\%}$ can be derived by determining the required time within the slow component, which is required to reach 10% of the slow signal amplitude, corresponding to a 90% recovery. In a similar fashion $\tau_{1/e}$ can be determined.

A method to estimate the impact of the JFET-like characteristics and the deviation from the standard RC behavior of the SiMPl R_Q was proposed by Jendrysik [33]. Assuming a standard RC element, the ratio of these two recovery times would result in

$$\frac{\tau_{90\%}}{\tau_{1/e}} = \frac{\ln(0.1)}{\ln(1/e)} \approx 2.3\,. \tag{7.3}$$

In the case of SiMPl and its time dependent quench resistor however, this ratio will start deviating from 2.3 towards larger values, with increasing deviation indicating a larger discrepancy from the expected linear behavior and more impact of the JFET-like characteristics.

The adapted method of determining the recovery time for SiMPl devices can be utilized in a second step of the static simulations. An initial state is defined with the

Back and Edge contact being biased at a specific overbias voltage V_{ob}, while Center is held at V_{bd}. The recovery process is then simulated by increasing the voltage at Center to V_{ob} and tracking the current I_r between Center and Back. Due to the deviating depletion region in the bulk for different V_{ob}, the current and consequently the recovery times can be expected to vary with overbias voltage (see Fig. 7.3b)). The recovery time can be derived from the measured I-V-curved by utilizing the displacement current relation

$$I_r = \frac{\mathrm{d}Q}{\mathrm{d}t} = C_D \frac{\mathrm{d}V}{\mathrm{d}t} \ . \tag{7.4}$$

This allows calculation of the required time $\mathrm{d}t$ for a voltage step $\mathrm{d}V$, using the data of I_r and C_D from the simulations. Depending on the desired level of recovery, i.e. the percentage of the potential difference ΔV between breakdown and operation, various recovery times can be defined and derived, as explained in Sec. 5.3.4. As an example, the a recovery of 90%, corresponding to 10% of ΔV will be considered. Thus, the recovery time can be calculated via Eq. (7.4) and by summation over all voltage steps $\mathrm{d}V$ required for the desired recovery state. In the case of infinitesimal voltage steps, the summation leads to an integral given by

$$\tau_{rec,90\%} = \int_{\Delta V}^{0.1\Delta V} \frac{C_D}{I_r(\Delta V)} \mathrm{d}V \ , \tag{7.5}$$

which can then be calculated numerically with pre-defined voltage steps, chosen to be $\mathrm{d}V = 1$ mV.

The dependence of the recovery times on V_{ob}, as seen in Fig. 7.3b), can be explained by the non-linearity of the current characteristics. With increasing V_{ob}, the fraction of the curve corresponding to the highest values of R_Q and thereby leading to longer recovery times, becomes more negligible for reaching e.g. 10% of ΔV. Thus, an increase of V_{ob} can be expected to result in shorter recovery times with the magnitude of the decrease being depending on the recovery level in question.

The static simulations provide an early and easy means of identifying a feasible parameter space in regards to the pitch/gap combinations. Inspection of the simulated region during the operational biasing conditions as well as the investigation of the recovery times can already reveal combinations that will lead to pinch-off or potential non-quenching. Pinch-off can e.g. be identified by severely long recovery times, since the volume of R_Q would be depleted, resulting in recovery only taking place by means of thermal generation. Hence, the parameter space can be limited to only promising combinations for the fabrication of wafers.

It should be noted that comparisons of previous simulation studies with experimental data of older batches of SiMPl have exhibited generally smaller recovery times for measured data, compared to simulated ones. Thus the assumption can be made that the extension of the depletion region is slightly underestimated in the simulations, resulting in a smaller R_Q.

Finally, first estimates regarding the breakdown voltage can be made utilizing the static simulations. SDevice allows the implementation of charge multiplication in high-field areas including the Geiger breakdown. Making use of the model proposed by Van Overstraeten [36] (see Sec. 3.1.3), it is then possible to log the voltage at which the ionization integrals reach 1, thus initiating an avalanche breakdown.

7.2.2 Transient simulations

SDevice features avalanche generation within its framework to e.g. determine the breakdown voltage. However, analysis of the quenching and recovery behavior in this fashion

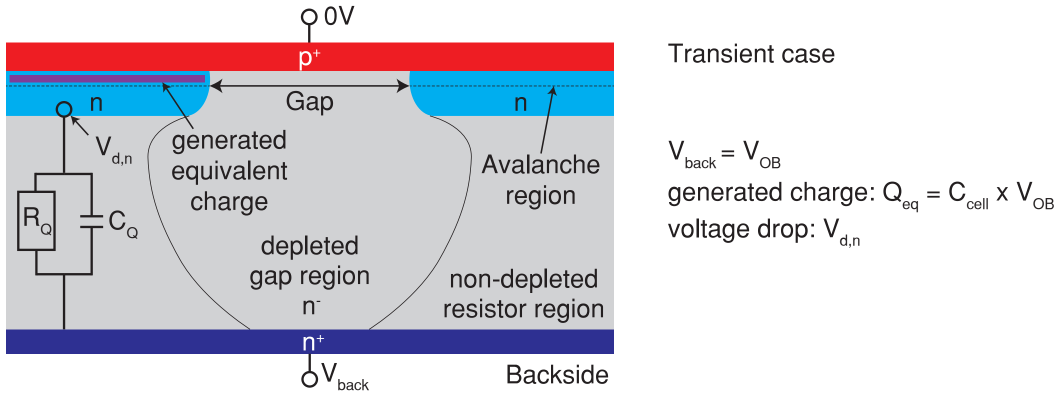

Figure 7.5: Schematic cross-section of the process sequence of transient TCAD simulations for SiMPl devices. The voltage settings are listed on the right. The transient simulations allow the evaluation of the recovery time as well as the internal voltage drop $V_{d,n}$ as a function of time. This can be achieved by generating a charge equivalent to the one created during an avalanche breakdown in the high-field region. In addition, the internal quench capacitor C_Q can be investigated this way (see text).

is not possible, as the tool bases all its calculation on carrier densities rather than discrete particles. Thus, quenching will never occur, as the number of charge carriers in the high-field region will never reach zero, because of the non-zero carrier density. A workaround can be achieved via the transient or time dependent simulations.

In this procedure, avalanche creation is disabled and instead an equivalent charge, corresponding to the diode capacitance and bias voltage according to Eq. (3.11) is generated within the high-field region. This mirrors a situation of the cell having initiated a Geiger breakdown and creating an amount of charge carriers in compliance to to its capacitance. The generation itself is based on a Gaussian time distribution with $\sigma = 2$ ps resulting in the complete generation within a few picoseconds, which was found to be comparable to the actual avalanche build-up time according to [100].

The auxiliary contacts of the static simulations can now be omitted, returning the design of the simulation region to the initial SiMPl design as seen in Fig. 7.5. The topside is biased at 0 V while the backside is held at V_{ob}. SDevice allows logging of the potential and current at the internal anode (deep n) as well as the current at the external contacts as a function of time after the charge has been generated. This, in turn, enables the extraction of various parameters.

The progression of the potential at the internal anode can be seen in Fig. 7.6a) for two different V_{ob}. Due to the generation of charges ($t = 0$ ns), the voltage will drop, simulating a quenching procedure and slowly charge back to the operational voltage after all charge carriers left the depletion region, akin to a recovery. The maximum voltage drop at the internal anode $V_{d,n}$ is expected to be equal to the applied overbias voltage and offers a means of verifying the simulation procedure. Recording the generated charge Q_{eq} and $V_{d,n}$, can be further utilized to cross-check the resulting diode capacitance C_D via Eq. (3.11).

While no direct statement can be made regarding R_Q, the quench capacitance C_Q can be extracted. As already explained, the signal charges within the first nanoseconds of the SiPM signal shape can be attributed to C_Q, thus by integrating the measured current at the external contacts, C_Q can be obtained by making use of the displacement current relation of Eq. (7.4).

Finally, the recovery time can be extracted more easily compared to the previous

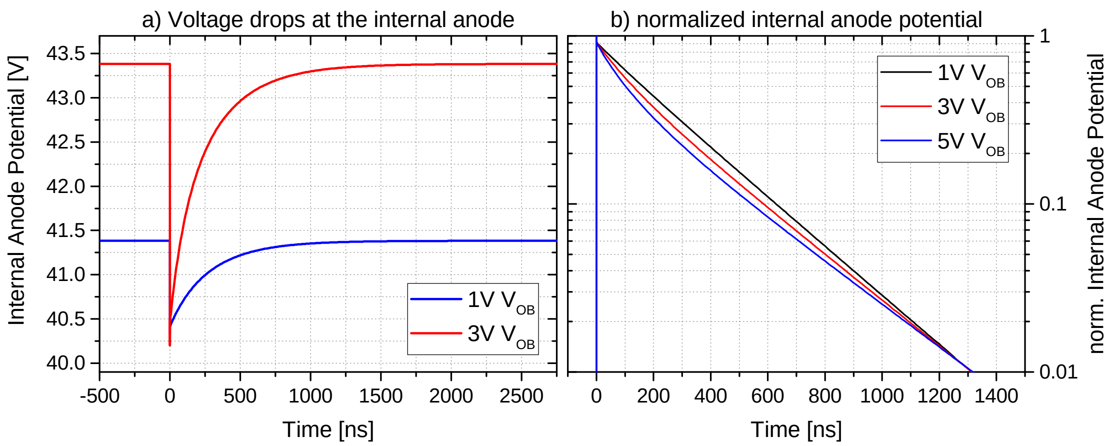

Figure 7.6: Results of transient simulations of a SiMPl device for the internal anode potential. The time progression of the potential of the internal anode of the simulated SiMPl cell is shown in a), with the charge creation taking place at $t = 0$ ns. Cases of two different V_{ob} are depicted with $V_{bd} \approx 40.25$ V. Due to the charge creation (simulation of an avalanche breakdown) the potential quickly drops to V_{bd} and can be considered quenched after the charge generation. This is followed by the recovery to V_{ob}. The progression of the normalized internal anode potential can be seen in b), depicted three different cases of V_{ob}. This mirrors the recovery of the device and can be seen to depend on V_{ob} (see text). The non-linear behavior of R_Q is apparent by the shape of the curves as a linear line would be expected for an exponential decay.

section. By logging the potential at the internal anode, the time stamp for a certain level of recovery after the initial voltage drop can be extracted, as the direct time evolution of the potential is available. The impact of V_{ob} in the recovery time mentioned in the previous section can also be seen in the results of the transient simulations, as depicted in Fig. 7.6b). Here the normalized voltage drop and its time progression is shown for various V_{ob}. As stated above, higher overbias voltages (if the quenching condition can still be fulfilled) result in shorter recovery times due to the non-linearity of the I-V-characteristics caused by the JFET-like behavior of the bulk resistor. The shape of the curves also indicate the deviation of the expected exponential decay experienced in standard RC elements.

7.2.3 Radiation induced damages

An additional advantage of Synopsys is the possibility of introducing radiation damage to the simulated device. This includes ionizing as well as non-ionizing types of damage. In the case of ionizing radiation damage, the implementation was achieved by indirect means via introducing a fixed positive charge in the SiO_2-Si interface. Regarding non-ionizing radiation damage, trap levels can be added to a certain region of the simulated device. The type of the defect (donor or acceptor) and their energy level within the band gap (according to the definitions in Sec. 4.1.3) have to be provided, allowing simulations to take their impact into account. This, however, can lead to issues, as the result relies heavily on the incorporated model of defect creation by non-ionizing radiation damage.

Various models discussing the type of defect, as well as their energy level and rate of creation in dependence of the equivalent neutron fluence have been introduced [101–107]. Initial models were based on single [101] or two-defect approaches [102], while later ones suggested the now mostly accepted three-defect-state case [103–106], consisting of two

Table 7.1: Parameters of the radiation induced defect levels incorporated in the device simulations of Synopsys SDevice. The energy levels in relation to the conduction (E_C) or valence band (E_V) for the three defects of the model are listed. The first two represent acceptor states, while the third corresponds to a donor state. Furthermore the cross-sections for electron σ_n and holes σ_p are given, in addition to the defect specific introduction rate η. Data taken from [105].

Energy level	σ_n [cm^2]	σ_p [cm^2]	η [cm^{-1}]
$E_C - 0.42$ eV	$2 \cdot 10^{-15}$	$1.2 \cdot 10^{-14}$	13
$E_C - 0.50$ eV	$5 \cdot 10^{-15}$	$3.5 \cdot 10^{-14}$	0.08
$E_V + 0.36$ eV	$2 \cdot 10^{-18}$	$2.5 \cdot 10^{-15}$	1.1

acceptors and one donor. Depending on the bulk material, the energy levels, capture cross-sections and generation rates can vary in all suggested models. In addition, many models are only valid up to certain equivalent neutron fluences. The most commonly accepted models, namely the "Perugia" model [103] and the "3D" model [104] are valid up to $2.2 \cdot 10^{16}$ neq/cm^2 and $1 \cdot 10^{16}$ neq/cm^2, respectively and were shown to be in good agreement. However, both are based on a p-type silicon bulk and are thereby not applicable for this study. On the other hand, the 3D model is based on a model by Petasecca [105] which also provides the necessary data for n-type silicon.

Hence, the model parameters from [105] were implemented in this study and are listed in Table 7.1. It features their energy levels with respect to the conduction (E_C) or valence band (E_V), the respective cross-sections for electron σ_n and holes σ_p as well as their introduction rate η. The acceptor level at $E_C - 0.42$ eV is associated with a di-vacancy (V_2) defect, while the one closer to midgap $E_C - 0.50$ eV is attributed to a di-vacancy oxygen complex (V_2O).

This method of modeling bulk related radiation damage still offers only a first order approach to the problem at hand, as more complex issues like defect cluster cannot be realized at this point in time. Furthermore, the implementation of a complete modeling scheme, featuring an extensive set of defects and their contributions to SRH statistics is currently computationally not feasible, thus requiring the above simplified approach.

7.3 Monte Carlo methods

Synopsys SDevice offers the possibility of determining the breakdown voltage by calculation of the ionization integral. However, since the utilized TCAD tools are all based on carrier densities, some deviation can be expected for the simulation of a Geiger breakdown as it requires a discrete particle model, since the triggering and quenching of an avalanche are statistical processes. Thus Monte Carlo methods can be deployed to solve these issues, as they describe a numerical approach based on the theory of probability. Utilizing such Monte Carlo simulations allows the calculation of the Geiger breakdown and its trigger or Geiger probability as a function of the electric field distribution within the high-field region which is moreover dependent on the applied bias voltage.

The dependence of the trigger probability on the bias voltage has already been studied

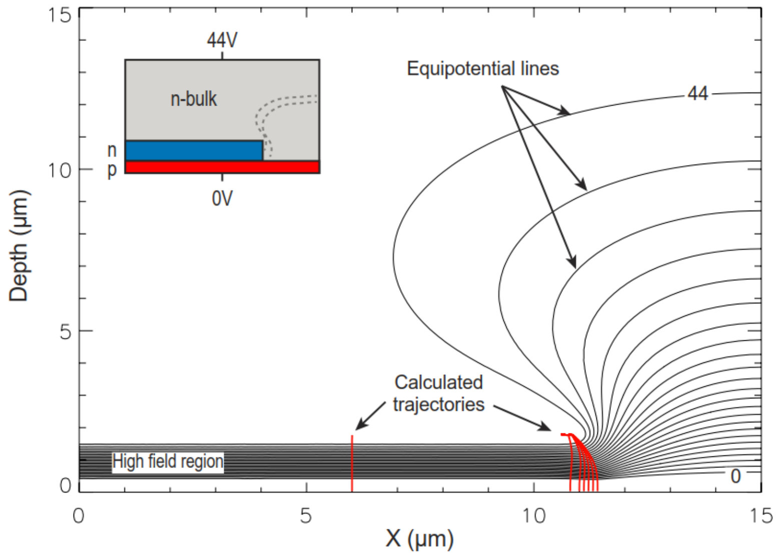

Figure 7.7: Procedure of the Monte Carlo breakdown simulations involving the calculation of the charge trajectories. The plot shows the equipotential lines of the simulated SiMPl structure shown in the inlet. By utilizing the extracted electric field, the trajectories for initial charge carriers (red lines) created at different spots within the high-field region and thereby the corresponding breakdown probability can be calculated. In order to investigate potential edge breakdown, charges are created close to the surface (depth of zero) and within the central area of the high-field region ($X \approx 6$ µm) and multiple spots at the edge region ($X \approx 11$ µm). Picture taken from [33].

by Oldham [108] and McIntyre [109]. The findings can be utilized to investigate possible issues at the edge regions of the SiMPl cells due to local electric field peaks, potentially resulting in an early breakdown (edge breakdown). In addition, the nominal breakdown voltage for various technological parameters pertaining to the high-field region can be investigated and cross-checked with the ones obtained by TCAD simulation tools.

For this purpose, the electric potential distribution of the desired region of the active area of the device can be exported from the TCAD simulation tool TeSCA at different V_{ob}. The data is then processed with an analysis program[4] in order to obtain the trajectory of a charged particle based on the electric field components. The movement is calculated step-wise for every grid point according to the electric field vector and utilizes the grid provided by the simulation tool and obtained via Delaunay triangulation (more details describing this procedure can be found in [33]). This step is repeated until a grid point with a field below a pre-defined threshold, usually not enabling impact ionization, is reached.

The result of such a procedure can be seen in Fig. 7.7, where the trajectories of charged particles are shown as red lines. The plot shows the resulting equipotential lines of the edge region of a SiMPl device, illustrated by the inlet. A trajectory located in the homogeneous area of the high-field region ($X \approx 6$ µm) will be compared to the multiple ones located in the edge area ($X \approx 11$ µm).

The stored electrical field distribution of the trajectory can then be further analyzed with a Monte Carlo simulation tool[5] in which the ionization coefficients α for every increment of the trajectory are numerically calculated. The program utilizes the model

[4]written in Interactive Data Language (IDL) and provided by Rainer Richter
[5]written in C++ and provided by Hans-Günther Moser

by Van Overstraeten [36] (see Sec. 3.1.3) in order to determine the trigger probability $P(\Delta d)$ for a trajectory increment Δd at a given bias voltage:

$$P(\Delta d) = 1 - e^{-\alpha \Delta d} \, . \tag{7.6}$$

Newly generated charge carriers are also accounted for in the subsequent calculations in order to correctly describe the avalanche production during the path of the charge carriers. An avalanche breakdown is considered achieved, if the number of charge carriers exceeds a pre-defined threshold, which is given by Ramo's theorem [110] and usually amounts to roughly 2000 charge carriers. If this number is not reached by the end of the simulation procedure, the event will not be counted as an avalanche breakdown. The overall Geiger efficiency for a specific bias voltage can then be obtained by repeating this procedure 10^4 times to allow for sufficient statistics.

If local electric field peaks are present in certain areas of the sensitive region of the device, such simulations will be able to pinpoint their location and confirm if a potential early breakdown phenomenon will occur, thus allowing the adaptation of technological parameters in order to avoid such issue.

In order to analyze the trigger probability for a arbitrary number of initially generated charge carriers, a modified version of the above Monte Carlo tool was provided by Jendrysik [33, 111]. It enables the determination of the trigger probability as a function of absorption depth and allows the definition of a most probable value (MPV) in terms of the number of initially generated charge carries. Hence, the case of a minimum ionizing particle (MIP) can be simulated by choosing a MPV of approximately 80 electron-hole pairs per µm as discussed in Sec. 3.3. The initial charges are then generated within the specified region via normal distribution and thereafter treated as the starting point of the above Monte Carlo procedure.

8 Devices under test

This study features various types of devices under test (DUT) from different production batches of SiMPl, namely SiMPl3, SiMPl4 and SiMPl5. The goal of SiMPl3 was the investigation of technological parameters in regards to the annealing of the high-field implant, in order to improve the performance of the previous prototypes. The individual wafers and therefore devices were not thinned down, limiting their uses to basic static characterizations and photon emission microscopy measurements.

SiMPl4 was aimed to be the next main batch of devices for low level photon detection and incorporated the findings of SiMPl2 and SiMPl3 as well as adding additional novel technological aspects. The devices were produced on SOI material with a reduced sensor thickness d_{SiMPl4}, allowing for dynamic characterizations in addition to the ones mentioned for SiMPl3.

The goal of SiMPl5 was the utilization of devices in the DSiMPl project for high energy particle tracking applications. Thus the designs were adapted to fit this purpose since active quenching and readout electronics would be incorporated and the wafer thickness was reduced further compared to SiMPl4, leading to $d_{SiMPl5} \ll d_{SiMPl4}$. The main purpose of the DUTs were general static characterization, photon emission microscopy measurements and first proof-of-concept dynamic measurements as well as coupling to the novel readout electronics for first evaluations.

The various DUTs can be mainly categorized as SiMPl arrays, the novel static test devices and diodes and will be introduced in the following sections.

8.1 SiMPl arrays

The majority of the devices located on a SiMPl wafer is made up of chips containing a differing number of avalanche arrays, depending on their pitch/gap combination. Including various combinations of pitch and gap size allows the investigation of the impact of the quench resistor on the recovery time and maximum overbias voltage. Thus, a proper trade-off depending on the application at hand can be found within certain pitch/gap combinations. The following section will focus on these array devices of different design with slight variations for each batch.

8.1.1 SiMPl4

SiMPl4 was design with the traditional application of photon detection in mind. Thus the main focus lies in chips containing SiMPl avalanche arrays of varying sizes with two different geometrical styles, namely hexagonal and square-shaped pixels. The majority of the arrays will feature hexagonal pixels with their array sizes being categorized as 30x30, 10x10, double flower (19 pixels), flower (7 pixels) and single cells (see left hand side of Fig. 8.1). In case of of the square-shaped ones the array sizes are 10x10, 5x5, 3x3 and single cells (see right hand side of Fig. 8.1).

The layouts of the chips shown in Fig. 8.1 can vary, depending on the pitch/gap combination, as larger pitch sizes will not allow the placement of e.g. four 10x10 arrays due to spacial constraints. In general, all hexagonal chips feature at least three 10x10

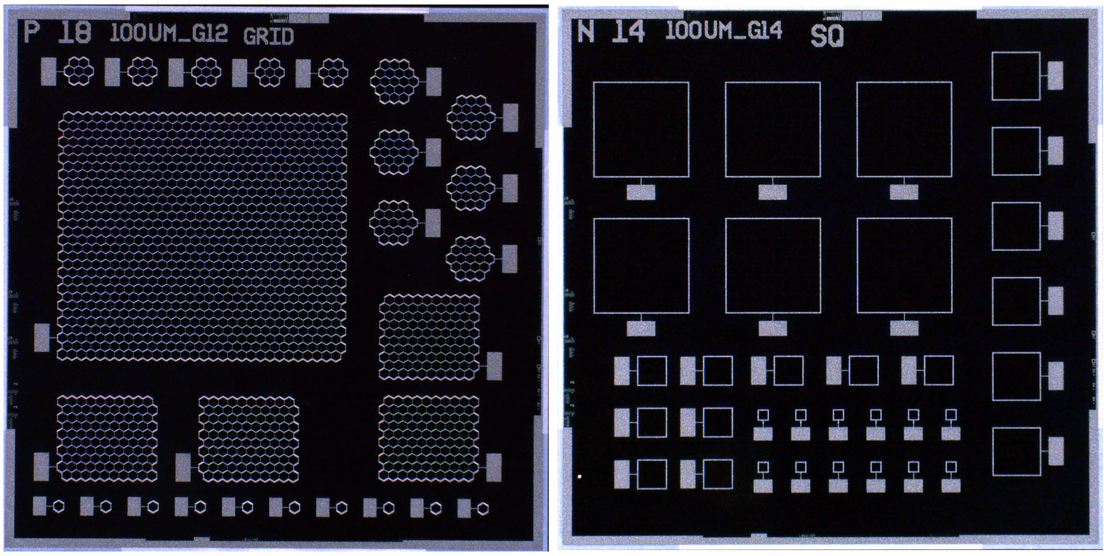

Figure 8.1: Example of a SiMPl chip with hexagonal (left) and square-shaped pixels (right). Arrays of varying sizes are placed on one chip with the layout depending on the pitch/gap combination featured on the chip (written at the upper edge of the pixel). The hexagonal arrays feature an aluminum grid in the gap region, allowing for a clear distinction of each pixel within the array, while the squared ones do not contain this grid. See text for details on arrays sizes and total number of arrays per chip.

arrays and flower and double flower structures as well as roughly ten single pixel cells with a total number of devices ranging from 19 to 26. In the majority of the cases a single 30x30 array will be included. In case of the square-shaped devices, only two layouts exist, one of which can be seen in Fig. 8.1 with a total number of 31 and 33 structures, respectively.

The pitch size of the arrays ranges from 100 µm to 130 µm with gap sizes between 6 µm and 30 µm in various combinations. Roughly one half of the chips feature a aluminum grid within the gap region, for possible timing and radiation hardness improvements, which can be seen in the hexagonal example of Fig. 8.1. The thickness of the devices is chosen with passive quenching in mind and requires thinning of normal wafer material and thus a SOI procedure. The topside contacting of the arrays is achieved via the designated aluminum pad next to the respective structure, directly connecting to the p^+-topside, while the backside can be accessed with the cutting edge surrounding the entire chip.

Apart from the adapted wafer thickness, the above descriptions also apply to the array structures of the SiMPl3 batch. While the technological aspects of SiMPl3 and SiMPl4 are considerably different, SiMPl3 wafers feature an almost identical amount of chips with similar array structures with deviations in terms of pitch/gap combinations. These arrays, however, cannot be utilized for dynamic characterizations since SiMPl3 wafers were not thinned down, thus limiting their use to static characterizations and photon emission microscopy measurements.

8.1.2 SiMPl5

In contrast to SiMPl4, the goal of SiMPl5 was not a traditional design and operation for light detection, but a potential single pixel layout, as well as tracking of charged particles. This shift of planned application can also be seen in the design of the corresponding

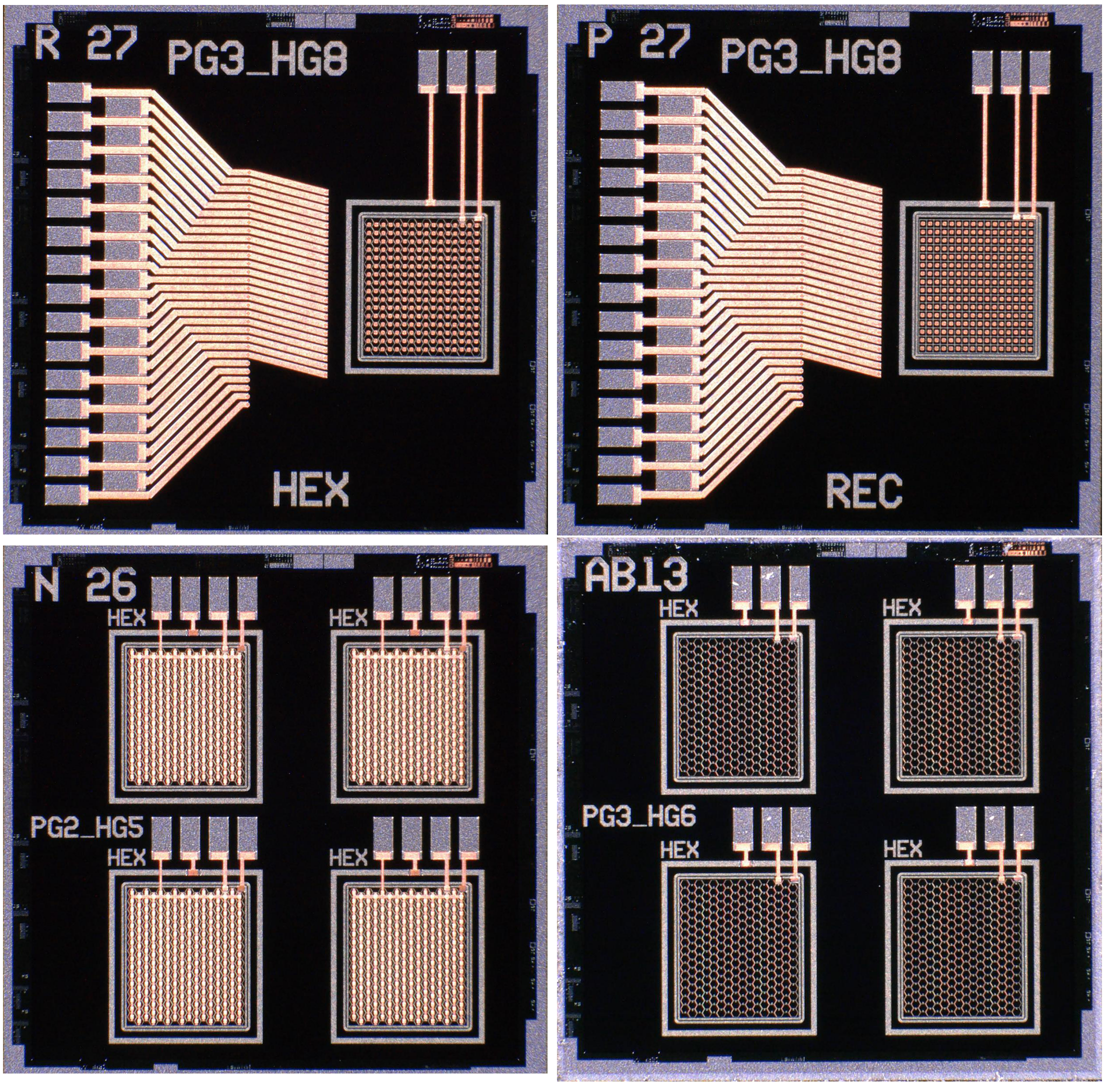

Figure 8.2: Examples of SiMPl5 arrays for flip-chipping (upper row) and classic arrays for default operation (bottom row). The flip-chipping device feature a 16x16 array of hexagonal (left) or square-shaped (right) pixels with individual copper pads for bump-bonding of the dedicated readout electronics. The additional copper lines and pads on the side allow contacting of said electronics. The contact pads on the upper edge enable biasing of the guard ring, aluminum grid and backside. The specific gap combination is written next those contacts (see text). The lower row depicts the two different layouts of the classic arrays for preliminary testing purposes. The "four contact" variation features an additional contact for the added copper grid for connection (left), while the "three contact" variant omits this copper grid and achieves connection via the already incorporated aluminum grid (right).

SiMPl5 structures, which are to be utilized for the DSiMPl project.

While the traditional use of hexagonal and square-shaped pixels is still present (see Fig. 8.2 upper row), the utilized pitch size was reduced to reflect the potential for higher spacial resolutions. SiMPl5 only features pitch sizes of 50 µm and two different gap sizes, namely the p-gap (PG) and high-field-gap (HG). Due to the nature of a desired single pixel readout, the previously common p^+-topside implant is now structured, resulting in the additional gap between two adjacent p^+-topside implants. The HG is comparable to the gap of previous SiMPl batches, depicting the effective gap between two neighboring high-field regions. Values for PG are ranging from 2 µm to 4 µm and HG sizes vary between 5 µm and 15 µm.

The majority of the chips located on the wafer feature a single 16x16 array, as depicted in the upper row of Fig. 8.2, with copper pads deposited on each pixel of the array as under bump metalization layer. The array also contains an aluminum grid which can be contacted directly, as well as an outer guard ring. Backside contacting and consequent biasing is not achieved by the cutting edge but via a sophisticated contact connected to an implant reaching towards the backside.

These chips can be found in one of four variations, depending on their number of contacting pads towards the upper edge of the chip. The variation depicted in Fig. 8.2 is one containing contacts to all three features, namely biasing, guard and grid. The main purposes of the latter is to alleviate the impact of ionizing radiation damage within the gap region as will be explained later. While the biasing contact is always present, different variations of the layout can omit the means for contacting the guard or grid in four different combinations for testing purposes. Thus, the impact of one of these components, like the guard ring can be investigated by comparison of arrays with and without.

The intended purpose of these chips is flip-chipping to the dedicated active quenching readout electronics via the pads located on the pixels. Additional bumps can be placed on the 29 long copper lines next to the array, which end in easily accessible contact pads on the left edge of the chip. These allow further contacting of the first testing iteration of electronics for purposes of e.g. power supply and general operation.

Contacting of individual pixels in such arrays for testing is rather difficult by means of a probe station, due to the small central pad diameter of roughly 30 µm, in addition to being unfeasible if the entirety of the array needs to be investigated. For this reason, arrays with a connected topside implant were designed and also placed on the SiMPl5 wafers. The two different variations can be seen in the lower row microscope photographs of Fig. 8.2. All of these chips feature four identical arrays with a specific gap combination written in the central left region of the chip and corresponding to the same gap combinations found on the previously discussed chips. The left one depicts the "four contact" layout, due to the four contacting possibilities for each array. Three of these four are identical to the ones explained above, namely backside bias, guard and grid with the addition of a second copper grid as means of connecting all pixels of the array, effectively creating a device similar to a classic SiMPl array. It has to be noted, however that these arrays feature a drastically reduced vertical bulk resistor compared to classic SiMPl arrays and are therefore not capable of passive quenching.

The "three contact" layout on the right hand side, omits the additional copper grid and makes use of the aluminum grid located in the gap area of the array for connection of the individual pixels, thus requiring one less contact. This layout can be considered more feasible for photon emission microscopy measurements as the view on the array is not blocked by the additional copper grid. Both layout variations offer a means of investigating the preliminary quality of the SiMPl5 wafers without the need for sophisticated readout electronics and flip-chipping.

8.2 Static test devices

In the course of this thesis, novel devices, labeled "static test devices" were developed and will be presented in the following.

The main idea of this design was to enable two different things: First, offer a means

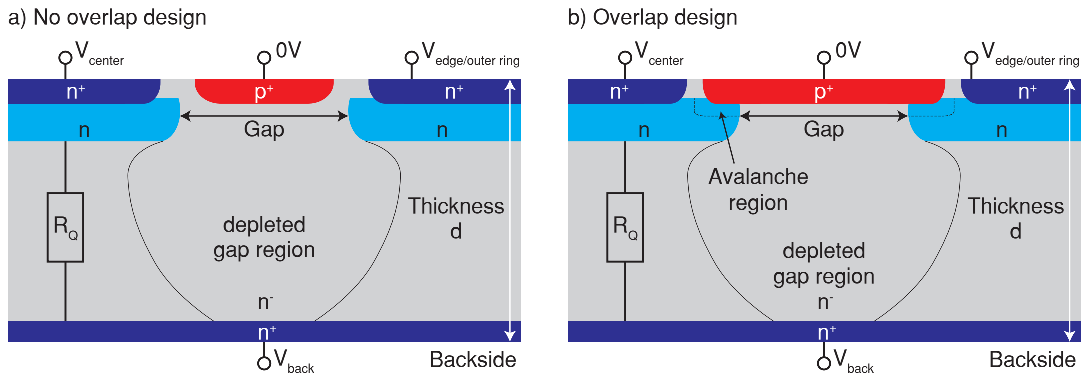

Figure 8.3: Schematic cross-section of the layout of the novel static test devices. The design is reminiscent of the layout of the static simulation procedure of Synopsys with added n^+-implants to provide a means to directly contact the deep n-implant and thereby R_Q within the bulk. Two different cases were implemented, depending on the size of the p^+-topside implant in the gap region between two pixels. In a) the implant is limited solely to the gap area, leading to no overlap between the deep n and p^+-implant, thus being labeled "no overlap"-case. In b), however, the implant is extended to allow an overlap and thereby the formation of a high-field region, resulting in the label "overlap"-case. Designs are not to scale.

of directly accessing the bulk integrated quench resistor as this was not experimentally possible up to this point, since the method of applying a forward bias and extracting the quench resistor in conventional SiPMs is not applicable here, due to R_Q only forming under reverse bias. Second, provide an opportunity to directly compare the static simulations with experimental data to assess the overall quality of the static simulations.

The design of the static test devices is derived from the layout of the static simulations performed in Synopsys TCAD, as seen in the schematic cross-section in Fig. 8.3. In order to access the deep n implant and thereby R_Q, the p^+-topside implant was limited to the gap region and an additional n^+-auxiliary implant for contacting ("center") was included. To simulate a pixel within an array, the design was chosen to mimic the flower layout of the SiMPl arrays in case of hexagonal pixels and the 3x3 layout of the square-shaped ones, thus ensuring the central pixel to be placed under potential conditions correlating to an array pixel. For symmetry purposes and direct correspondence to the simulation layout of the static test devices, the edge pixel - or outer ring in case of the simulations - also included an auxiliary n^+-topside contact, however in contrast to the simulations, the physical devices do not offer any means of direct contacting of these edge pixels. This should not pose any issue, however, as the applied backside potential will reach through the bulk towards the topside, leading to the desired potential conditions.

Finally, two different designs were developed, depending on the condition of the p^+-implant limited to the gap region. The first design places the implant solely within gap so that no overlap between p^+ and deep n can occur, thus inhibiting any potential for an avalanche process taking place (labeled "no overlap"). In contrast, the second design extends the p^+-implant far enough to allow the formation of a high-field region and thus avalanche breakdown without running the risk of creating an lateral breakdown between p^+ and n^+, as sufficient technological simulations were carried out to determine the minimum safe distance between these implants (labeled "overlap").

Microscope photographs of the final chips featuring these devices can be seen in Fig. 8.4. The left hand photograph depicts the variation found on SiMPl4 wafers with a total

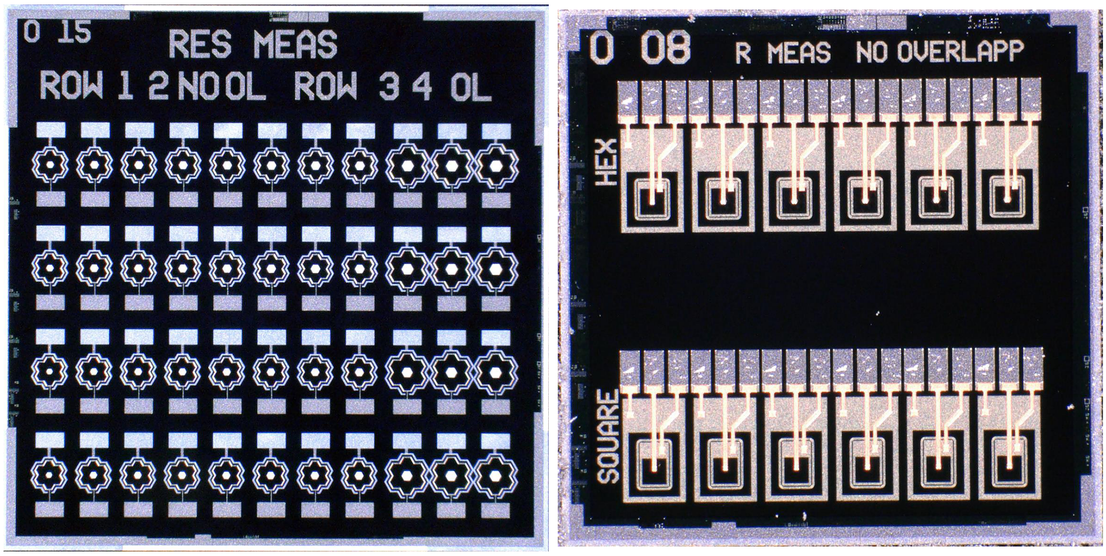

Figure 8.4: Microscope photographs of chips containing the novel static test devices. The left hand side shows the case for SiMPl4 wafers with a total of 44 structures per chip with an even split between the overlap cases. Contacting of the backside and p^+-implant is achieved via the aluminum pads while the central pixel requires direct contacting of the central aluminum deposit. The variation of SiMPl5 wafers is depicted in the right hand side photograph, featuring hexagonal and square-shaped pixels. Contrary to SiMPl4 all necessary contacts are accessible via the outer pads and the overlap cases are now separated on chip level. See text on detail regarding the pitch and gap sizes.

of 44 structures per chip, 22 with the "overlap" and the other 22 with the "no overlap" design. The devices provide two aluminum pads for contacting the p^+-implant located around the central pixel in the gap region and the backside via a reach-through implant in the bulk. The central pixel is read out by contacting its topside directly, as indicated by the aluminum in the center. All chips are identical and include various pitch/gap combinations with pitch sizes of 100 µm and 130 µm with varying gaps ranging from 8 µm to 30 µm, depending on the pitch. The static test device chips are located on different areas of the wafer and amount to a total of 9 chips per wafer.

In the case of SiMPl5, seen on right hand side of Fig. 8.4 only 12 structures per chip are present, the upper half exhibiting hexagonal pixel, while the lower half is design with square-shaped ones. The general layout and contacting scheme is similar to that of the SiMPl4 variation except that the central pixel can be accessed via a sophisticated contact thanks to the additional copper lines. The distinction between the overlap cases now takes place on chip level, as stated by the label at the upper chip edge, leading up to a total number of 28 chips per wafer. Analogous to the array design, only a pitch size of 50 µm was included with gap sizes varying between 8 µm and 30 µm, depending on the shape of the pixels.

The wafers of the SiMPl3 batch do not feature any static test devices.

8.3 Diodes

The diodes utilized in this study consisted of various different sets in terms of production. One set is placed on the SiMPl production wafers for quality testing purposes and is therefore specific to the individual SiMPl wafer and its technological characteristics, such

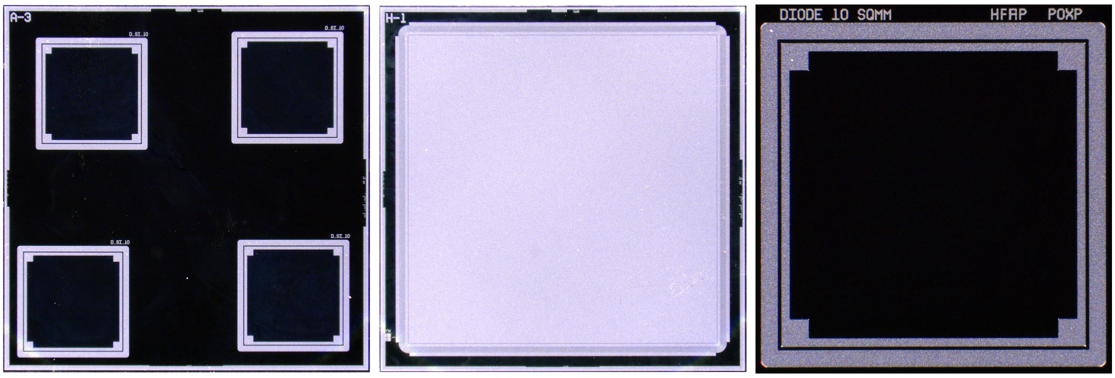

Figure 8.5: Microscope photographs of diode chips and structures utilized in this study. The one shows a chip featuring four smaller diode structures with $A = 10$ mm^2, with a zoom in of a single structure seen in the right photograph. A chip with only a single larger structure with $A = 100$ mm^2 is depicted in the central photograph with the central area covered by aluminum and featuring a multiple guard ring structure opposed to the single guard ring of the smaller counterparts.

as the sensor thickness and implant parameters of the p^+-implant. Diodes of this set include the ones found on the wafers of all three SiMPl batches in question.

Furthermore, two additional wafers, consisting solely of diodes were manufactured to provide additional devices for radiation hardness studies. These were processed on thinned SOI wafers with their thicknesses chosen identical to their respective SiMPl batches, namely one for SiMPl4 and the other for SiMPl5.

Regardless of the respective batch, all diodes feature a n-type bulk, a n^+-backside and a p^+-topside diode implant. Contacting of the backside is achieved by a cutting edge surrounding the entire chip. In addition, guard ring structures are located on the topside, found in either a single guard ring or multiple guard ring variation. The diode chips can feature either a single diode structure with larger cross-section or multiple smaller ones as shown in Fig. 8.5. The microscope photographs show examples of said diode chips, the first one featuring four smaller diode structures ($A = 10$ mm^2), shown in more detail in the third photograph while the second shows a single larger one ($A = 100$ mm^2). In the case of the smaller devices, only a single guard ring can be observed in contrast to the multiple guard ring structure of the larger diode. A total of four different diode sizes can be found across all diode sets with cross sections of 10 mm^2, 25 mm^2, 36 mm^2 and 100 mm^2. In total, 102 diode chips across all sets, resulting in 166 diode structures were utilized in this study.

They can be used to determine the leakage current levels as well as the effective doping concentration of the wafer and are essential for the investigation of the impact of radiation damage on the wafer material.

8.4 Irradiation facilities and doses of devices

The neutron irradiations of this study were performed at the 250 kW TRIGA Mark II research reactor of the Jožef Stefan Institute (JSI) in Ljubljana, Slovenia. The reactor can provide a flux of fast neutrons ($E > 100$ keV) up to $5{\cdot}10^{12}$ n/(cm^{2}s) with a continuous neutron energy spectrum. According to [112] the hardness factor of the NIEL hypothesis was found to be $\kappa = 0.88 \pm 0.05$. Further information regarding the reactor, its layout, neutron fluxes for each individual irradiation tube and more detailed energy spectra can be found in [113]. The uncertainty of the experienced irradiation fluence can be approximated to roughly 10% [114].

The choices regarding the irradiation doses and fluences were made according to the estimates for two of the possible experimental applications for SiMPl devices as tracking detectors, namely the International Linear Collider (ILC) and the Compact Linear Collider (CLIC). The estimates for expected radiation exposure for devices located closest to the interaction points within the barrel region of the detector can be found in the respective Technical and Conceptual Design Reports [3, 9].

In terms of non-ionizing radiation damage, the following annual fluences Φ_a, given in 1 MeV neutron equivalent according to NIEL scaling were estimated:

$$\Phi_a(\mathrm{ILC}) \approx 10^{11}\,\frac{\mathrm{neq}}{\mathrm{cm}^2}/\mathrm{year} \qquad \text{and} \qquad \Phi_a(\mathrm{CLIC}) \approx 4\cdot 10^{10}\,\frac{\mathrm{neq}}{\mathrm{cm}^2}/\mathrm{year}\,.$$

The ionizing radiation damage is given as Total Ionizing Dose (TID) and is gauged to amount to

$$\mathrm{TID}_a(\mathrm{ILC}) \approx 1\ \mathrm{kGy/year} \qquad \text{and} \qquad \mathrm{TID}_a(\mathrm{CLIC}) \approx 200\ \mathrm{Gy/year}\,.$$

According to these numbers, equivalent neutron fluences were chosen for this study, in order to account for a 10–15 year operation duration for both experiments and even beyond for the purposes of investigating the overall radiation hardness of the devices and the influence of type inversion on the SiMPl performance. Thus the DUTs utilized in the radiation hardness study, including diodes, SiMPl arrays and static test devices were irradiated with the following neutron fluences, given in 1 MeV neutron equivalent:

$$\Phi_{neq} = 5\cdot 10^{9},\ 1\cdot 10^{10},\ 5\cdot 10^{10},\ 1\cdot 10^{11},\ 5\cdot 10^{11},\\ 1\cdot 10^{12},\ 5\cdot 10^{12},\ 1\cdot 10^{13},\ 5\cdot 10^{13},\ 1\cdot 10^{14},\ 5\cdot 10^{14}\,.$$

In terms of ionizing radiation damage, no actual irradiation was carried out as will be explained in Sec. 9.4.4, however simulation studies were performed, dealing with the potential impact of ionizin radiation damage on SiMPl devices up to TIDs greatly surpassing the estimated amount for 10 to 15 years of exposure in both of the considered experiments.

After irradiation, all devices were stored at approximately $T = 258$ K during storage and transport, to avoid any uncontrolled annealing taking place. Before measurements, all DUTs underwent the controlled annealing scenario of $(80\mathrm{min}, 60°\mathrm{C})$ as established in Sec. 4.1.4.4, thus providing a stable environment in regards to the impact of room temperature annealing in the time frame of the measurements.

Finally, the author would like to acknowledge that this project has received funding from the European Union's Horizon 2020 Research and Innovation programme under Grant Agreement no. 654168.

9 Detailed simulation and experimental studies of SiMPl and DSiMPl

This chapter will deal with the main simulation and experimental studies regarding the most recent SiMPl iterations. First, it will focus on the development process of the newest batches, namely SiMPl3, SiMPl4 and SiMPl5 and their first characterizations and feasibility studies. Due to the possible applications of SiMPl device, an entire section will also deal with the topic of radiation damage and its impact on said SiMPl devices. Afterwards, the first electron detection efficiency measurements performed with SiMPl will be presented. Finally, the results of an investigation pertaining to the cause of one of the major issues afflicting the batches of this study will be discussed.

9.1 Third prototype - SiMPl3

Following the first feasibility studies of the earlier SiMPl prototypes (see Sec. 6.3), additional iterations of devices which improve upon the performance and deal with the issues and shortcomings seen in the previous batch, were scheduled for development. In a first step, the main problems observed for SiMPl2 devices were being focused on. These issues included the overall high dark count rate and the regular occurrence of edge breakdown within the arrays.

Hence, the main goal of the next iteration of SiMPl devices, labeled SiMPl3, was the reduction of these effects by improvement of certain technological parameters, as will be explained in the following sections. In contrast to the previous batch, SiMPl3 was produced on standard non-SOI wafer thickness material ($\sim$ 700 µm), as the main technological aspects for investigation did not require a nominal quenching behavior and since the required material was limited and not available at the time of production.

The first step in this approach was a thorough simulation study of the impact of the relevant parameters via process and device simulations. Afterwards, the production of SiMPl3 based on the findings of the simulation studies was carried out and the devices were characterized and the results were compared to the simulations.

9.1.1 Simulation studies of SiMPl3

The main aspect of this simulation study lies in the optimization of parameters like the energy and dose of the individual implants forming the high-field (HF) region as well as the implantation angle and the angle of the photo resist edge. In addition, the annealing conditions of the deep n implant also play an important role, as sub-optimal choices can lead to inhomogeneous electric field distributions in the HF region and potential edge breakdown. In a final step, the resulting profiles can be implemented in Monte Carlo simulations of the Geiger efficiency to estimate their feasibility in said aspects.

9.1.1.1 Technological aspects

Edge breakdown

As mentioned above, edge breakdown within the array was one of the major issues for the first SiMPl devices. It describes phenomenon of the avalanche arrays exhibiting a higher Geiger efficiency in the edge areas compared to the center of the cell, thus leading to an early breakdown at lower bias voltages. Even at voltages sufficient for the rest of the cell to enter Geiger mode, the edge region will dominate the avalanche generation, due to the increased Geiger efficiency and the need for recovery of a cell. An example of an array affected by edge breakdown is shown in the photo emission microscopy photograph in Fig. 9.1. The overall warmer colors indicate a higher amount of light emission and thus increased breakdown activity in the edge regions, thereby reducing the effective area of a cell.

Edge breakdown in the high-field region is caused by an increased Geiger efficiency in the edge area, which, in turn, is a direct result of the electrostatic potential and conversely the electric field distribution in said region after applying an external bias. The electrostatic potential can be derived via the Poisson equation (3.1) and is dependent on the charge density and thereby doping concentration of the n and p regions. Figure 9.2 depicts the edge region of two different doping profiles of the SiMPl deep n implant with a) optimized and b) non-optimized parameters, obtained via process simulations. In both cases a trace of phosphorus towards the surface can be seen where it will make direct contact with the p^+ implant. In the case of a), this trace is more distinct compared to b), meaning that a higher impurity concentration is present. Considering the Poisson equation, this will lead to increased electrical fields in the case of a) and thus increase the risk of edge breakdown occurring, while a profile like b) will result in a homogeneous breakdown behavior over the entire cell.

The resulting electric field distribution along the x-direction of the HF region after all additional implantations for both cases can be seen in Fig. 9.3, where the edge is located at $X \approx 11$ µm. The electric field data was extracted via device simulations

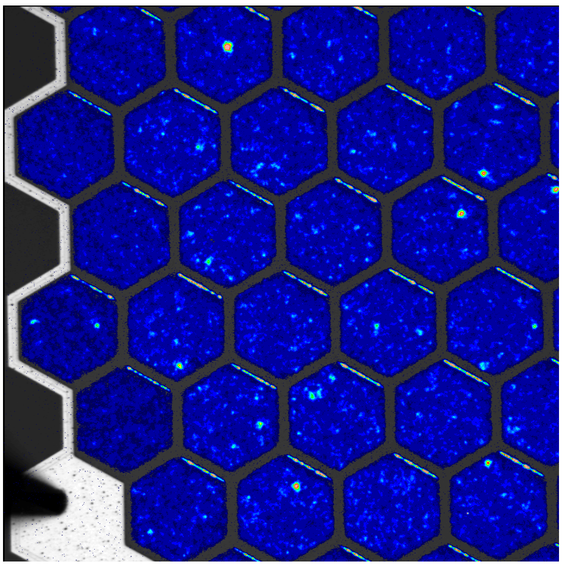

Figure 9.1: Example of a SiMPl array affected by edge breakdown. The photo emission microscopy measurement shows a higher activity in the edge regions, indicated by the warmer colors compared to the rest of the cell.

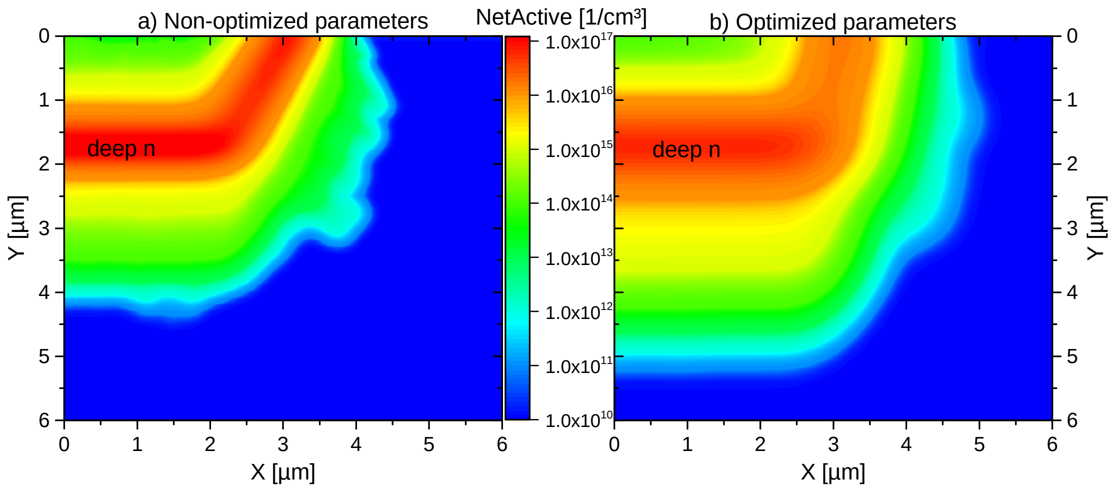

Figure 9.2: Juxtaposition of the resulting deep n profile after annealing with a) non-optimized and b) optimized technological parameters. Both plots depict the same edge region of the deep n implant while the color coding represents the active doping concentration. In a) the relevant technological parameters, like the photo resist angle and implant angle were chosen without optimization in mind, resulting in a very distinct trace of the n implant towards the surface with high particle concentration. This trace will later result in local electric field peaks (see Fig. 9.3) and thus edge breakdown. A case with optimized angles is shown in b), where the trace is less pronounced, thereby not leading to edge issues.

after applying an operational voltage 1 V above breakdown. The increased phosphorus concentration within the trace will lead to a peak in the electric field (red line) causing an increased Geiger efficiency compared to the rest of the cell. In the case of optimized parameters, uniformity along the entire HF region can be observed (blue line).

In order to avoid a doping profile similar to Fig. 9.3 crucial parameters for the deep n implant, including the ion beam implantation angle, the photo resist angle and the annealing scenario have to be studied and optimized.

Photo resist and implantation angle

The structuring of the areas affected by implants during the wafer processing is usually achieved via the deposition of a photo resist which absorbs the incoming particle beam, thus effectively limiting the area of the final doping profile. In the course of this study it was found that two of the most important parameters for the issues at hand were the angle of the incoming particle beam Θ_{ion} of the resulting deep n implant as well as the angle of the photo resist edge Θ_{res} utilized to structure said implant.

In terms of these angles, a doping profile like the one depicted in Fig. 9.2a) is caused if flat angles are chosen. For Θ_{ion}, this means angles deviating from a perpendicular particle beam ($\Theta_{ion} \neq 0°$) and in the case of Θ_{res}, a photo resist edge with $\Theta_{res} < 90°$. Thus, a perpendicular ion beam with $\Theta_{ion} = 0°$ impinging on a $\Theta_{res} = 90°$ photo resist would be preferred in order to achieve profiles not resulting in edge breakdown.

Hence technology and device simulations explained in Sec. 7.1 were performed to determine a safe parameter space. Synopsys TCAD incorporates the means for numerical (Monte Carlo) simulations. This aspect is of great importance, since analytical models do not describe channeling of the incoming particle beam to a satisfactory degree. Channeling is the crystal lattice orientation-dependent effect of the ion beam reaching

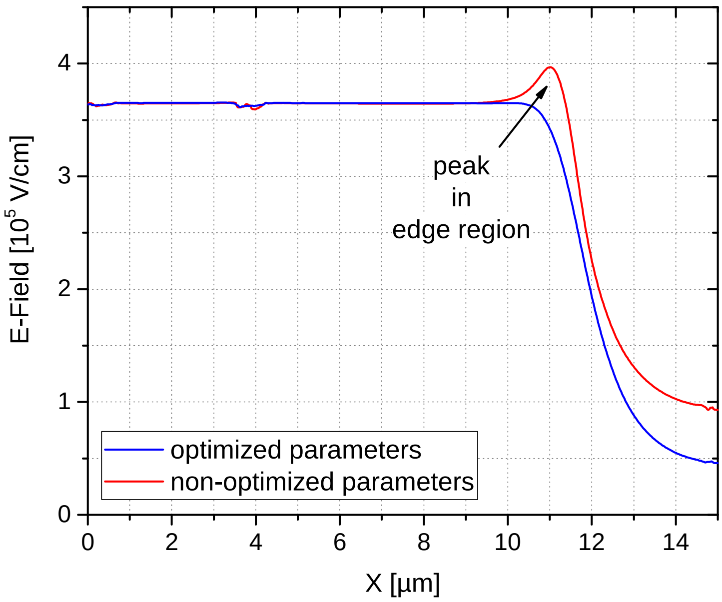

Figure 9.3: Electric field distribution of the high-field region in radial direction. The edge of the high-field region is located close to $X = 11$ µm, where in case of non-optimized technological parameters (red line), a peak in the electric field distribution can be observed. This peak stems from non-optimized deep n profiles as seen in Fig. 9.2a) and will inevitably result in edge breakdown.

far higher ranges within the silicon lattice. This effect can occur if the beam orientation coincides with particular crystal axes and is also dependent on the beam energy. However, already small deviations from these perfect axis orientations will lead to strong discrepancies in the implantation depth, thus channeling should be avoided to ensure a homogeneous depth profile of the implant.

Therefore, channeling limits the choice of Θ_{ion}, as it will take place in the utilized material for an ion beam perpendicular to the surface $\Theta_{ion} = 0°$. As a result, a trade-off between a steep ion beam angle and the avoidance of channeling has to be found.

Various deep n profiles after annealing for different values of Θ_{ion} ranging from 0° to 7° are depicted in Fig. 9.4. The impact of channeling is visible for $\Theta_{ion} = 0°$ (red line) where an increased propagation distance of the phosphorus particles results in a broadened profile with an overall lower peak concentration by a factor of 3 compared to $\Theta_{ion} \geq 2°$, where channeling is suppressed. While $\Theta_{ion} = 1°$ features a similar peak concentration of $8 \cdot 10^{17}$ cm^{-3} (compared to $9 \cdot 10^{17}$ cm^{-3}) and peak position, a distinct tail towards higher depth values is visible, indicating partial channeling taking place. Hence, $\Theta_{ion} = 2°$ was chosen to avoid channeling while aiming for steep implantation angles.

In a similar fashion, the angle of the photo resist edge has to be chosen carefully. The structuring of the photo resist can be achieved by chemical etching or by exposure to certain wavelengths of light, depending on the material. The smaller Θ_{res}, the higher becomes the risk of a more pronounced trace of the deep n implantation due to the decreasing thickness and stopping power along the photo resist edge (see Fig. 7.1). Thus a Θ_{res} as close as possible to 90° is required in order to achieve the majority of the phosphorus dose being deposited in the desired depth instead of the trace in the edge region. The final values for Θ_{res} depend on the photo resist material and method utilized for structuring but will never result in a perfect angle of $\Theta_{res} = 90°$. In the case of SiMPl,

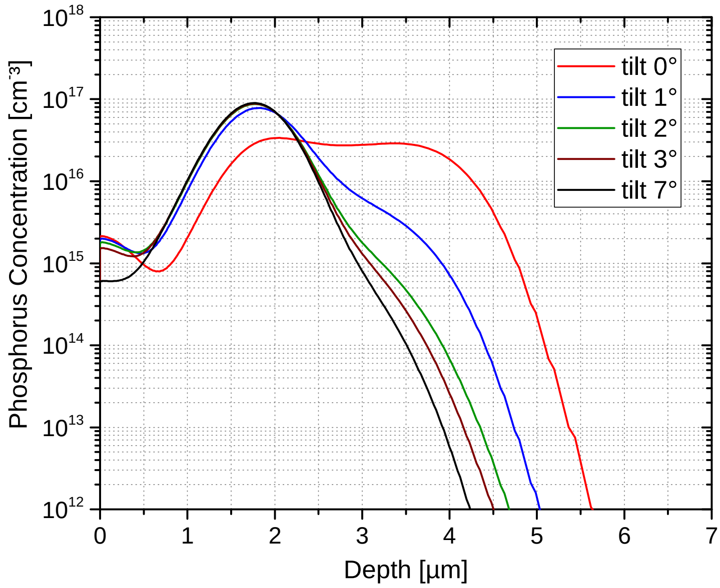

Figure 9.4: Impact of channeling on the deep n doping profile. Simulated cases for different implantation or "tilt" angles Θ_{ion} are shown as different colored lines, ranging from 0° to 7°. The impact of channeling is clearly visible for $\Theta_{ion} = 0°$, as the profile is broadened and reaches deeper into the silicon (see text).

the steepest achievable photo resist angles were measured to be $\Theta_{res} = 85° \pm 3°$.

In this context, various simulations regarding different possible combinations of Θ_{ion} and Θ_{res} were carried out and the resulting electric field distribution (and breakdown probabilities) investigated to find feasible values and combinations resulting cases like Fig. 9.2b). The results will be discussed in Sec. 9.1.1.2 after the introduction of the different annealing procedures, since the impact of all crucial parameters on the resulting breakdown behavior is interlinked.

Annealing procedure

After the implantation of a specific doping profile it still requires undergoing an annealing scenario. The main reason for this annealing is providing the implanted ions the means to traverse the lattice and form new stable defects within, thereby changing their electrical properties (see Sec. 4.1.3). Hence this procedure can also be referred to as the electrical activation of the implanted ions. In addition, depending on duration and temperature, the ions will be able to diffuse into the lattice, thus resulting in a drastic change of the doping profile compared to before.

An important technological aspect during the production of SiMPl3 was the optimization of the deep n annealing scenario as it can have multiple impacts on the performance of the SiMPl devices. First, it can directly influence the edge breakdown, as ion diffusion will affect the trace of the deep n implant. This way edge breakdown can be directly impacted and completely avoided with a proper choice of annealing parameters or, on the contrary, enhanced if no optimization has taken place. Furthermore, depending on the annealing parameters, the shape of the electric field along the depth of the device and therefore along the HF region, can be adapted. Finally, the resulting leakage current withing the HF region can be reduced by choosing a proper annealing scenario, as annealing also allows otherwise stable defects to recombine with their counterparts or diffuse out of the material, thus reducing the amount of generation centers.

Table 9.1: Summary of the parameters for the various annealing scenarios of the deep n implant. The temperature T, duration t_i and atmosphere during annealing are given. The different annealing durations can be distinguished via $t_1 < t_2 < t_3 < t_4$. The labels "inert", "wet" and "dry" translate to a N_2, H_2O and O_2 atmosphere, respectively.

Annealing scenario	Temperature [°C]	Duration	Atmosphere
#1	950	t_1	inert
#2	950	t_4	inert
#3	1000	t_1	inert
#4	1000	t_4	inert
#5	950	t_1	wet
#6	900	t_2	wet
#7	950	t_1	dry
#8	950	t_4	dry
#9	1000	t_1	dry
#10	1000	t_3	dry
#11	1050	t_1	dry
#12	1050	t_3	dry

Since previous SiMPl iterations suffered from edge breakdown, a rough estimate of potentially problematic parameter spaces for annealings could be obtained and as a result, 12 different annealing scenarios for investigation were derived. These scenarios vary in terms of annealing temperature T, duration t and atmosphere during the procedure and will be labeled by their numbers with "annealing #1 – #12" in the rest of this study. While the individual durations t_i cannot be disclosed, the other parameters are summarized in Table 9.1. The label "inert" denotes an atmosphere of N_2 during annealing, "wet" a H_2O atmosphere and "dry" O_2.

The impact of the annealing scenario on the deep n profile was already included in the simulations shown in Fig. 9.2 and Fig. 9.3, as they were part of the optimization procedure. As explained above, the combined results will be presented in Sec. 9.1.1.2. In general, a higher temperature enables the formation of additional complexes in the lattice, as certain temperature thresholds are reached. Defect formation is also affected by the atmosphere through saturation of specific atoms, making them readily available in the formation process. A longer duration allows for increased diffusion, usually resulting in broadened doping profiles.

An analysis of the electric field in the direction of the depth, i.e. perpendicular to the surface, also reveals deviating results, depending on the applied annealing scenario, as illustrated in Fig. 9.5. Here the absolute electric field distribution within the homogeneous middle part of the HF region is depicted after different annealing cases for the identical implantation parameters. While all displayed cases are able to reach the required field strength of roughly $3.5 \cdot 10^5$ V/cm, the shape can differ vastly. In general higher overall fields increase the breakdown probability, in turn resulting in potentially higher PDE values, however the homogeneity also needs to be taken into account. Cases like the one shown for annealing #12 do offer a higher peak field strength but it decreases linearly over the width of the HF region, compared to cases like annealing #4 where the electric field is smaller but nearly constant within the entire HF region. The latter will yield overall higher Geiger efficiencies, as charge carriers created in the second halt of the HF area will still have a high possibility of triggering an avalanche, whereas the

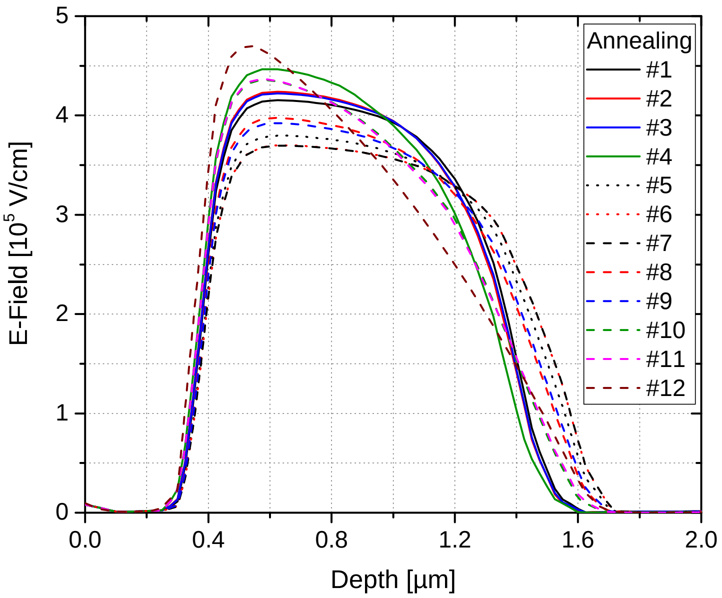

Figure 9.5: Electric field distribution of the high-field region along the depth. The results for all 12 annealing scenarios are shown as different colored lines with the inert cases being solid, the wet ones dotted and the dry cases dashed. A homogeneous profile, like seen for annealing scenarios #1 and #4 is preferred over a linearly decreasing one, as represented by #12 (see text).

former only provides high trigger rates if charges are created close to the surface (or peak region in general). Thus, annealing scenarios leading to results as seen for annealing #1 and #4 are preferable.

Finally, the parameters of the annealing scenario will have a direct impact on the measured leakage current within the HF region. This current needs to be as low as possible in order to ensure optimal device performance as thermal generation can also trigger an avalanche breakdown. Due to the traversal of the phosphorus ions of the deep n implant through the surface area, a high concentration of lattice defects caused by said ions can be expected. The annealing provides a means of "healing" those defects and can thereby reduce the amount of remaining generation centers if chosen properly.

As seen in Sec. 4.1.4 overall higher temperatures and durations of annealing procedures will decrease the amount damages in the lattice more effectively, however, it needs to be taken into account, that the temperature scale for implantation annealings differs vastly from the ones utilized in radiation annealing. The choice is consequently not trivial as higher temperatures are required in the former, but these would also enable previously stable and electrically inactive defects to interact with other defects in the lattice, thus potentially forming new generation centers.

9.1.1.2 Monte Carlo simulations of the Geiger efficiency

After extraction of the electric field distribution of various technological parameter combinations, the results can be integrated into Monte Carlo simulations in order to derive their Geiger efficiencies for different bias voltages. The general procedure of these simulations was already explained in detail in Sec. 7.3.

Only the most promising technological parameter sets in terms of implant parameters and angles of the photo resist edge were included, according to the simulation procedures shown above. However, it was decided to include all 12 annealing scenarios in order to

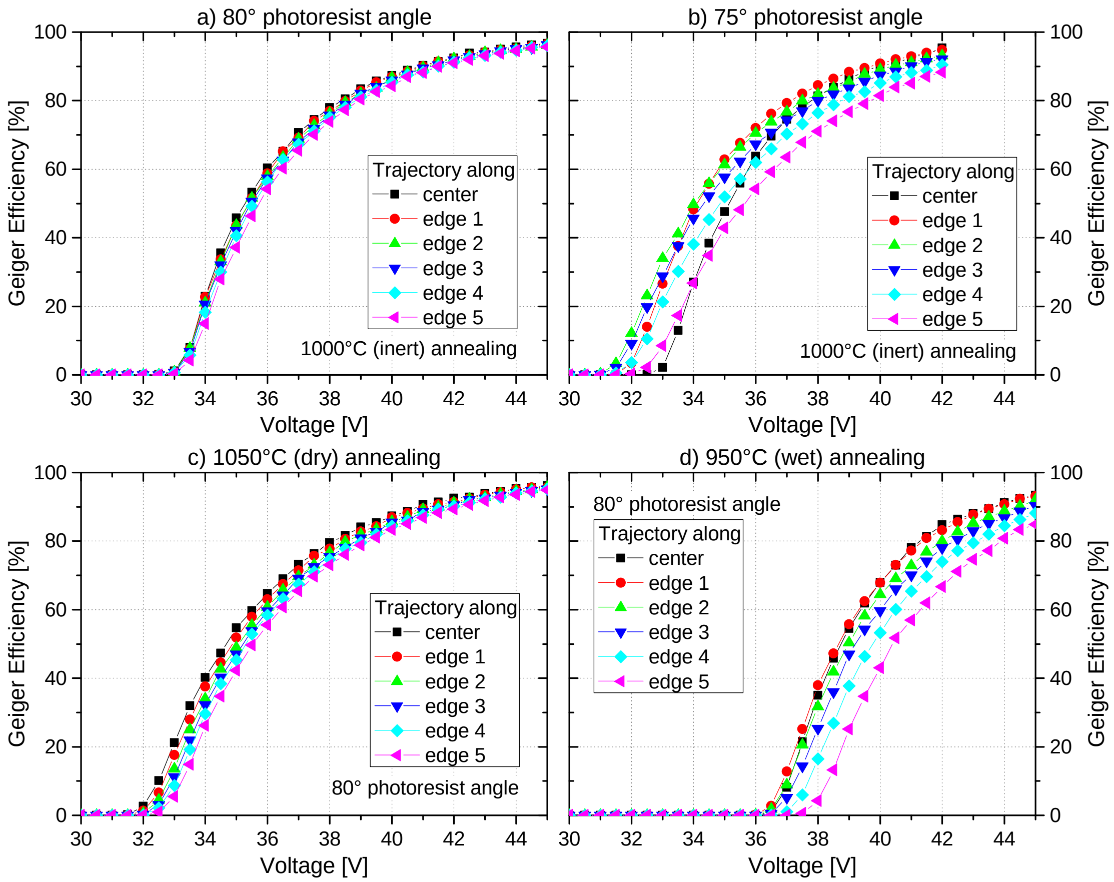

Figure 9.6: Monte Carlo simulation of the Geiger efficiency for different simulated high-field profiles of SiMPl3. The different symbols and colored lines each represent a different location of the simulated trajectory of the initially created charge carriers. The various cases labeled "edge" are each located around the edge region of the HF area, while "middle" is located in the center of the HF region. In cases a) and b), the impact of Θ_{res} is showcased for an identical Θ_{ion} and annealing scenario. The impact of the annealing scenario can be seen in c) and d), in which Θ_{res} and Θ_{ion} were identical.

allow cross-checking between the simulation framework and the experimental results. Thus, the most promising parameter sets were incorporated in the process simulations for every annealing scenario, and afterwards Monte Carlos simulations of the Geiger efficiency for all cases were carried out.

Exemplary results of the simulations are depicted in Fig. 9.6, highlighting the impact of the different parameters discussed above. In order to examine the potential of edge breakdown, the simulations included multiple points of initial charge generation within the HF region. These are labeled as "middle", characterizing the homogeneous center of the HF area and "edge x", representing various coordinates within the edge region. Afterwards the Geiger efficiency is plotted for different bias voltages for the aforementioned trajectories.

A choice of $\Theta_{res} = 80°$, $\Theta_{ion} = 2°$ and annealing #4 ($T = 1000°\mathrm{C}$) will result in the simulation data shown in a). Here an uniform breakdown behavior can be seen, meaning that the trajectories along the edge and central region of the HF region exhibit the same breakdown voltage and increase of the Geiger efficiency, thus suggesting no edge breakdown. The impact of Θ_{res} is exemplified if a) is compared to b), which featured the same annealing scenario but with a smaller $\Theta_{res} = 75°$. For this case, the edge trajectories have higher Geiger efficiencies compared to the center of the HF region and start the avalanche breakdown 1 V − 1.5 V earlier, which will manifest as edge breakdown. This also showcases the issue of the edge breakdown dominating the avalanche behavior even at higher voltage after the center of the cell is also able to initiate a Geiger discharge, as the Geiger efficiency of the edge region will always be higher.

Figure 9.6c) features identical parameters to a) in terms of Θ_{res} and Θ_{ion} but differs in annealing (scenario #12). In both cases edge breakdown can be ruled out, however in c) the edges exhibit slightly decreased efficiency values compared to the center. This is overall not detrimental to the device operation, however a case like a) is preferred due to the homogeneity and the resulting larger active area if the edges are not suppressed.

The impact of the annealing scenario for identical Θ_{res} can also be seen by comparing c) to d) (annealing #5), where the choice of annealing will cause edge breakdown. The influence of the annealing scenario, however, can be seen to be less severe compared to the impact of Θ_{res}, as the difference in breakdown voltage due to annealing is seen to be < 0.5 V. This trend could be observed for all utilized annealing scenarios.

In general, the impact of Θ_{res} and Θ_{ion} on the edge breakdown potential was found to be larger compared to the one stemming from the annealing scenario. A summary of the investigation pertaining to potential edge breakdown will be given with a comparison to the measured data in Table 9.2 in Sec. 9.1.2.

9.1.2 Measurements of SiMPl3

Following the extraction of all relevant technological parameters from the simulations, the production of SiMPl3 could be carried out. In total 12 wafers, one for each annealing scenario, were processed, with all other parameters being identical and chosen according the simulation results. All SiMPl3 wafers were characterized with the setups described in Sec. 5.2 and 5.4 with an ambient temperature of approximately 298 K.

9.1.2.1 Comparison to SIMS measurements

In order to ascertain the reliability of the simulated doping profiles for the utilized parameter space, the simulated data was compared to profiles obtained via secondary ion mass spectrometry (SIMS) measurements. In this procedure, the elemental composition of the surface layers including the HF implantations can be determined by sputtering the target area with a focused ion beam and analyzing the ejected secondary ions to obtain the doping profile.

Test structures, containing the p^+ and deep n located on all wafers of SiMPl3 were utilized and the profiles of both implantations for scenarios #3 and #12 were measured. The results and a comparison to the simulated data can be seen in Fig. 9.7.

In a) the results for the topside boron implant are depicted, which do not depend on the annealing scenario. An overall good agreement in terms of peak concentration and peak position between the SIMS data (blue) and simulation (red) can be seen. A slight discrepancy can be seen comparing the tail of the profile towards increased depths as the simulation performs slight overestimation in this regard.

A similar observation can be made in both cases of the deep n profiles in b). Specifically in the case of annealing #3 a distinct tale is visible in the simulations, whereas the SIMS data does not indicate a similar feature. This discrepancy could be attributed to an overestimation of channeling within the simulation framework, however all relevant parameters were chosen according to the findings of Fig. 9.4 and should thereby sup-

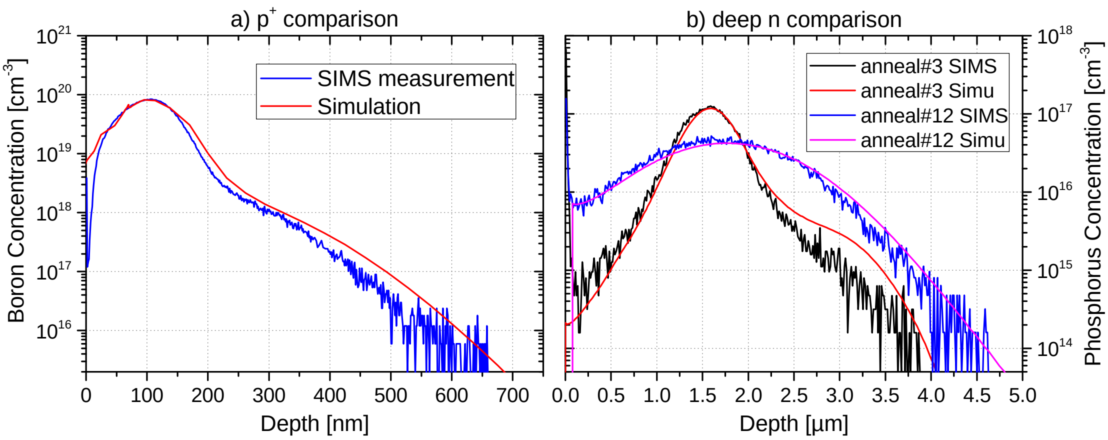

Figure 9.7: Comparison of the simulated and measured SIMS profiles for a) the boron (p^+) and b) the phosphorus (deep n) implants. In a), good agreement can be seen in the peak region, while the simulation slightly overestimates the concentration in the tail of the profile. In the case of deep n, the resulting profiles of two different annealing scenarios were investigated (#3 and #12). While an overall good agreement can be found for #12, a discrepancy can be seen for #3, where a more pronounced tail is featured in the simulation results.

press channeling. Another possibility lies in an increased error margin of Θ_{ion} resulting in angles which can enable channeling taking place.

In general, a satisfactory accordance between simulation and SIMS data was found to confirm the reliability of the simulation framework, however the observed discrepancies have to be taken into account when comparing later simulation data to measurements, as small deviations can possibly be attributed to them.

9.1.2.2 Current-voltage measurements

The prime focus of these measurements was the evaluation of the leakage current levels before breakdown, as well as the breakdown behavior within the individual pixels and on wafer level. For the purpose of the leakage current, HF diodes were utilized, which are normal diodes with the addition of the deep n implant, thus enabling avalanche breakdown at a sufficient bias voltage, similar to the SiMPl arrays. They are preferred in terms of current level evaluations due to the inclusion of a guard ring structure properly defining the measured volume. A total of 8 HF diodes were available per wafer.

The breakdown behavior can be extracted from the SiMPl array I-V-curves and multiple array chips located on different regions of the wafer, namely the upper and lower left and right areas were chosen to account for wafer level deviations.

Examples of various I-V-measurements of SiMPl3 arrays are displayed in Fig. 9.8. A comparison of the I-V-data of the same chip of each wafer can be seen in a). Depending on the annealing scenario, the breakdown voltage also changes, as the diffusion of the implanted ions directly impacts the resulting profile of the p-n-junction forming the HF region. A maximum difference between the two scenarios #7 and #12 of roughly 7.5 V can be observed. Furthermore it can be seen that the various annealings result in different current levels.

The data of all arrays of a chip of wafer #4 is shown in b), including 30x30, 10x10, double flower and flower structures. In all cases a very homogeneous breakdown voltage of approximately $V_{bd} \approx 32.5$ V can be observed. The different current levels before

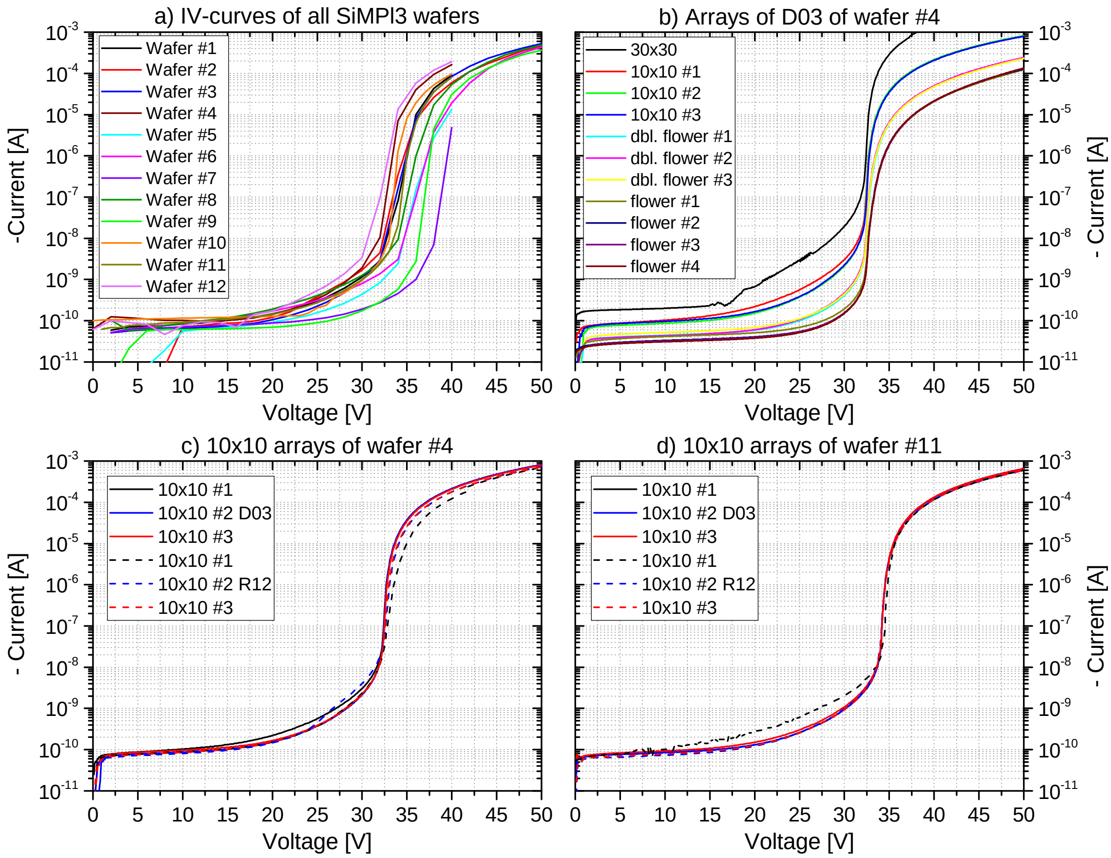

Figure 9.8: Measured I-V-curves of SiMPl3 arrays. In a) a comparison of 10x10 arrays of every wafer is shown, resulting in different V_{bd} depending on the annealing scenario. The data of all arrays of a single chip of wafer #4 can be seen in b), exhibiting a homogeneous breakdown behavior on chip level. c) and d) exemplify the homogeneity of V_{bd} on wafer level for cases #4 and #11, respectively. Here, the measured data of the 10x10 arrays of two chips located in different regions of the wafer is compared.

breakdown stem from the difference in array size.

In order to analyze the homogeneity of V_{bd} over the wafer, chips in different corner regions were evaluated. Examples for two of the most promising scenarios #4 and #11 are depicted in Fig 9.8c) and d), respectively. In both cases three 10x10 arrays of the two corner chips D03 (lower left) and R12 (upper right) were measured and are plotted as solid lines for one chip and dashed lines for the other. For annealing #4 a $V_{bd} \approx 32.5$ V and for #11 a $V_{bd} \approx 34$ V can be found. In both cases no deviation due to the position of the chip on the wafer can be seen.

The results of the current level measurements before breakdown, performed on the HF diodes are summarized in the second column of Table 9.2. Here the measured current per area for $V = 10$ V is listed for every annealing scenario. The lowest current levels can be found for case #9 with (6.3 ± 1.7) pA/mm^2, while the highest value of (25.8 ± 2.4) pA/mm^2 was observed for case #6. In general, lower absolute current levels and small deviations are preferred in terms of leakage current, thus cases like #1, #5, #6 and #12 are considered less promising compared to the rest.

9.1.2.3 Photon emission microscopy measurements

Even though it is possible to spot severe cases of edge breakdown by analyzing the current behavior, in general photon emission microscopy measurements are considered a more reliable method. The same devices characterized in the previous section were also investigated in this regard and examples of the measured results are depicted in Fig. 9.9.

Over all, two different behaviors could be observed. First, a nominal behavior is depicted in the upper row pictures for devices of wafer #4 with a 5x and 0.75x magni-

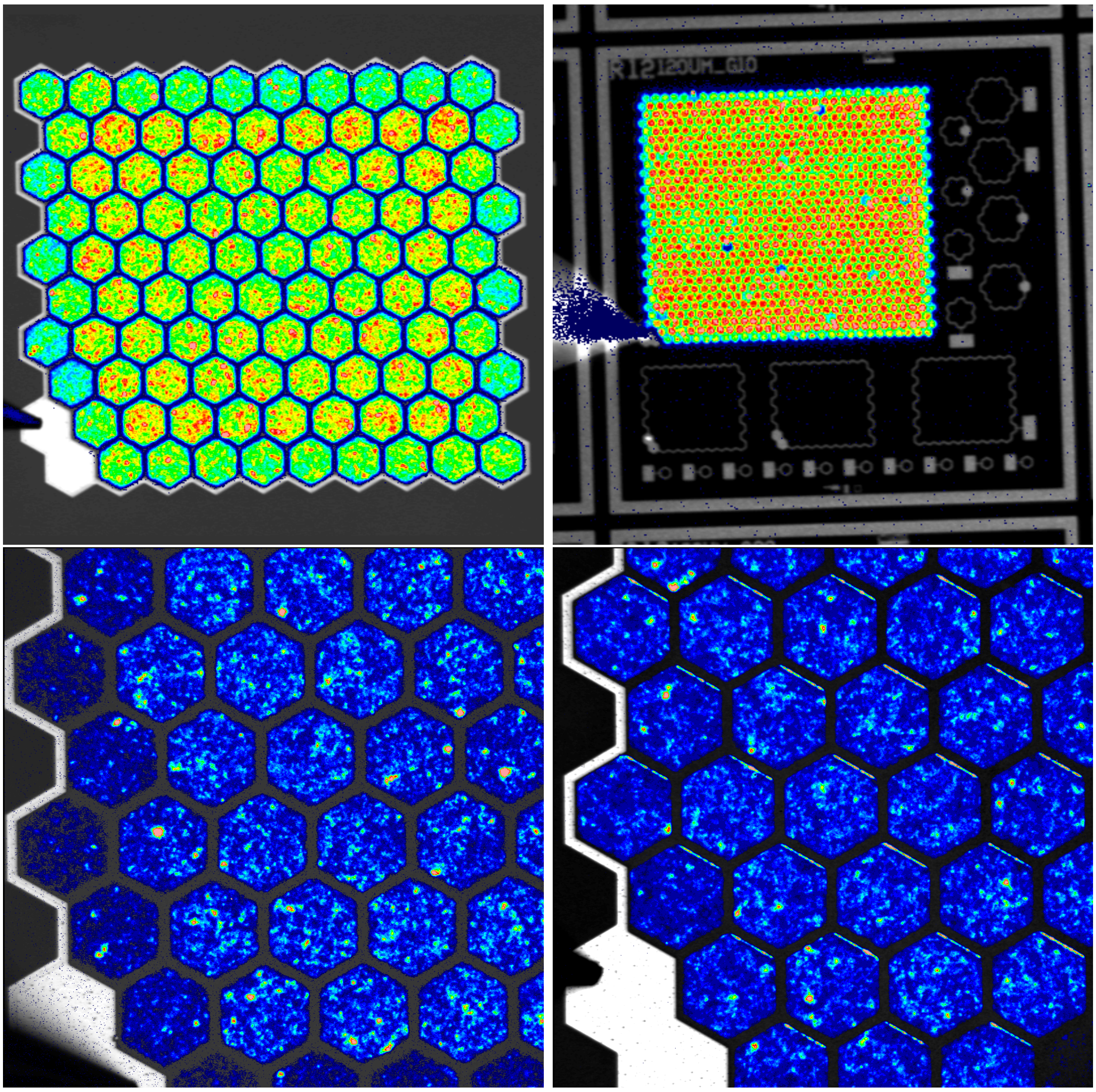

Figure 9.9: Examples of photo emission microscopy measurements of SiMPl3 arrays. The upper row depicts cases with nominal behavior for a magnification of 5x (left) and 0.75x (right) of annealing #4 chips. On the left, activity in all cells and the entire area of the cells can be seen, with the central cells exhibiting more activity due to the impact of OCT. On the right, a 30x30 array is shown, featuring multiple cells with hot-spots. The lower row showcases a magnification of 20x. Nominal behavior can be seen on the left (annealing #11), while a case with edge breakdown can be seen on the right (annealing #7). One or more edges of the cells exhibit far higher activity than the rest of the cell, thus reducing the effective area of the array.

Table 9.2: Summary of the mean HF diode current before breakdown and the edge breakdown status of all measured SiMPl3 wafers. If edge breakdown is labeled "yes", all investigated devices (all regions) of the corresponding wafer exhibited edge breakdown, while "partial" means that only certain regions of the wafer were affected. The last two columns show the prediction of the simulation studies for two different values of Θ_{res}. Measurements yielded $\Theta_{res} = 85° \pm 3°$.

Annealing scenario	Current/Area [pA/mm^2]	meas. edge breakdown	sim. edge $\Theta_{res} = 80°$	sim. edge $\Theta_{res} = 85°$
#1	13.4 ± 4.1	no	no	no
#2	10.1 ± 4.4	no	no	no
#3	8.5 ± 1.2	partial	no	no
#4	10.1 ± 0.6	no	no	no
#5	13.9 ± 8.7	partial	yes	no
#6	25.8 ± 2.4	partial	yes	no
#7	6.7 ± 1.3	yes	yes	yes
#8	8.1 ± 1.6	yes	no	no
#9	6.3 ± 1.7	yes	yes	yes
#10	9.4 ± 2.3	partial	no	no
#11	7.7 ± 1.0	partial	no	no
#12	13.1 ± 0.3	no	no	no

fication on the left and right, respectively. The hexagonal shape of the pixels is clearly discernible. The entire array exhibits light emission and thus activity with the central cells being more active due to optical cross-talk. The 30x30 array on the right features an over all homogeneous breakdown behavior, however roughly ten pixels show signs of hot-spots resulting in the affected cells being dominated by these spots. A small amount of such spot can be expected during production and is no need for concern.

The lower row depicts a magnification of 20x with the left hand side showing a corner of a 10x10 device of wafer #11. Nominal breakdown behavior can be observed with some localized areas with higher activity. This is an artifact of the limited exposure time during measurement, as longer times would result in a more homogeneous distribution as the avalanche occurs uniformly random within the active area.

The lower right hand side of Fig. 9.9 highlights a case (wafer #7) in which edge breakdown is prevalent. The upper right edge of all visible pixel exhibit a far higher avalanche activity compared to the rest of the cell, thereby effectively limiting the active cell area as the edge region will always feature higher Geiger efficiencies. This does not imply a total inactivity of the remaining cell areas, however the affected edges will dominate the breakdown behavior and thus the entirety of the pixel.

A summary of the breakdown behavior for all 12 annealing scenarios is listed in the third column of Table 9.2. Cases labeled as "partial" exhibited discrepancies in terms of edge breakdown, as only specific chips were affected while others demonstrated nominal performance. The severity also differed from scenario to scenario as fewer chips were, for example, affected on wafer #11 with the breakdown being far less pronounced and only occurring roughly 100 mV before the rest of the cell breakdown. In contrast, in cases labeled "yes" all measured devices were affected by edge breakdown.

The most likely cause for this, is an inhomogeneity of the photo resist edges and subsequently Θ_{res}. The measurements performed to determine the steepness of Θ_{res} were limited to a single area of the wafer and could deviate in other regions.

A comparison to the predicted breakdown behavior from simulations can be made via the last two columns of Table 9.2. Here the simulation results are listed for all annealing scenarios and two different values of Θ_{res}. Considering $\Theta_{res,meas} = 85° \pm 3°$, distinct discrepancies to the simulated case of $\Theta_{res,sim} = 85°$ can be observed, as only annealings # 7 and #9 were predicted to result in edge breakdown, while the measurements showed six more annealing cases to be affected, either fully or partially.

Assuming a smaller angle of $\Theta_{res,sim} = 80°$, a better conformance to the measurements can be found, as cases like #5 and #6 now also feature edge breakdown. However annealings #3, #8, #10 and #11 are still expected to not be affected, opposite to the observations of the measurements.

The reason for this discrepancy may again be found in the photo resist angle and a higher error margin than expected. As mentioned above, the measurements to determine Θ_{res} were limited and could thus underestimate the overall error. The simulations have shown that certain cases would require an error margin $\Delta\Theta_{res} > \pm 5°$ in contrast the one measured one of $\Delta\Theta_{res} = \pm 3°$.

The deviations of edge breakdown on wafer level as well as the discrepancies between simulation and observation could thus be both attributed to inhomogeneities of the photo resist. Confirmation of the above assumptions is, however, not possible after the production of the wafers was finished, as the photo resist in question was already removed in later steps. These issues pertaining to the photo resist need to be taken into account in future productions to avoid experiencing similar discrepancies.

9.1.3 Conclusion

After analysis of all available simulation and experimental data, a specific set of technological parameters, as well as two annealing scenarios were chosen as feasible for being featured in the next batches of the SiMPl production. The implantation angle of the ion beam was chosen to be $\Theta_{ion} = 2°$ in order to avoid channeling while still providing a steep enough angle to reduce its contribution to an increased chance of edge breakdown. A photo resist material providing edge angles close to $\Theta_{res} = 90°$ will be chosen with additional investigatory measurements to avoid inhomogeneities resulting larger error margins and thus edge breakdown.

In terms of the annealing scenarios, cases like #7, #8 and #9 with a distinct case of edge breakdown over the entire wafer were ruled out. It was preferred to include annealings with different atmospheric conditions, however since both "wet" cases (#5 and #6) resulted in edge issues and the highest currents, only "inert" and "dry" can be chosen. From the former, cases #2 and #4 featured the smallest leakage current levels without exhibiting edge breakdown. Annealing scenario #4 was considered the better option due to the smaller deviation in leakage currents and higher electrical fields.

In the case of the "dry" annealings, only #12 exhibited nominal breakdown behavior, but featured a higher current level than the two scenarios with only partial edge breakdown. Taking the results of Fig. 9.5 into account, it can be seen that #12 has a sub-optimal electric field distributions with a linear decrease in depth compared to #10 and #11. Annealing scenario #11 was thus deemed more feasible despite the partial edge breakdown occurrence, due to the already explained low severity of the breakdown phenomenon and the lower leakage current levels compared to case #10.

Following this result, the next iterations of SiMPl productions were chosen to feature multiple wafers containing both preferred annealing scenarios #4 and #11.

9.2 Fourth prototype - SiMPl4

The main goal of the prototype batch labeled SiMPl4 was the production of an improved iteration of devices with the focus at low level photon detection. By incorporating the findings of SiMPl2 and SiMPl3 as well as a sophisticated entrance window for certain wavelengths of light, the aim was to achieve performances comparable to or better than those of commercially available SiPMs. In contrast to SiMPl3, SiMPl4 was produced on thinned SOI material in order to enable passive quenching of the devices.

The discussion will be structured in a similar fashion to the one of SiMPl3. First, the simulation studies, including process and device simulations, as well as the entrance window engineering will be presented, introducing both batches of SiMPl4. In addition, more detailed simulations regarding characteristic SiPM parameters will also be discussed. Afterwards, the experimental studies will be presented, encompassing the data of various types of devices.

9.2.1 Simulation studies of SiMPl4

Following the results of SiMPl3, the technological improvements were adapted and also incorporated into the TCAD simulation framework, while additional technological aspects were included. One of these aspects was related to the implant parameters of the topside p^+-implant in order to optimize the entrance window for photons within the visible spectral range. The resulting improvements for this entrance window engineering will be presented below.

Opposite to SiMPl3, static and transient simulations were performed for the fourth prototype, since the obtainable information from such simulations, namely recovery timing, quenching behavior and breakdown estimates, play an important role when designing the final layout and cell sizes for properly thinned devices. Hence this section is going to discuss the results of the stationary simulations for design considerations, as well as the estimates for the resulting breakdown voltage. Lastly, transient simulations were performed and their results will be compared to the stationary ones.

9.2.1.1 Entrance window engineering

The sensitivity of optical devices can be optimized for specific wavelengths in order to maximize the respective PDE, thus improving the device performance for certain low light level applications and telescope or calorimeter readout.

The common approach to this end consists of two separate steps. First, by adapting the composition of the topside layers, namely the coating layers on top of the silicon, the reflectance of the substrate surface can be minimized and thus the transmittance for specific wavelengths maximized. Second, in order to enable the detection of shorter wavelengths the sensitive region of the detector needs to be located as shallow as possible due to the reduced absorption depth of shorter wavelengths.

The latter can be achieved by adjusting the technology parameters of the p^+-implant to allow the formation of a shallow high field region. There are, however, limitations as a minimum implanted boron concentration after annealing is required to properly form the high field region as well as to saturate the interface defects located in the SiO_2-Si interface. Technology simulations to this end were performed and parameters for a compromise between the required boron concentration and shallow high-field region could be found and were subsequently implemented in the technology procedure. Subsequent Monte-Carlo simulations were also performed (as discussed in Sec. 9.1.1.2), due to the components of the avalanche implants changing slightly and the results suggested that

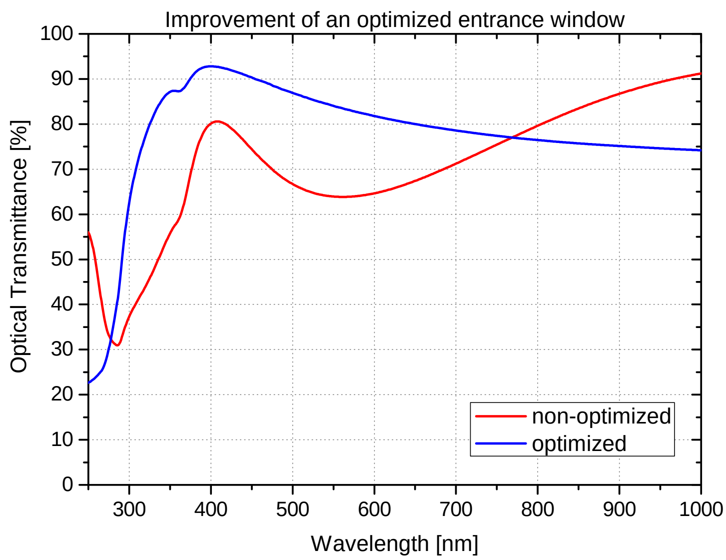

Figure 9.10: Impact of an improved entrance window for the optical transmittance of SiMPl4 devices. The optimized entrance window (blue) is shown for the relevant optical spectrum in comparison to the entrance window of the previous prototypes (red). A peak transmittance of roughly 92.8% at a wavelength of 400 nm can be observed. The simulation was performed at an incident angle of 0°.

no edge breakdown would appear.

In regards to the composition of the topside of the device, silicon can have various coating layers with different thicknesses. These consist of Si_3N_4 and SiO_2, which are deposited on top of the silicon. In order to optimize the optical transmittance, the thickness of the individual layers needs to be modified, resulting in a varying transmittance, depending on the wavelength. A simulation of this procedure was performed using the simulation tool *OpenFilters* [115], which utilizes the transfer-matrix method. The tool allows the variation of the surface layer thicknesses as well as the wavelength and angle of the incident light for determining the resulting reflectance and transmittance.

It is impossible to achieve a transmittance $> 90\%$ for a large range of wavelengths, hence a focus must be set on the wavelengths relevant for possible future applications. Due to silicon becoming nearly transparent for long wavelengths, an upper limit of 1000 nm was chosen. Conversely, according to the limitations imposed by the absorption depth and the achievable shallowness of the high-field region, the lower limit was set to 250 nm, as shorter wavelengths would be absorbed in non-sensitive areas of the detector.

The resulting simulated optical transmittance is presented as blue line in Fig. 9.10. An incident angle of 0° was chosen. Examining the resulting transmittance, a consistently high value $> 75\%$ for wavelength between 325 nm and 1000 nm can be observed, while the region of 375 nm to 450 nm even presents values $> 90\%$. A peak transmittance of roughly 92.8% can be found for a wavelength of 400 nm, which is commonly featured experiments by virtue of the use of wavelength shifting fibers or plastic scintillators.

As a comparison, the entrance window corresponding to the previous SiMPl prototypes is also depicted in Fig. 9.10 as red line. Clear improvements over the majority of the wavelength spectrum can be observed. Solely for wavelengths > 760 nm and < 280 nm the non-optimized case shows increased transmittance compared to the optimized one. In the case of the longer wavelengths, this region can be considered less impactful for the applications in mind, while the shorter region only appears to be more efficient. In reality, the previous prototypes did not include an optimization of the topside implant, thus they were not able to make use of this improved transmittance. Overall, sacrifices in the edge regions of the targeted spectrum in order to increase the transmittance for the majority of the more relevant region, was determined to be the most reasonable course of action.

Therefore, the extracted parameters in regards to the p^+-implant as well as the layer composition of Si_3N_4 and SiO_2 were implemented in the technological procedure of SiMPl4 and culminated in the batch labeled SiMPl4-1. In order to ascertain the potential impact of the parameters necessary for the enhanced entrance window, a second batch with a deeper, less shallow p^+-implant was produced in addition, labeled SiMPl4-2. The parameters for the deep n implant, as well as the annealing scenarios were identical for both batches. If not mentioned otherwise, the following discussions regarding the simulation studies will consider the case of SiMPl4-1.

9.2.1.2 Stationary simulations

The next step in the simulation procedure deals with the feasibility studies via device simulations of the technological aspects investigated in the previous section. This entails studies of the theoretical maximum overbias voltage, recovery times and by implication effects like pinch-off and non-quenching, as consequence of the implemented technological parameters.

The simulations were performed with Synopsys according to the procedure explained in Sec. 7.2.1, allowing the extraction of the theoretical maximum overbias voltage $V_{ob,max}$ with regards to the 20 µA rule of thumb as well as the recovery times $\tau_{90\%}$ and $\tau_{1/e}$ under an assumed overbias voltage $V_{ob} = 5$ V. The evaluation of these parameters in addition to the analysis of the simulation area under nominal operational conditions can be utilized to determine the feasibility of pitch-gap combinations for SiMPl4 devices. This way, extreme cases resulting in pinch-off and non-quenching can also be avoided (see Sec. 6.1).

SiMPl4 focused on pitch sizes > 100 µm, namely 100 µm, 110 µm, 120 µm and 130 µm, each with according gap sizes. A summary of the obtained parameters via static simulations for annealing scenario #4 is presented in Table A.1. The fill factor FF, theoretical maximum overbias voltage $V_{ob,max}$, the recovery times $\tau_{90\%}$ and $\tau_{1/e}$ as well as the ratio $\tau_{90\%}/\tau_{1/e}$ are listed for each pitch-gap-combination included in the simulations. In addition, the final column lists notes in case of pinch-off or non-quenching occurring for the specific geometry. A visual representation is shown in Fig. 9.11, with a) depicting $V_{ob,max}$, b) $\tau_{90\%}$, c) $\tau_{1/e}$ and d) the ratio $\tau_{90\%}/\tau_{1/e}$.

It can be observed that gap sizes below a certain threshold will most likely result in the device entering the non-quenching regime, noticeable by small values of $V_{ob,max}$ and fast cell recharge. This can be witnessed for gap sizes of 6 µm and 10 µm for pitches of 100 µm and 130 µm, respectively. On the other hand, choosing a gap size too large will result in pinch-off, allowing $V_{ob,max}$ far beyond 5 V but also leading to unreasonable recovery times up to multiple minutes, since the recovery process will only occur due to thermal generation of charge carriers in those instances. Pinch-off will set in for gap sizes of 16 µm and above for a pitch size of 100 µm and for gap sizes of 18 µm and above for a pitch size of 110 µm.

By increasing the gap size, $V_{ob,max}$ will also increase, however, reaching cases where $V_{ob,max} > 5$ V usually signifies the risk of entering the pinch-off regime. The recovery times increase with gap size, due to the quench resistor becoming smaller, thus leading to decreased currents within the bulk region. The values are comparable to the ones

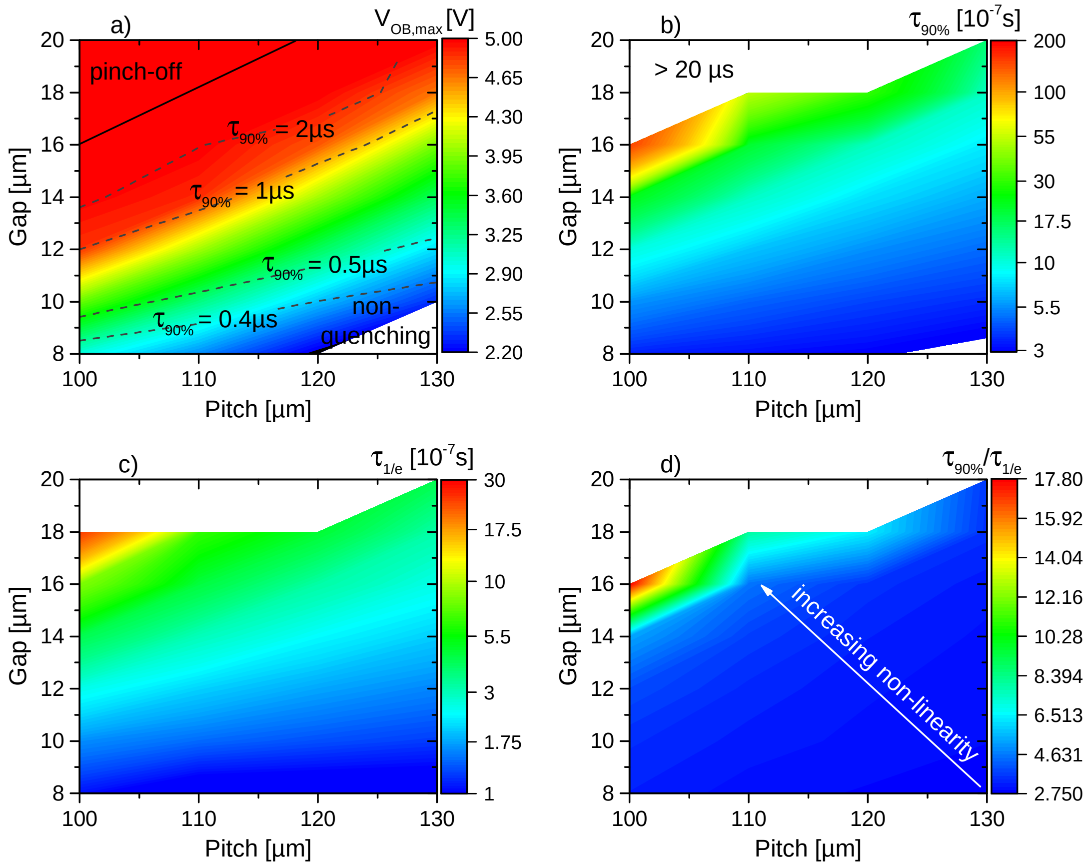

Figure 9.11: Results of the static simulations of SiMPl4 for various pitch-gap-combinations. $V_{ob,max}$ can be seen in a), denoting areas of pinch-off at increased relative gap sizes and non-quenching for small gaps. The recovery times $\tau_{90\%}$ and $\tau_{1/e}$ are shown in b) and c), respectively, while d) depicts the ratio $\tau_{90\%}/\tau_{1/e}$. Here, an increase in non-linearity stemming from the bulk depletion can be identified through higher values of $\tau_{90\%}/\tau_{1/e}$.

obtained from previous SiMPl prototypes and range in the hundreds of nanoseconds for the relevant geometries. Instances like pitch/gap of 100/12, 110/14, 120/16 and 130/18 can be considered the best choice options for device production as they find the best possible trade-off between a high fill factor and $V_{ob,max}$, while still providing acceptable recovery times. If the recovery time is a limiting factor for possible applications, $V_{ob,max}$ can be lowered for the benefit of reducing τ and instances like 100/8, 110/10 and 130/12 become favorable.

The main goal of these first simulations was to provide thorough estimates in order to finalize the design of the first SiMPl4 batch in terms of geometries and their frequency on the wafers. While focus was placed on the cases considered to be "optimal", geometries expected to result in pinch-off and non-quenching were also included in the final designs in order to confirm the simulation results.

9.2.1.3 Breakdown simulations

Due to the change in technological parameters for the implants concerning the avalanche region, the breakdown voltage V_{bd} is expected to change as a consequence. Hence, simulations were performed in order to determine the estimated breakdown voltage and

Table 9.3: Comparison of breakdown voltages V_{bd} obtained by simulations with Synopsys TCAD and Monte Carlo (MC) simulations. For cross-check purposes, two different energies of the deep n implant were simulated ($E_{n,1}$ and $E_{n,2}$).The two different energies of the p^+-implant $E_{p,1}$ and $E_{p,2}$ denote the respective batches SiMPl4-1 and SiMPl4-2, respectively. In all scenarios a very good agreement between both simulation tools can be observed (see text).

V_{bd} [V]		annealing #4				annealing #11			
		Synopsys		MC		Synopsys		MC	
		$E_{n,1}$	$E_{n,2}$	$E_{n,1}$	$E_{n,2}$	$E_{n,1}$	$E_{n,2}$	$E_{n,1}$	$E_{n,2}$
SiMPl4-1	$E_{p,1}$	39.1	20.5	39.0	20.5	37.1	–	37.3	–
SiMPl4-2	$E_{p,2}$	34.7	–	34.5	–	33.2	–	33.6	–

in addition, two different tools were utilized and multiple technological parameters were included for the purpose of validating the extracted data.

The breakdown voltages were extracted for both batches of SiMPl4, first directly via Synopsys TCAD and in addition via the Monte Carlo method explained in Sec. 7.3, by focusing on the trajectory case starting within the center of the pixel. In order to determine the validity of the results obtained by Synopsys, the energies of the deep n and p^+-implants were varied in the simulations, making a cross-check between both frameworks possible.

Two different energies $E_{n,1}$ and $E_{n,2}$ were chosen for the deep n implant, with $E_{n,1}$ representing the case of the actual SiMPl4 devices, while $E_{n,2}$ is lower, thus expected to lead to lower values of V_{bd}. In the case of p^+, two different energies $E_{p,1}$ and $E_{p,2}$ were included. $E_{p,1}$ represents the parameters for SiMPl4-1 with respect to the improved entrance window and the less shallow p^+-implant of SiMPl4-2 is given by the increased energy $E_{p,2}$.

A summary of the extracted values for V_{bd} is shown in Table 9.3. Both simulation frameworks were utilized for both relevant annealing scenarios of the deep n implant (#4 and #11), with scenario #11 exhibiting slightly lower breakdown voltages than scenario #4. This effect, however, is in accordance to expectations derived from the different annealing parameters and poses no issue.

Overall, a very good agreement between the results of both simulation tools can be observed with small discrepancies ranging from 0% to 1.5%. The higher energy $E_{n,1} > E_{n,2}$ is reflected in the breakdown voltage as $V_{bd}(E_{n,1}) > V_{bd}(E_{n,2})$. This can be explained by the increased width of the HF region requiring higher voltages to reach the electric fields necessary for an avalanche breakdown. An analogous observation can be made in regards to $E_{p,1}$ and $E_{p,2}$.

9.2.1.4 Transient simulations

The transient simulations were performed according to the procedure explained in Sec. 7.2.2. This will allow comparison to the extracted parameters of the static simulations and can thus serve as a confirmation of the simulation procedure. In addition to the recovery times to 90% of the oberbias voltage V_{ob} ($\tau_{90\%}$) and 1/e-th of V_{ob} ($\tau_{1/e}$), the voltage drop at the internal anode V_d, the bulk capacitance C_Q and the capacitance of the avalanche cell C_D were evaluated for different applied V_{ob}. A summary of the

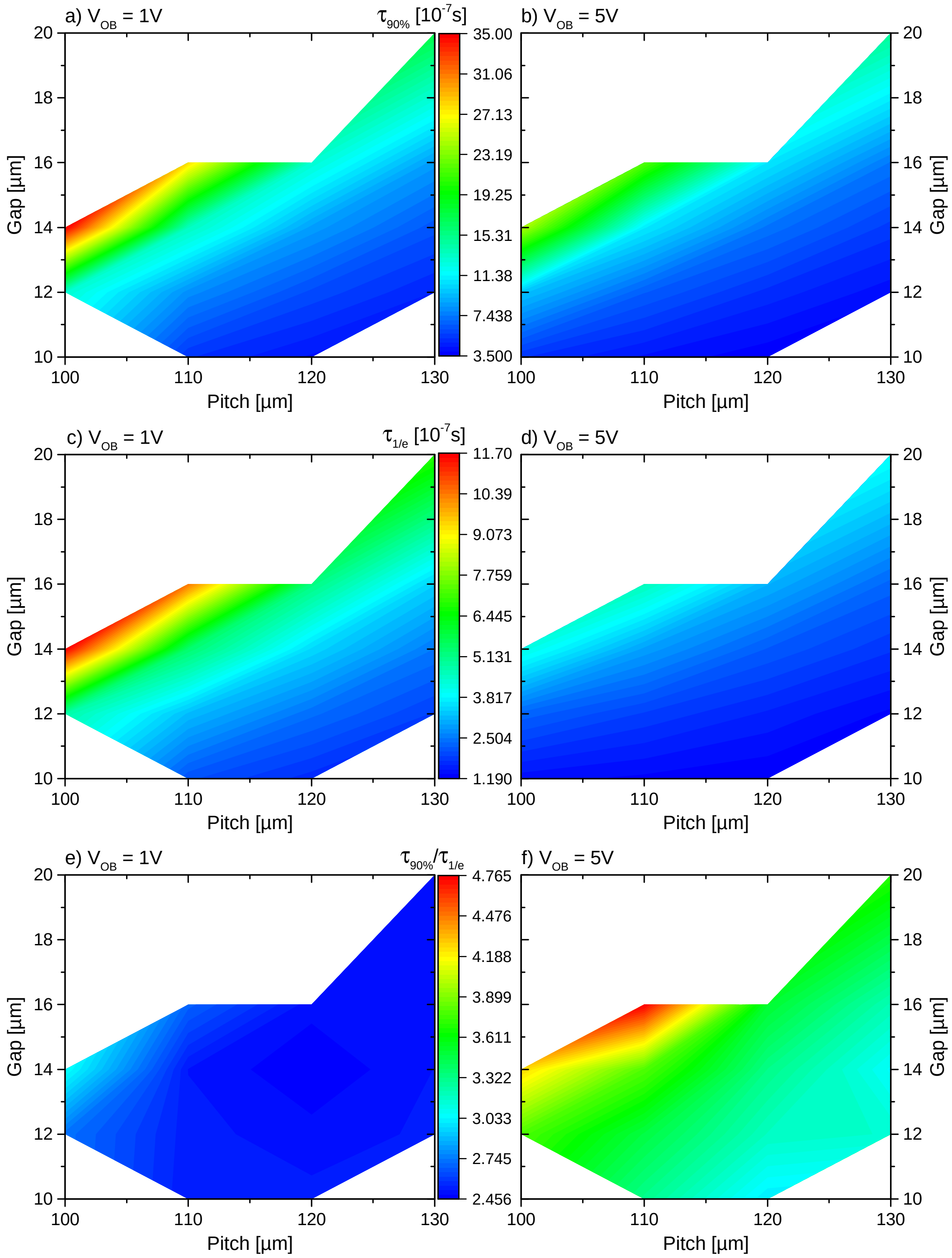

Figure 9.12: Recovery times $\tau_{90\%}$ (a) and b)) and $\tau_{1/e}$ (c) and d)), as well as the ratio $\tau_{90\%}/\tau_{1/e}$ (e) and f)) for different V_{ob}, extracted from transient simulations. Analogous trends to the ones observed in the static simulations are visible (see text). The detailed results are listed in Table 9.4.

extracted results is listed in Table 9.4.

The findings of the previous sections were utilized to narrow down the relevant geometries, hence not all pitch-gap-combinations are included. The fill factor FF for every

Table 9.4: Summary of transient simulation results for SiMPl4 (see text).

pitch [µm]	gap [µm]	FF [%]	V_{ob} [V]	V_d [V]	C_Q [fF]	C_D [fF]	$\tau_{90\%}$ [10^{-7} s]	$\tau_{1/e}$ [10^{-7} s]	$\tau_{90\%}/\tau_{1/e}$
100	10	81.0	1	–	–	–	–	–	–
			3	3.2	15.4	452	5.90	1.90	3.11
			5	5.4	15.9	450	5.30	1.40	3.79
	12	77.4	1	1.0	14.0	445	13.1	4.80	2.73
			3	3.1	14.1	443	11.1	3.20	3.47
			5	5.3	14.4	441	9.80	2.30	4.26
	14	74.0	1	1.0	13.0	435	35.9	11.7	3.07
			3	3.1	13.0	433	28.7	6.30	4.56
			5	5.1	13.1	432	24.7	4.20	5.88
110	10	82.6	1	1.0	20.0	585	5.30	2.10	2.53
			3	3.1	20.3	583	4.70	1.70	2.77
			5	5.2	20.9	582	4.30	1.30	3.31
	12	79.4	1	1.0	18.5	574	8.10	3.20	2.53
			3	3.0	18.7	572	7.30	2.50	2.92
			5	5.1	19.1	570	6.60	1.90	3.48
	14	76.2	1	1.0	17.2	560	13.6	5.40	2.52
			3	3.0	17.2	559	12.1	3.80	3.19
			5	5.0	17.4	557	11.0	2.90	3.79
	16	73.0	1	1.0	15.9	545	28.0	10.4	2.69
			3	2.9	15.9	544	24.2	6.50	3.72
			5	4.9	16.1	543	21.9	4.60	4.76
120	10	84.0	1	1.0	24.4	700	4.30	1.70	2.53
			3	3.2	24.7	698	4.00	1.40	2.86
			5	5.3	25.4	696	3.60	1.20	3.00
	12	81.0	1	1.0	22.8	689	6.00	2.40	2.50
			3	3.1	22.9	687	5.50	2.00	2.75
			5	5.2	23.4	685	5.10	1.60	3.19
	14	78.0	1	1.0	21.3	677	8.60	3.50	2.46
			3	3.0	21.3	675	7.90	2.80	2.82
			5	5.1	21.6	673	7.30	2.20	3.32
	16	75.1	1	1.0	19.9	662	13.0	5.20	2.50
			3	3.0	19.9	661	11.9	4.00	2.98
			5	5.0	20.1	659	10.9	3.10	3.52
130	12	82.4	1	1.1	26.4	783	4.80	1.90	2.53
			3	3.3	26.5	780	4.50	1.60	2.81
			5	5.4	27.0	778	4.10	1.30	3.16
	14	79.6	1	1.1	24.9	774	6.30	2.50	2.52
			3	3.2	24.9	772	5.90	2.10	2.81
			5	5.3	25.3	770	5.50	1.80	3.06
	16	76.9	1	1.0	23.5	763	8.50	3.40	2.50
			3	3.1	23.5	761	7.90	2.80	2.82
			5	5.2	23.8	759	7.40	2.30	3.22
	20	71.6	1	1.0	21.2	738	17.2	6.90	2.49
			3	3.0	21.1	736	15.9	6.90	3.06
			5	5.0	21.3	734	14.8	4.00	3.70

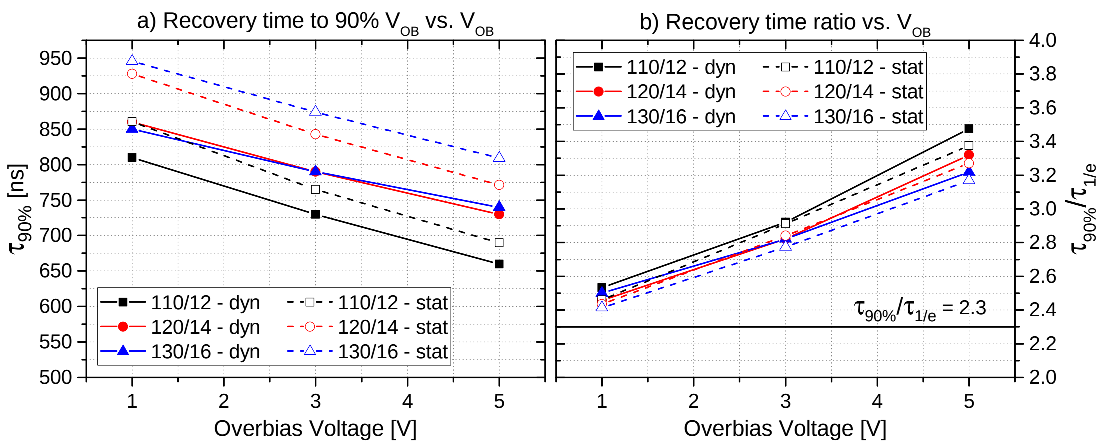

Figure 9.13: Comparison of recovery time $\tau_{90\%}$ obtained by static and transient simulations for different V_{ob} (a)) and behavior of ratio $\tau_{90\%}/\tau_{1/e}$ with increasing V_{ob} (b)). In both plots, the filled symbols represent the transient simulation results and the hollow ones the static ones, respectively. Values for different pitch/gap-combination (given in µm) are included. In a), a decrease of $\tau_{90\%}$ with increasing V_{ob} can be seen in both simulation cases due to the non-linearity of the quench resistor, however the static results suggest overall higher recovery times. The solid line in b) corresponds to the theoretically expected value of $\tau_{90\%}/\tau_{1/e} \approx 2.3$. Increasing V_{ob} leads to higher deviations from this expectation value for all geometries independent of the simulation case.

geometrical variation is also listed, as well as the ratio $\tau_{90\%}/\tau_{1/e}$, which can be used to determine the influence of the non-linear behavior of the quench resistor within the detector bulk, as explained in more detail in Sec. 7.2.1.

The first observation is the good agreement of V_d with V_{ob}, as should be expected, due to V_{ob} being the applied voltage. In instances with smaller gap sizes, values slightly higher than the respective V_{ob} can be seen, which is caused by overall higher currents because of the reduced resulting values for the quench resistor R_Q. They can, nevertheless, be considered to be in excellent agreement with theoretical expectations.

The extracted values for C_Q and C_D stay almost constant with the same geometrical variation, as they are independent of V_{ob}. The small change can be attributed to the change in the depletion region within the gap-region of the bulk due to different bias voltage applied to the device. Notwithstanding, the changes can be considered negligible and are thus also in accordance to expectations.

The behavior of the recovery times is also depicted in Fig. 9.12 with the first row illustrating $\tau_{90\%}$ at two different V_{ob} and the second row $\tau_{1/e}$. Both recovery times, $\tau_{90\%}$ and $\tau_{1/e}$, can be seen to behave as previously established and expected (see Sec. 7.2.1). With increasing overbias voltage, τ decreases based on the non-linear behavior of R_Q and analogous to the static simulations, an increase in gap size results in an increase of τ due to the increase of R_Q. A comparison of the absolute values for $\tau_{90\%}$ between the values extracted via transient and static simulations is presented in Fig. 9.13a). Even though both methods yield results similar in scope, the static ones (filled symbols) suggest slightly larger recovery times for all geometrical variations compared to their transient counterparts (hollow symbols). In both cases, the trend of decreasing recovery times with increasing overbias voltages is clearly visible. The same behavior could be observed for $\tau_{1/e}$.

In terms of the ratio $\tau_{90\%}/\tau_{1/e}$ the same pattern in regards to the geometrical variation can be observed as in the static simulations. As seen in Fig. 9.12e) and f), by increasing the gap size, the ratio also increases, thus straying away from the theoretically expected value of roughly 2.3. The same is true for increasing V_{ob}, but the relative change in this scenario is much more prominent with an extreme of 91.5% between 1 V and 5 V for 100/14 compared to 55% caused by geometrical variations between 100/10 and 100/14 at $V_{ob} = 5$ V. Both instances thus depict the influence of the JFET-like characteristic of the bulk integrated quench resistor of the SiMPl concept. This is visualized in Fig. 9.13b), where the results of both transient and static simulations for various geometries are compared for different overbias voltages. Contrary to the absolute recovery times, no clear trend in terms of which method would suggest higher deviations from the expected value can be seen here. However, the spread of the obtained values seems to increase with increasing V_{ob}, which can further be attributed to the impact of the non-linearity of R_Q.

Since both simulation methods lead to consistent results, these can be considered verified within the scope of the simulation framework. Overall the extracted values suggest recovery times in the range of 350 ns to 2.5 µs in the case of $V_{ob} = 5$ V. Increased recovery times do not pose an issue, as the main goal of SiMPl4 was a high yield at low light level applications, rather then fast devices. Thus, the simulations present promising results for the next batch of device production.

9.2.2 Static measurements of SiMPl4

Following the necessary technology and device simulations, the required parameters for processing of the next SiMPl batches were extracted. After the production was finished, multiple wafers, including both annealing scenarios deemed adequate, were available for further characterizations.

The following section will elaborate upon the stationary characterization measurements performed, starting with the wafer level analysis of the SiMPl4-1 and SiMPl4-2 batches, which mainly focus on I-V-curves and the respective photon emission microscopy photographs. This will also include a comparison of the measured breakdown voltages to the simulated ones shown above. Afterwards, the results from the characterizations of the novel static devices will be presented and compared to simulations.

9.2.2.1 Wafer level characterizations

After the finalization of the wafer production for the two SiMPl4 batches, wafer level characterizations were performed in order to investigate the quality of the devices and to ensure their feasibility for more dedicated characterizations later on. If not mentioned otherwise, all of the following measurements were performed on uncut wafers with the setups described in Sec. 5.2 and Sec. 5.4 with an ambient temperature of approximately (298 ± 0.5) K.

After initial tests on multiple wafers with chips located in different regions of the wafer, two wafers of SiMPl4-1, one for each annealing scenario were chosen for detailed characterizations. Wafer #5 denotes annealing scenario #11 and wafer #8 annealing #4. In the case of SiMPl4-2, only one wafer (wafer #11) corresponding to annealing scenario #4 was measured in detail. The array chips utilized contain avalanche arrays of different sizes and were introduced in Sec. 8.1.1.

Investigation of the measured I-V-curves and respective photon emission microscopy photographs resulted in various observations, of which examples are given in Fig. 9.14. Proper working devices of different sizes of the same chip (E16) of SiMPl4-1 and annealing #4 are shown in the upper row graph. The current levels before breakdown vary according to array size and are comparable to the previous SiMPl batch despite featur-

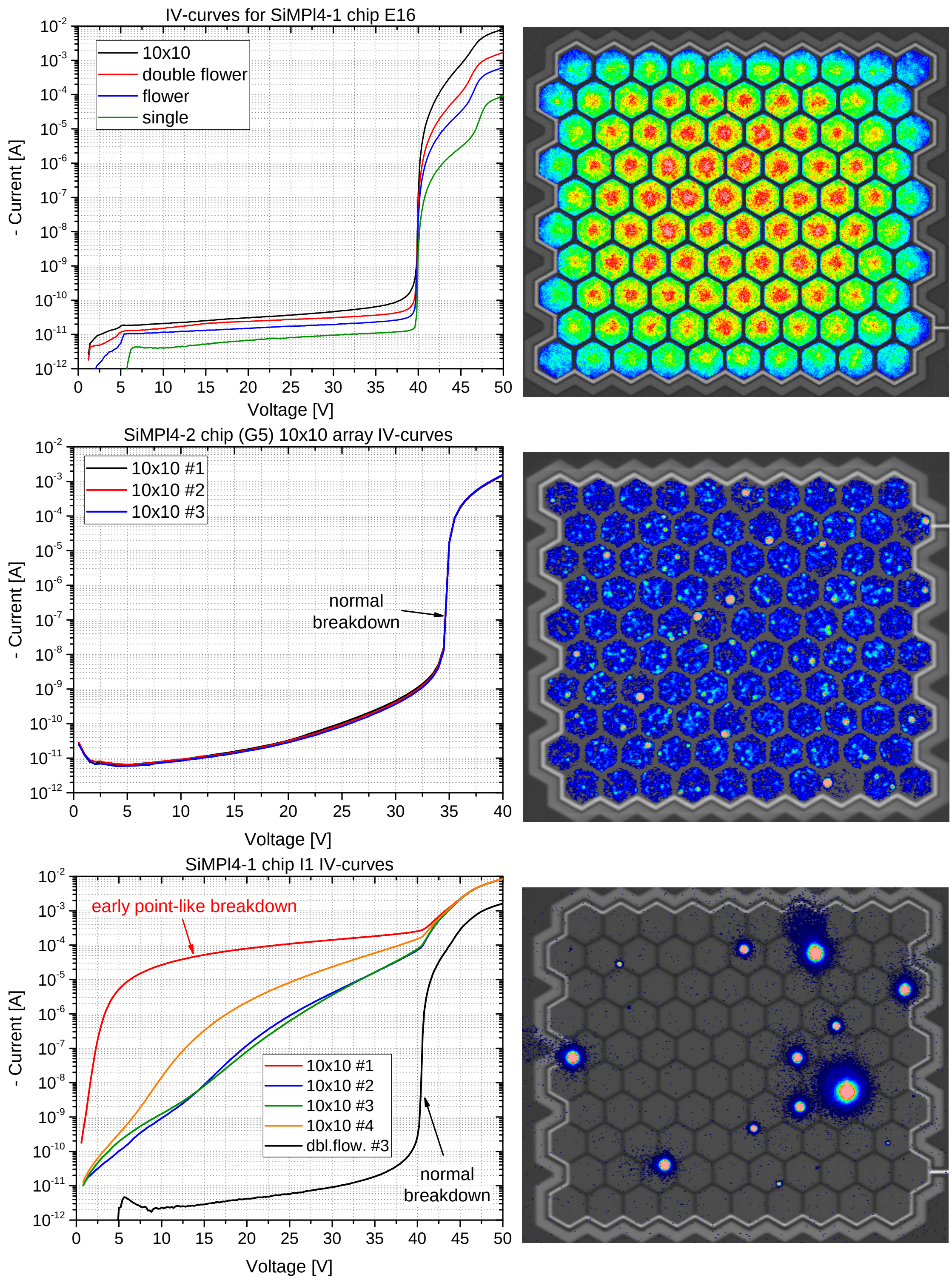

Figure 9.14: Examples of I-V-curves (left) and the corresponding photon emission microscopy photographs (right) of SiMPl4 devices. Proper working devices of SiMPl4-1 with different array sizes and a homogeneous breakdown voltage on chip level are depicted in the upper row. Arrays of SiMPl4-2 affected by hot-spots and increased currents are shown in the middle and devices exhibiting an early point-like breakdown in the lower row. The early point-like breakdown are present on both batches and dominate the breakdown behavior of the entire array. See text for details.

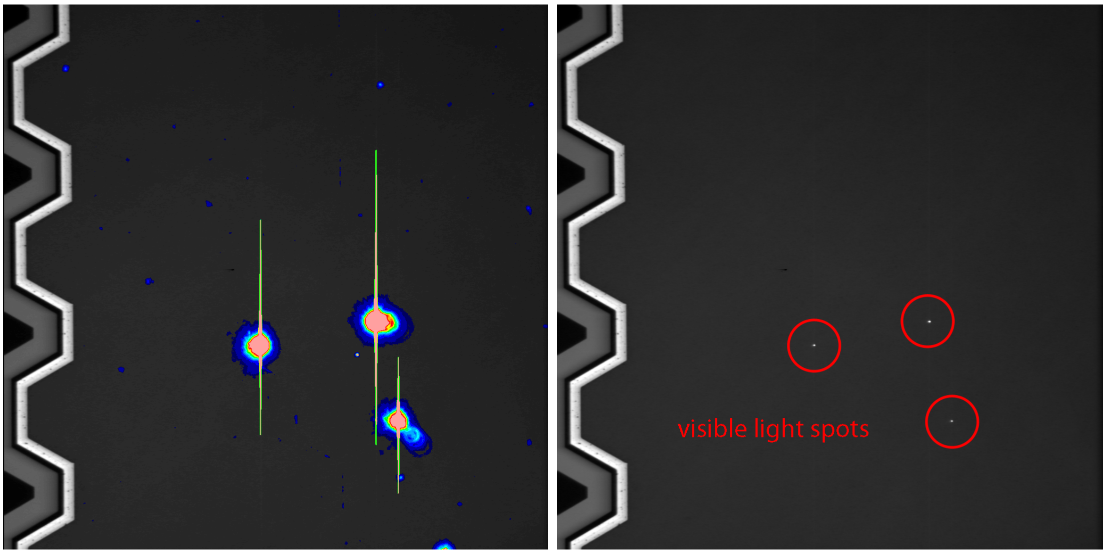

Figure 9.15: Illustration of the severe cases of point-like defects in a SiMPl4-2 device. The measurements were taken at a bias voltage of 10 V and the left hand side depicts the corresponding photon emission microscopy photograph. Three very distinct spots with high light intensity can be seen clearly. The right hand side shows the same area of the array but depicts a microscopy photograph (black and white picture), where three white spots are visible at the same locations, indicating high light emission on a visible level.

ing a shallow p^+-implant for the enhanced entrance window. A homogeneous breakdown behavior on chip level with $V_{bd} = 40$ V is visible for all sizes. The corresponding photon emission microscopy photograph of the 10x10 array measured at $V_{ob} = 3$ V is shown in the right hand side and depicts a uniform emission over the entirety of the array with no edge breakdown or hot-spots being detectable. The increased light intensity in the central pixels stems from the contribution of optical cross-talk. Equivalent behavior of the proper working devices was also found on wafer #5 for annealing #11 of SiMPl4-1.

In the case of SiMPl4-2, representative measurements of proper working 10x10 arrays of chip G05 (annealing #4) are given in the middle row left hand side graph of Fig. 9.14. Compared to SiMPl4-1, the breakdown voltage is lower due to the increased depth of the topside implant, but nonetheless a homogeneous breakdown behavior is visible. The current level before breakdown can be observed to be consistently higher compared to equally sized arrays of SiMPl4-1 chips with a difference of over an order of magnitude for a voltage $V_{bd} - 5$ V.

The emission photograph in the middle right hand side corresponds to one of the I-V-curves of the SiMPl4-2 chip showing activity within the entire array. However, numerous hot-spots are clearly detectable, which do not lead to an early breakdown according the measured current-voltage characteristics. These spots start to exhibit light emission at the same bias voltage as the rest of the cell, but it can easily be seen that they display significantly higher light levels compared to the rest of the array. This leads to the assumption that the increased current generation within of the SiMPl4-2 arrays stems from these hot-spots. While the severity and frequency of the hot-spots varies from array to array, all measured devices exhibited the presence of distinct hot-spots.

It is not known, why the hot-spots and conversely an increased current level can mainly be found on SiMPl4-2 devices and not SiMPl4-1. The opposite would be expected due to the deeper p^+-implant like in the case of SiMPl4-2 usually being considered safer

Table 9.5: Yield of all in-depth tested wafers of both SiMPl4 batches. The classification is based on the devices being heavily affected by the point-like early breakdowns. The individual yield for all hexagonal variations of devices is listed, as well as (if applicable) the ones for the quadratic structures. Wafers #5 (annealing #11) and #8 (annealing #4) of SiMPl4-1 and wafer #11 (annealing #4) of SiMPl4-2 were investigated in detail. In terms of SiMPl4-1, annealing #4 appears to result in an overall higher yield than #11 and SiMPl4-2 displayed generally greater yield numbers for all devices (see text).

Yield [%]		SiMPl4-1		SiMPl4-2
		Wafer #5	Wafer #8	Wafer #11
hex	30x30	6.4	13.8	17.3
hex	10x10	50.0	59.0	83.3
hex	dbl. flower	77.3	86.1	95.9
hex	flower	88.8	94.2	98.5
hex	single	97.4	98.6	99.2
square	10x10	–	–	94.0
square	5x5	–	–	100
square	3x3	–	–	100
square	single	–	–	–

by avoiding surface contributions or damages (see Sec. 9.6).

Another type of device behavior is depicted in the lower row of Fig. 9.14. The graph shows the I-V-curves of 10x10 and double flower arrays of a SiMPl4-1 chip (I01) with annealing #4. All three 10x10 structures (colored lines) exhibit a very early avalanche breakdown compared to the properly working double flower device (black line), with the most severe case being the red line and the breakdown occurring at a bias voltage below 5 V. Its photon emission microscopy photograph measured at $V = 10$ V $< V_{bd}$ can be seen on the right hand side. Several spots exhibiting early point-like breakdowns can be observed even at these low voltages. Increasing the voltage did not result in the rest of the array becoming equally active since the point-breakdown spots dominated the entire characteristic of the affected structures. The appearance of these early point-like breakdowns does not show any signs of systematic behavior on chip level and appears to be random.

One of the severe cases of the early point-like breakdown can be seen in Fig. 9.15. On the left, the emission photograph of SiMPl4-2 10x10 array measured at $V = 10$ V $< V_{bd}$ is shown with three distinct point-like breakdown spots visible. The right hand side photograph omits the emission measurement and only shows a standard microscopy photograph of the same area measured at the same voltage. Here, three distinct white spots are visible at the exact locations of high light emission of the emission pictures and which only start appearing if a sufficient bias voltage is provided to the device, meaning that these bright spots are actual visible light emitted by the device. This is unexpected, since the light levels emitted during an avalanche of this magnitude should not be visible without sophisticated emission cameras. Therefore, this observation would imply extreme levels of avalanche activity in the device within these spots at already low bias voltages.

The early point-like breakdown was observed on both batches and both annealing scenarios. In order to quantify the severity of this issue, all chips containing hexagonal structures of both SiMPl4-1 wafers and the SiMPl4-2 wafer were measured in addition to the quadratic devices of the SiMPl4-2 wafer. In terms of the hexagonal devices, this

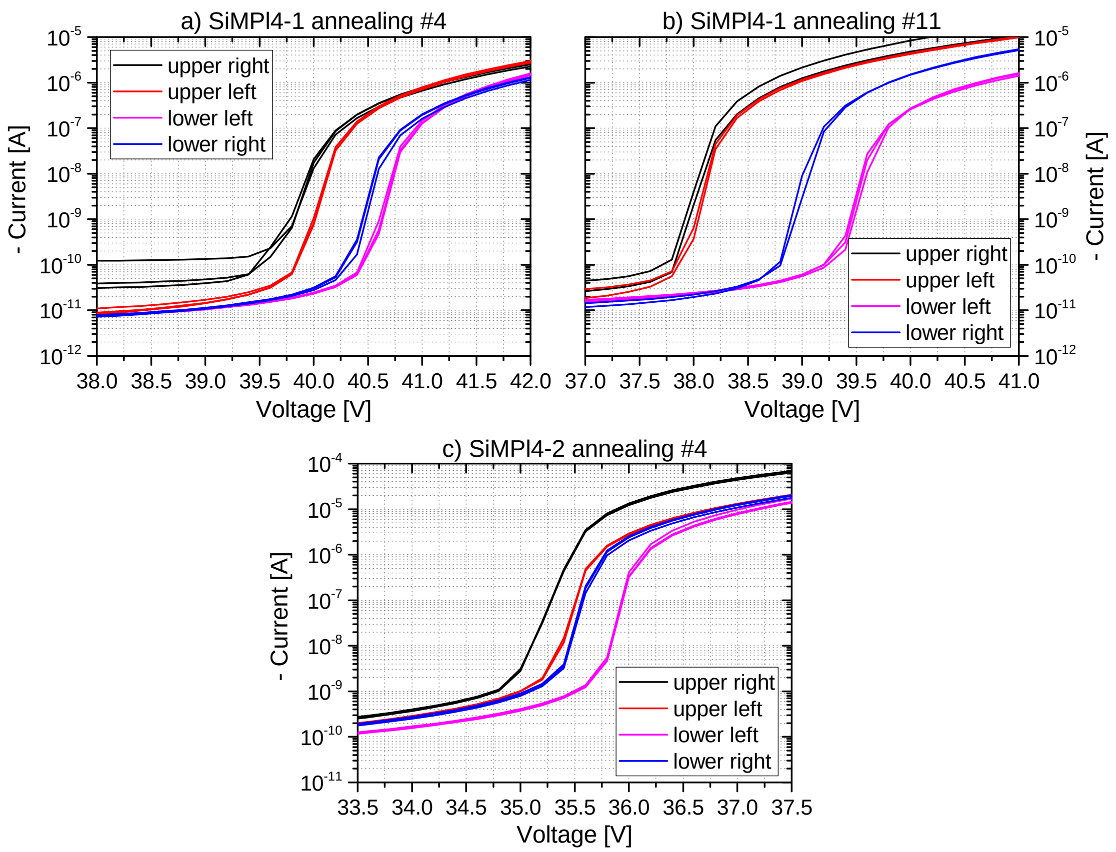

Figure 9.16: Shift of the breakdown voltage of both SiMPl4 batches, dependent on wafer position. Both annealing scenarios for SiMPl4-1 are depicted in a) and b), respectively, while c) shows annealing #4 of SiMPl4-2. The I-V-curves are centered around V_{bd} for an easier distinction. The colors represent chips, located in different areas of the wafer and feature multiple lines corresponding to arrays within those chips. A clear left-right and upper-lower discrepancy can be seen, leading to overall higher values of V_{bd} in left and lower regions of the wafers in all cases (see text).

resulted in 261 measured chips per wafer, each with varying numbers of structures. In total 482 30x30, 1710 10x10, 2410 double flower, 2154 flower and 4960 single pixel devices were evaluated and the yield determined on the basis of the devices being negatively affected by the point-like early breakdowns. In the case of the quadratic ones, a total of 22 chips, containing 167 10x10, 168 5x5 and 228 3x3 structures were investigated.

The obtained yield for all measured wafers, divided by shape and array size is summarized in Table 9.5. Overall, a decrease in yield with increasing device size can be observed which is reasonable due to the probability of the point-like defects occurring within one array increasing with its size. This manifests itself most severely in the yield of the 30x30 structures, which lies at 6.4% and 13.8% for SiMPl4-1 wafer #5 and #8, respectively and at 17.3% for wafer #11 of SiMPl4-2. No position dependency of the defects can be detected as all regions of the wafers seem to be affected. In general, it would appear that annealing scenario #4 produces higher yield numbers compared to annealing #11 for SiMPl4-1 wafers. In order to confirm this assumption for SiMPl4-2 as well, 30 10x10 devices of ten chips located on various areas of a different wafer with annealing scenario #11 were measured for comparison resulting in a 30% yield in contrast to the 83% obtained from annealing #4 on wafer #11.

Table 9.6: Comparison of the simulated and measured breakdown voltage for SiMPl4 devices. The comparison includes SiMPl4-1 and SiMPl4-2 cases and both relevant annealing scenarios. The error for the measured values arises from variations in V_{bd} on wafer level. In general, all measured values can be considered in very good agreement with the simulated ones.

V_{bd} [V]	annealing #4			annealing #11		
	Synopsys	MC	Meas	Synopsys	MC	Meas
SiMPl4-1	39.1	39.0	39.9 ± 0.8	37.1	37.3	37.9 ± 0.8
SiMPl4-2	34.7	34.5	35.2 ± 0.5	33.2	33.6	33.3 ± 0.2

A comparison between the two SiMPl4-1 wafers and the single SiMPl4-2 wafer highlights a generally higher yield for the latter. Hexagonal array sizes smaller than 10x10 exhibit a low percentage in the single digits of devices affected by the early point-like breakdown. In the case of the quadratic arrays, the yield for the 10x10 devices reaches 94% with smaller sizes even featuring a perfect yield. While the hexagonal 30x30 devices seem to be heavily affected in all cases by the early breakdown issue, a sufficient amount of devices, mainly the 10x10 were deemed to be utilizable for further in-depth characterizations for both SiMPl4-1 and SiMPl4-2.

In terms of the breakdown voltage V_{bd} a very uniform behavior on chip level was visible for all devices not affected by the early point-like breakdown. On wafer level, a shift dependent on the location could be observed. This is illustrated in Fig. 9.16 for the characterized wafers of SiMPl4-1 and SiMPl4-2. Each color represents a chip located in different corners of the wafer and the multiple lines of an identical color represent devices of the same chip.

In all cases, a clear left-right and upper-lower discrepancy can be detected. The former results in deviations of V_{bd} ranging from roughly 0.1 V to 0.5 V, while the latter appears to be more distinct with discrepancies of 0.5 V to 1.5 V. The maximum difference in V_{bd} can be found between the upper right and lower left corner and is largest in the case of SiMPl4-2 wafer #5 (annealing #11) with $\Delta V_{bd}(\mathrm{w5}) \approx 1.6$ V. For SiMPl4-1 wafer #8 and SiMPl4-2 wafer #11 (annealing #4) the shift was measured to be $\Delta V_{bd}(\mathrm{w8}) \approx 0.82$ V and $\Delta V_{bd}(\mathrm{w11}) \approx 0.75$ V, respectively.

A similar behavior was not observed during the characterization of SiMPl3. This issue can originate from inhomogeneities in beam energy and angle of the ion beam during the implantation procedures of the two topside implants making up the high-field region. These would result in depth variations of either the p^+ or deep n implant, thus altering the width and thereby the breakdown voltage of the high-field region. Overall, this issue can be considered not problematic as the total shift is fairly small compared to the total breakdown voltage and since a high level of uniformity was achieved on chip level.

The breakdown voltages obtained from the total wafer evaluation of SiMPl4-1 wafers #5 and #8 as well as SiMPl4-2 wafer #11 and a comparison to the simulated values are given in Table 9.6. In addition, a limited sample size (10 chips) of SiMPl4-2 wafer #3 corresponding to annealing scenario #11 was also measured to provide its breakdown voltage. The simulations were discussed in detail in Sec. 9.2.1.3. In all cases, only proper working devices without early point-like breakdowns were included. The error of the measured values mainly stems from the aforementioned deviations on wafer level.

In all cases a very good agreement between simulation and measurement can be found. The absolute values of SiMPl4-1 are larger than SiMPl4-2 due to the shallow nature of the p^+-implant of the improved entrance window resulting in an increased width of the high-field region. Annealing scenario #11 features a higher temperature compared to #4 leading to a higher potential for diffusion, thus resulting in a smaller width of the high-field region and thereby smaller breakdown voltage.

The discrepancy between measured and simulated values in all cases is < 1 V and roughly similar in terms of absolute values, with SiMPl4-1 exhibiting a ΔV_{bd} between 0.6 V and 0.9 V and SiMPl4-2 between 0.1 V and 0.7 V. In both cases, annealing scenario #11 presents smaller deviations to the simulations, however the limited sample size in the case of SiMPl4-2 needs to be taken into account. Considering the relative discrepancy however, the deviation of V_{bd} is roughly 2% in all presented cases apart from SiMPl4-2 annealing #11 with only 1%. Overall, this result can be considered as a confirmation of both applied simulation tools for the determination of the breakdown voltage.

Contrary to the simulated predictions, a number of chips of all tested wafers exhibited clear edge breakdown with varying severity and frequency, depending on the wafer itself and the chip's position within the wafer. The effect is illustrated in the photon emission photograph of Fig. 9.17, depicting an array of a SiMPl4-1 chip of wafer #8. Every cell within the array exhibits increased light intensity and thereby avalanche activity in either the right or upper right edges or both. In the most severe cases the edge breakdown can be observed to occur roughly 0.2 V earlier compared to the rest of the cell, according to the emission photographs. This, however was not visible in the respective I-V-curves, which featured a nominal breakdown behavior. This discrepancy can be attributed to the photon emission photographs only allowing for measurement of relative light levels, thus potentially suppressing low level activities in the rest of the cell if the edge activity reaches certain thresholds.

The wafer layout illustrations of Fig. 9.17 visualize the location dependence of the edge breakdown by indicating if a measured chip is affected by it (red) or not (green). This investigation was carried out for SiMPl4-1 wafers #5 and #8 and SiMPl4-2 wafer #11. In all three cases, the edge breakdown occurs in the upper and upper right region of wafer. The highest severity and frequency was found in the upper right corner chips and venturing further away from said area, the issue would start to become gradually less pronounced and frequent. While a chip in the upper right corner like S13 (see emission photograph) has every cell exhibit pronounced edge breakdowns on one or multiple edges, a chip located close to the center of the wafer like I08 will only show edge breakdowns in fewer than ten cells on average. The severity in this case is also reduced with the edge activity being visible but practically on the same level as the rest of the cell. In addition, the difference in breakdown voltage between the edge and center of the cells also becomes smaller, the further to left or towards the lower rows the chips are located.

According to the simulations of the previous sections, no edge breakdown should occur, since the parameters were chosen in order to suppress it and no indication of edge breakdown was visible in the simulated results. The most likely cause are variations in the angle of the photo resist edge, as discussed in Sec. 9.1.1.1. Due to the unavailability of the previous photo resist material, it was changed between the production of SiMPl3 and SiMPl4 resulting in edge angles of the new resist of $\Theta_{res}(\text{SiMPl4}) = 80° \pm 2°$ compared to $\Theta_{res}(\text{SiMPl3}) = 85° \pm 3°$. In Sec. 9.1.1.1 it was already established that larger deviations in Θ_{res} are likely due to the observed edge breakdown in annealing cases which should not be affected according to simulations. Furthermore, in both SiMPl3 and SiMPl4 the sample size of the measured edges to determine Θ_{res} was limited to a small region of the wafer, thus location dependent deviations are possible. Combined

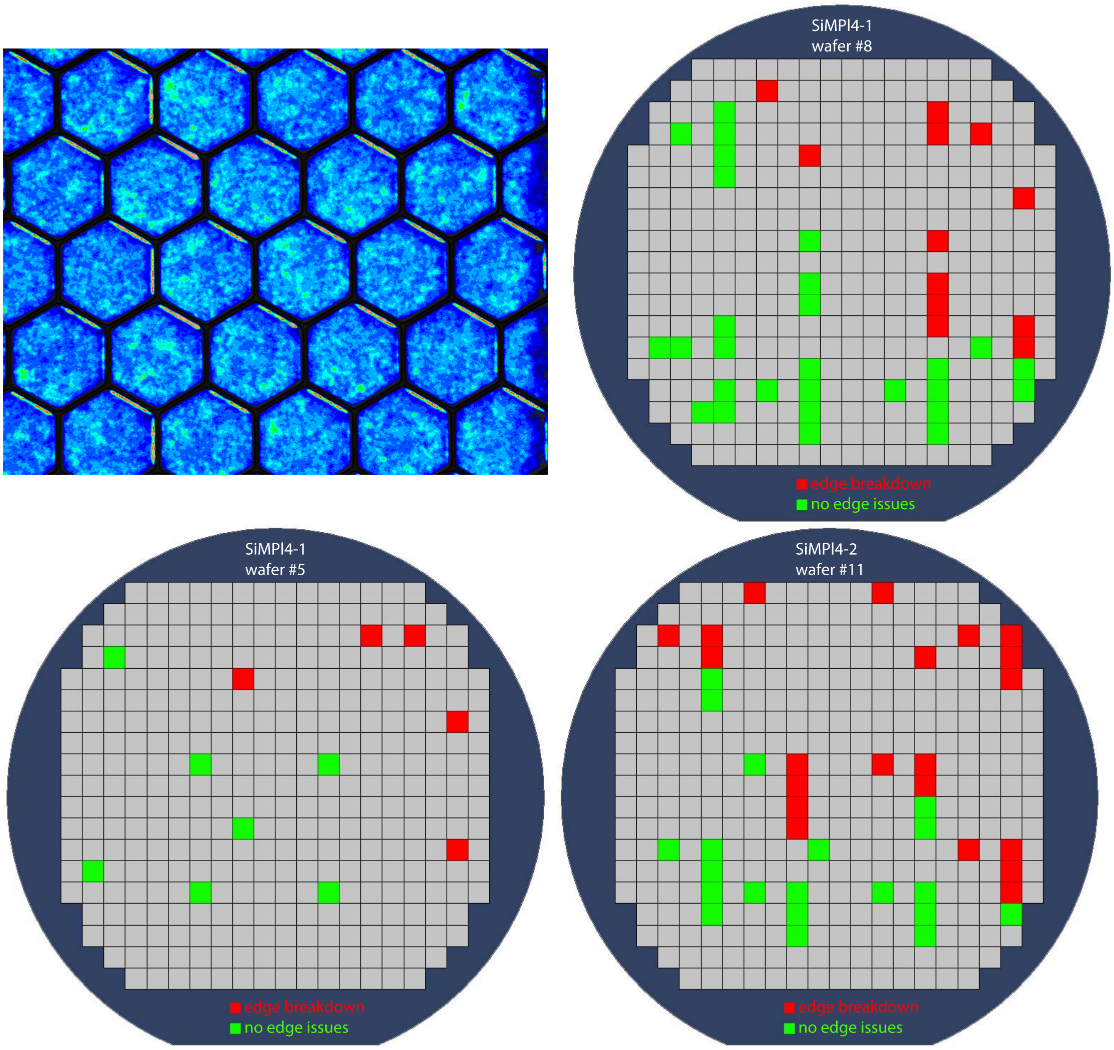

Figure 9.17: Summary of the observed edge breakdown in both batches of SiMPl4. The photon emission microscopy photograph illustrates the issue on a SiMPl4-1 chip of wafer #8, in which the right and upper right edges of the cells exhibit higher avalanche activities compared to the rest of the pixel. The location dependence of the effect is visualized by the wafer maps indicating affected (red) and unaffected (green) chips for three measured wafers. A clear trend of the issue occurring predominantly in the upper right regions of the wafers can be observed with a gradual decrease in frequency and severity towards the lower left areas (see text).

with the overall smaller measured Θ_{res} of SiMPl4 the experienced edge breakdown is likely caused by inhomogeneities of the photo resist edge. Nevertheless, the amount of devices not affected by this issue is still sufficiently large in order to allow further detailed characterizations of the SiMPl4 batches.

9.2.2.2 Static test devices

As explained in Sec. 8.2, the novel static test devices were design in the course of this study to allow direct comparison with static simulations and to provide access to the bulk-integrated quench resistor. In the case of SiMPl4, a total of 9 chips were included in the design per wafer, with each chip featuring 44 structures, 22 of the "no overlap" and

22 of the "overlap" design. As the overlap structures were dominated by the avalanche current after breakdown, the data provided in this section will be based solely on the "no-overlap" case. Hence the data of a total of 198 static test structures per wafer was measured and analyzed and the quenching and recovery behavior were extracted for both SiMPl4-1 and SiMPl4-2 chips. The measurement procedures were performed analogous to the static simulation procedures explained in Sec. 7.2.1.

Quenching

An example of the measured quenching behavior of one SiMPl4-2 chip is depicted in Fig. 9.18a). All geometrical variations present on the chip can be seen, as well as the current limit for estimating $V_{ob,max}$ as suggested by Cova. The dashed lines of the same colors as the solid ones represent the second identical structure of the chip, as all geometries are included twice.

The overall trend, which was already observed during the static simulations, can also be seen here. Choosing a small gap size in comparison to the pitch size leads to only small potential overbias voltages and in extreme cases to non-quenching. By increasing the gap size, $V_{ob,max}$ can be seen to increase as well, although potential pinch-off needs to be considered, as cases like 100/30 exhibit currents below 1 µA even for large potential differences, thus representing said cases of pinch-off. The deviations in $V_{ob,max}$ within the same geometrical cases on chip level were observed to be in the tens of mV up to ≈ 100 mV and no overall systematic trend therein could be observed. The behavior of the measured SiMPl4-1 devices was found to be analogous to SiMPl4-2.

In order to investigate potential deviations on wafer level, a specific geometry, namely 130/16 was measured on every chip of a SiMPl4-1 and SiMPl4-2 wafer and the results can be seen in Fig. 9.19a) and b), depicting the case of SiMPl4-1 and SiMPl4-2, respectively. Since the chips are located in all regions of the wafer, location dependent issues should be identifiable. The deviations on wafer level can be seen to be larger compared to chip level, amount to roughly 0.6 V in extreme cases for both batches. Again, no systematic

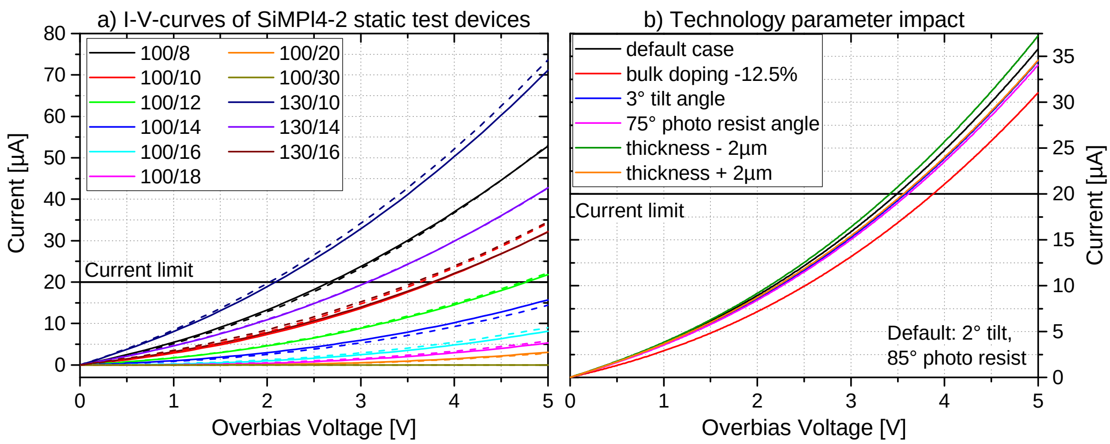

Figure 9.18: Measured and simulated quenching curves of static test devices. In a) all geometrical variations of one individual chip are shown. The dashed lines of the same color as the solid lines represent the identical pitch/gap variation of the same chip, since every variation is present twice on each chip. Small variations can already be seen on chip level. The simulated data in b) depicts the impact of various technological parameters on the quenching curves compared to the default case (see text). The rule-of-thumb current limit is given in both plots as 20 µA.

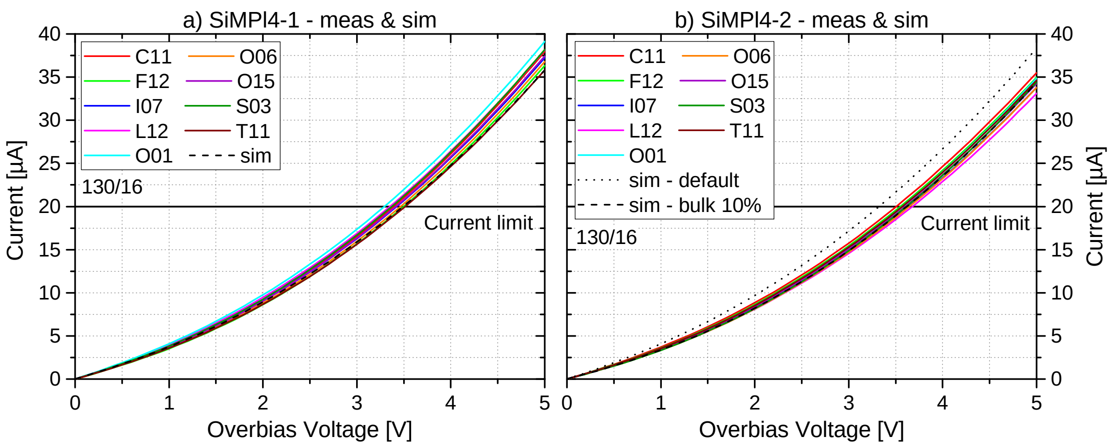

Figure 9.19: Measured quenching curves of the same geometrical variation (130/16) on every available chip on the wafer. SiMPl4-1 wafer #8 is shown in a) and SiMPl4-2 wafer #11 in b). In both cases a deviation of $V_{ob,max}$ given by the current limit can be observed. The simulated equivalents are also given. In the case of b) an adaptation of the bulk doping level in the simulations was performed (dashed line), as suggested by the measured data (see text).

behavior or position dependency could be observed. A summary of all extracted values of $V_{ob,max}$ is listed in Table 9.7 with the measured errors stemming from the aforementioned wafer level deviations. The cases with pitch size 100 and gap sizes larger that 16 resulted in pinch-off and were thereby not included.

A comparison to the simulated quench behavior is also included in Fig. 9.19. In the case of SiMPl4-1, in a first approximation a good agreement between the measured and simulated curves can be observed. The simulations of SiMPl4-2, however, suggest a smaller $V_{ob,max}$ with $\Delta V_{ob,max} \approx 0.5$ V, translating into an overall smaller value of R_Q and thereby larger currents. This simulation (dotted line) represents a "default case" with all technological parameters chosen according to the nominal cases and manufacturer specifications. Choosing a 10% reduced bulk doping level results in the dotted line of Fig. 9.19b) and shows better accordance with the measured data. This suggest a lower bulk doping level of the measured SiMPl4-2 wafer compared to the given specifications, which is well within the error margin provided by the wafer manufacturer and therefore not unexpected. Hence, all simulations pertaining to the SiMPl4-2 cases were adapted to the reduced bulk doping level going forward.

The final results of the simulations are also given in Table 9.7. Their displayed trend is identical to the measured one, albeit overall smaller values of $V_{ob,max}$ were obtained ranging from 1% to 13% smaller with regards to the error margin. The deviation appears to be larger for smaller pitch sizes and decreased in the case of pitch 130 with increasing gap size. Both SiMPl4-1 and SiMPl4-2 (after bulk doping correction) display the same trend with similar levels of deviation.

In order to identify the cause of this discrepancy, various technological parameters were modified within the simulation framework and the impact on the quench behavior documented. The result can be seen in Fig. 9.18b) with the "default case" being depicted as black line and all variations as colored lines. The resulting change in $V_{ob,max}$ is listed in Table 9.8.

The previously discussed reduction of the bulk doping level can be seen to increase $V_{ob,max}$ due to the higher resistivity of the bulk. Here a 12.5% reduction yields an increase in $V_{ob,max}$ of roughly 10%. Choosing a tilt angle Θ_{ion} of 3° compared to the default of

Table 9.7: Summary of the extracted quenching behavior from experimental data and comparison to simulations. The values for $V_{ob,max}$ for each pitch/gap variation and resulting fill factor (FF) are listed. The error in the experimental data is dominated by the variations of wafer level rather than chip level. For a pitch size of 100 µm, a gap larger than 16 µm will result in pinch-off. The simulated values for SiMPl4-2 were obtained from the adapted bulk doping level case (see text).

			$V_{ob,max}$ [V]			
			SiMPl4-1		SiMPl4-2	
pitch [µm]	gap [µm]	FF [%]	Synopsys	measured	Synopsys	measured
100	8	84.6	2.18	2.42 ± 0.08	2.35	2.70 ± 0.09
	10	81.0	3.08	3.44 ± 0.13	3.24	3.71 ± 0.10
	12	77.4	4.03	4.52 ± 0.19	4.16	4.69 ± 0.15
	14	74.0	> 5.0	> 5.0	> 5.0	> 5.0
	16	70.6	> 5.0	> 5.0	> 5.0	> 5.0
	18	67.2				
	20	64.0	pinch-off		pinch-off	
	30	49.0				
130	10	85.2	1.90	2.00 ± 0.12	2.05	2.13 ± 0.10
	14	79.6	2.93	2.99 ± 0.10	3.08	3.16 ± 0.14
	16	76.9	3.50	3.47 ± 0.12	3.62	3.66 ± 0.13

Table 9.8: Simulation of the impact of various technological parameters on $V_{ob,max}$ and $\tau_{90\%}$. The simulated case represents a SiMPl4-1 device with 130/16 at $V_{ob} = 5$ V. In the default case, the tilt angle and photo resist angle are set to 2° and 85°, respectively. All values are the result of the listed parameter exclusively.

		value due to				
	Default case	12.5% reduced bulk doping	3° tilt	75° photo resist	thickness +2 µm	thickness −2 µm
$V_{ob,max}$ [V]	3.50	3.88	3.58	3.62	3.56	3.42
$\tau_{90\%}$ [10^{-7}s]	5.08	6.53	5.32	5.42	5.20	4.95

2° also leads to an increase of $V_{ob,max}$ by 3%. A similar impact can be observed for a smaller photo resist angle $\Theta_{res} = 75°$ compared to the standard 85°. In order to account for potential thickness variations of the wafer, a deviation of $d \pm 2$ µm was included and an increase in d can be seen to have the same impact as the other parameters mentioned before, while a decrease in d results in smaller values of $V_{ob,max}$.

An impact from a reduced photo resist angel Θ_{res} is very likely according to the observations regarding edge breakdown in the previous section. However, it cannot be the dominating reason as this would result in a position dependent behavior of $V_{ob,max}$ (similar to the edge breakdown), which was not observed. A more likely explanation is a combination of different parameters resulting in the total observed deviation. The case of $\Theta_{ion} = 3°$ reflects the findings of Sec. 9.1.2.1 in which a less pronounced doping profile tail was visible in the SIMS measurements compared the simulations performed with $\Theta_{ion} = 2°$. By increasing Θ_{ion} in the simulations a similar situation can be achieved, better reflecting the SIMS profile. In addition, small deviations (or increased in the case of SiMPl4-2) of the nominal bulk doping level are common and the observed deviations in $V_{ob,max}$ would translate to bulk doping variations well within the provided error margins.

In conclusion, the most likely explanation for the discrepancy between simulations and measurements is a combination of the above effects. While Θ_{res} is likely smaller compared to the nominal value and the deep n profile better represented with a larger Θ_{ion}, mirroring the smaller profile tail, it is most probable that an interplay of both these parameters as well as a bulk doping variation are the cause for the higher measured values of $V_{ob,max}$. Within this context, the simulations and measurements of both batches can be considered to be in good agreement.

Recovery

Following the quenching behavior, the recovery characteristics were also investigated and are summarized in Table 9.9. Here, the extracted recovery times to 90% ($\tau_{90\%}$) and 1/e-th ($\tau_{1/e}$) of V_{ob} are listed for various V_{ob} as well as their ratio $\tau_{90\%}/\tau_{1/e}$ for both the experimental and simulated data. SiMPl4-1 values are listed in the upper half and SiMPl4-2 in the lower one. The geometrical cases resulting in pinch-off were not included.

The previously observed characteristic of decreasing recovery times with increasing V_{ob} can be seen. Higher overbias voltages result in a smaller impact of the high resistance region within the recovery I-V-curves, and thus the longest time steps. Hence, in order to reach the desired recovery status (90% or 1/e-th), the part responsible for noticeably increasing the recovery times becomes more and more negligible. Identical to before, the error of the measured values is dominated by the variations on wafer level. This behavior can also be observed in Fig. 9.20a), where $\tau_{90\%}$ for various V_{ob} is depicted. Different pitch/gap combinations are included, while the filled out symbols represent the experimental data and the hollow ones the results from simulations.

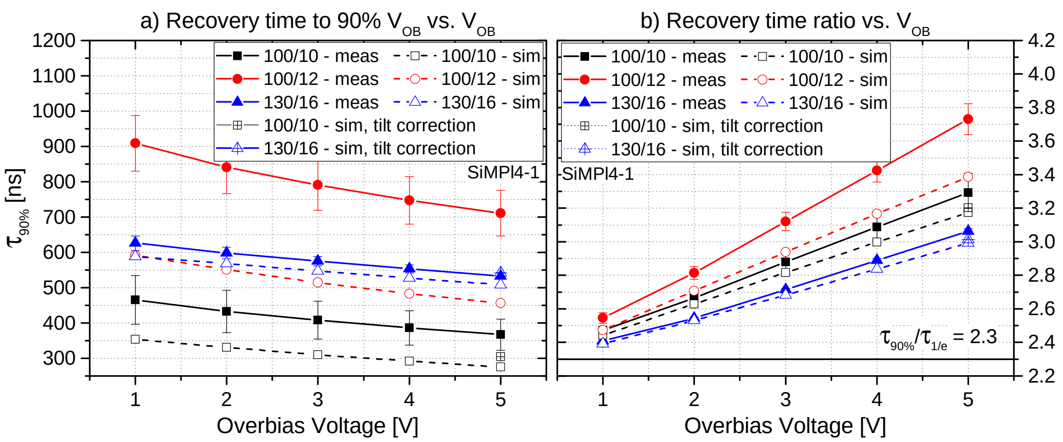

Figure 9.20: Comparison of measured and simulated recovery time $\tau_{90\%}$ for different V_{ob} (a)) and behavior of ratio $\tau_{90\%}/\tau_{1/e}$ with increasing V_{ob} (b)). The data for different pitch/gap combinations is given in both plots. In both plots, the simulated case of a smaller tilt angle is also included ("tilt correction"). In a), $\tau_{90\%}$ can be seen to decrease with increasing V_{ob} for both experimental and simulated data. The decrease stems from the non-linearity of R_Q and is more pronounced for cases with larger bulk depletion areas. The solid line in b) represents the theoretically expected value for the recovery time ratios of $\tau_{90\%}/\tau_{1/e} \approx 2.3$. An increasing deviation of this expected value with increasing V_{ob} can be observed in all cases.

Table 9.9: Recovery times for SiMPl4-1 (upper half) and SiMPl4-2 (lower half).

pitch [µm]	gap [µm]	V_{ob} [V]	$\tau_{90\%}$ [10^{-7} s] sim	$\tau_{90\%}$ [10^{-7} s] meas	$\tau_{1/e}$ [10^{-7} s] sim	$\tau_{1/e}$ [10^{-7} s] meas	$\tau_{90\%}/\tau_{1/e}$ sim	$\tau_{90\%}/\tau_{1/e}$ meas
100	8	1	2.11	2.44 ± 0.22	0.87	1.02 ± 0.09	2.43	2.46 ± 0.02
		3	1.84	2.11 ± 0.15	0.66	0.78 ± 0.06	2.77	2.78 ± 0.02
		5	1.63	1.87 ± 0.11	0.53	0.61 ± 0.03	3.09	3.08 ± 0.03
	10	1	3.54	4.38 ± 0.42	1.45	1.81 ± 0.15	2.44	2.47 ± 0.02
		3	3.10	3.80 ± 0.36	1.10	1.34 ± 0.11	2.82	2.88 ± 0.06
		5	2.76	3.39 ± 0.31	0.87	1.04 ± 0.07	3.17	3.26 ± 0.07
	12	1	5.92	8.42 ± 1.49	2.39	3.42 ± 0.36	2.47	2.55 ± 0.08
		3	5.14	7.23 ± 1.27	1.75	2.38 ± 0.26	2.94	3.12 ± 0.11
		5	4.56	6.44 ± 1.04	1.35	1.75 ± 0.19	3.39	3.67 ± 0.19
	14	1	11.0	17.0 ± 4.95	4.30	6.40 ± 0.68	2.55	2.66 ± 0.16
		3	9.33	14.4 ± 4.46	2.90	4.09 ± 0.53	3.22	3.53 ± 0.35
		5	8.21	13.8 ± 3.53	2.13	2.94 ± 0.40	3.85	4.63 ± 0.51
	16	1	27.3	86.1 ± 34.7	9.63	20.9 ± 2.72	2.84	3.64 ± 0.84
		3	22.0	69.9 ± 34.9	5.38	9.23 ± 1.81	4.08	6.36 ± 2.02
		5	18.9	62.5 ± 25.2	3.61	5.78 ± 0.74	5.24	10.5 ± 2.93
130	10	1	2.62	2.82 ± 0.25	1.10	1.19 ± 0.09	2.38	2.40 ± 0.01
		3	2.40	2.54 ± 0.23	0.92	0.98 ± 0.07	2.61	2.63 ± 0.02
		5	2.21	2.33 ± 0.21	0.78	0.81 ± 0.06	2.84	2.88 ± 0.04
	14	1	4.51	4.81 ± 0.34	1.89	2.01 ± 0.10	2.38	2.40 ± 0.01
		3	4.19	4.40 ± 0.30	1.58	1.65 ± 0.08	2.64	2.67 ± 0.02
		5	3.88	4.06 ± 0.28	1.33	1.36 ± 0.07	2.91	2.99 ± 0.04
	16	1	5.88	6.09 ± 0.45	2.46	2.54 ± 0.15	2.39	2.41 ± 0.01
		3	5.47	5.58 ± 0.41	2.04	2.06 ± 0.12	2.68	2.71 ± 0.02
		5	5.08	5.16 ± 0.38	1.70	1.68 ± 0.10	2.99	3.07 ± 0.05
100	8	1	2.81	3.17 ± 0.20	1.15	1.30 ± 0.07	2.45	2.43 ± 0.01
		3	2.42	2.83 ± 0.18	0.86	1.02 ± 0.05	2.83	2.75 ± 0.03
		5	2.12	2.56 ± 0.16	0.67	0.83 ± 0.04	3.18	3.08 ± 0.04
	10	1	4.67	5.49 ± 0.40	1.89	2.22 ± 0.12	2.47	2.47 ± 0.01
		3	4.03	4.86 ± 0.35	1.40	1.70 ± 0.09	2.89	2.86 ± 0.04
		5	3.57	4.41 ± 0.32	1.08	1.35 ± 0.07	3.29	3.26 ± 0.07
	12	1	7.85	9.44 ± 1.13	3.13	3.76 ± 0.27	2.51	2.53 ± 0.13
		3	6.73	8.30 ± 0.97	2.21	2.72 ± 0.20	3.04	3.05 ± 0.13
		5	5.94	7.53 ± 0.88	1.67	2.08 ± 0.15	3.55	3.62 ± 0.15
	14	1	14.7	18.7 ± 2.85	5.63	7.18 ± 0.67	2.61	2.67 ± 0.06
		3	12.3	16.0 ± 2.45	3.64	4.65 ± 0.47	3.38	3.53 ± 0.15
		5	10.8	14.6 ± 2.24	2.61	3.32 ± 0.31	4.12	4.39 ± 0.27
	16	1	37.9	257 ± 308	12.4	39.5 ± 8.68	2.97	4.05 ± 3.84
		3	29.9	94.9 ± 99.4	6.69	12.7 ± 2.54	4.47	6.99 ± 6.02
		5	25.7	76.6 ± 79.6	4.37	6.46 ± 1.42	5.88	10.1 ± 6.69
130	10	1	3.38	3.34 ± 0.22	1.41	1.40 ± 0.08	2.39	2.39 ± 0.01
		3	3.08	3.08 ± 0.20	1.16	1.18 ± 0.06	2.65	2.62 ± 0.01
		5	2.81	2.86 ± 0.19	0.97	1.00 ± 0.06	2.91	2.86 ± 0.05
	14	1	5.78	5.71 ± 0.55	2.41	2.35 ± 0.17	2.40	2.40 ± 0.01
		3	5.33	5.33 ± 0.51	1.98	1.97 ± 0.14	2.69	2.66 ± 0.02
		5	4.91	4.99 ± 0.48	1.64	1.67 ± 0.12	3.00	2.98 ± 0.06
	16	1	7.54	7.41 ± 0.67	3.13	3.10 ± 0.21	2.41	2.41 ± 0.01
		3	6.95	6.86 ± 0.61	2.53	2.53 ± 0.17	2.74	2.73 ± 0.02
		5	6.42	6.38 ± 0.57	2.07	2.07 ± 0.14	3.10	3.07 ± 0.08

In terms of geometrical variations, larger effective pixel areas will result in smaller recovery times, due to the decreased values of R_Q. Therefore, increasing the gap size will lead to reduced current flows and thereby increased recovery times.

The observation of higher measured recovery times compared to the simulations is consistent with findings of $V_{ob,max}$, since increased values of $V_{ob,max}$ translate to overall lower current levels and thus increased recovery times. The deviations are below 5% for a pitch size of 130 and increase with decreasing gap sizes. In the case of a 100 µm pitch, the deviation ranges from 13% to 40% for gaps 8 to 14, respectively, while gap 16 results in deviations of a factor larger than 3. These can be explained by the increased impact of the non-linearity of R_Q with increased gap sizes relative to the pitch.

Considering more stable geometries like the cases with a pitch of 130 µm, the impact of the technological parameters in the recovery times can be analyzed similar to $V_{ob,max}$ with the results being listed in Table 9.8. The same observations can be made, which are consistent with the ones of $V_{ob,max}$. Thus, the above explanation is also applicable for the deviations between the simulations and measured data of the recovery times. For illustration, two cases of a simulated recovery time at $V_{ob} = 5$ V with an adapted tilt of $\Theta_{ion} = 3°$ were included in Fig. 9.20, depicting a reduced deviation. Analogous to $V_{ob,max}$, the measured and simulated recovery times can be considered in good agreement with respect to the impact of the technological parameters.

In the case of the ratio $\tau_{90\%}/\tau_{1/e}$ an increase in the deviation from the theoretically expected value of 2.3 for increasing V_{ob}, as illustrated in Fig. 9.20b) and Table 9.9 can be seen. However, considering pitch/gap combinations in the operational regime such as 130/14 and 130/16, $\tau_{90\%}/\tau_{1/e}$ remains small (≤ 3) suggesting reduced non-linearity. The contrary is visible for increased relative gap sizes like in 100/16, which are close to a pinch-off scenario. In these cases the discrepancy between simulated and measured values of $\tau_{90\%}/\tau_{1/e}$ becomes larger, compared to the otherwise very good agreement for the majority of the analyzed pitch/gap combinations.

Summary

In summary, the goal of the static test devices can be considered achieved. For the first time, it was possible to access the bulk resistor directly to allow direct comparisons to the static simulations. Comparison and slight deviations to the simulated devices provided the means of an in-depth analysis and thus, it was possible to ascertain the type and level of impact of various technological parameters on the quenching and recovery behavior, which can be vital for future iterations of SiMPl. After identification and adaptation of the relevant parameters, a good agreement between measured and simulated data within this context could be achieved. Higher values of $V_{ob,max} > 3$ V can be obtained for larger gap sizes, making geometrical combinations like 130/16 or 100/12 feasible cases, if longer recovery times are not an issue. On the contrary, if shorter recovery times ($\tau_{90\%} < 450$ ns) at the cost of a reduced $V_{ob,max}$ are favored, reduced gap sizes will offer viable options like in the cases of 100/12 and 130/14. Due to the various geometrical combination, a proper trade-off adjusted to the application at hand should be achievable.

It has to be taken into account that the results of the static test devices will deviate from the ones obtained with actual SiMPl arrays to a certain extend, since the layout and thereby the depletion region within the bulk differs slightly. Nonetheless, the static test devices can still be utilized as an approximation for the choice of actual SiMPl arrays for in-depth testing.

9.2.3 Dynamic measurements of SiMPl4

After the initial static measurements and wafer level characterizations, devices for dynamic tests can be chosen according their determined performance. A total of 50 chips, 25 per batch, including all relevant pitch-gap-combinations were bonded to readout-carrier boards in order to allow measurements on the dedicated setups.

In terms of the dynamic measurements SiMPl4 devices can be divided in two categories with regards to their performance. First, are all arrays of the SiMPl4-1 batch featuring an aluminum grid located in the gap regions of the cells as described in Sec. 8.1.1. In order to assure proper contacting of said grid, an additional p^+ implant was deposited underneath it with a higher beam energy and thus depth compared to the topside entrance window p^+ implant. As a consequence, the depletion width within the bulk was increased, resulting in an increased R_Q in the case of the those devices. The other category of devices includes the remainder of SiMPl4-1 and all SiMPl4-2 chips.

The methodology behind the individual measurements was already explained in Sec. 5.3 and will be applied here, if not mentioned otherwise. The measurements will include amplitude spectra, followed by a detailed look at the dark current and dark count rates. Afterwards, an attempt at determining the optical cross-talk probability as well as the afterpulsing probabilty will be discussed.

9.2.3.1 Dark count rate

The dark count rate (DCR) was measured as explained in Sec. 5.3.5 while the overbias voltage V_{ob} and temperature T were varied throughout the procedure. An overall increased DCR compared to the previous SiMPl batch (SiMPl2) was observed in all cases. While studies of SiMPl2 [33] have shown that cooled operation was necessary due to the increased leakage current stemming from the deep n implant and its subsequent damaging impact on the crystal lattice of the surface layers, similar issues were expected for SiMPl4, albeit to a lesser extend, as some technological aspects were improved.

In general, the SiMPl4-1 devices with a gap grid exhibited a lower DCR compared to the rest of SiMPl4 and cooling was necessary in all cases. The lower DCR of the gap grid devices can most likely be attributed to the increased bulk resistor suppressing the current flow. Figure 9.21a) presents measurements of the DCR per mm^2 at various V_{ob} of a SiMPl4-1 chips with gap grid. The expected increase of the DCR with increasing V_{ob} can be seen for all temperatures, since the trigger probability for an avalanche breakdown also increases with V_{ob}. Contrary to [33], no increased steepness at higher V_{ob} can be observed. The opposite visible here with the DCR reaching a plateau at several tens of MHz for half of the investigated temperatures. It is likely that the array reaches saturation, leading to deviations from the expected response as seen in Sec. 5.3.9.

The equivalent measurements for a SiMPl4-2 device are shown in Fig. 9.21c). Compared to a) the absolute values of the DCR can be seen to be in the range of multiple MHz at $T = 233$ K while the SiMPl4-1 devices only reach roughly 200 kHz at the same temperature. For $V_{ob} = 1$ V a DCR larger by a factor of 100 can be observed in the non-gap-grid cases. Even at $T = 233$ K saturation will be reached due to the overall significantly higher DCR levels. While a gradual scaling with temperature could be observed in a), c) exhibits further saturation as an increase of T will only lead to minimal changes in the DCR as it reaches values above 10 MHz.

Comparing the results of a) to the ones obtained by [33] reveals absolute DCR levels several factors larger than the previously measured values of SiMPl2 and a difference of one order magnitude in the case of c) for similar voltage levels and temperatures.

The temperature scaling of the measured DCR merits further investigation. Accord-

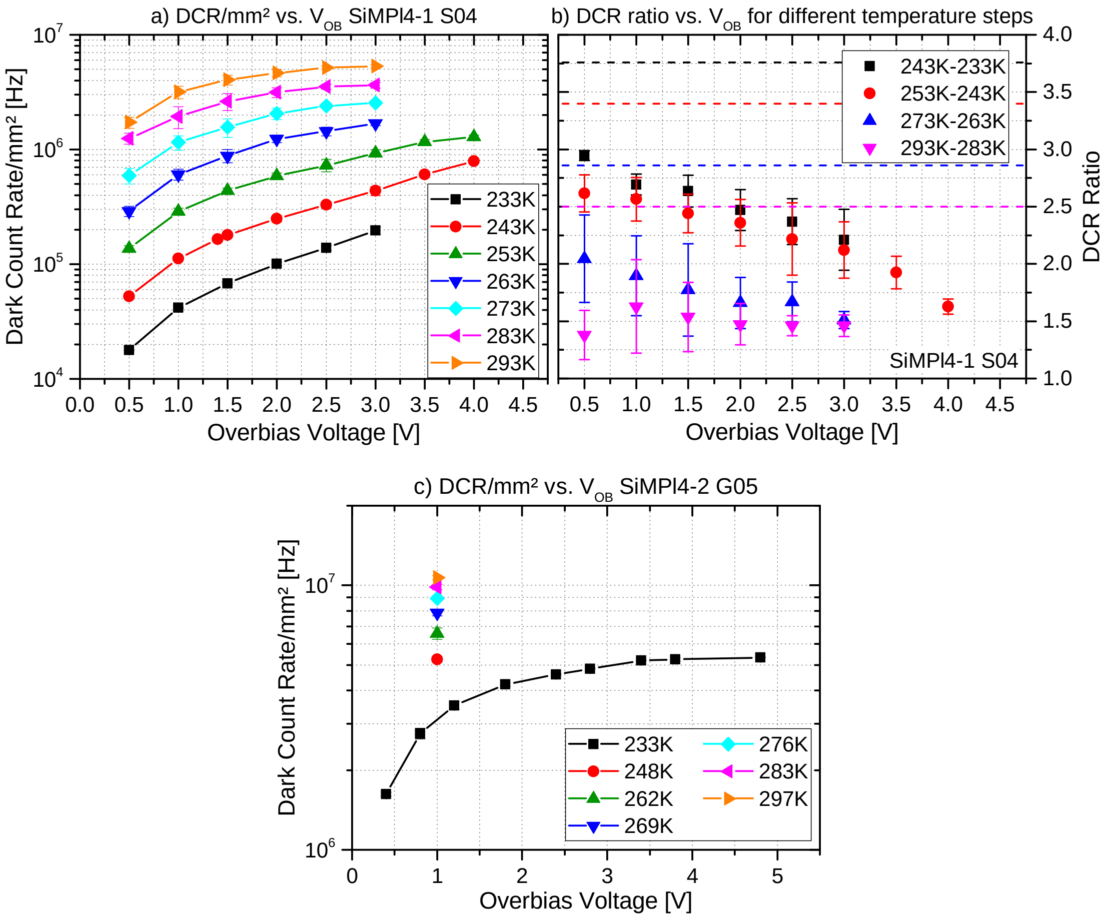

Figure 9.21: Measured DCR/mm^2 and the resulting ratio between the individual temperature steps. The same SiMPl4-1 10x10 array was utilized for the results shown in a) and b). In a) an increase of the DCR with increasing T and V_{ob} can be seen. Initial stages of a saturation trend can be observed at higher rates. In b), the ratio of the DCR for each temperature step can be seen for various V_{ob}, with the respective expected values as dashed lines of the same color. A clear discrepancy from the expectation becomes more apparent the higher V_{ob} becomes. An analogous data set of a) for a SiMPl4-2 device is shown in c). More distinct features of operation in saturation can be observed (see text).

ing to SRH a temperature scaling of the dark current and thereby DCR in silicon given by Eq. (5.4) can be expected. Figure 9.21b) depicts the DCR ratio of the measurements shown in a) for various temperature differences and overbias voltages. Detailed values can be found in the left hand side of Table 9.10 for $V_{ob} = 1$ V. The respective expected ratios for the various temperature steps are given as dashed lines of the same color as the data points. All measured instances show ratios below the expected ones. The ratio decreases with increasing absolute temperature and V_{ob}. For the temperature step 293 K – 283 K no significant changes of the DCR ratio are visible within the limits of the measurement error. Measured DCR ratios of the SiMPl4-2 device from Fig. 9.21c) at $V_{ob} = 1$ V are also given in Table 9.10 on the right. A similar trend can be observed, albeit more severe as the ratios for higher temperature steps result in values close to 1.

The decrease of the determined ratios for higher temperatures can most likely be attributed to the devices operating in saturation, thus not allowing the expected increase

Table 9.10: Measured DCR ratios for different temperature steps of SiMPl4-1 and SiMPl4-2 devices. Data taken at $V_{ob} = 1$ V. The expected ratios according to SRH for each step is also given. An overall deviation from the expected values can be observed for both SiMPl4-1 and SiMPl4-2. The ratios obtained for SiMPl4-2 are consistently close to 1 (see text).

SiMPl4-1 S04			SiMPl4-2 G05		
ΔT [K]	expected ratio	DCR ratio	ΔT [K]	expected ratio	DCR ratio
233 - 243	3.76	2.69 ± 0.09	234 - 248	6.11	1.59 ± 0.07
243 - 253	3.40	2.57 ± 0.19	248 - 262	5.07	1.25 ± 0.07
253 - 263	3.10	2.11 ± 0.28	262 - 269	2.12	1.20 ± 0.07
263 - 273	2.86	1.90 ± 0.35	269 - 276	2.04	1.14 ± 0.04
273 - 283	2.67	1.69 ± 0.44	276 - 283	1.97	1.10 ± 0.03
283 - 293	2.50	1.63 ± 0.41	283 - 297	3.55	1.08 ± 0.03

to occur. However, reducing the temperature to achieve DCR values in the range of hundreds of kHz should not lead to the arrays operating in saturation. Hence, a temperature scaling according to SRH statistics can be expected but was not observed for both categories of devices. Therefore, the assumption can be made, that an additional mechanism besides thermal generation contributes to the charge generation within the arrays.

In order to further analyze this issue, the Arrhenius plot of the measured DCRs can be determined. By plotting the logarithm of the DCR per area versus $1/(k_B T)$, with k_B being the Boltzmann constant, a linear fit can be applied to the data points, corresponding to a function $\sim \exp(-E_a/(k_B T))$, with E_a being the activation energy of the defects responsible for the DCR. According to SRH an energy close to midgap $(E_g/2)$ can be expected, as was the case for SiMPl2, seen in [33].

The results of this evaluation are shown in Fig. 9.22a) for SiMPl4-1 gap-grid devices and b) for a SiMPl4-2 device. The Boltzmann factor k_B is already incorporated into the x-axis and the logarithm of the measured DCR was calculated for the y-axis. The linear fits can be seen as red lines and allow the determination of E_a depending on V_{ob}. In a) values for E_a of 0.46 eV, 0.39 eV and 0.30 eV can be obtained for 1 V, 2 V and 3 V overbias voltage, respectively. All found values result in $E_a < E_g/2$ with a decrease in E_a with increasing V_{ob}. In the case of SiMPl4-2, E_a can be seen to be even smaller, leading to $E_a \approx 0.1$ eV for $V_{ob} = 1$ V. This result indicates more shallow defect levels with respect to the band gap in both cases as the cause for the measured DCRs of the devices.

All of the above results combined suggest that a process which does not adhere to SRH statistics and becomes more prevalent for increased voltages is contributing significantly to the dark current and thereby DCR. One such possible mechanism can be found in trap-assisted tunneling (TAT). In this process, free charge carriers within a depletion region can be created by electrons or holes tunneling into their respective band via an intermediate trap state within the band gap, as described by e.g. Hurkx [116]. These charge carriers can then be accelerated and potentially initiate an avalanche breakdown. This effect requires a sufficiently large electric field in the order of 10^5 V/cm or higher to start occurring, which is present during Geiger operation of the SiMPl devices.

The process of TAT does not follow SRH statistics and could therefore explain the

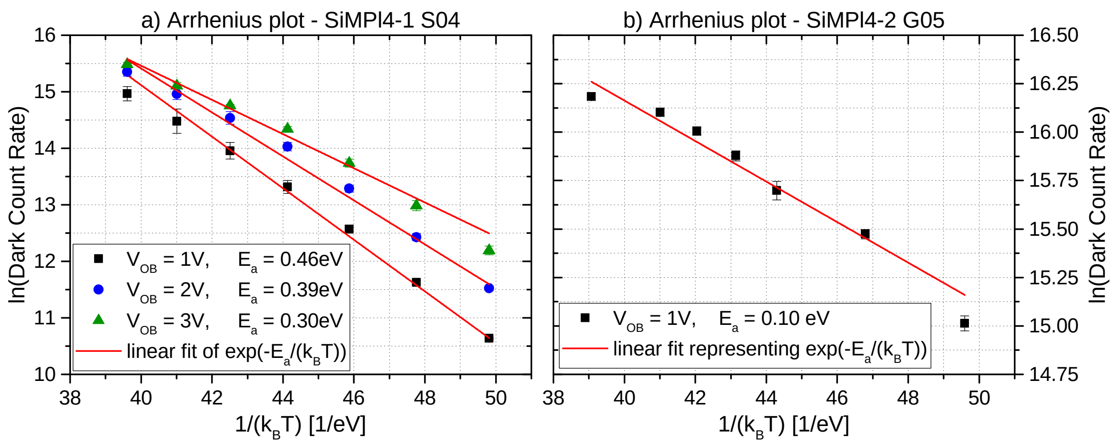

Figure 9.22: Arrhenius plot of the measured DCR of a) a SiMPl4-1 and b) a SiMPl4-2 device. Data of a 10x10 array at different V_{ob} was analyzed. The natural logarithm of the DCR was taken, thus allowing to apply a linear fit to the data, which corresponds to an exponential decay, in order to determine the activation energy E_a of the defects, responsible for the measured DCR. This procedure yielded a slightly more shallow levels of E_a compared to $E_g/2$.

temperature scalings observed in Fig. 9.21 and Table 9.10 for lower temperature steps, since increased amounts of current would be created in addition to the thermal contributions. Increasing deviation from the expected DCR ratio for increased V_{ob} can be attributed to higher contributions from TAT at increased electrical fields. This is also reflected in the results of the Arrhenius plots and the extracted E_a. A more shallow energy level can be the result of multiple defect level contributions with a portion being more shallow than mid gap. By increasing V_{ob}, an increased number of these shallow defects will start contributing due to the increased electrical field, thus reducing the extracted E_a further. The overall higher DCR of SiMPl4-2 devices and the extracted values of $E_a \approx 0.1$ eV can be interpreted as a generally higher concentration of these defect states being responsible for the observations made.

This assumption would furthermore coincide with the findings of Sec. 9.2.2.1, namely the early point-like breakdowns as well as the hot-spots. It is possible that all three issues originate from the same underlying mechanism and are symptoms with different levels of severity. This will be investigated in more detail in Sec. 9.6.

9.2.3.2 Amplitude spectrum

The amplitude spectra of several SiMPl4-1 and SiMPl4-2 chips were recorded in complete darkness at $T = 253$ K. A measurement window with respect to the trigger event of 10 ns was defined and the waveforms were evaluated for multiple overbias voltages.

The resulting amplitude spectrum can provide information on the overall device performance, since effects like edge breakdown or inhomogeneities in the gain will manifest themselves as broadening of the individual photoelectron peaks. All SiMPl4-2 devices as well as the SiMPl4-1 devices without the gap grid exhibited a behavior similar to the one displayed in Fig. 9.23a). The plot depicts the resulting amplitude spectrum of a 10x10 array, measured at $V_{OB} = 3$ V. It appears as if only the first two p.e. peaks are present with the second one being broadened by parasitic effects. This, however, cannot be stated with certainty as the observed waveforms culminating into the shown amplitude spectrum clearly also displayed higher amplitudes, surpassing the supposed height

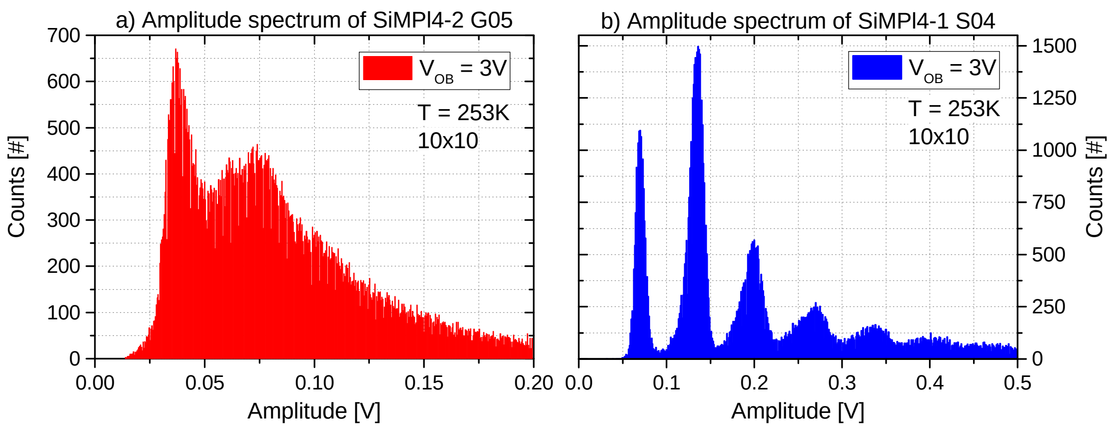

Figure 9.23: Measured amplitude spectra of two different SiMPl4 devices. In both cases the measurement was taken at $T = 253$ K and $V_{OB} = 3$ V. Spectra similar to the one shown in a) can be witnessed for the majority of the investigated device, supposedly featuring only two p.e. peaks which appear to be very broad and can thus be interpreted as not suitable for further characterizations (see text). A small fraction of SiMPl4-1 chips, on the other hand, features amplitude spectra comparable to the one displayed in b). Here, the five/six p.e. peaks can be distinguished but are still affected by the increased DCR and other issues (see text).

of the 2 p.e. amplitude. In addition due to the increased dark count rate in those cases a clear baseline could not be defined, which in turn also makes a distinction between regular photoelectron pulses and afterpulses impossible. Thus, no further information can be extracted from these amplitude spectra.

SiMPl4-1 chips featuring a gap grid exhibited the behavior shown in Fig. 9.23b). An amplitude spectrum of a 10x10 device at $V_{OB} = 3$ V is presented with 5-6 clearly distinguishable photoelectron peaks. This is comparable with a measurement with low light level illuminations further illustrating the impact of the increased DCR. Furthermore, the shape of the peaks is also affected by the increased DCR and baseline jumping, as the peaks are broad and become indistinct for higher numbers of fired cells. By analyzing the distance between two photoelectron peaks U_Δ, the gain G of the device can be extracted via Eq. (5.1), resulting in $G = 2.1 \cdot 10^6$ for the example shown in Fig. 9.23b). However, due to the issues presented in the previous section and their detrimental effect on the performance of the devices, a detailed analysis in this regard was omitted. A more detailed reasoning for this decision will be given at the end of this investigation in Sec. 9.2.3.5.

9.2.3.3 Optical cross talk

Due to the fact that optical cross-talk (OCT) in SiPMs is caused by hot carrier luminescence during the avalanche breakdown process, the increased dark count rate discussed in the previous section will have a severe impact on the optical cross-talk of SiMPl4 devices. Even though, many factors contribute to the OCT, like gain, pitch and gap size and V_{ob}, it will be shown that both SiMPl4 batches will be dominated by the excess in DCR in this regard. The OCT was determined using the methods explained in Sec. 5.3.6. By comparing the dark count level at a 1.5 p.e. threshold to the one at 0.5 p.e. threshold, the OCT can be calculated with the help of Eq. (5.6).

An example of such staircase plots for a 10x10 array of one of the SiMPl4-1 chips with

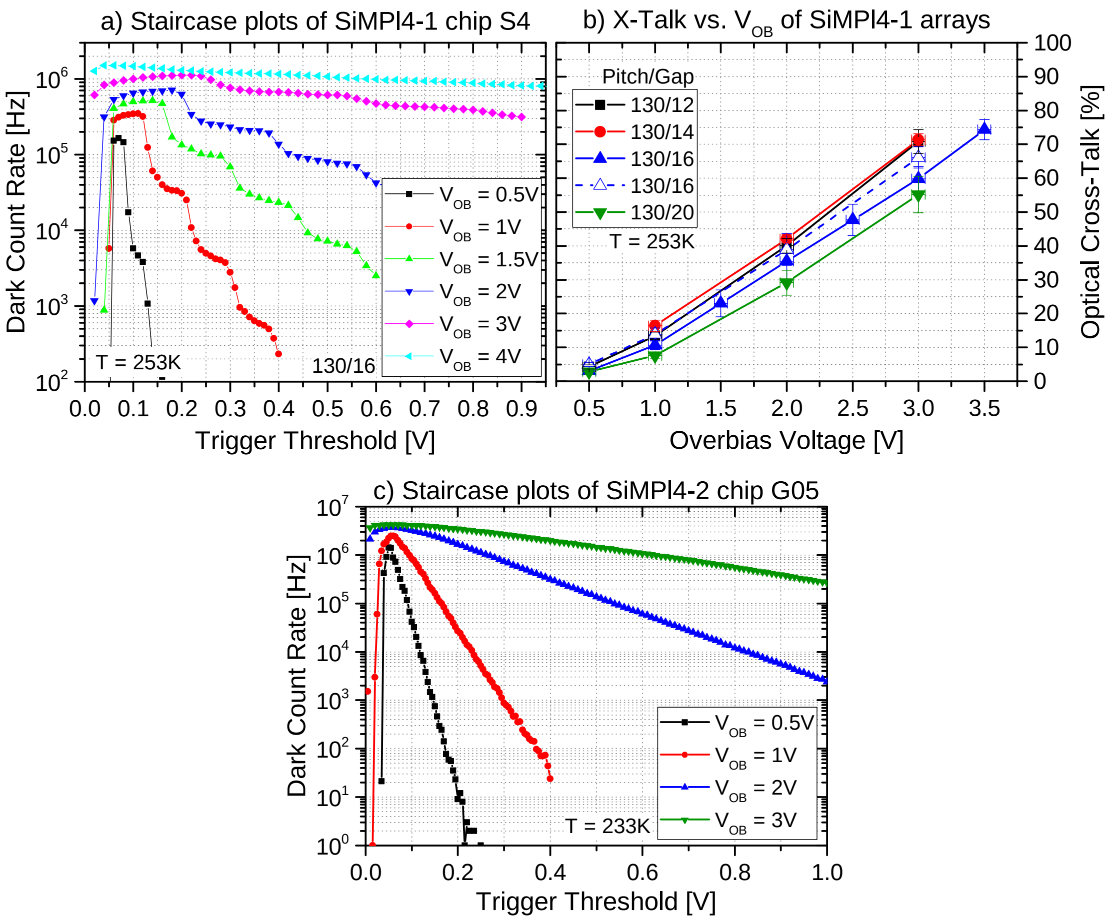

Figure 9.24: Staircase plots of two SiMPl4 chips for different V_{ob} and the respective optical cross-talk probability. Both chips featured a 130 µm pitch with a gap size of 16 µm and a 10x10 array was utilized for measurements. The staircase plots in a) and c) show the DCR at different trigger threshold levels measured at $T = 253$ K with the different colored lines each represent a different V_{ob}. Only plots like a) could be facilitated to determine the OCT probability as shown in b). Here, a slightly non-linear increase with V_{ob} can be observed, however the overall levels are higher than expected (see text).

a gap grid is given in Fig. 9.24a). The device in question features a pitch of 130 µm and a gap size of 16 µm with hexagonal shaped pixels. The DCR is shown for varying trigger threshold levels and the different colored plots each represent an overbias voltage ranging from 1 V to 4 V. All measurements were taken at $T = 253$ K. A distinct staircase trend is visible with the various DC levels corresponding to the individual p.e. thresholds. The overall level of dark counts increases with V_{ob} stemming from an increased gain and trigger probability for an avalanche breakdown. Above $V_{ob} = 4$ V, no distinct DC levels are detectable any longer, thus preventing the determination of the OCT.

The resulting optical cross-talk probability at different V_{ob} of this device and other SiMPl4-1 10x10 arrays with the gap grid and different pitch/gap combinations is depicted in Fig. 9.24b). The expected non-linear increase can be observed, albeit less pronounced than in previous measurements. This can be explained by the gain and Geiger probability increasing as well with V_{ob}. An increased gap size results in smaller overall OCT levels as seen in the case of 130/20 with roughly 55% for $V_{ob} = 3$ V. The highest levels can be seen for 130/12 and 130/14, which is generally unexpected as the smaller gap size should result in higher OCT contributions. An OCT probability for $V_{ob} = 3$ V of 70% was derived for these cases. Discrepancies between the two 130/16 devices are visible, indicating deviations on chip level, as both were 10x10 arrays of the same SiMPl4-1 chip.

Compared to the non-optimized batch of SiMPl2, the obtained values are considerably higher, with a pitch/gap combination of 130/12 reaching roughly 40% for $V_{ob} = 2$ V. In contrast, a device of the SiMPl2 batch with the same pitch/gap combination only reached an OCT probability of approximately 25% at $V_{ob} = 2$ V measured at $T = 253$ K.

The behavior of the remaining SiMPl4-1 chips and the entirety of the SiMPl4-2 chips is depicted in Fig. 9.24c). It illustrates the same measurements as a) with a SiMPl4-2 10x10 array at $T = 233$ K. As can be seen, no actual "staircase" is visible in the measured data, resulting in the absence of distinct dark count levels for different trigger thresholds at all overbias voltages. Consequently, a determination of the OCT probability becomes impossible. Measurements at $T = 253$ K exhibited the same behavior, hence the temperature was reduced to 233 K in an attempt to limit the DCR and to enable the formation of the required "staircases".

In conclusion, the impact of the previously shown increased DCR can be clearly seen to negatively impact the optical cross-talk characteristics, thereby degrading the performance of the measured devices. In light of this and the findings of Sec. 9.2.3.1 it was deemed not feasible to continue with an in-depth analysis of the OCT. A more detailed reasoning for this decision will be given at the end of this investigation in Sec. 9.2.3.5.

9.2.3.4 Afterpulsing

Attempts at determining the afterpulsing probability were made with all available chips of SiMPl4-1 and SiMPl4-2. Defects present within the detector bulk can trap charge carriers and release them again after a characteristic delay time τ, thus decreasing the single photon resolution of the devices, since the released charges can trigger additional avalanches. This investigation was of particular interest, as every defect has a specific delay time and determining the corresponding τ to the defects causing the previously discussed issues might be able to give more insight into the nature of these defects.

The measurements were performed according to the methods explained in Sec. 5.3.7 at various temperatures and overbias voltage. Figure 9.25 depicts one of the resulting time spectra of a 10x10 array determined at $T = 233$ K and $V_{ob} = 1$ V. All tested devices exhibited similar time spectra for all tested temperatures and overbias voltages. Contrary to the previously demonstrated time spectrum, no distinction of two separate contributions within the spectrum can be detected. Compared to Fig. 5.11, where an increased count rate for smaller Δt was visible, here only one component can be observed which appears to be similar to the thermal contribution of Fig. 5.11.

Attempting to apply a double exponential decay fitting function to the data yields the red curve and the two extracted delay times of $\tau_1 = (350 \pm 552)$ ns and $\tau_2 = (227 \pm 69)$ ns. The corresponding single exponential decay components are also illustrated as blue and green lines. Compared to the overall fit function, it appears that only one of the components contributes significantly (green line) while the other (blue line) has only a negligible impact. This can also be seen in the delay times extracted, as τ_1 features an absolute error of almost a factor 2 of the value itself. In addition, both τ are in the same order of magnitude which is also commonly not observed.

It could be assumed that no afterpulsing contribution was measured due to the previously experienced high dark count rate, thus resulting in only visible contributions from the thermal component. This assumption, however, is in contrast to the extracted

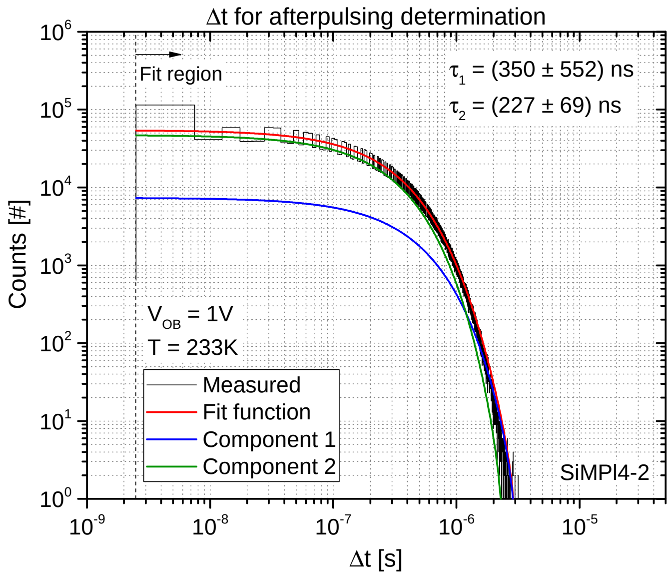

Figure 9.25: Attempt at a afterpulsing measurement with SiMPl4 chips. The time spectrum was measured with a 10x10 array at $T = 233$ K and $V_{ob} = 1$ V. Contrary to expectations, no clear distinction of two or more components can be made as the resulting curve appears to feature only thermal contributions if compared to the shape of Fig. 5.10. Applying a double exponential decay fit (red line) yields the two time constants τ_1 and τ_2 both featuring values uncharacteristic for thermal contributions. Plotting the corresponding function to the measured data reveals the other colored lines (blue and green), of which one seems to dominate in terms of contribution to the overall fit function. See text for details.

τ_i if compared to the usually observed delay time for thermal components which was measured to be in the order of tens of µs. It is thereby unclear if the observed shape pertains solely to the thermal contribution or if multiple components are present but the overall measurements are heavily impaired by the issues discussed in previous sections. Therefore, extracting the afterpulsing probability from the measured time spectra of the available chips was not possible.

9.2.3.5 Conclusion

Following the above investigations, it was apparent that SiMPl4 was affected by an uncharacteristically high dark count rate and other potential issues in addition to the point-like early breakdowns seen during wafer characterizations. Even in the case of the handful of SiMPl4-1 device less restricted by the increased DCR, the dynamic measurements still lead to results inferior to the previous prototypes of SiMPl2. Furthermore, all other tested chips could not provide data which could be analyzed to determine certain aspects like the optical cross-talk probability or the afterpulsing probability.

Regarding the data of the SiMPl4-1 chips with a gap grid, it was not completely evident what caused the results to be sub-par compared to the previous batch or if the quality of the results was directly linked to the overall issues present on the wafers. Due to the latter being very likely, it is therefore also uncertain in which capacity these issues are impacting the measurements seen in the above sections. While trap-assisted tunneling seems to be the most likely cause for the issues at hand, it is not possible to ascertain the exact level at which the overall quality is impacted. Hence, it lies in the realm of possibility that these results are completely dominated by the issues affecting the wafers. It is, for example, not known if the early breakdowns and the increased DCR are directly connected or separate issues altogether, as the origin of said conundrums could not yet be identified.

Therefore, it was concluded to forgo further detailed dynamic characterization of the SiMPl4 devices until it would be possible to properly decouple the exhibited behavior from the issues present in the batches. It was instead decided to focus on investigating said problems in order to allow for a thorough understanding of the cause and underlying mechanisms. This procedure will be covered in Sec. 9.6.

9.2.4 Summary

By incorporating the conclusions and possible improvements of SiMPl3, as well as taking the drawbacks encountered in SiMPl2 into account, SiMPl4 was aimed to be the next major batch for photon detection devices.

In a first step, additional technological simulations in order to improve the optical entrance window were performed and provided the necessary technological data needed for the implementation in the processing procedure. Stationary simulations allowed the extraction of crucial parameters like the maximum potential overbias voltage $V_{ob,mx}$ at which quenching would still be possible, as well as the recovery times $\tau_{90\%}$ and $\tau_{1/e}$, giving a first estimate on the expected timings of the final devices and allowing to identify the most feasible pitch/gap variation for production, thus avoiding effects like pinch-off and non-quenching. In addition, an approximation for the breakdown voltage V_{bd} could also be gauged within the simulation framework. Finally, transient simulations offered means to estimate the cell and quench capacitances C_D and C_Q, respectively and thus another method of obtaining the recovery time. A comparison of the recovery times obtained by both methods showed good agreement, further validating the simulation framework.

With all simulated results providing enough data for the production of the SiMPl4-1 and SiMPl4-2 batches, the first wafers were analyzed in multiple regards. While a sufficient amount of devices showed promising first results in terms of static I-V-measurements, a significant number also featured early point-like breakdowns, dominating the behavior of the affected arrays as well as hot spots within certain arrays. Nonetheless, the static measurements were able to confirm the simulated breakdown voltage to a satisfying degree and the thorough analysis of the novel static test devices also offered a first-time opportunity to compare the static simulations to actual experimental data. It was possible to attribute the observed deviations to different technological parameters and a good agreement could thereby be found between simulations and measurements within this context. Thanks to this investigation, the most promising pitch/gap variations depending on the possible application could be determined.

Finally, an attempt at dynamic characterizations of the SiMPl4 devices was carried out. Even though, devices with proper breakdown behavior were utilized, the results were dominated by a strongly increased dark count rate and unstable baseline, making proper dynamic characterizations nearly impossible and the endeavour was deemed not feasible, as it was not certain wether the overall findings would be inherent to the devices or results of the issue at hand. Considering the results of the wafer level analysis, an increased defect concentration and as a result an increased impact of TAT seemed to be the likely explanation for the observed behavior. In addition, judging from the statistics of the measured devices it can be assumed that all devices on the available wafers will be impacted by similar problems. It was speculated that these issues are connected to the early point-like breakdowns and will be explored in more detail in Sec. 9.6.

9.3 Fifth prototype - SiMPl5 (DSiMPl)

SiMPl5 was contrived with application in particle tracking (DSiMPl) in mind as explained in Sec. 6.4. The development took place parallel to SiMPl4, resulting in similar issues affecting SiMPl5. Due to the intended incorporation of active quenching and readout electronics, the focus of the simulation and experimental studies shifted in terms of main topics. The simulation procedure and results will be discussed first, detailing certain novel aspects which needed to be considered for SiMPl5 in contrast to all previous prototypes. Afterwards, the current progress regarding experimental investigations of SiMPl5 devices will be presented, including multiple types of test devices located on the wafers. Lastly, the current progress of the DSiMPl project will be discussed, as well as a future roadmap.

9.3.1 Simulation studies of SiMPl5

The overall simulation procedure of SiMPl5 is similar to the one presented for SiMPl4, albeit with a shift in the focus in order to accommodate for the different application in mind. Similar to SiMPl4, all technological improvements gained from SiMPl3 were adapted in the technological element of the simulation, however, other aspects were prioritized, due to the intended application, hence, no entrance window engineering was performed.

Instead issues including the distance of certain implantations, as well as the total thickness of the devices were investigated. This also translated into the follow-up task, namely the stationary simulations, in which the impact of the thickness and other variables on the total resulting backside resistor and its linearity were analyzed. Lastly, transient simulations were carried out, however not the recovery timings were of interest, as the cell recharge will be handled by the electronics, but the expected voltage drops and the extraction of parameters like the vertical capacity C_{vert} (formerly C_Q) and others potentially impacting the readout electronics.

9.3.1.1 Technology process simulations

For the most part, the simulation procedure regarding the technology processing of SiMPl5 is comparable to the previously explained one for SiMPl4. However certain differences arise due to the nature of the intended application, thus requiring additional or, in some aspects, less simulation work to be performed.

Again, various parameters involving the p^+ and deep n were investigated, although, since there was no necessity for an optical entrance window, the requirements for the former and the final topside layer composition were more relaxed. Overlapping issues were already discussed during the investigation of the SiMPl4 batches.

However, by implementing a structured p^+ topside implant a novel issue needed to be addressed in order to avoid a form of edge breakdown, unlike the one previously encountered. As already shown, stemming from the implant particle beam being slightly non-perpendicular to the wafer surface, the deep n profile will exhibit a "tail" towards the surface. Combined with a structured topside implant, this can lead to suggested edge and lateral breakdowns if the distance of the edges of both implants is not optimized.

This issue is illustrated in Fig. 9.26, showing the cases for a distance z_e of the edge of the deep n and the p^+ implants of 0 µm (left) and 2 µm (right). The upper row depicts the doping concentration of the gap area between two pixels and the lower one the resulting absolute electrical field for the same area. It is easy to see that a choice of z_e = 0 µm would lead to an increased electrical field at the edge area of the pixel,

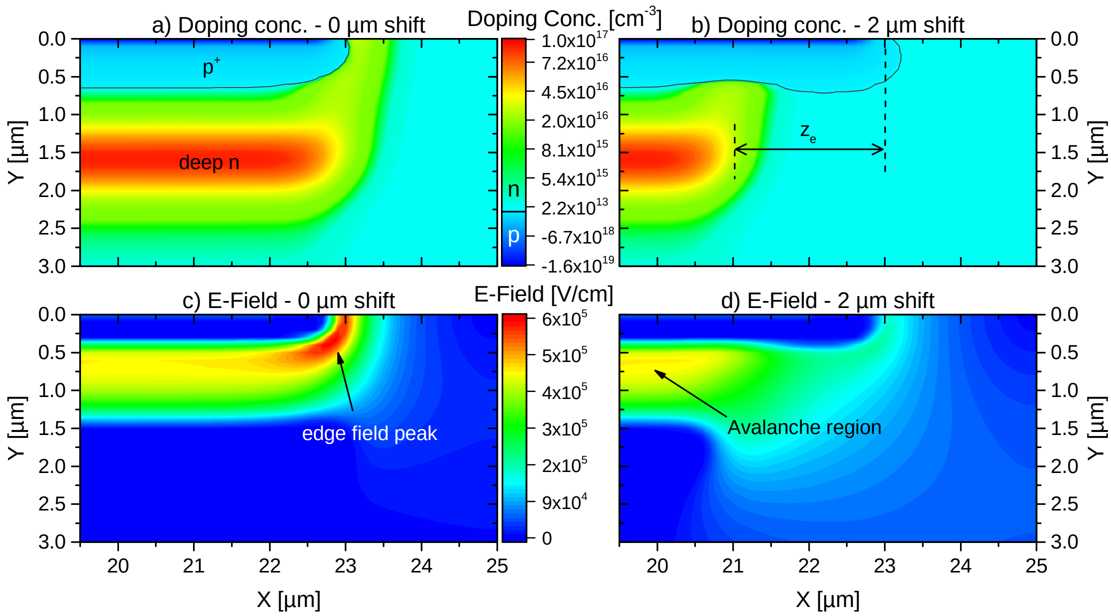

Figure 9.26: Zoomed-in cross-section of the simulation layout of SiMPl5 prototypes for the investigation of the requirements for the distance between the edges of the p^+ and deep n implants. The picture focuses on the edge region of an pixel with a) and b) depicting the doping concentration and c) and d) the resulting absolute electrical field for the same area. Two different distances z_e are illustrated with $z_e = 0$ µm on the left and $z_e = 2$ µm on the right. The potential danger of edge breakdown can be identified for values of z_e below a certain threshold (see text).

which would very likely result in edge breakdown or even possibly a lateral breakdown in those regions. In order to avoid this potential problem, z_e was increased in increments until a solution with an additional margin for error was found which did not exhibit this behavior. The simulations yielded that a minimum of $z_e = 1.5$ µm was required to avoid the aforementioned issues, as can also be seen in the right hand side of Fig. 9.26. Here $z_e = 2$ µm and the resulting absolute electrical field implies a uniform breakdown behavior within the entirety of the high-field region.

Theoretically, choosing a large value for z_e without additional simulations would have been sufficient to avoid the issue, however, increasing z_e would also mean reducing the fill factor of the final array. Therefore, in order to provide the maximum possible detection efficiency, the minimum safe distance z_e needed to be extrapolated. The final designs on the wafers incorporated this result but also added further values of z_e ranging from 1.5 µm to 6 µm for testing purposes.

In regards to the distance between two adjacent p^+ implants, denoted as p-gap, previous studies [117] have shown that p-gap sizes of 2 µm or less will result in couplings between the two implants. Therefore, p-gaps of 3 µm and 4 µm were chosen and few instances of 2 µm sizes were also included for testing purposes. This leads to a minimum gap sizes between the deep n implants, making this the effective gap size, of 6 µm and a maximum of 15 µm included in the first prototype batch.

9.3.1.2 Stationary simulations

It was already explained in Sec. 6.4 that due to the active quenching approach for DSiMPl, the readout electronics will be responsible for the quenching and recover of the

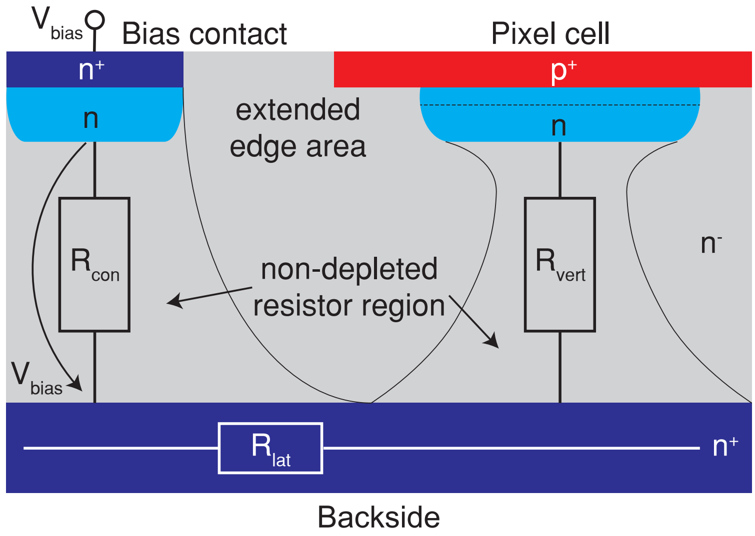

Figure 9.27: Schematic illustration of the different contributions to R_{back} in the case of a DSiMPl sensor device (not to scale). R_{vert} is defined in the same fashion as for the classical SiMPl devices by the non-depleted volume underneath the high-field area. The horizontal sheet resistance is given by the backside implant and might contribute to R_{back} and, in addition, lead to a voltage drop for the applied bias voltage. The same holds true for R_{con} which is defined by the biasing contact at the edge of the device (see text). Note that the depiction is not to scale, meaning that the distance between the outermost pixels of an array and the edge area with the biasing contact are multiple pixel pitches apart.

individual cells within the array. As a consequence, the requirements on the detector bulk become less demanding, since it is no longer a crucial part of the quenching and recovery cycle, thus allowing for optimization in different aspects. Considering tracking applications, small cell sizes and minimal thicknesses of devices are desirable but cannot be chosen arbitrarily. Now, new specifications have to be met in order to be compatible with the electronics or to be feasible from a design aspect.

The first major issue lies in the resulting resistance value of the backside contact of the devices. It will be connected, for biasing purposes, via a topside contact to the electronics, which have certain limitations in regards to resulting resistance, thus imposing a limit on the parameter space of the design of the devices. In terms of the maximum allowed backside resistance that will be experienced by the electronics, a limit of roughly $R_{back,lim} \approx 1\ \text{k}\Omega$ was given in order to assure optimal performance. While reaching this value would still not result in a non-working condition, an as low as possible value would be desired for improved operations.

When considering the backside resistance, three different components have to be taken into account:

$$R_{back} = R_{vert} + R_{sheet} + R_{con}\ . \tag{9.1}$$

First, the vertical constituent resulting from the non-depleted area underneath the avalanche region R_{vert}, which was previously the quench resistor, second, the horizontal sheet resistance R_{sheet}, present throughout the whole structure and defined by the backside implant, and third, the vertical resistor of the topside contact (most commonly the cutting edge) resulting between top and backside R_{con}.

These three components are illustrated in more detail in Fig. 9.27. Since the backside is contacted via the cutting edge at the top of the devices, the latter two components have to be considered, not only because of the additional resistance resulting from them but also because of the possibility of a voltage drop across R_{con} and R_{sheet}, which would lead to a reduced effective bias voltage applied to the devices. R_{con} can be obtained with the common resistance formula

$$R = \varrho \, \frac{l}{A} \; , \tag{9.2}$$

where l is the length and A the area of a resistor with resistivity ϱ. According to Eq. (3.8), ϱ is directly tied to the doping concentration of the material, thus by choosing appropriate parameters for the n^+-topside contact in combination with the deep n high-field implant, significantly low values for ϱ_{con} can be achieved. This will also be aided by the backside implant, which diffuses into the bulk due to the wafer bonding process. In addition, the contact area A_{con} can also be chosen freely (to a certain extend) to further decrease the influence of the bulk doping component. By combining those measures, a negligibly small R_{con} can be achieved, leading to a negligible additional contribution or voltage drop.

The sheet resistance R_{sheet} is independent of the size of the device and defined by the backside n^+ doping. It can be simulated within the Synopsys framework and was extracted for the utilized backside doping profile. In addition, a rough estimate can be made, taking the backside doping into account. The estimate and simulation yielded the following results:

$$R_{sheet}(\text{est}) \approx 6\ \Omega/\square \qquad \text{and} \qquad R_{sheet}(\text{sim}) \approx 8\ \Omega/\square \; .$$

Both results can be seen to be in very good agreement and suggest that no significant impact can be expected due to the sheet resistance in terms of a voltage drop. Regarding the subject of a total resistance contribution, the issue depends on the final values for R_{vert}. However, it will be shown in the following, that for the parameter space in question and for the resulting values for R_{vert}, R_{sheet} will not lead to any impactfull contributions and can thus also be neglected. It should be noted that a direct measurement of the sheet resistance for confirmation was not possible with the available devices, as biasing was achieved via the cutting edge and there would always be contribution from R_{cut}, which is not well defined for the current batch, but can nevertheless assumed to be of no consequence for the total resulting backside resistance.

Taking the above findings into consideration, it can be deduced that the total backside resistance will be dominated by the bulk resistor $R_{back} \approx R_{vert}$. Since the effective doping concentration of the bulk is already fixed, only the thickness of the devices and individual cell size can be adapted to meet the imposed requirements. The pitch was chosen to be 50 µm and the gap sizes were chosen in accordance to the results of the previous section, as well as from experience from previous SiMPl batches and the general desire for a high fill factor.

The simulations for this issue did not make use of the static test device layout, since the goal was to estimate the final resistance of the actual devices, which also include a structured p^+ contact. Hence, this and the outcome of Sec. 9.3.1.1 had to be taken into account, eventually resulting in the schematic of the simulation layout depicted in Fig. 9.28. Equal to the previous cross-section layouts, only one half of the cell and half of the neighboring one are depicted since the simulation will be performed in quasi 3D via cylindrical approximation, which is, again, achieved by rotation around the axis $x = 0$. Similar to the static test devices, an auxiliary contact is required in order to have access to the internal anode, formed by the deep n implant, thus reducing the size of the p^+ topside implant.

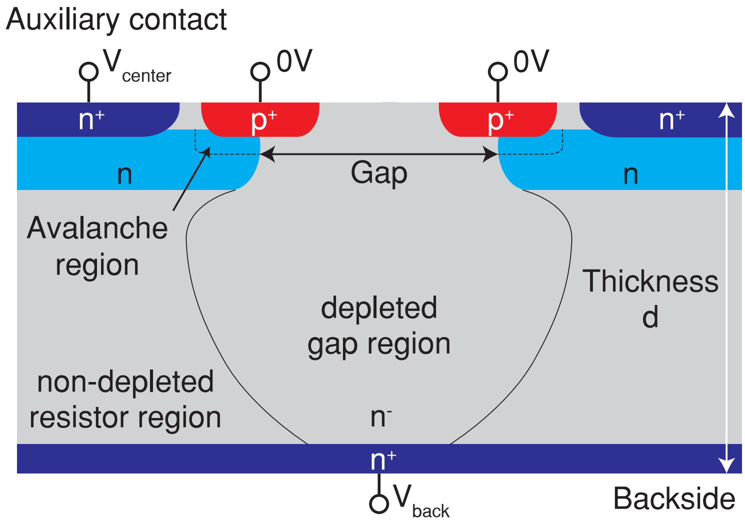

Figure 9.28: Schematic cross-section of the prototype device for first simulation studies of DSiMPl. Contrary to the static test devices, this layout features a segmented p^+ topside implant for the central and edge pixel. The aim is to investigate the technological and device specific limitation on the choice of structure thickness for future devices. The incorporation of auxiliary contacts and the device simulation procedure itself is similar to that of the recovery simulations shown in previous sections. By measuring the current between V_{center} and V_{back} the vertical resistance R_{vert} can be extracted (see text). Avalanche generation was turned off during the simulation.

The gap sizes for this simulation study were 8, 10, 12, 14 and 16 µm with respect to the distance of the two neighboring deep n implants (h-gap). To avoid edge breakdown, a safe distance of the edges of the p^+ and deep n implant of 3 µm was chosen. Therefore, the p-gap for each h-gap case is given by p-gap = h-gap − 6 µm. Note, that this will result in a p-gap of 2 µm for a h-gap of 8 µm, which is not feasible in practice, since it will most likely lead to capacitive couplings between the two neighboring p^+ contacts, but will be included in the scope of the simulations as this effect will not be of significance for static procedures.

The final parameter influencing R_{vert} is the thickness of the device, as it will effectively change the length of the vertical resistor. This will impact R_{vert} two fold, since it also increases the fraction which is defined by the bulk resistivity and not the backside. This was not an issue, when dealing with devices designed for single photon detection applications as their thicknesses were sufficiently large. However, in the case of SiMPl5, a minimal possible thickness is desired so that a low mass detector concept can be achieved. As will be shown below, this will result in a dominant impact of the backside implant on the structures for certain thicknesses. This discussion will also tie into the investigation of the previous section, since the thickness of the devices is another important technological parameter that needs to be analyzed via process simulations beforehand. But, due to its direct relation to R_{back} it was chosen to cover it here rather than in Sec. 9.3.1.1.

When considering the need for low mass detectors, one would instinctively aim at as low as possible thicknesses. In a first approach, simulations with thicknesses d_{ini} of $d_{ini,1}$, $d_{ini,2}$, $d_{ini,3}$ and $d_{ini,4}$, with $d_{ini,1} < d_{ini,2} < d_{ini,3} < d_{ini,4}$ ranging from 7 µm to 13 µm were performed and the feasibility of the results in terms of general functionality was

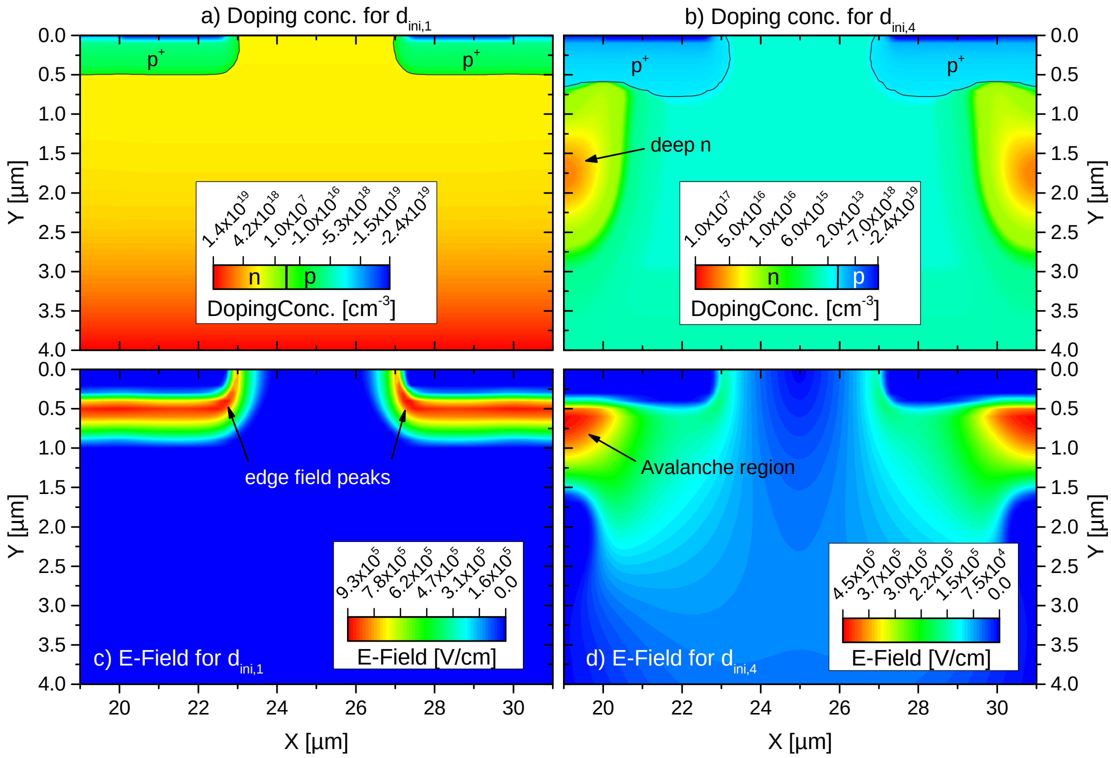

Figure 9.29: Illustration of the impact of device thickness on the overall feasibility via TCAD simulations. The doping concentration (negative concentrations translate to p-type doping) for structures with thickness $d_{ini,1}$ (left) and $d_{ini,4}$ (right) is depicted in a) and b) while c) and d) show the resulting absolute electrical field after applying V_{bias} to the backside. Note that the scaling in all plots is not shared due to the extreme difference in resulting concentrations/fields. The necessity for a minimum thickness d_{min} is apparent, due to the potential danger of increased edge breakdown at the segmented p^+ topside implants for smaller values of d.

investigated. An example of the results is presented in Fig. 9.29, showing the comparison of structures with $d_{ini,1}$ and $d_{ini,4}$. The doping concentration is depicted in a) and b) while c) and d) show the resulting absolute electrical field when a biasing voltage at the backside of 37 V is applied. From this it is already apparent that a minimum thickness will be required in order to facilitate proper operations.

In the case of $d_{ini,1}$ (a) and c)), the entire bulk of the device will be dominated by the backside implant. The deep n implant will not be distinguishable any longer, leading to the creation of a high-field area, formed between the top and backside dopings. Combined with the need for a structured p^+ topside implant, this will result in an increased absolute electrical field in the edge region of the structured p^+ topside, thus consequently being responsible for increased edge breakdown. In contrast, by increasing the thickness to i.e. $d_{ini,4}$, as shown in Fig. 9.29b) and d), the deep n will still be distinguishable from the backside and the resulting electrical field indicates no significant risk of edge breakdown occurring in the device.

From this first investigation, it could be established that a minimum thickness of $d_{min} = d_{ini,3}$ will be required in order to obtain a well defined high-field region and avoid running into trouble with edge breakdown issues. Therefore, the next simulation step, aiming to determine R_{vert} for feasible values of d as well as the aforementioned geometrical variations, featured thicknesses ranging from a minimum of d_{min} up to d_5, with

$$d_1 = d_{min} + 2\ \mu\text{m}$$
$$d_2 = d_{min} + 3\ \mu\text{m}$$
$$d_3 = d_{min} + 4\ \mu\text{m}$$
$$d_4 = d_{min} + 5\ \mu\text{m}$$
$$d_5 = d_{min} + 6\ \mu\text{m}.$$

The design of the previous simulations was again utilized for this step. In order to obtain the most accurate depiction of the behavior of R_{vert}, the procedure to extract the recovery I-V-curves from previous sections was mimicked. Both p^+ contacts were kept at a 0 V bias voltage. The auxiliary contact for the center pixel and the backside were then pre-ramped to the simulated breakdown voltage V_{bd} (depending on the annealing scenario), while the outer cell was not specifically contacted. This should not cause any disturbance, since the small resistivity and low thickness of the material will ensure that the outer cell will always be on the same potential as the backside. The backside biasing was then increased to $V_{bd} + 5$ V and the resulting current at the center auxiliary contact was read out. Finally, R_{vert} was derived by applying a linear fit on the resulting I-V-curve. In addition, the goodness-of-fit R^2 of the linear fit was analyzed to determine to which degree the SiMPl-characteristic non-linearity of the I-V-curve would be present for this bulk material with decreased thickness. The avalanche generation was turned off during simulations, otherwise the extracted currents above V_{bd} would be dominated by the avalanche current.

In order to account for a likely variation of the doping concentration over the wafer area, the impact on R_{vert} of an error margin of ±10 % on N_{eff} was also included. Examples of the resulting I-V-curves are shown in Fig. 9.30. In a) the effect of the 10 % variation in N_{eff} and a different gap size for a specific thickness of d_2 are presented. It can be seen that the deviation of the bulk doping (dashed red line) has no significant

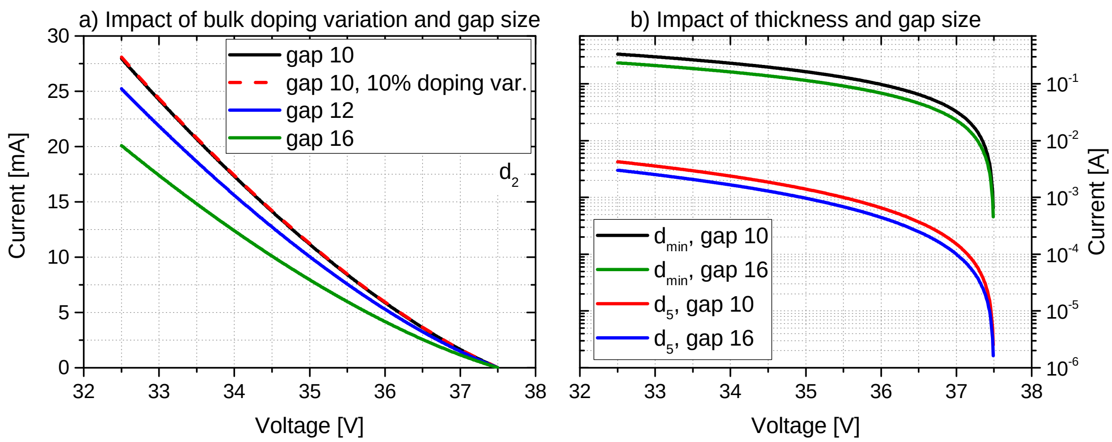

Figure 9.30: Examples of I-V-curves extracted from Synopsys simulations for the purpose of highlighting the impact of a) a ±10 % bulk doping level variation (dashed red line) and gap size (colored lines) and b) thickness and gap size. While the bulk doping leads to insignificant deviations, the effect of the gap size needs to be considered. The largest influence stems from different thicknesses, as it can result in currents differing in orders of magnitudes. The non-linear behavior, commonly associated with SiMPl devices, is also visible but far less pronounced in this case. The vertical resistor R_{vert} can be extracted by applying a linear fit on the I-V-curves.

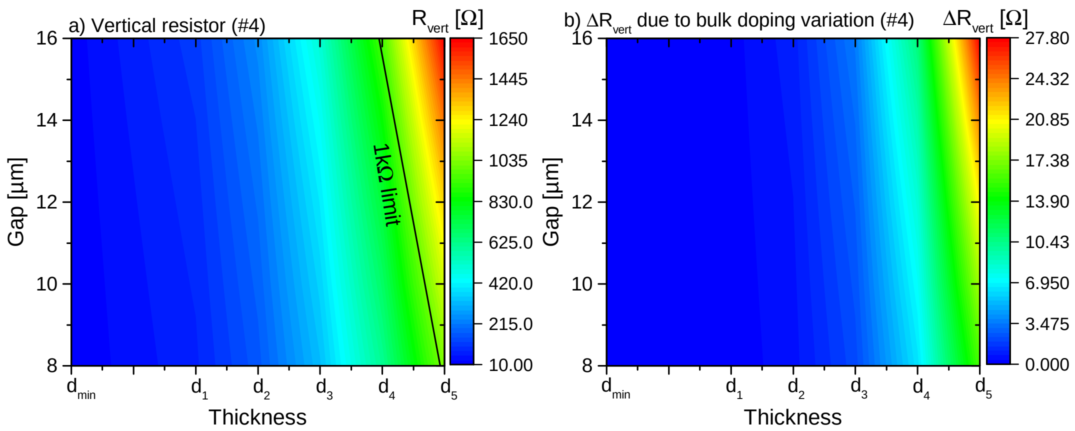

Figure 9.31: Impact of gap size and thickness as well as bulk doping variation on R_{vert} extracted from TCAD simulations. The absolute values for R_{vert} in a) can be seen to increase with increasing gap size and thickness, while the impact of a 10 % bulk doping variation ΔR_{vert} shown in b) can be considered negligible compared to the corresponding absolute values. Only annealing case #4 is depicted, however both cases yielded practically identical results (see Table A.2).

impact on R_{vert}. On the other hand, increasing the gap sizes (different colored solid lines) will decrease the slope of the curve, thus leading to an increase in R_{vert} which is in accordance to Eq. (9.2) for smaller thicknesses, while the deviation starts increasing for higher ones. Nevertheless, the change will need be considered since it will be substantial, as shown below.

Figure 9.30b) compares the impact of the gap size on different thicknesses. It is easy to see that the dominant factor affecting the R_{vert} will be the thickness of the device, while the relative change due to different gap sizes seems to be equal for both thicknesses and comparatively small. Comparing the lowest to the highest thickness utilized in the simulations, a difference in the resulting current of two orders of magnitude can be detected, which later translates into an equal deviation in terms of resistance.

The final results of the second step simulations are summarized in Fig. 9.31 and Table A.2 and show the resulting vertical resistor R_{vert} depending on the gap size as well as thickness of the devices. The simulations were performed for both annealing scenarios of the deep n implant which were deemed viable from the studies of the SiMPl3 prototypes in Sec. 9.1. Figure 9.31a) depicts the absolute values for R_{vert}, while Fig. 9.31b) shows the variation ΔR_{vert} stemming from a 10 % bulk doping variation for one annealing scenario (#4).

The first thing to observe is that increasing d, will have the most impact on R_{vert}, as already established. A higher d results in a larger contribution of the bulk doping level on the vertical resistor. As a rough estimate, an increase of about a factor of two for every micro meter added thickness can be expected, leading to a total difference of two orders of magnitude between d_{min} and d_5, which is also in accordance to the simulated currents. The geometrical variation in gap size will contribute a relative difference up to roughly 59 %, when comparing the smallest (8 µm) to the largest (16 µm) gap size and is seemingly constant throughout all values of d. As already touched upon, the impact of a bulk doping level variation of 10 % on R_{vert} (labeled ΔR_{vert}) can be seen to be negligible compared to geometrical factors, since it only amounts to an average relative deviation of approximately 0.6% for all thicknesses and a maximum relative deviation in the case of d_5 and gap = 16 µm of 1.7% .

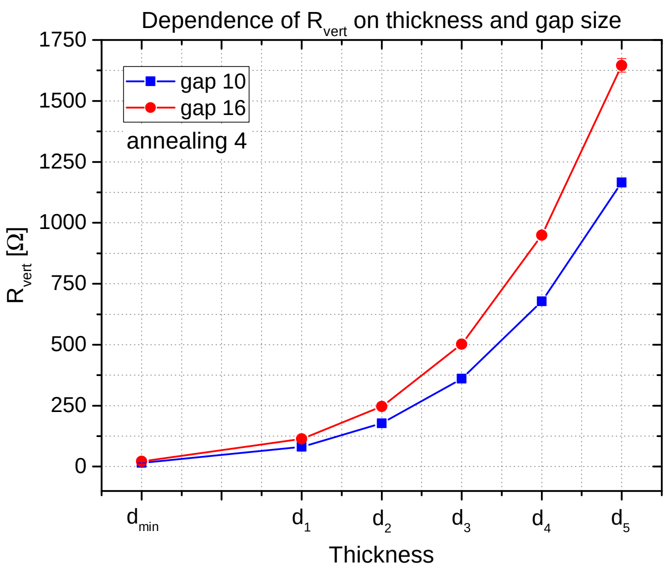

Figure 9.32: Illustrative demonstration of the impact of the device thickness and gap size on the vertical resistor R_{vert}. Opposed to Eq. (9.2), an non-linear increase with thickness can be observed for R_{vert}, most likely caused by the additional impact on the shape of the bulk resistor. As a consequence, the influence of the gap size also increases for higher thicknesses. The error bars denote the effect of a 10 % bulk doping level variation and are for the most part smaller than the actual data points.

A brief overview of this behavior is illustrated in Fig. 9.32, depicting the impact of the thickness and gap size on the resulting R_{vert}. The increase due to d according to Eq. (9.2) should be linear but a stronger dependence is visible. This is caused by the effect of the change in thickness on the general shape of the bulk resistor, in addition to the direct increase. It also effects the impact of the gap size, as it becomes larger for increased thicknesses. In comparison, the error bars due to the bulk doping variation are, for the majority, not visible as they are smaller than the data points themselves.

The circumstances are identical for both annealing scenarios, though annealing #4 seems to result in slightly smaller resistances for $d > d_1$, however only leading to insubstantial differences of a few percent. In order to evaluate the linearity or non-linearity of the I-V-curves used to determine R_{vert}, the goodness-of-fit parameter R^2 can be utilized, as it indicates how close to an optimal linear curve the extracted data was. Values close to 1 translate to a very good agreement with an ideal linear curve. This can be easily observed in the cases of the smallest thickness, but by increasing d, R^2 slowly starts to decrease. This can interpreted as the devices starting to exhibit the aforementioned JFET-like behavior, which was already seen for all instances of the thick SiMPl devices and was also already visible in Fig. 9.30. This makes predictions regarding R_{vert} less reliable in those cases, since it is extracted by means of the slope of a linear fit applied to the I-V-curves and thus the obtained values for the higher thicknesses need to be treated with caution.

Due to the analysis of the simulated data, choosing a final thickness for device production was possible. It was established above that $R_{back} \approx R_{vert}$, hence Table A.2 can directly be utilized for this task. Taking the aforementioned requirement of $R_{back} < 1\ \mathrm{k}\Omega$ into account, all thicknesses above d_3 can already be excluded. In the case of d_4, the majority of the values for R_{vert} fit the criteria, however, the larger gap size designs will get very close and as mentioned above, a generally smaller resistance is desirable.

This decision also aligns with the preferential choice of avoiding cases exhibiting more pronounced non-linearity. While d_{min} and d_1 result in the smallest R_{vert} and highest linearity, these small thicknesses should also be avoided, as total thickness variations over a wafer due to the thinning procedure are very common. This might lead to outcomes in which the resulting thickness of the devices could lead to technological issues like the one regarding edge breakdown, discussed in Fig. 9.29.

Therefore, in order to avoid potential risks from overthinning and to meet the requirements, set by the electronics, a final thickness of $d_{final} = d_2$ was chosen. The devices can be expected to feature resistances below 250 Ω and the thickness leaves enough room for error in both directions in case of an increased total thickness variation over the wafer. While the degree of linearity is not as optimal as in the case for lower thicknesses, it should still prove suitable for the tasks at hand.

9.3.1.3 Breakdown simulations

The breakdown voltage V_{bd} was simulated for SiMPl5 devices, analogous to SiMPl4, as discussed in Sec. 9.2.1.3.

Again, the values were extracted directly via Synopsys TCAD and via Monte Carlo methods and included energy of the deep n implant for comparison. Only one variant of the p^+ topside implantation was included, which corresponds to the deeper, higher energy variant of SIMPl4-2.

The results are listed in Table 9.11 for both relevant annealing scenarios and can be seen to be in very good agreement in all cases. The discrepancies are similar to the results of SiMPl4 and range from 0.5% to 1.4%.

9.3.1.4 Transient simulations

Other important issues which need to be dealt with regarding the design of SiMPl5 include the extraction of an estimated value for the bulk capacitance (quench capacitance in the previous cases) so that the electronics can be developed accordingly and the total expected voltage drop at the topside contact, as the electronics are only able to handle a limited voltage range. Both of those aspects can be evaluated with the help of transient simulation utilizing the SiMPl5 layout.

The general procedure of the transient simulations is basically identical to the one explained in Sec. 7.2.2, however slight changes had to be implemented in both the layout and device settings of the simulated device. Figure 9.33 depicts the adjusted simulation layout and will, again be performed in quasi 3D, via rotation around the axis $x = 0$.

Table 9.11: Comparison of the breakdown voltages V_{bd} obtained by simulations with Synopsys TCAD and Monte Carlo (MC) simulations for SiMPl5. For cross-check purposes, two different energies of the deep n implant were simulated ($E_{n,1}$ and $E_{n,2}$). Both relevant annealing scenarios (#4 and #11) are included. In all cases a very good agreement between both simulation tools can be observed.

	annealing #4				annealing #11			
	Synopsys		MC		Synopsys		MC	
	$E_{n,1}$	$E_{n,2}$	$E_{n,1}$	$E_{n,2}$	$E_{n,1}$	$E_{n,2}$	$E_{n,1}$	$E_{n,2}$
V_{bd} [V]	35.7	18.8	35.3	19.0	34.0	20.9	34.5	21.0

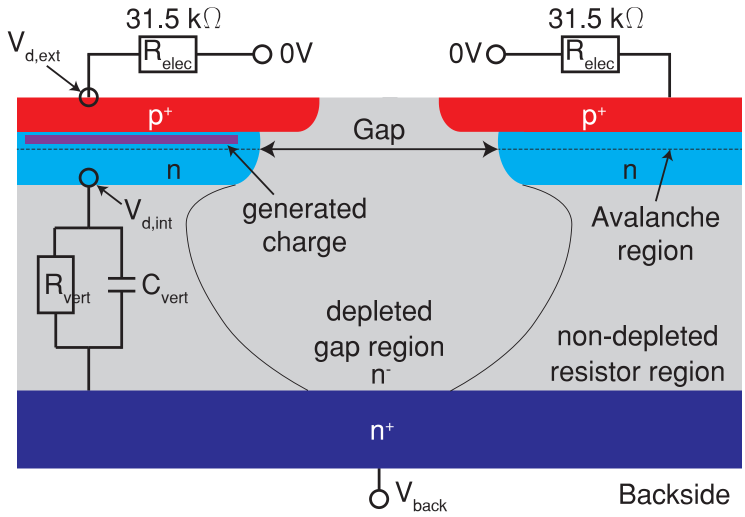

Figure 9.33: Schematic cross-section of the transient simulation layout for SiMPl5. In contrast to previous SiMPl prototypes, the SiMPl5 iconic segmented p^+ topside implant is included as well as an added external resistor R_{elec} to the two topside contacts. This resistor represents the readout electronics and is expected to have a value of roughly $R_{elec} \approx 31.5$ kΩ (see text). The process of extracting the bulk capacitance C_{vert} is identical to the method explained in Sec. 7.2.2. In addition, the voltage drops at the external contact $V_{d,ext}$ and internal anode $V_{d,int}$ will be tracked and evaluated.

The major changes compared to SiMPl4, apart from the variation in thickness, are the inclusion of the segmented p^+ topside implant and the addition of an external resistor to the two topside contacts, representing the readout electronics which will be connected via bump-bonding. According to [118], the estimated total resistance value experienced by the devices from the topside will be roughly $R_{elec} \approx 31.5$ kΩ.

The necessity of the inclusion of the external resistor stems from the potential charge loss during the charge creation phase of the simulation. As previously explained, a charge equivalent to the high-field capacity will be created within roughly 100 ps in order to simulate an avalanche breakdown. However, due to the extremely low resistvity of the bulk material, large fractions of the charge would already be siphoned out of the device before the total amount could be created. This in turn would falsify the total voltage drops at the external contact $V_{d,ext}$ and internal contact $V_{d,int}$, as well as the extracted bulk capacitance C_{vert}. Hence, the inclusion of R_{elec} is of the utmost importance for an accurate simulation framework.

As mentioned above, $V_{d,ext}$ will also be evaluated, since the readout electronics might only have a limited voltage range that should not be exceeded and in addition a similar voltage drop at the internal anode $V_{d,int}$ will be tracked in order to assure that substantial voltage changes are also not present at the backside.

The data for $V_{d,int}$, $V_{d,ext}$, C_{vert} and C_D resulting from the transient simulations, performed at an overbias voltage of $V_{ob} = 5$ V is listed in Table 9.12. Different geometrical variation for both relevant annealing scenarios (#4 and #11) were included and even though, the final thickness was established in the previous section, thicknesses of $d_{final} \pm 1$ µm were included for the purpose of evaluating the impact of potential total thickness variations.

In a first step, the quality of the simulations can be confirmed by comparing the

Table 9.12: Results of SiMPl5 transient simulations regarding the internal ($V_{d,int}$) and external ($V_{d,ext}$) voltage drops, as well as the bulk capacitance C_{vert} and the high-field capacitance C_D. The simulations were performed at an overbias voltage of $V_{ob} = 5$ V and the values are organized by geometry for both relevant annealing scenarios. An external voltage drop close to V_{ob} can be observed for all cases while $V_{d,int} < 1$ V. The bulk capacitance can be seen to be heavily dependent on the thickness of the device, leading to deviations in C_{vert} up to 208% for certain gap sizes. By comparing the extracted values for C_D the quality of the simulation can be confirmed (see text).

thick	gap [µm]	annealing #4 $V_{d,int}$ [V]	$V_{d,ext}$ [V]	C_{vert} [fF]	C_D [fF]	annealing #11 $V_{d,int}$ [V]	$V_{d,ext}$ [V]	C_{vert} [fF]	C_D [fF]
d_{final} − 1µm	8	0.44	4.21	61.0	115.9	0.49	4.18	54.2	115.7
	10	0.35	4.21	75.1	105.3	0.39	4.19	66.5	105.1
	12	0.29	4.17	91.3	95.2	0.32	4.15	80.2	95.1
	14	0.23	4.12	111.1	85.6	0.26	4.10	96.3	85.5
	16	0.19	4.05	134.4	76.7	0.22	4.02	114.2	76.5
d_{final}	8	0.67	4.34	41.2	117.8	0.73	4.32	37.3	117.4
	10	0.55	4.34	49.8	107.1	0.60	4.32	44.8	106.7
	12	0.46	4.30	58.0	96.9	0.52	4.28	51.5	96.7
	14	0.40	4.24	65.9	87.5	0.45	4.22	57.7	87.2
	16	0.36	4.16	72.6	78.6	0.41	4.14	62.4	78.3
d_{final} + 1µm	8	0.92	4.37	30.0	121.8	0.99	4.33	27.6	121.8
	10	0.78	4.37	35.3	110.7	0.84	4.34	32.4	110.8
	12	0.68	4.32	39.4	100.5	0.74	4.29	35.9	100.7
	14	0.63	4.25	42.3	91.1	0.69	4.21	38.1	91.2
	16	0.59	4.16	43.6	82.1	0.66	4.12	38.9	82.2

extracted values for the high-field capacity C_D to the calculated ones, using the common capacitor equation (see Eq. (3.11)). The expected values for the listed gap sizes obtained by calculations are:

$$C_D(8) = 119.1 \text{ fF} \qquad C_D(10) = 108.2 \text{ fF} \qquad C_D(12) = 97.1 \text{ fF}$$

$$C_D(14) = 87.1 \text{ fF} \qquad C_D(16) = 77.7 \text{ fF}$$

A good agreement of all available thicknesses with the calculated expectations is visible, however, C_D appears to be dependent on d which is surprising, since it should not have any impact on C_D after a certain thickness threshold is passed so that the backside implant cannot reach into the high-field region. It is unlikely to be a remnant of partial charge carriers loss due to low resistivity bulk, as R_{elec} was included and the charges were monitored. While the data would suggest a continued impact of the backside doping even for thicknesses deemed safe by the stationary simulation, an uncertainty within the simulation framework is also possible and needs to be considered. Nevertheless, in all instances the values are in sufficient agreement with expectations with only marginal deviations due to d, making further analysis of the results feasible.

By applying $V_{ob} = 5$ V, an external voltage drop $V_{d,ext}$ close to V_{ob} can be expected, due to the breakdown behavior of the SiPM. In all listed cases $V_{d,ext} > 4$ V can be observed with the different values for different gap sizes being attributed to the increased spread of the generated charge within the active area for larger gap sizes. It can be seen that the deviation in $V_{d,ext}$ for different thicknesses becomes almost non-existent for d_{final} and $d_{final} + 1$ µm, compared to $d_{final} - 1$ µm, which, again, could lead to the conclusion that the latter case still experiences more influence of the backside implant. Regardless, all instances show a deviation from the expected value $V_{ob} - V_{d,ext} < 1$ V, thus not implying the danger of a potential overshoot outside of the capabilities of the electronics and in general also providing confirmation of the quality of the simulation data.

The impact of the backside doping can be seen clearly in the case of $V_{d,int}$, as the smallest thickness exhibits the smallest changes in the potential at the internal anode, due to the high doping levels of the backside implant compared to the bulk doping. Hence, it is expected to see increasing values for $V_{d,int}$ the larger the contribution of the bulk doping level becomes, which is also displayed by the simulated results. The maximum voltage drop can be found for $d_{final} + 1$ µm but still remains less than 1 V. In total, $V_{d,int}$ does not seem to pose any danger for the electronics as the resulting backside potential change will be less than $V_{d,int}$.

Finally, evaluation of the bulk capacitance C_{vert} reveals multiple important facts. First, a heavy dependence on the thickness can be seen as for the case $d_{final} - 1$ µm the deviation for different gap sizes can reach up to 120%, while $d_{final} + 1$ µm results in only 45%. Simultaneously, when considering a constant gap size, the thickness variation can lead to discrepancies ranging from 103% to 208%. Again, the reason can be found within the impact of the backside implant on what is considered the bulk of the device. For a set thickness an increase in C_{vert} with increasing gap size can be seen, which is in accordance to the displayed behavior of $V_{d,int}$, since the bulk capacitance is calculated via the displacement current resulting in $C_{vert} = q/V_{d,int}$.

In the case of the established final thickness d_{final} values between 41.2 fF and 72.6 fF can be estimated with both extremes being in the same order of magnitude. Accounting a total thickness variation of ±1 µm the range will extend from 30.0 fF to 134.4 fF which still spans less than one order of magnitude difference in total. Taking this into consideration, the assumption can be made, that the impact of C_{vert} might be negligible for the design of the electronics, based on its resulting electrical impedance

$$Z_{C_{vert}} = \frac{i}{\omega C_{vert}} \,, \tag{9.3}$$

where i is the imaginary unit and ω the circular frequency. With

$$\omega = 2\pi f = \frac{2\pi}{t} \tag{9.4}$$

an estimate for $Z_{C_{vert}}$ can be made by approximating the pulse duration t with the length of the fast signal component of a SiMPl5 signal. Assuming $t \approx 1$ ns and $C_{vert} = 37.3$ fF, leads to $Z_{C_{vert}} \approx 4.3$ kΩ and therefore to $Z_{C_{vert}} \gg R_{vert}$, as given by the results of the previous section. Even assuming only the sub nanosecond rise time of the fast component of the signal being relevant, i.e. $t \approx 100$ ps, would result in $Z_{C_{vert}} \approx 430$ Ω which is still almost a factor of 3 larger than the bulk resistor for the respective gap size $R_{vert} = 164$ Ω. Hence, it can be assumed that the current flow through the bulk will be dominated by R_{vert} making C_{vert} less pertinent in design matters.

9.3.2 Static characterizations of SiMPl5

After all necessary data was obtained from technology and device simulations, production of the first prototype wafers of SiMPl5 could start and proceeded parallel to SiMPl4.

The following section will deal with the experimental characterizations of these wafers in order to determine the quality of the devices for future, more sophisticated experiments.

First, a general wafer level characterization was performed, investigating the overall quality of the production, and also allowing comparison with the simulated breakdown behavior. This step is also of importance for identifying and distinguishing areas of different device quality within the wafers for later choice of sensor arrays. Afterwards, the specifically designed static test device will be analyzed and the results compared to the ones obtained by TCAD simulations.

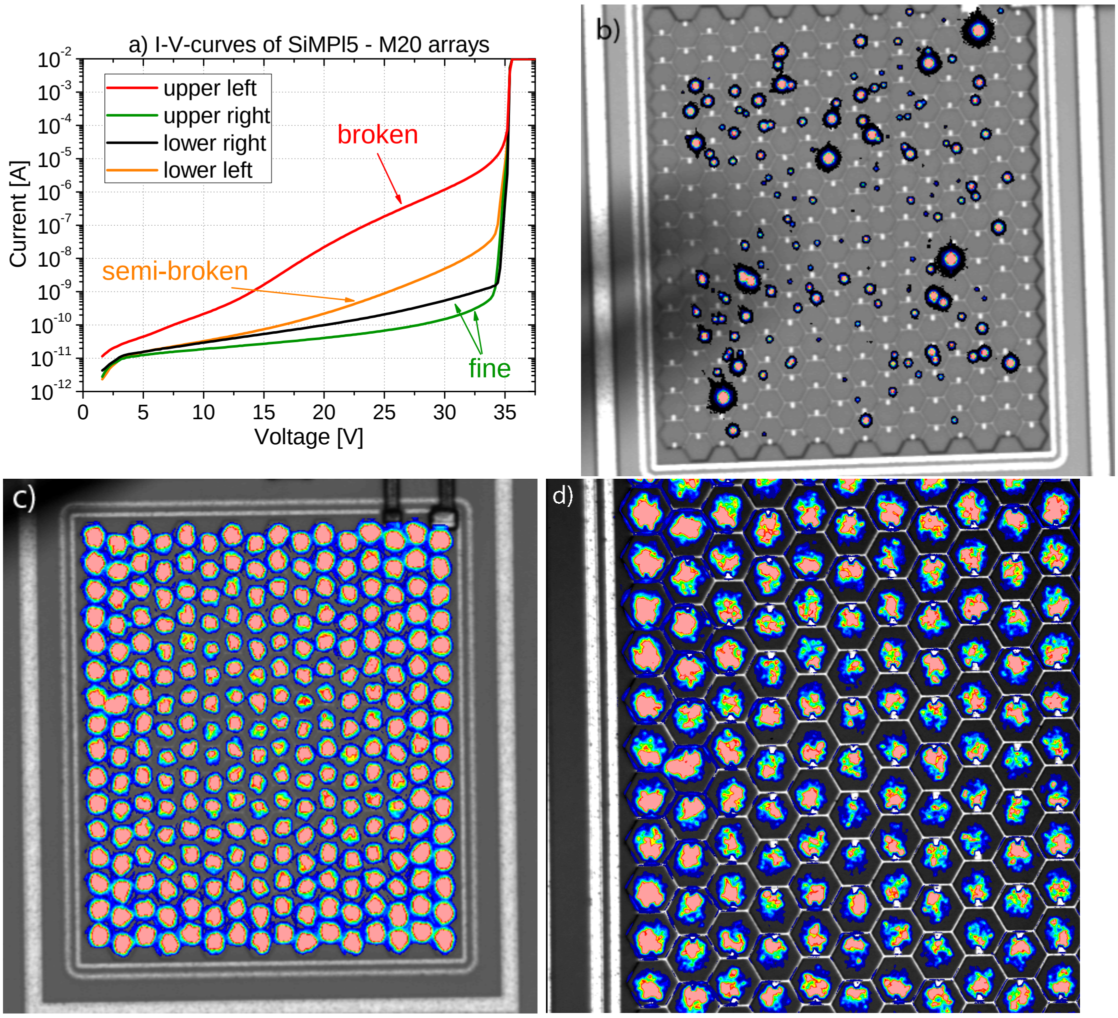

Figure 9.34: Examples of measured I-V-curves from shortened SiMPl5 arrays and one corresponding photon emission microscopy photograph. a) depicts the measured I-V-curves of a SiMPl5 chip, containing four shortened array structures. Of those four, two are properly functional (green and black line), while one can be considered semi-broken (orange) and the final one broken (red), as the breakdown starts occurring several volts earlier than desired. The respective photon emission microscopy photograph of the broken array is shown in b), clearly illustrating the same point-like early breakdown issue, as witnessed for the SiMPl4 devices in previous sections. It was taken at $V_{bias} = 31$ V, which is several volts below $V_{bd} \approx 34.7$ V. One of the properly working devices can be seen at different magnifications in c) and d).

9.3.2.1 Wafer level characterizations

As explained in Sec. 8, the majority of the SiMPl5 arrays is designed with flip-chipping in mind, meaning that the common I-V-characterizations like in the case for SiMPl4 are not feasible, since only single pixels can be contacted. For this reason, the two different types of shorted arrays were included. The pixels are connected either by the interpixel aluminum grid or via a sophisticated copper grid one layer above the aluminum. This allows investigations similar to the ones performed for optical SiMPl devices.

Three wafers, one for annealing scenario #11 and two for scenario #4 (chosen in Sec. 9.1) were measured and therefore, a total number of 528 chips, each containing four array structures, were catalogued, resulting in available data from 2112 structures. Identical to the procedure of SiMPl4, the measurements were performed within a dark box with an ambient temperature of roughly 298 K. The extracted I-V-curves were afterwards analyzed in regards to their breakdown behavior and current levels at lower voltages.

Unfortunately, similar to SiMPl4, all wafers exhibit the same issues in terms of point-like defects and early breakdowns within the arrays. Figure 9.34a) shows an example of a chip with two arrays which are working as intended (black and green lines) and two which suffer from early breakdown to different degrees. While the orange line indicates only few volts earlier breakdown and low current levels at low voltages, the red line represents a case where the entirety of the breakdown behavior is dominated by the hotspots. The corresponding photon emission microscopy measurement result for this quadrant at a lower bias voltage than V_{bd} is shown in Figure 9.34b), clearly indicating that an inhomogeneous point-like early breakdown occurs withing certain areas of the array.

In a few rare cases, an even more unusual breakdown behavior can be detected, as illustrated in Fig. 9.35. The left hand side shows the normal microscopy picture of the array structure at $V_{bias} = V_{bd}$ showing nothing out of the ordinary. In addition, the photon emission picture also shows no increased amount of light. However, increasing the voltage to $V_{bias} = V_{bd}+1$ V results in the picture on the right hand side, where actual light emission from the device can be observed. Is seems to be more pronounced at the

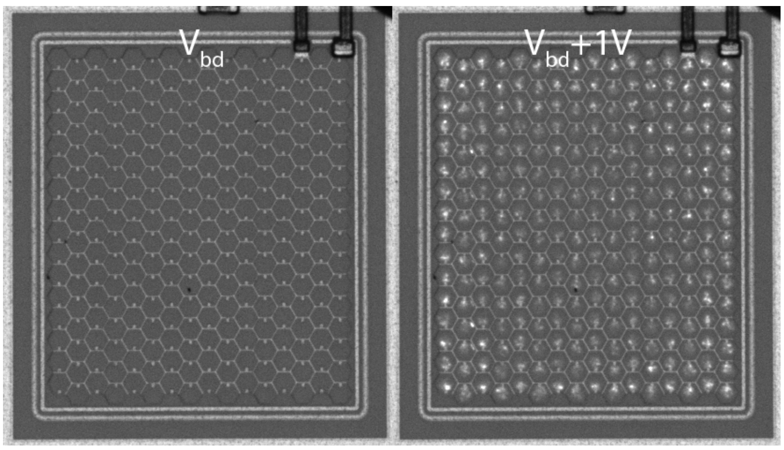

Figure 9.35: Example of an extreme case of unusual avalanche breakdown of SiMPl5. At $V_{bias} = V_{bd}$ (left) nothing can be seen in the normal microscopy picture but increasing the voltage to $V_{bias} = V_{bd} + 1$ V (right) light can be seen emitted from the device. It is not a result of early edge breakdown and appears to be more pronounced at the edges of the array.

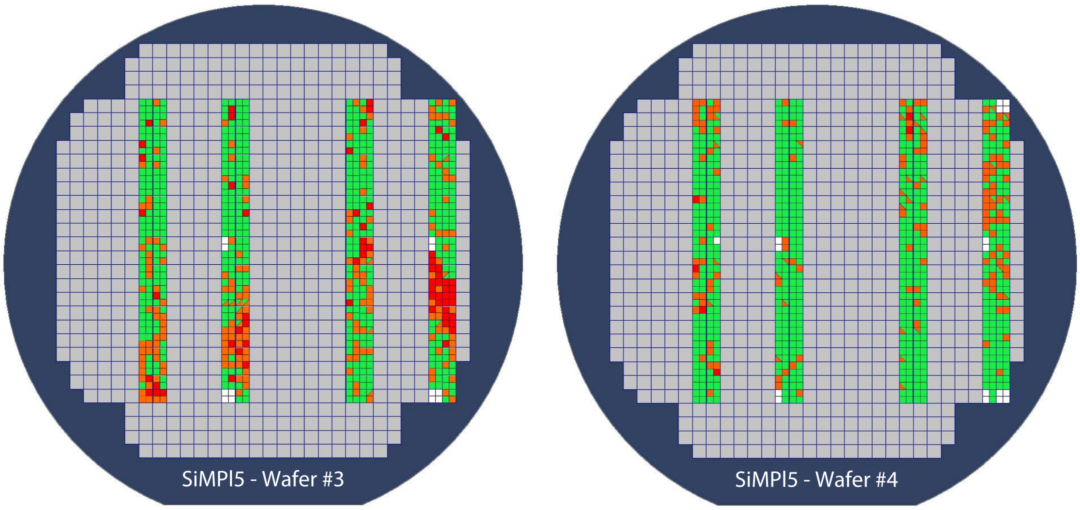

Figure 9.36: Yield map of the measured shortened array devices of SiMPl5 wafers #3 (left) and #4 (right). The colored squares represent the available array devices (four forming one chip), which were measured and categorized by their quality via different colors, green meaning fine, orange semi-broken and red broken (see Fig. 9.34). In certain cases a square was divided into two triangles, indicating a normal breakdown behavior but increased current levels. The total yield of shortened array structures for wafer #3 was roughly 66% and roughly 82% for wafer #4.

edge of the array and, by increasing the magnification, cannot be attributed to pixel edge breakdown. The reason for this behavior is currently still unknown and requires further investigation.

By checking the photon emission microscopy results of the normal case devices for $V_{bias} > V_{bd}$ it can be seen, that all wafers are not affected by edge breakdown. In regards to the point-like defects, again, annealing scenario #11 displays the issue more frequent and severe compared to scenario #4, thus all further characterizations focused on the two respective wafers, namely wafer #3 and #4.

In an attempt to quantify the early breakdown issue by i.e. localizing it to a specific area of the wafer, a yield map was created from the data of all measured array structures for both wafers. The resulting maps are depicted in Fig. 9.36, with a) representing wafer #3 and b) wafer #4. Every square represents one chip on the wafer and gray chips are excluded due to them not being an array structure chip. The pertinent chips are then divided into four quadrants in accordance to their layout and assigned a color, representing their status. Red and orange generally mean defect and affected by the point-like defect issue with red denoting a severe case and orange a less severe one. On the other hand, green indicates a proper working device, which is fit for further analysis. In rare instances, a quadrant is divided in two triangles of green and orange color, representing cases were breakdown behavior can be considered normal but the current levels beforehand are unusually high and thus also a reason for concern, since that would potentially translate into higher dark count rates.

It is apparent that wafer #3 shows more cases of defective devices in general and within those also more severe ones, compared to wafer #4. Overall, the total yield of all shortened array structures for wafer #3 was roughly 66%, with wafer #4 sporting roughly 82%. The areas effected by faulty chips also differ for both wafers. Where wafer #3 showed the higher concentration of defect structures in the lower right and left parts of the wafer, wafer #4 yield map suggests avoiding the upper and central right areas.

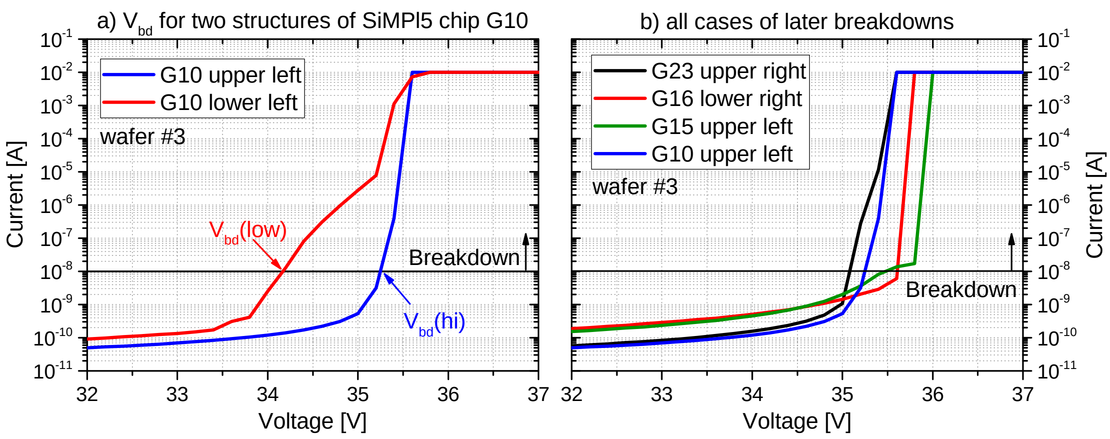

Figure 9.37: Illustration of the breakdown behavior of array structures, SiMPl5 chips. a) depicts two different instances of breakdown behavior observed on the same chip. The majority of the arrays exhibits the earlier breakdown represented by the red line, compared to only 4 of arrays of wafer #3 having a higher V_{bd} like in the case of the blue line and which are depicted in b). The difference in shape between curves with V_{bd}(low) and V_{bd}(hi) suggests an early breakdown mechanism in the case of V_{bd}(low) (see text).

An explanation for this observation is currently not known, as any influence of implant beam angles or photo resist angles should affect both wafers in the same fashion, since both wafers underwent the exact same processing steps with identical parameters. This could, however, point towards stress induced defects as will be discussed in Sec. 9.6.

Focusing on areas which displayed minimal danger of hotspots, further characterizations can now be performed. Regarding only chips considered completely fine, first, the current level at lower bias voltages of V_{bias} = 10 V was checked for all available devices of both wafers. The resulting currents were in the range of 4 pA – 15 pA, with wafer #4, for the majority, exhibiting smaller values closer to 4 pA, while wafer #3 generally showed higher ones closer to 15 pA. This observation is most likely linked to the increased occurrence of point-like defects on wafer #3, but cannot be quantified at this point in time.

Investigation of the breakdown behavior of the functional arrays yielded another unexpected result, as illustrated in Fig. 9.37a). For this measurement, two structures of one chip of wafer #3 were analyzed and exhibited a notable discrepancy in terms of V_{bd} and the shape of the I-V-curve around V_{bd}. The blue curve, representing the upper left array of the chip, behaves as expected, showing a steep increase of I after the breakdown has occurred. However, in the case of the lower left array (red line), the breakdown takes place roughly 1.1 V earlier, leading to a less steep incline, followed by an initial decrease in steepness and then resulting in a final steeper increase again, identical to the other array. A reasonable assumption would be that this effect is caused by early breakdown phenomena like edge breakdown or the point-like defects, by having the breakdown of the cell being preceded by the early breakdown, but none of these anomalies were observed in this instance. In fact, the majority of the properly functional array devices exhibit this breakdown behavior and only 4 of the 704 arrays in the case of wafer #3 can be seen to show the expected (blue) current curve, while wafer #4 exhibits none. Figure 9.37b) depicts these 4 cases of wafer #3, however, due to the limited quantity no systematic behavior of the respective V_{bd} can be deduced.

Similar to SiMPl4, the dependence of V_{bd} on the structure position within the wafer was investigated. For this purpose, chips with the largest possible vertical and horizontal

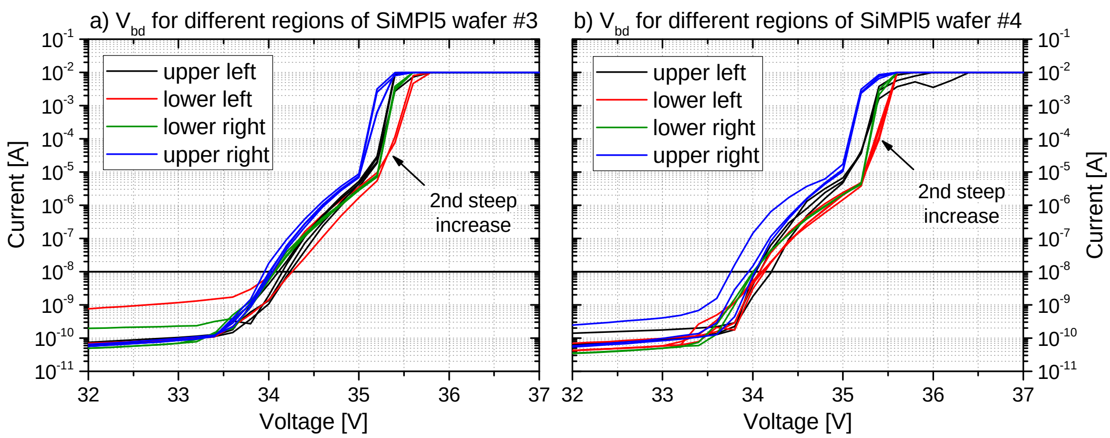

Figure 9.38: Breakdown behavior of SiMPl5 arrays in different areas of the wafer (a) wafer #3, b) wafer #4). The listed positions are with respect to the wafer flat being at the bottom. No systematic discrepancy stemming from the position within the wafer can be detected, when considering a threshold current 10 nA to identify V_{bd}, however taking the second steep increase at higher voltages into account, a left-right and upper-lower discrepancy becomes visible (see text).

distance from each other were chosen and their breakdown voltages investigated. Due to the limited number of available devices, exhibiting the expected breakdown behavior (blue line), it was only possible to perform this research with the other case devices (red line), since only they were located in the crucial regions of the wafer.

Figures 9.38a) and b) exemplify the results by showcasing the I-V-curves of multiple arrays structures located in four different corners of the available testing area of wafer #3 and #4, respectively. Here, all arrays located in the same wafer area are depicted in the same color. The findings indicate no systematic deviation in V_{bd} between the upper and lower half, as well as left and right half chips if a current of 10 nA is chosen as the point of an avalanche breakdown. In both cases a large deviation of V_{bd}(low) can be seen over the entire wafer (see Table 9.13). It is, however, possible that the early breakdown behavior seen in the utilized I-V-curves could falsify this result, as the early breakdown itself is a highly irregular process.

If the voltage at which the second steep increase of I takes place is taken into account, an upper-lower, as well as a left-right discrepancy can be observed. Arrays located in the upper area of the wafer, with respect to the wafer flat, display a potentially lower V_{bd} compared to lower arrays closer to the flat. Similarly, the breakdown voltages appear lower for devices to the right compared to the ones on the left, depending on their vertical position as lower right and upper left arrays exhibit a similar behavior. The biggest discrepancy can be found between lower left and upper right structures, suggesting a similar asymmetry to the one observed for the SiMPl4 wafers.

A comparison to the measured breakdown voltages V_{bd}(low) and V_{bd}(hi) as well as a comparison to the ones resulting from TCAD and Monte Carlo simulations is given in Table 9.13. The methodology behind obtaining the simulated values was already described in Sec. 7.2 and 7.3. Both simulated results are in very good agreement, showing a divergence of only 1.1%. The measured values for V_{bd}(low) result in $V_{bd,meas}$(low) $=$ (34.1 ± 0.23) V and $V_{bd,meas}$(low) $= (34.0 \pm 0.22)$ V for wafers #3 and #4, respectively, exhibiting a deviation from the simulated values due to early breakdown. The errors are comparable for both wafers and show no systematic behavior.

Quantification of the upper-lower and left-right discrepancy depends on the voltages

Table 9.13: Comparison of the simulated and measured breakdown voltage for SiMPl5 devices. The simulated data obtained by Synopsys and Monte Carlo (MC) tools was extracted with the methods explained in Sec. 7.2 and 7.3, respectively. Only 4 arrays exhibit the expected higher V_{bd} (Meas (high)), while an early breakdown can be observed for the rest. Measured values of wafer #3 and #4 are listed in the upper and lower row, respectively. The higher measured values of V_{bd} are in excellent agreement with the simulated data. See text for details.

	Synopsys	MC	Meas (low)	Meas (high)
V_{bd} [V]	35.7	35.3	34.1 ± 0.23	35.3 ± 0.26
			34.0 ± 0.22	–

at which the second steep increase in I starts occurring and was considered not feasible due to the limited number of available arrays in each sector of the wafer and due to the potential impact of the preceding early breakdown. Nevertheless, the available data suggests an estimated deviation of $\Delta V_{bd}(2\text{nd}) < 0.25$ V in the case of upper-lower and left-right with a maximum deviation $\Delta V_{bd}(2\text{nd}) < 0.5$ V between the lower left and upper right corner. In the case of the higher breakdown voltage, $V_{bd,meas}(\text{high}) = (35.3 \pm 0.26)$ V can be observed, which is in very good agreement to the simulated data, further suggesting these cases to represent the nominal breakdown behavior.

9.3.2.2 Resistance measurements and comparison to simulations

The final step in the static characterization procedure was the evaluation of the static test devices of SiMPl5 (see Sec. 8.2). In contrast to SiMPl4, those devices were not used to investigate the quenching and recovery behavior of array structures due to the inclusion of an active quenching scheme for SiMPl5. In this case, they were utilized to analyze the total backside resistance experienced by the readout electronics at the biasing contact, as was explained in Sec. 9.3.1.2.

Previously, it was established that $R_{back} \approx R_{vert}$ if a sufficiently large contact sizes for the biasing contact is implemented, thus decreasing R_{con} drastically. This was considered in the design of the static test devices and should therefore result in data dominated by R_{vert}.

The measurements were performed with the identical method and in the same environment as the rest of the wafer characterizations. The p^+ contact was kept at a constant 0 V but for the topside n^+ and the backside biasing contact, two different scenarios were employed as will be explained below. For the majority of the measurements, however, the backside was biased to $V_{bd} + V_{OB}$ with $V_{OB} = 5$ V while the topside contact was then ramped from V_{bd} to $V_{bd} + V_{OB}$ in order to simulate operational situation for the device. The resulting current was then read out and the resistance extracted via a linear fit on the I-V-curve.

When proceeding to measure a resistor, one would initially assume that any voltage range should yield the same results, which would allow the inclusion of the static test devices with an overlap area, as the voltages could be chosen low enough to not enable an avalanche breakdown. However, this does not hold true since the shape of the non-depleted area of the bulk, forming R_{vert} depends on the applied biasing voltage. Even for the reduced thickness, this impact can still be witnessed. To emphasize this fact,

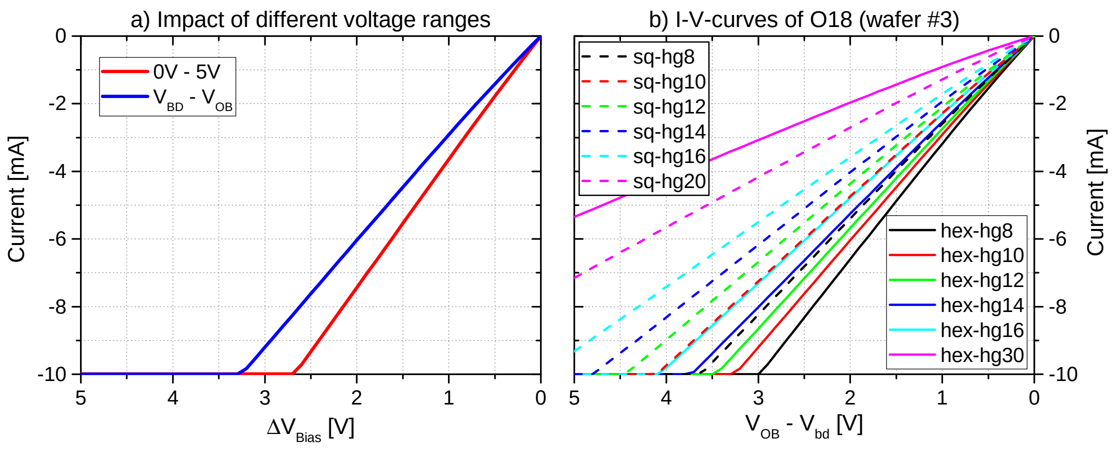

Figure 9.39: Impact of different bias voltage ranges on the resulting I-V-curves for static test devices of SiMPl5 (a)) and illustration of all available I-V-curves for one static test device chip (b)). For a) one case features the voltage range 0 V to 5 V and the other one V_{bd} up to $V_{op} = V_{bd} + 5$ V. In the case of b), the chip O18 was completely characterized and the resulting I-V-curves for hexagonal structures are represented by solid lines while the quadratic ones are depicted as dashed ones. In both cases R_{vert} can be extracted via linear fitting of the resulting curve (see text).

two measurements at different biasing voltage ranges were taken and the resulting I-V-curves can be seen in Fig. 9.39a). In one case, the applied voltage at the backside biasing contact ranged from 0 V to 5 V (red line) and in the other one from the breakdown voltage V_{bd} up to $V_{op} = V_{bd} + 5$ V (blue line). The initial constant value stems from the measured current still being in current-compliance of the SMU and afterwards, a nearly linear increase for both cases with different slopes can be seen. As the slope s translates directly to the resistance via $R = 1/s$ it is clear that the resulting values for R_{vert} are different due to the shape of the bulk being impacted by V_{bias}.

This can be directly illustrated when comparing the resulting values for R_{vert} for all the hexagonal structures of one chip, measured with each biasing range, as listed in Table 9.14. In all instances the lower bias option also results in a lower R_{vert} which indicates that the depletion region in the bulk is not fully formed at this point. In accordance to this, the deviation also varies with gap size and increases the larger the gap size becomes, reaching a maximum discrepancy of 31.2% in the case of a gap of 30 µm, thus emphasizing the importance of the choice of the biasing range. Hence, a biasing scenario which is representative of the final operational situation was chosen for all the following measurements.

Consequently, this biasing choice also means, that, similar to SiMPl4, the devices designed with an overlap region between the p^+ topside and deep n implant cannot be evaluated since the avalanche current will dominate all measured I-V-curves, thus reducing the number of available chips by half. A total of 14 chips could therefore be measured, with each chip containing 6 hexagonal and 6 quadratic structures with identical gap sizes, except the largest one, resulting in a total of 168 devices.

An example of the resulting I-V-curves of one chip is shown in Fig. 9.39b), where each color represents a specific gap size with the solid lines depicting hexagonal structures and the dashed ones their quadratic counterparts. The expected trend of larger gap sizes resulting in higher values of R_{vert} can be seen for both hexagonal and quadratic structures. Looking at devices with equal gap size but different geometry, a higher resis-

Table 9.14: Comparison of the impact of different biasing ranges on the resulting values of various gap sizes of R_{vert} for hexagonal structures of chip O18. In all instances the lower bias option will result in a lower R_{vert}, suggest different bulk depletion conditions compared to the higher operational voltage range. The deviation becomes more prevalent with increasing gap size.

	gap [µm]					
R_{vert} [Ω]	8	10	12	14	16	30
0 V − 5 V	260.2	280.2	290.2	320.2	330.2	702.2
$V_{bd} - V_{op}$	296.5	322.9	342.8	369.4	403.7	921.3

tance can be witnessed in the case of the quadratic devices compared to the hexagonal ones. This is also in accordance with the designs as the overall size of the non-depleted area of the hexagonal layout is expected to be larger.

A quantitative evaluation can be made by comparing the results listed in Table 9.15. The first half depicts the extracted values for R_{vert} for the case of the hexagonal structures, sorted by gap size and given for the measured chips, while the second half shows the respective values for the case of the quadratic structures. In addition, the mean value and error obtained from the measured data is given. A comparison to the simulated data can only be made for the hexagonal devices since the simulations did not include the quadratic case.

A general increase of R_{vert} with increasing gap sizes can be seen in all cases. Including the extreme gap case of 30 µm, the difference between smallest and largest gap size will be larger than a factor of 3. In the case of the quadratic structures, the maximum gap size was 20 µm which results in a factor slightly below 2.

Wafer level deviations can be investigated by comparing the I-V-curves and respective resistances of identical gap and geometry cases of all available chips. Since the chips are located in various regions of the wafer, local variations in the thickness can impact the resulting resistance values. Such a comparison can be seen in the left hand side of Fig. 9.40 for the case of hexagonal pixels with a gap size of 10 µm. The individual different colored lines each represent one chip on the wafer and a clear discrepancy on a chip to chip basis is visible. This can be translated to local resistance distribution over the wafer, as depicted on the right side of Fig. 9.40. The extracted value for R_{vert} of the aforementioned I-V-curves is written next to the a white square, each representing respective static test device location on the wafer.

The values and their positions suggest that the lower half of the wafer has a larger thickness than the upper half, with the lower half exhibiting the highest value of 351 Ω, while the upper central chip sports the lowest one with 274 Ω. After the thinning of the sensor wafers for the SiMPl5 project, their thickness was measured, resulting in a total thickness variation (TTV) ranging from (0.58 ± 0.09) µm to (1.39 ± 0.27) µm. The simulation results of the previous section, i.e. Table A.2 have shown that a 1 µm variation in thickness can result in changes in R_{vert} in the range of roughly a factor of 2. Taking this and the measured TTV into account, the observed variation in R_{vert} over the wafer lies well within the margin of the TTV.

When also considering the data obtained via TCAD simulations, a distinct discrepancy from the measured data becomes apparent, as seen in the left plot of Fig. 9.40. The

Table 9.15: Listing of obtained values for R_{vert} of all available static test devices of wafer #3. The values are sorted by gap size and geometry with the upper half depicting the hexagonal cases and the lower half the quadratic (square) ones. A comparison to the results, obtained by TCAD simulations are also given for the hexagonal geometry. The expected behavior of an increased R_{vert} with increasing gap size can be observed. A generally higher R_{vert} can be seen for quadratic devices compared to hexagonal ones due to the different effective area in the layout. Overall, all relevant gap sizes feature values for R_{vert} far below the imposed limit of 1 kΩ.

		gap [µm]					
R_{vert}(hex) [Ω]		8	10	12	14	16	30
	Sim	134.9	151.8	169.9	190.5	214.7	658.2
chip	AD09	265.0	309.2	302.1	317.3	338.9	775.1
chip	B25	282.7	303.5	321.3	350.0	377.0	865.1
chip	M01	316.4	350.8	387.8	426.7	471.7	1091.1
chip	M30	258.9	278.0	302.3	335.4	363.8	855.4
chip	O08	300.2	331.7	362.5	406.8	437.5	1010.1
chip	O15	309.0	355.1	405.9	444.1	453.5	977.9
chip	O18	296.5	322.9	342.8	369.4	403.7	921.3
chip	O25	268.8	287.6	313.5	338.3	366.2	831.6
chip	P01	298.7	331.2	362.4	387.4	421.6	973.4
chip	P30	243.2	274.2	294.2	303.8	327.9	741.0
chip	V30	275.3	296.1	326.8	373.0	389.4	904.5
	mean	283.2	312.7	338.3	368.4	395.5	904.2
	error	±22.9	±27.8	±37.1	±44.9	±46.6	±104.5

		gap [µm]					
R_{vert}(square) [Ω]		8	10	12	14	16	20
chip	AD09	351.2	353.3	391.6	438.6	464.3	587.3
chip	B25	339.9	388.0	443.6	482.6	544.4	695.6
chip	M01	379.5	437.1	489.3	550.5	623.4	823.5
chip	M30	302.1	341.6	377.1	441.0	481.3	635.7
chip	O08	375.5	425.5	471.7	521.7	602.4	764.7
chip	O15	399.1	435.5	510.5	528.4	586.4	779.9
chip	O18	359.6	406.8	440.1	474.6	530.3	691.4
chip	O25	319.0	377.2	406.2	444.8	511.0	631.2
chip	P01	365.9	418.9	463.5	513.1	582.1	757.1
chip	P30	264.1	307.0	339.8	368.3	427.1	535.3
chip	V30	343.7	395.9	415.6	480.2	541.8	701.0
	mean	345.4	389.7	431.7	476.7	535.9	691.1
	error	±38.5	±41.8	±51.3	±52.0	±61.2	±87.8

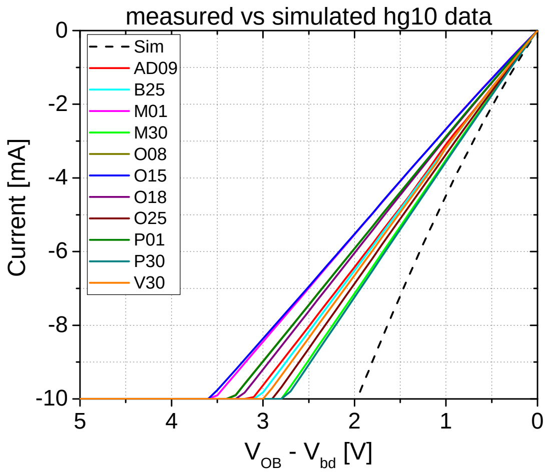

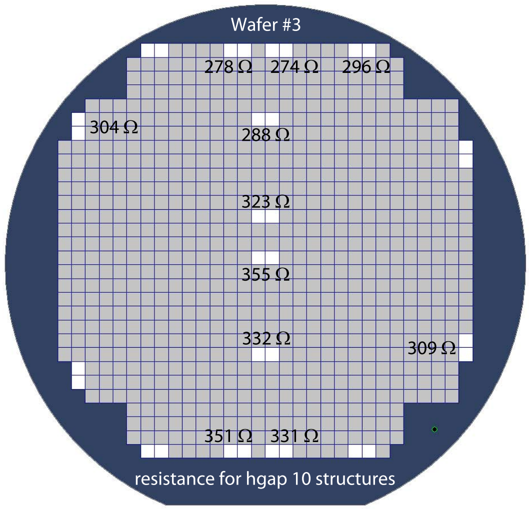

Figure 9.40: Dependence of the obtained I-V-curves and resulting R_{vert} on the position of the respective chip on the wafer and comparison to data simulated with Synopsys. On the left hand side, the I-V-curves of the same geometry (hex) and gap size (10 µm) for all available chips are depicted as solid colored lines, while the data obtained from simulations is given as a dashed line. A clear discrepancy of the measured to the simulated data is visible, as well as a less linear behavior of the simulated data compared to the measured one (see text). In addition, a dependency of the resulting R_{vert} on the chip position on the wafer can be seen and is summarized for gap 10 µm structures on the right hand sides wafer map. Each white square represents an available static test device and the respective measured value is displayed next to it.

dashed line represents the respective result from Synopsys and two statements can be made: First, a more distinct non-linearity compared to the measured data can be identified for the simulated case. Table 9.15 omitted the quality-of-fit parameter R^2 for the linear fit, as all cases showed $R^2 > 0.999$, indicating a linear behavior. The simulation on the other hand only yielded $0.988 < R^2 < 0.992$, thus suggesting a less linear characteristic I-V-curve, as is also visible in Fig. 9.40. Second, the measured values exhibit a larger value for R_{vert} for all gap sizes, which can in addition also be seen in Table 9.15. In many cases a discrepancy of more than a factor 2 can be seen. This discrepancy could be attributed to the contribution from the backside implant. It is possible that due to a different amount of outdiffusion into the bulk, the impact on R_{vert} from the backside is larger than anticipated. An accurate simulation of said backside implant, however, is currently still not possible, since the parameter space of the Synopsys framework was not optimized for such instances. As such, only approximations were possible, leading to potential deviations.

Comparing the hexagonal to the quadratic structures, it was already established that the resulting R_{vert} will be larger for the quadratic ones due to the layout. The deviation between both geometries increases with increasing gap size and varies slightly from chip to chip, as shown in Fig. 9.41a). As an example, the discrepancies for chip "O18" range from 21.3% to 31.4%.

On the other hand, comparing both geometries within the same chip one would expect a deviation equal to the deviation in size A_{hex}/A_{sq} of the central pixel of the test device, corresponding to the size of the deep n implant. This is not the case though, as the ratio R_{sq}/R_{hex} can be seen to be larger (see Fig. 9.41b)). This effect also appears to increase with increasing gap size as the difference between A_{hex}/A_{sq} and R_{sq}/R_{hex} increases from

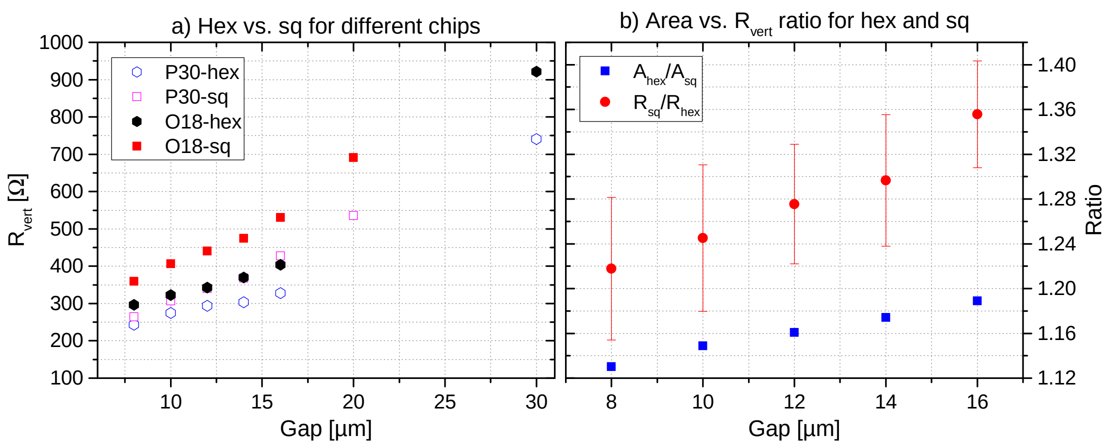

Figure 9.41: a) Comparison of the resulting R_{vert} for hexagonal and quadratic structures of two different static test device chips and b) comparison of the ratio of the effective area and resulting R_{vert} for hexagonal and quadratic devices. For a) the filled symbols represent chip O18 while the hollow ones represent P30. A clear deviation in R_{vert} due to the different effective areas of the two geometries can be seen, resulting in smaller values for the hexagonal geometry. The deviation also depends on wafer position and gap size (see text). In the case of b), a similar ratio for the effective areas of both geometries and the respective resulting values of R_{vert} would be expected. The discrepancy between both geometries dependent on the gap size is clearly visible, indicating a difference in depletion area within the bulk.

0.09 ± 0.06 to 0.17 ± 0.05. The TTV and variations in bulk doping concentration should be small enough on a chip level to not cause this issue and a non-linear I-V-behavior can also be ruled out due to the quality-of-fit parameter R^2 being close to 1 in all measured cases. Thus, the assumption can be made that the difference in both ratios is caused by a deviation in lateral bulk depletion depth, depending on the geometrical shape, resulting in an effective bulk resistor area different from the previously presumed A_{hex} and A_{sq}.

The data suggests either an increased lateral depletion depth in the case of A_{sq}, the opposite for A_{hex} or a combination of both. While a 3D simulation study performed in [33] has indicated a clear difference between pixel size and effective bulk area, the simulations were modeled after the classic SiMPl layout for optical applications. Hence, a quantitative comparison is not possible due to the vastly different layouts. A sophisticated 3D simulation will be required for further analysis and is the subject of future investigations.

In summary, even with the increased values obtained from measurements compared to the simulated ones, all are still well within the acceptable range. Taking into account the restriction imposed by the readout electronics, a value for $R_{back} \approx R_{vert} > 1$ kΩ needed to be avoided in order to enable proper functionality. With the exception of the gap 30 µm case for some chips, all sizes and both geometrical variations yielded values far below this limit. It also needs to be noted that these maximum gap cases are only included on these devices for testing purposes and are not considered for the final array structures. Hence, it can be concluded that the array devices of the first SiMPl5 batch are all suitable for further processing and later experimental investigations in terms of compatibility with the readout electronics.

9.3.3 Summary and current progress

Various simulation studies have been performed prior to the production of the first SiMPl5 prototypes. In terms of technological parameters, the required energy and dose of certain implants but also novel aspects like the minimum distance between the edges of the now structured topside p^+ and the deep n implant were optimized. A choice below this minimum would result in increased edge breakdown potential and thus needed to be avoided.

Further simulation studies tackled the issue of specifying a thickness for the devices, as it directly influences the resulting backside resistance. Due to compatibility aspects with the future readout electronics, a soft limit was imposed on the maximum value of R_{back} which needed to be taken into account when choosing the final thickness. By implementing additional simulation steps, other components of R_{back} were found to be negligible and a - compared to be previous iterations of SiMPl devices - very small thickness could be chosen for the first prototypes, resulting in sufficiently small values for R_{back} for all considered gap sizes. Simulations, however, also suggested a heavy dependency on the thickness, making the production strongly dependent on the quality of the thinning process and the outdiffusion of the backside implant.

Transient simulations allowed for extraction of C_{vert} and the expected voltage drops at the front and backside of the device after an avalanche breakdown. Analyzing C_{vert}, also suggested that it can most likely be neglected in regards to the design of the readout electronics, due to its impedance being at least an order of magnitude larger than R_{vert}.

After completion of the production of the first SiMPl5 wafers, wafer level characterizations were performed on all available test structures in order to determine the overall quality of the production and compare the obtained data with the simulations. Investigation of the I-V-curves showed a similar problem to the one already discussed for SiMPl4, namely the point-like early breakdown occurrences within the whole wafer area. In addition, an uncharacteristic behavior in terms of the breakdown voltage for the properly working devices was observed, in which a slightly earlier breakdown than expected can be seen for the majority of the available devices. Values for the breakdown voltage obtained via simulations suggest the cases with higher breakdown voltages to exhibit the nominal behavior. The cause for this and if this is linked to the aforementioned issues is not known at this point in time and requires additional investigations.

In a next step, the data of the novel static test devices was analyzed and compared to the respective simulated data. Overall larger values for R_{back} were obtained with the measured data compared to simulations, however the trend displayed due to a change in gap size or geometry was for the majority in accordance to expectations. Deviations in R_{vert} over the entire wafer area have been shown to be within the margin of the measured TTV according to the simulated data. In total, the measurements resulted in values for R_{back} still below the imposed limit of 1 kΩ for all relevant gap sizes. The above argument, however, can still be considered valid, even if the measured values for R_{back} are slightly higher than simulated, since the resulting impedance of C_{vert} can still be expected to be far larger than 1 kΩ.

Despite the issues with point-like early breakdowns and slight deviations from the simulated data, the yield and quality were sufficient to be able to make use of the designated array devices for further flip-chipping procedures. By cataloging potentially problematic areas within the wafers, a more educated choice of chips for future testing was possible. Nevertheless, additional steps were required before actual arrays could be deployed. The reason for this stems from the unusually small bump size utilized for the flip-chipping procedure, as the bumps are supposed to be only 22 µm in diameter. Hence,

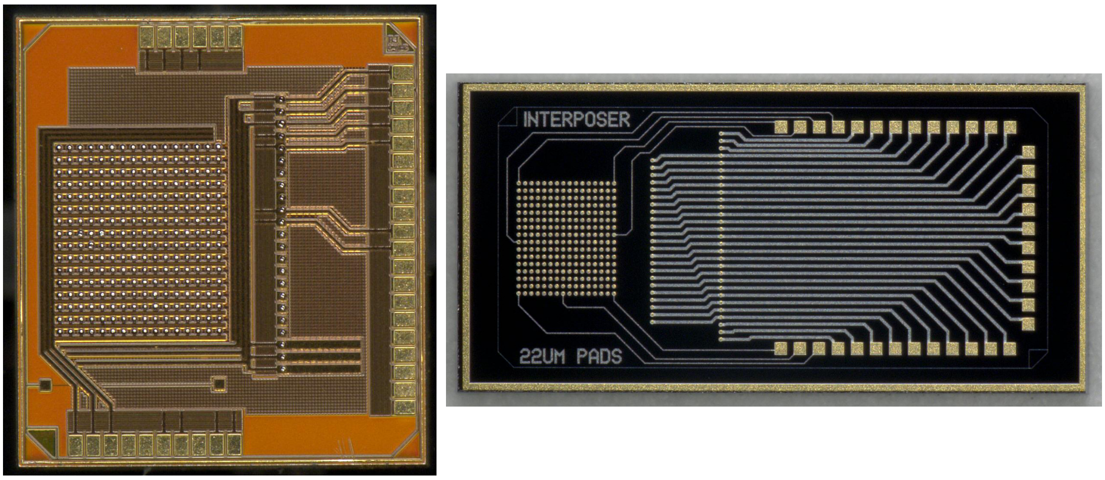

Figure 9.42: Microscopy photographs of the flip-chip test module (left) and the silicon interposer device (right). Bumps with a diameter of 22 µm were deposited on the pads of the test module, which required multiple iterations due to the small bump size. Afterwards, the module was connected via flip-chipping to the interposer (see Fig. 9.43).

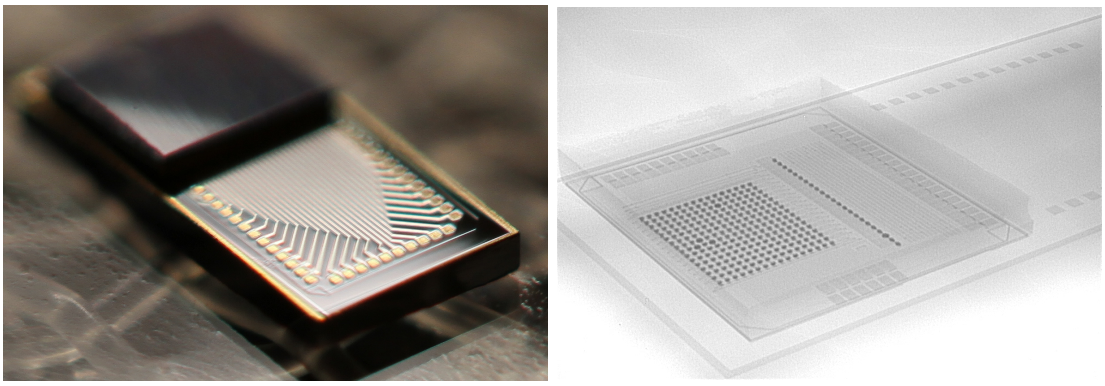

Figure 9.43: Microscopy (left) and x-ray photograph (right) of the flip-chipped test hybrids. The separate devices shown in Fig. 9.42 were connected via flip-chipping for further evaluation purposes. The x-ray picture illustrates the proper placement and (near) uniformity in bump size (seen as darker spots).

dedicated test modules were designed in order to allow practice runs on the placement of the bumps on the designated pads. One of these modules is depicted on the left hand side of Fig. 9.42. Multiple iterations were necessary to achieve the illustrated quality and uniformity of the deposited bumps.

Following the successful placement of the bumps, special test structures, labeled as silicon interposers and shown on the right hand side of Fig. 9.42, were fabricated in order to optimize and test the flip-chipping procedure itself. By connecting the interposer with the other module, basic connectivity as well as signal transmission quality can be investigated before the actual array devices undergo the same procedure. The first step, namely the mechanical aspect of the flip-chipping proved successful, as can be seen in Fig. 9.43. On the left, a microscopy photograph of the combined devices can be seen and the respective x-ray image is depicted on the right hand side. A proper placement and flip-chipping can be observed as the bumps are in perfect alignment with interposer pads. Four slightly bigger bumps are visible but are no cause for concern since the size is within an acceptable margin.

The next step requires quality assurance regarding the signal transmission between both devices. For this purposes, prototypes of the designated readout electronics will be utilized and connected via wire bonding to the test hybrids. This way the interconnectivity between the two structures can be tested, in order to ensure no cold soldering joints are present in the final hybrids.

At the moment of writing, this was still a work in progress, hence no discussion of the results can be given here. As soon as these experimental validation are completed, the procedure will be scheduled to be repeated with actual sensor arrays for first sensor-hybrid evaluations.

9.4 Impact of radiation damage on SiMPl4 and SiMPl5

Due to possible applications of SiMPl devices in radiation rich environments, radiation hardness studies were carried out with SiMPl4 and SiMPl5 material (see Chap. 4 and Sec. 6.5). In a first step the commonly studied changes due to non-ionizing radiation damage were investigated with diodes comprised of SiMPl material. The majority of the potential changes in SiMPl performances of SiMPl4 and SiMPl5 devices and their respective characteristics can be extracted from the studies regarding the static test devices, presented afterwards. This is followed by an attempt to quantify the impact on the dynamic behavior of SiMPl4 device. Finally, the potential impact of ionizing radiation damage on the detector performance will be discussed. All discussions will also feature a comparison to simulation studies of radiation damage performed in the TCAD Synopsys framework.

9.4.1 General non-ionizing irradiation characterizations

In a first step, the common effects, like leakage current increase and the change in effective doping concentration of non-ionizing radiation damage on the material of SiMPl4 and SiMPl5 will be investigated. This will be done by utilizing diode wafers of SiMPl material. A detailed pre-characterization of all irradiated diode devices will be presented, followed by the actual investigation of the impact of the non-ionizing radiation damage after specific fluences, as well as a comparison to simulated data. This will also include a brief discussion on the extracted fit parameters related to the change in effective doping concentration.

9.4.1.1 Diode pre-characterization and comparison to simulations

Before irradiation, all sets of diodes, introduced in Sec. 8.3, were pre-characterized in terms of their reverse bias current and their capacitance. The capacitance measurements can afterwards be utilized to obtain the full depletion voltage and thereby the effective doping concentration of the bulk material N_{eff}. All measurements were performed on a probe station described in Sec. 5.2, while the diodes where placed in a darkbox with an ambient temperature of 298 K.

Current measurement

In order to obtain the reverse bias current and thus the bulk leakage current, the p^+-diode contact and the guard ring on the top were both biased at a fixed voltage of 0 V, while the backside contact was used to apply a positive bias voltage. Contacting of the backside was achieved via the cutting edge on the outer rim of the chips. Depending on the diode material, the backside bias voltage ranged from 0 V to 10 V in the case of

Table 9.16: Summary of the measured reverse bias current of all diodes structures utilized in this study. The mean values for each diode size are given for both thick and thin diode chips. Sizes ranging from 10 mm^2 to 100 mm^2 can be found on the diode wafer chips while the SiMPl4 wafer only contained 10 mm^2 diodes. The final row shows the overall mean current per volume I/V for all sizes combined for both thick and thin diodes.

		Leakage Current/Volume [nA/cm^3]		
		thick		thin
		Dio	SiMPl4	Dio
Area [mm^2]	10	37.7 ± 4.3	66.3 ± 14.4	250.7 ± 20.5
	25	31.8 ± 5.8	–	215.8 ± 54.3
	36	27.6 ± 7.6	–	188.3 ± 50.4
	100	20.2 ± 9.9	–	74.0 ± 43.9
mean		26.7 ± 10.6	66.3 ± 14.4	151.5 ± 85.1

the thin material with a resistivity of 125 Ωcm and between 0 V and 20 V for the thick 1.5 kΩcm material. The resulting diode current at the diode contact was then evaluated. The evaluation of such a measurement can be seen in Fig. 9.44. The plot depicts the reverse bias current of a 100 mm^2 diode structure in blue with its guard ring current in red.

For the purpose of evaluating the radiation damage, a current value at a fixed bias voltage should be chosen. In this context, a voltage at which the bulk is already fully depleted is the most reasonable choice as the currents can be observed to change very little afterwards. Hence, the current values for the comparison of before and after irradiation were measured at 10 V and 20 V for the thin and thick batch, respectively.

A total of 102 diode chips, resulting in 166 diode structures were utilized and characterized for this study. Overall, all diodes showed the expected behavior at a reverse bias situation and were therefore suitable for further studies. An overview of the extracted current values for later comparison is given in Table 9.16. The mean value for a specific diode size for each set of diodes can be seen, as well as an overall mean for the leakage current per volume.

Figure 9.45 depicts the distribution of the measured leakage current per volume I/V for the a) thick and b) thin diode sets. The different colors denote the different sizes of diodes and are stacked on top of each other. A distinct spread in both cases stemming from the individual sizes can be observed, leading to the overall larger error of the total mean value. The comparatively high leakage current of the thin diodes can be attributed to impact of the backside implant on the depleted volume. Due to the very low thickness, basically the entire depleted area of the bulk overlaps with the backside implant, leading to a high concentration of defect and thus increasing the leakage current.

Diodes with an inherently higher leakage current were chosen for irradiation with higher doses, since the current increase will be orders of magnitudes higher and thereby not affected by the initially higher currents. Conversely, the diodes structures with the smallest initial leakage current were irradiated with the smallest doses.

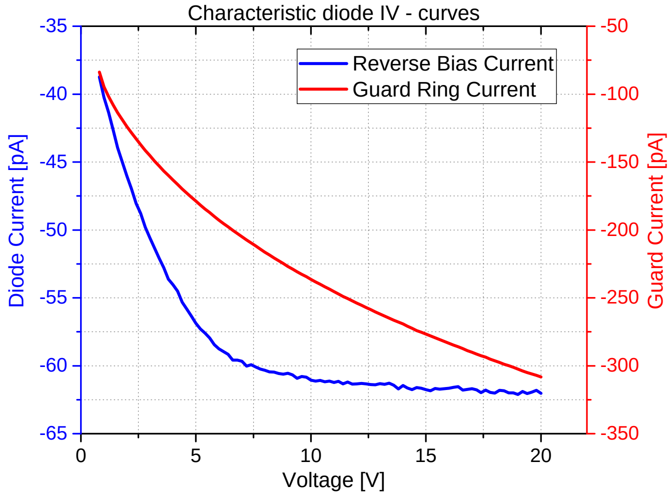

Figure 9.44: Example of a reverse bias current measurement of a diode. The measured diode current is presented in blue and the guard ring current in red with their respective scalings left and right. The data was obtained from a 100 mm^2 structure.

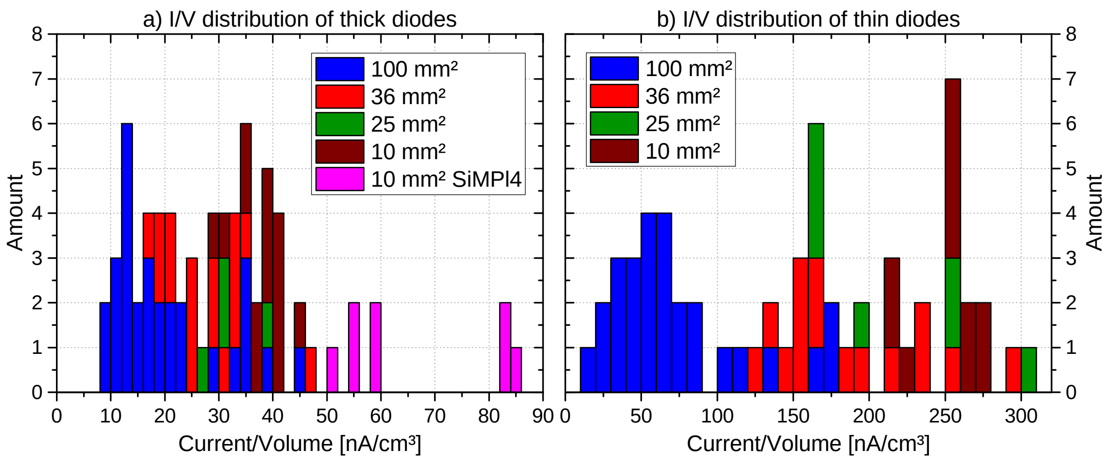

Figure 9.45: Leakage current per volume I/V distributions for both sets of diodes. Thick diodes of the diode wafer and and SiMPl4 wafers are shown in a), while b) depicts the thin diodes of the diode wafer. The different colored bars represent the different diode sizes and are stacked on top of each other. The overall spread in the total mean of I/V (see Table 9.16) can be attributed to the different current levels of the various diode sizes.

Capacitance measurement

For the capacitance measurements the voltage sweeps for the different batches of diodes are identical to the ones above and the guard ring was kept floating during the measurement. A resulting C-V plot can be found in Fig. 9.46 (blue line and blue scale), however a more useful variant of this data is given in the form of a $1/C^2$-V plot (red line and scale). In order to evaluate the quality of the measurement procedure, simulations of the diode devices for all technological parameters were carried out with Synopsys and the measurements re-enacted within its framework. For comparison, the simulated equivalents of the capacitance measurement in Fig. 9.46 are represented by the dashed lines. The simulation exhibits a slightly smaller total capacitance than the measured data, which, again, is easier to identify by making use of the $1/C^2$-curve.

Another important parameter that can be extracted from the simulated data is the effective thickness $d_{depl,\text{eff}}$ of the diode devices. As previously explained, the implanted doping of the detector material, especially the backside doping, will diffuse in all directions, thus increasing its volume in the bulk. This, in turn, limits the possible space charge region and thereby effectively reduces the full depletion width d_{depl} of the diode pn-junction by several µm, depending on the backside doping and respective annealing scenarios. Effective thicknesses for both thick and thin materials were extracted from simulations, resulting in

$$d_{depl,\text{eff}}(\text{thick}) = d_{depl}(\text{thick}) - 11.5\ \mu\text{m} \qquad \text{and} \qquad d_{depl,\text{eff}}(\text{thin}) = d_{depl}(\text{thin}) - 8.7\ \mu\text{m}\ .$$

Obtaining the effective depletion width now also allows for a more accurate calculation of the capacitance via Eq. (3.11) and for an overall comparison of the determined values for C. Such a comparison can be found in Table 9.17, where the calculated, simulated and measured results of C for thick and thin diodes of different sizes are summarized.

In the case of the thick devices the simulated and calculated values for all sizes are in perfect agreement, while the measured values (column "Meas") exhibit deviations of

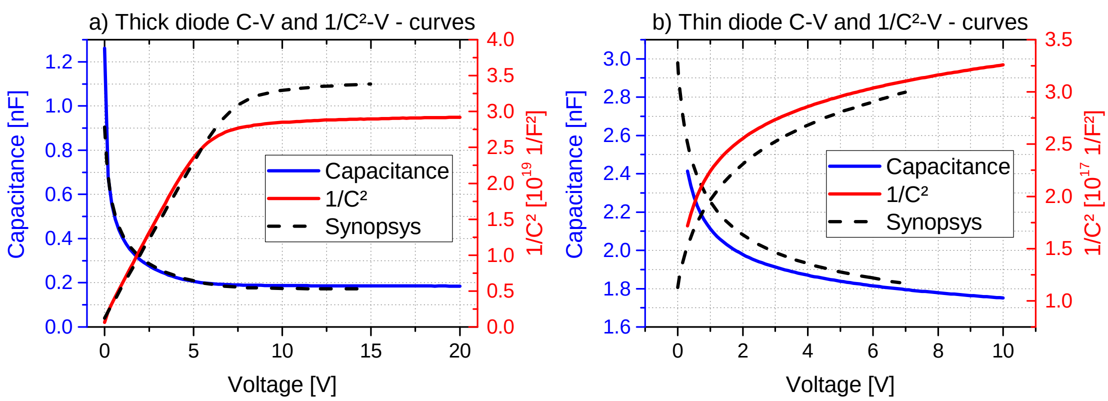

Figure 9.46: Example for capacitance and $1/C^2$ measurements of a diode. In both plots, the blue line and blue scale on the left represent the capacitance measurement, while the red ones (right scaling) illustrate the calculated $1/C^2$-curve for a 100 mm^2 diode structure. For comparison, the dashed lines represent the simulated equivalents obtained via Synopsys. A small discrepancy between measured and simulated data can be seen. a) A thick diode structure was measured and exhibits a final capacitance of roughly 185 pF after full depletion. b) In the case of a thin diode structure, the point of full depletion is difficult to identify, as is the final capacitance, which is assumed to be roughly 1.75 nF.

Table 9.17: Comparison of diode capacitance values, obtained by different means. Calculated, simulated and measured values of C for the different sizes of diode structures are listed. For the calculated values the reduced depletion width and therefore effective thickness of the devices, obtained via simulations within Synopsys was utilized.

Area	Capacitance [pF]						
	thick				thin		
[mm^2]	Calc	Sim	Meas	Meas (g)	Calc	Sim	Meas
10	17.7	17.3	20.4 ± 0.7	–	195	182	178.2 ± 6.2
25	44.3	43.3	48.1 ± 0.4	–	488	455	439.9 ± 17.9
36	63.7	62.3	69.1 ± 0.5	62.5 ± 0.6	703	655	635.3 ± 31.3
100	177	173	184.9 ± 1.2	–	1950	1820	1692.1 ± 62.8

up to 15.3%. The measured capacitance tends to be higher than the ones obtained by other means, but are nonetheless in good agreement within the limits of accuracy of the measurement. A possible reason for the increased values is the biasing status of the guard ring during measurements as will be discussed below.

However, looking at the case of the thin devices, the deviations between each means of acquisition are more pronounced. A maximum discrepancy of roughly 6.8% between simulation and calculated data and 15.2% between measured and simulated data can be found. In addition, the previous trend of increased values of C obtained from measurements seems to be reversed here. A possible reason for this disparity might lie in the extremely small thickness of the devices and the consequent composition of the depleted bulk region. Since the backside implant makes up a large portion of this region, an abrupt *pn*-junction case can not be found any longer. Instead, a perpetual change of the depletion width with increasing reverse bias voltage can be experienced. This also causes the expected plateau region of the capacitance measurement to be less distinct (see Fig. 9.46 b)), making the bulk area never truly fully depleted compared to the thick devices. As a consequence, extracting the full depletion voltage and effective doping concentration will be more difficult and will oftentimes yield less reliable results in the case of the thin diodes.

It is a commonly accepted procedure to perform the capacitance measurement with the guard ring structure not being biased during the measurement, as it is thought to have no substantial effect on the result. However, according to a study by Fretwurst [119], the guard ring and lateral extension of the depletion zone will have a significant impact on the measured capacitance. It was found, that grounding the guard ring yielded results which are in better agreement with the nominal and simulated data compared to leaving the guard ring floating. In addition, it appears as if this effect will increase the smaller the cross-section of the diode is.

To confirm this phenomenon, the set of thick diode structures with an area of 36 mm^2 was analyzed again, this time grounding the guard ring. Furthermore, the frequency of the capacitance measurement was varied in order to confirm if any impact may arise from it and to find the optimal one for the evaluations at hand. Figure 9.47 shows some exemplary results, depicted in the shape of $1/C^2$-curves. The diode chips in question featured four equally sized diode structures with different circumferences of 24, 26, 30 and 40 mm.

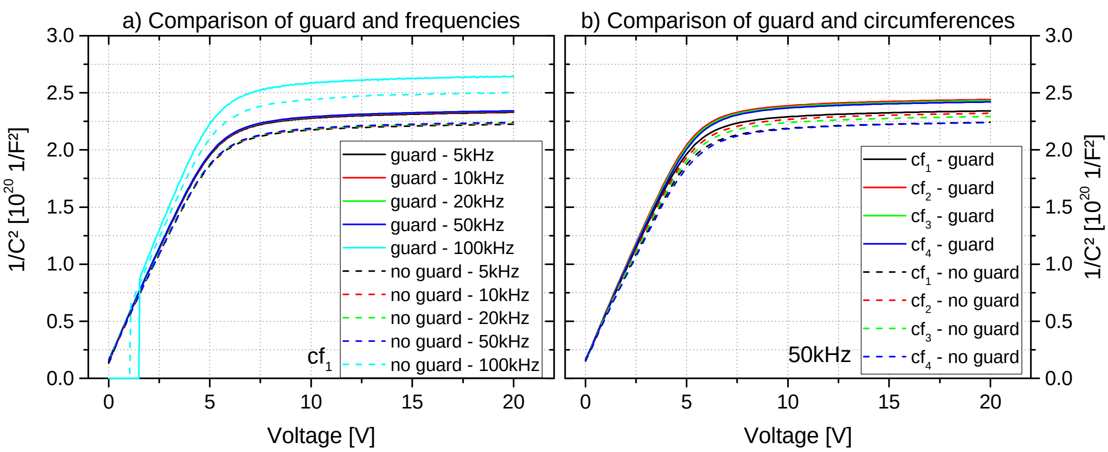

Figure 9.47: Investigation of the impact of the guard ring and measuring frequency of a capacitance measurement. A thick diode chip with four diode structures of equal area but different circumference was measured with and without biasing the guard ring to 0 V while alternating the measuring frequency between 5 kHz, 10 kHz, 20 kHz, 50 kHz and 100 kHz. a) The impact of a biased guard and different frequencies for the same structure of circumference cf_1 is depicted. b) The impact of the guard biasing at a frequency of 50 kHz on the different circumferences is shown (see text).

In Fig. 9.47a), the impact of different frequencies on one specific circumference structure (different colors), as well as the impact of the guard biasing (solid and dashed line) can be seen. In terms of frequency, it can be seen that only 100 kHz shows a significantly different result, which, when translating the $1/C^2$-curve into a capacitance, yields values beneath the one expected by calculations and simulations. While the remaining ones show similar results, it was later found that after irradiation of the diode chips, a frequency of 50kHz yielded the most stable results and was hence also chosen to be the most reliable one. When discussing the impact of the guard ring, it is easy to witness that grounding the guard ring will lead to smaller values for C which are also listed in Table 9.17 under the column "Meas (g)". Comparing those values to the one obtained by simulations and calculations validates the study of [119].

The impact of different circumferences on C depending on the guard biasing is depicted in Fig. 9.47b). The frequency was constant (50kHz) for all measurements and the different colored lines represent the various circumferences, while the guard status is represented by solid and dashed lines. The same effect as above in the case of the guard biasing can also be seen here, further supporting [119]. In addition, the circumference seems to have a negligible influence on the resulting capacitance of the devices.

In summary, connecting the guard ring to ground during C-V measurements in order to adjust accordingly for edge effects will have a beneficial impact. The data in this thesis, however, was obtained without this correction in place, as this circumstance was not known in time and the data in Table 9.17 can be utilized for a quantification of the expected discrepancies. This, in turn, can be a possible cause for discrepancies in the below studies involving capacitance measurements.

After cross-checking the measured data with simulations and calculations, ensuring the feasibility of the results, the final step in regards to the capacitance characterizations can be performed. There are two different methods utilized in this study to obtain the full depletion voltage V_{depl} and effective doping concentration N_{eff} of the diode structures, as was explained in Sec. 5.2.2.

In most cases, assuming depletion voltages in the range of tens or even hundreds of volts, the built-in voltage V_{bi} can be neglected as it is several orders of magnitude smaller than V_{depl}. This, however is not the case here, as will be shown below, hence V_{bi} needs to be taken into account in both methods:

$$V_{bi}(\text{thick}) = 0.702 \text{ V} \qquad \text{and} \qquad V_{bi}(\text{thin}) = 0.767 \text{ V} .$$

By utilizing both methods, the results of Table 9.18 for V_{depl} and N_{eff} could be derived for both sets of diodes. Again, the values are grouped by size and the results for V_{depl} already incorporate V_{bi}. As stated before, the nominal values for N_{eff}, provided by the wafer manufacturers, are

$$N_{\text{eff}}^{nom}(\text{thick}) \approx 2.81{\cdot}10^{12}\ 1/\text{cm}^3{\pm}10\% \qquad \text{and} \qquad N_{\text{eff}}^{nom}(\text{thin}) \approx 3.51{\cdot}10^{13}\ 1/\text{cm}^3{\pm}10\% ,$$

leading to estimated full depletion voltage of

$$V_{depl}^{nom}(\text{thick}) \approx 6.73 \text{ V} \qquad \text{and} \qquad V_{depl}^{nom}(\text{thin}) \approx 0 \text{ V} .$$

The statement in regards to $V_{depl}(\text{thin})$ infers, that $V_{depl}(\text{thin}) \approx V_{bi}$ which, however, is not the case, as can be seen from the results of Table 9.18. Hence, a larger error margin for the specifications provided by the manufacturer has to be assumed. This already highlights the main issue with the thin batch of diode devices, since their depletion voltage is very similar to the already small built-in potential, making a more in-depth analysis even more difficult.

Table 9.18 features the measured and simulated values determined via both methods. By comparing the extracted values for N_{eff} of the simulation to the value given by the wafer manufacturer, a first quality check of the methods is possible, as this parameter was given to the simulation framework and thus must hold true. In the case of the thick devices, the extracted value of the simulation via the slope method is very close to the given one, translating to a depletion voltage of roughly 6.68 V. For the double linear fit method, $N_{\text{eff}} = 3.04 \cdot 10^{12}\ 1/\text{cm}^3$ was obtained which corresponds to a deviation slightly above 8% from the expected one.

Looking at the thin devices the situation becomes subverted as the slope method was not able to yield any useful results on the simulated data, due to the aforementioned shape of the $1/C^2$-curve. The only way to derive any result from the simulated data of the thin devices was with the help of the double linear fit method, even though the values show a discrepancy of 137% compared to the manufacturers estimate. It was already concluded that the error margin here might be higher than initially expected and the comparison of the data obtained for the thin devices, measured and simulated, with both methods supports this assumption.

For the double linear fit method the data extracted from the measurements is in very good agreement with the one obtained from the simulations. While simulated comparisons within the slope method data are not possible, comparing it to the data from the other method still shows more accordance than with the estimated value. The problem of the slope method can be seen clearly, as the derived $N_{\text{eff}} = 1.05 \cdot 10^{14}\ 1/\text{cm}^3$ is even higher and further apart from the estimate than in the other method. Overall, the double linear fit method appears to be the more reliable method when dealing with the thin diode devices of this study.

In the case of the thick devices the slope method shows better agreement in terms of the simulations and estimations. This also holds true, when considering the measured data in the slope method, as it exhibits results very close to the simulated ones. Nevertheless, the double linear fit method still provides an adequate means of obtaining V_{depl}

Table 9.18: Comparison of V_{depl} and N_{eff} of both diode batches, derived from measured data and simulations via different methods. The upper half of the table depicts the results obtained from the slope method, while the lower half show the ones derived from the double linear fit method. In both cases the structures are grouped by their size and thick devices are shown on the left and the thin ones on the right. In addition to the measured data of the diode wafer, the measured values for the diodes located on the SiMPl4 wafer are also presented, as well as the data given by TCAD simulations. The "total measured" line takes all measured results into account (see text).

	Slope method			
Area	thick		thin	
[mm^2]	N_{eff} [10^{12}/cm^3]	V_{depl} [V]	N_{eff} [10^{14}/cm^3]	V_{depl} [V]
10	3.21 ± 0.12	7.78 ± 0.33	1.09 ± 0.13	1.60 ± 0.28
25	2.86 ± 0.08	6.85 ± 0.21	1.05 ± 0.14	1.50 ± 0.30
36	2.56 ± 0.06	6.06 ± 0.17	1.11 ± 0.20	1.65 ± 0.44
100	2.65 ± 0.05	6.30 ± 0.13	0.99 ± 0.14	1.40 ± 0.30
SiMPl4 10 mm^2	3.01 ± 0.08	7.28 ± 0.20	–	–
Total measured	2.84 ± 0.27	6.80 ± 0.71	1.05 ± 0.16	1.52 ± 0.34
Simulated	2.79	6.68	–	–

	Double linear fit method			
Area	thick		thin	
[mm^2]	V_{depl} [V]	N_{eff} [10^{12}/cm^3]	V_{depl} [V]	N_{eff} [10^{13}/cm^3]
10	6.33 ± 0.37	2.39 ± 0.14	1.76 ± 0.02	8.10 ± 0.11
25	6.33 ± 0.17	2.39 ± 0.06	1.74 ± 0.02	8.02 ± 0.07
36	6.21 ± 0.12	2.61 ± 0.05	1.77 ± 0.04	8.14 ± 0.22
100	6.42 ± 0.10	2.43 ± 0.04	1.78 ± 0.03	8.19 ± 0.13
SiMPl4 10 mm^2	6.66 ± 0.15	2.51 ± 0.06	–	–
Total measured	6.39 ± 0.25	2.46 ± 0.11	1.77 ± 0.03	8.14 ± 0.15
Simulated	8.05	3.04	1.81	8.32

and N_{eff}, since the aforementioned simulated data only shows a 8% and the measured data only roughly a 12% deviation from the estimates and the other method, which are both still within the error margin of the manufacturers estimate. All things considered, it would seem that the slope method is more suitable for evaluation of the thick diode devices. It should be noted, however, that this will not hold true for higher radiation fluences as the region of the first linear fit of the $1/C^2$-curve will become more distorted, making applying the slope method less feasible the higher the fluence becomes.

Generally, neither V_{depl} nor N_{eff} are depending on the cross-section of the diode, as there is no direct relation. But, since the methods of obtaining both parameters depend on the shape of the capacitance curve, which in turn does have a dependency on the cross-section, it is valid to consider a second order influence on the final results. Subsequently, it is also in the realm of possibility that more accurate results can be achieved by considering the guard biasing during measurements.

Utilizing the data pertaining to the guard bias status available, the following was found: The double linear fit method produced nearly identical results for both V_{depl} and N_{eff} in both cases, with a deviation of roughly 0.1%, showing no real impact of the guard biasing when deploying this method. In the case of the slope method, however, the scenario with a grounded guard yielded a slightly lower value for V_{depl} of 5.66 V compared to 6.00 V, resulting in a discrepancy of 6%.

9.4.1.2 Evaluation of irradiated SiMPl materials

Leakage current increase

Damage induced to the lattice by non-ionizing means will inevitably lead to the creation of defect levels close to midgap, which in turn will be responsible for an increased leakage current within the detector bulk. This effect will be analyzed in the following by evaluating the leakage current increase of all available diodes of this study after irradiation with different neutron fluences, which were listed in Sec. 8.4.

In order to obtain a (semi) stable result and to provide data that can be compared to other studies, the annealing scenario $(80\text{min}, 60°\text{C})$, explained in Sec. 4.1.4.4, was used after the samples were stored at a temperature of approximately 258 K between irradiation and annealing. The measurements were performed in the same fashion as the related ones of Sec. 9.4.1.1 and a temperature correction of the measured currents in accordance to Eq. (4.26) was applied. A reference temperature of $T_R = 293$ K was chosen. Afterwards, the leakage current increase ΔI_{leak} was derived by calculating the difference of currents before and after irradiation.

Figure 9.48 depicts the resulting leakage current increase per volume $\Delta I_{leak}/V$ in dependence on the neutron equivalent fluence Φ_{neq} according to the NIEL hypothesis. The data of the thick devices is shown in a) while the one for the thin diodes is presented in b). In both cases, multiple sets of data were available, namely the measurements of the diode wafer diodes and the respective simulation obtained by Synopsys, as well as the results from the SiMPl4 diodes for the thick devices.

By applying a linear fit on each set of diode data, the current related damage rate α can be extracted, as the slope of the linear fit corresponds to α via Eq. (4.25):

$$\frac{\Delta I}{V} = \alpha \, \Phi_{neq} \; . \tag{9.5}$$

In all cases, a clear linear relation between $\Delta I_{leak}/V$ and Φ_{neq} can be observed with only few data points lying slightly of the linear range for the SiMPl4 diodes. Their currents in those instances exhibit larger values compared to the other diodes. This was

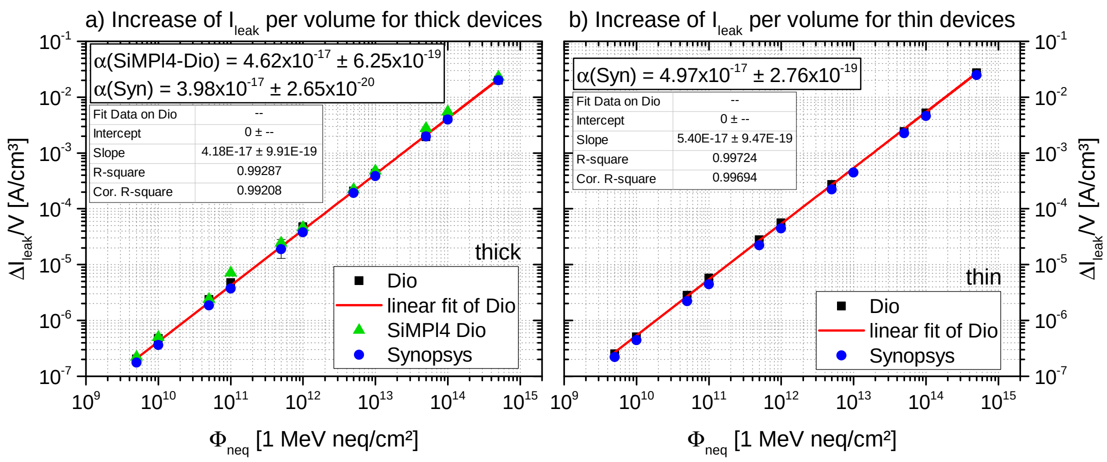

Figure 9.48: Fluence dependent leakage current increase per volume $\Delta I_{leak}/V$ of a) thick and b) thin diode structures. In both cases, the simulated data from Synopsys is also included and shows very good agreement with the measured values. The linear fits (red lines) are applied to the data sets of the diode wafer diodes in both scenarios and the fit box lists the resulting slope, which corresponds to the current related damage rate α, and the quality of the fit. The extracted damage rates for the other cases are also given. $\alpha_R \approx 4 \cdot 10^{-17}$A/cm can be expected from literature and previous studies.

Table 9.19: Summary of the current related damage rates α, obtained via simulation and measurements of diode structures. The error err(α) is given underneath the values for α. Previous studies indicate independence of material and that $\alpha_R \approx 4 \cdot 10^{-17}$A/cm can be expected. In the case of the thick devices, the obtained values are in very good agreement with α_R, while a slight discrepancy can be experienced with the thin case (see text).

	thick			thin	
	Dio	SiMPl4	Synopsys	Dio	Synopsys
α $[10^{-17}$ A/cm$]$	4.18	4.62	3.98	5.40	4.97
err(α) $[10^{-17}$ A/cm$]$	± 0.10	± 0.07	± 0.01	± 0.10	± 0.03

already observed before irradiation and is most likely another indication of additional defects present within those structures. The results, however, are still in very good agreement with the rest of the measured device. It can also be seen that the simulations of the diode structures including radiation damage are in excellent accordance with the measured data.

The boxes within the plots contain the information of the fit performed on the diode wafer diode measurements and the resulting value for α. The linear fits on the other sets of values are not explicitly shown, but the resulting current related damage rates are listed next to the fit boxes. An overview of all obtained values for α is also presented in Table 9.19. It was elaborated in Sec. 4.1.5.1 that α is not dependent on material and should generally provide a constant value close to $\alpha_R \approx 4 \cdot 10^{-17}$A/cm. This was achieved by the simulation of the thick devices with $\alpha_{thick}(\text{Syn}) = 3.98 \cdot 10^{-17}$A/cm, as well as the diode wafer diodes with $\alpha_{thick}(\text{Dio}) = 4.18 \cdot 10^{-17}$A/cm. As previously discussed, the generally higher current of the SiMPl4 diodes now also leads to slightly higher value of α_{thick}(SiMPl4-Dio) $= 4.62 \cdot 10^{-17}$A/cm, which can nonetheless still be considered in acceptable agreement.

The, by contrast, rather large values derived from the measurements and simulations of the thin devices, can most likely be attributed to the same cause as the initially already high leakage currents. These, in turn, most likely stem from the aforementioned diffused backside implant, which makes up the majority of the depletion region of the thin devices. The higher concentration of defect states in combination with the formation of additional ones caused by irradiation, could very likely lead to an increased value of α seen here.

In summary, apart from this small discrepancy due to the thin device layout, the obtained data on the increased leakage current due to irradiation indicate results which are in compliance with expectations from previous studies and can thereby also confirm the quality the of the irradiation procedure.

Change in full depletion voltage and effective doping concentration

Another important impact on the detector performance is the change of the effective doping concentration (and subsequent change in full depletion voltage), which can lead to type inversion. This effect stems from the combined effort of donor removal and the creation of acceptor states in the bulk. It is therefore of importance to identify the possible point - or fluence - of type inversion in order to determine if this effect will take place during the lifetime of the detector and how much it may compromise the detector performance. One way to achieve this is by evaluating the capacitance data of irradiated diodes as will be shown below. The measurement setup is equal to the non-irradiated case.

A direct relation between N_{eff} and V_{depl} was established by Eq. (3.10), hence a

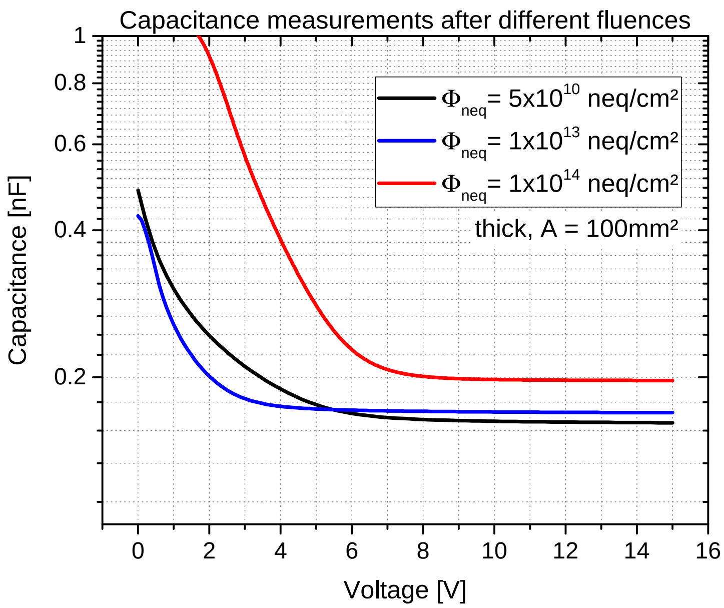

Figure 9.49: Capacitance measurements of diodes after different neutron fluences. All diodes measured were of equal thickness and cross-section and exhibited initial depletion voltages ranging from 6.30 V to 6.42 V. The different colored lines represent the experienced neutron fluences. Up to a certain Φ_{neq} it can be seen that the plateau region will be reached faster, thus lowering V_{depl}, wheres the highest fluence will result in increased values of V_{depl}.

change in N_{eff} will be visible in a capacitance measurement, such as the one shown in Fig. 9.49. The displayed data is that of three thick diodes with a cross-section of 100 mm^2, each having experienced a different total neutron fluence and being represented as the different colored lines. Depending on the applied method, the initial full depletion voltage ranged from 6.30 V to 6.42 V. Looking at the lowest fluence shown, $\Phi_{neq} = 5 \cdot 10^{10}$ neq/cm^2 (black), only a small shift is visible. The case, however changes for $\Phi_{neq} = 1 \cdot 10^{13}$ neq/cm^2 (blue), as the plateau can be seen to be reached at approximately half of the previously required voltage, thus indicating a lowered V_{depl}. Finally for the red curve ($\Phi_{neq} = 5 \cdot 10^{14}$ neq/cm^2), the situation reverts and the device exhibits an increase in V_{depl}, surpassing the initial value. This is attributed to the material undergoing type inversion.

The resulting change in full depletion voltage in dependence on the experienced neutron fluence has been measured for all available diodes and extracted via the two methods introduced in Sec. 5.2.2. In the case of the thick devices, the diode wafer diodes as well as the SiMPl4 diodes were evaluated and compared to the simulated data obtained with Synopsys. The result can be seen in Fig. 9.50a) for the slope method and Fig. 9.50c) for the double linear fit method.

Both sets of measured data show a similar behavior for both methods: Initially V_{depl} only changes marginally until a fluence of roughly $\Phi_{neq} = 5 \cdot 10^{12}$ neq/cm^2 is reached, where both start decreasing more drastically, followed by a suggested region of very small change again and finally leading to a severe increase for $\Phi_{neq} = 5 \cdot 10^{14}$ neq/cm^2. In both methods, the values for the SiMPl4 diodes show slightly higher results of V_{depl}, with the discrepancy between those and the other diodes being very small for low fluences in the slope method compared to the double linear fit method. However, starting from $\Phi_{neq} = 5 \cdot 10^{10}$ neq/cm^2, the deviation increases in the case of the slope method, while the other methods divergences decrease the higher the fluence becomes. This is in compliance with the conclusion from the previous section, in which the slope method proved to be more consistent with expectations in non-irradiated cases.

Due to the nature of the method it will decrease in efficiency if the shape of the evaluated $1/C^2$-curve becomes distorted, which is the case after irradiation. Then, the double linear fit method shows more consistent results for the measured data, which is also indicated by smaller error bars on the data points. The simulated data behaves equally in both methods but different from the measured ones as it shows only a small dip around $\Phi_{neq} = 1 \cdot 10^{14}$ neq/cm^2 and remains constant otherwise. The discrepancy in absolute values between simulation and measurement is on par with the results from Table 9.18 with the double linear fit case exhibiting a higher absolute value for V_{depl} and subsequent larger deviation from the measured data.

The situation regarding the thin devices, depicted in Fig. 9.50e), differs from the thick counterparts by merit of not being able to provide reliable results via the slope method applied to the simulated data, as was already mention in the previous section. Hence, only the resulting values of V_{depl} for the diode data, obtained with both methods and the simulated ones obtained via the double linear fit method are presented. In the case of the latter, constant values throughout all fluences can be observed with only a small dip being present at the highest available fluence. This is true for both the measured and simulated data, which are in good agreement. However, a very distinct deviation between the results of both methods can be seen, since the slope method sports smaller absolute values in addition to an irregular behavior which does not conform to the established theory. Furthermore, the limited applicability of the slope method on the thin structures can also be deduced from the large error margin of the evaluated data points.

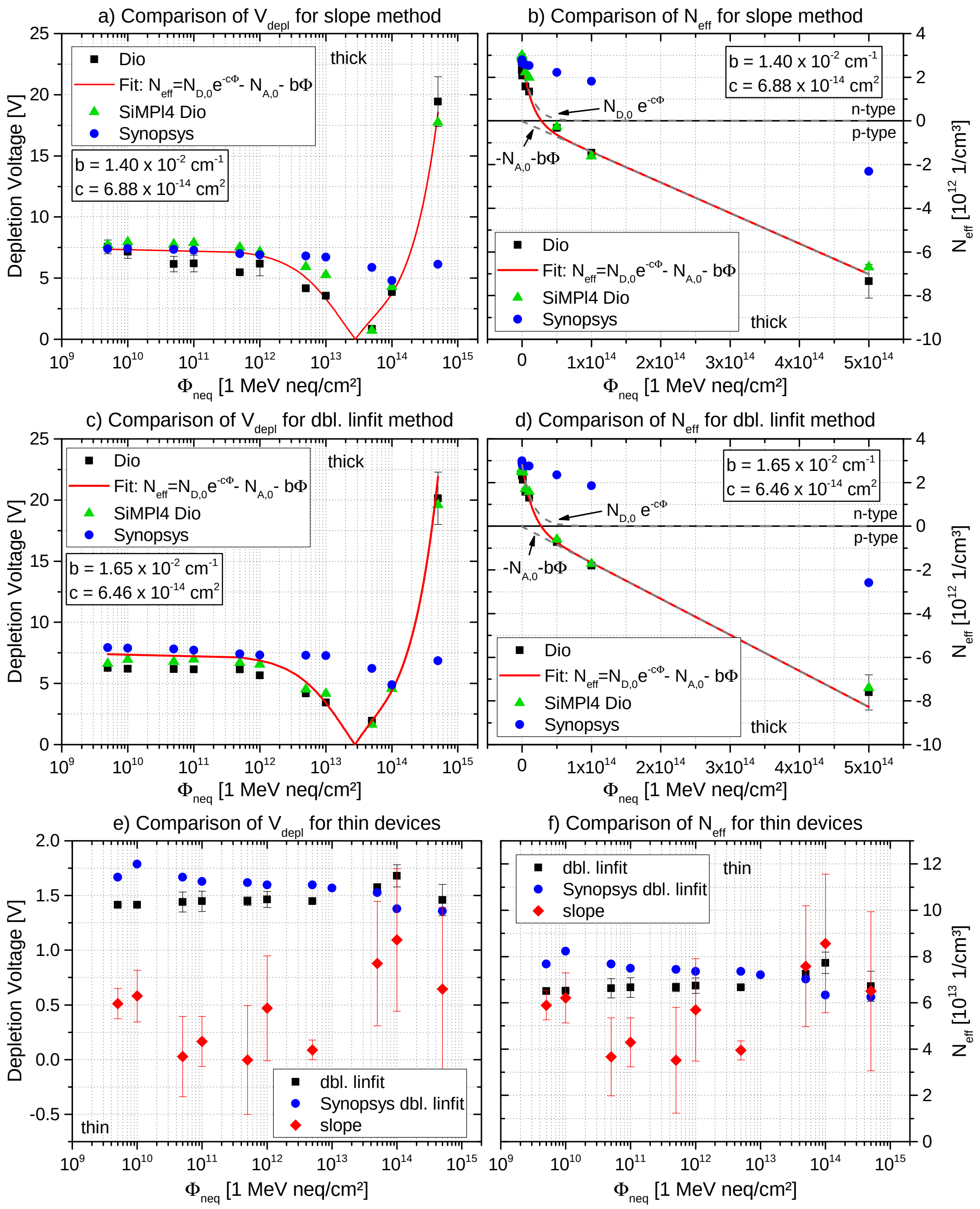

Figure 9.50: Summary of the change in depletion voltage and effective doping concentration after neutron irradiation. The values for V_{depl} and N_{eff} were extracted by the slope method and double linear fit method for thick and thin devices. The right hand side depicts the change in V_{depl} for the thick material via a) slope and c) double linear fit method, while the results for the thin devices are summarized in e). The left hand side shows the change in N_{eff} in b), d) and f) and is arranged analogous. The red line illustrates the fit according to Eq. (4.28), applied to the diode wafer diode data set and the boxes list the extracted fit parameters. This fit function was converted to an equivalent function for V_{depl} via Eq. (3.10) and included in the right hand side plots. Note that applying the slope method on the simulated data of the thin devices, as well as applying the fit on any dataset of the thin devices was not feasible (see text).

Figure 9.50b), d) and f) depict the respective results for the extracted effective doping concentration in the same fashion as above. Since N_{eff} and V_{depl} are directly related, the discrepancies between the measured and simulated data, as well as between the methods for both thicknesses are similar. Figure 9.50f) suggests that no major change in N_{eff} up to the maximum available fluence will take place, since there is only a very small decrease visible at $\Phi_{neq} = 5 \cdot 10^{14}$ neq/cm^2.

On the other hand, a different situation can be observed for the thick material. Here N_{eff} changes sign after a certain fluence and becomes increasingly negative. This means that the material underwent type inversion and effectively transitioned from n to p-type material due to the removal of donors and simultaneous creation of acceptors. This is true for both measured diode sets as well as the simulated data, albeit the simulation indicates type inversion taking place at a higher dose than the measured data.

In order to more accurately ascertain the suggested point of type inversion, a fit in the form of Eq. (4.28)

$$N_{eff}(\Phi) = N_{D,0}\, e^{-c\Phi} - N_{A,0} - b\,\Phi \tag{9.6}$$

can be applied to the displayed values of N_{eff} and in addition the fit parameters b and c can be obtained, the former being the probability to create an acceptor state by a hadron per unit length and the latter the donor removal cross-section (see Sec. 4.1.5.2). The constant $N_{D,0}$ represents the initial donor concentration and was chosen to be $N_{D,0} = 2.81 \cdot 10^{12}$ 1/cm^3, while $N_{A,0}$ conversely denotes the initial acceptor concentration in the bulk. Since the material is initially n-type, only a small impurity concentration of acceptors equal to 1% of the donor concentration can be assumed, leading to $N_{A,0} = 2.81 \cdot 10^{10}$ 1/cm^3.

The fit was applied to all available data sets and the resulting one for the diode wafer diodes (for each respective case) is depicted as red line in Fig. 9.50a)-d). The curve in the depletion voltages plots was obtained via converting the initial one with Eq. (3.10). The fluence at which type inversion is expected to occur can now be identified, as when N_{eff} or V_{depl} become zero and seems to be equal for both methods, namely $\Phi_{neq}^{ti} \approx 3 \cdot 10^{13}$ neq/cm^2. With this, the behavior of V_{depl} around this fluence can now be properly explained, as the values do not stay constant after the initial decrease, but continue decreasing more drastically, followed by an equally drastic increase afterwards. The dashed lines on the right hand side plots represent the individual components of Eq. (4.28) relating to the donor removal and acceptor creation, respectively.

In contrast, the simulations indicate that type inversion should occur at $\Phi_{neq}^{ti} \approx 2.5 \cdot 10^{14}$ neq/cm^2, which is a fluence roughly one order of magnitude larger than the one obtained from the measurements. This can most likely be attributed to the model used in the Synopsys software framework, as already mentioned in Sec. 7.2. The modeling of non-ionizing radiation damage is still not well understood and a subject of discussion, as the formation of an unifying ansatz is still underway. It is thereby likely that additional processes need to be included and the specific rates have to be adjusted for future studies.

It can be seen that this fitting procedure was not applied to the data of the thin material. The reason for this lies in the fact that no type inversion occurred there. In a case like this, the fitting will not yield feasible results as for example b will become negative, suggesting a removal of acceptors, which is not the case in reality. This was already found in studies like [68] and was thereby omitted.

Another important insight can be gathered by discussion of the resulting fit parameters b and c. As the topic of non-ionizing radiation damage is still part of an ongoing research, not every aspect is entirely understood, yet. For example, currently there exists no model which can precisely predict the point of type inversion for an arbitrary material

Table 9.20: Summary of the fit parameters b and c obtained by fitting Eq. (4.28) to the data of N_{eff} for different neutron fluences. The fit was applied to the experimental and simulated results of the thick devices, derived via both methods (slope and dbl. linfit). Fitting attempts on the results of the thin material were not feasible (see text). A drastic discrepancy of the simulated case compared to the measured cases further points to the model utilized in Synopsys being insufficient to accurately describe reality, thus requiring further improvements. In the case of the double linear fit method on the simulations, the fit of Eq. (4.28) did not converge, thereby not yielding any information on the error.

		Dio	SiMPl4	Synopsys
Slope method	b [10^{-2} 1/cm]	1.40 ± 0.19	1.40 ± 0.04	0.86 ± 0.31
	c [10^{-14} cm^2]	6.88 ± 1.52	3.58 ± 0.53	0.07 ± 0.15
Double linear fit method	b [10^{-2} 1/cm]	1.65 ± 0.22	1.49 ± 0.04	$1.07 \pm -$
	c [10^{-14} cm^2]	6.46 ± 0.58	6.17 ± 1.08	$0.01 \pm -$

and type of radiation. Only estimates based on previous studies with similar material and radiation source can be made. One possible step towards such a meta-model is developing models for b and c, as both can exhibit vastly different results depending on the aforementioned criteria. Such models would allow to utilize an ansatz like Eq. (4.28) for reliable predictions.

For this purpose, all obtained values for b and c are summarized in Table 9.20. In [68] the author attempted to compare multiple previous studies to find patterns and correlations, based on the thickness and resistivity of the material, as well as some of its manufacturing procedures, in addition to the type of irradiation. While no clear pattern nor model could be deduced, various trends were visible and discussed. However, since this is not the focus of this study, such an in-depth discussion will not be included here. Nevertheless, it can be noted that the experimentally obtained values in Table 9.20 are in good agreement with previous studies, while the simulated ones prove unreliable. There is no direct match in terms of the values for b and c, since a material like the one of this study was not included in the discussion, but they still behave within the established trends.

9.4.1.3 Summary

In order to determine the general impact of non-ionizing radiation damage on the material of SiMPl4 and SiMPl5 device, diodes of various cross-sections of the same material were pre-characterized and afterwards irradiated with equivalent neutron fluences up to $\Phi_{neq} = 5 \cdot 10^{14}$ neq/cm^2.

The investigation of the leakage current increase exhibited the expected behavior for the higher resistivity material (thick) of a linear increase of $\Delta I_{leak}/V$ with increasing Φ_{neq}, leading to current related damage rates α which are in very good agreement with previous studies. Furthermore, the simulations were also in excellent agreement with measured data.

The results of the lower resistivity material (thin), still showed the linear increase, but the obtained values for α for both measurement and simulation were higher than expected. Even though the reason for this might already be understood, as it likely caused by the diffusion of the backside implant making up the majority of the depleted region of the bulk, the impact still has to be considered with care, since this will inevitably lead to an increased dark count rate (DCR) of the SiMPl5 devices. Due to the DCR already being one of the biggest limiting factors for SiPMs in terms of radiation hardness, this result can be considered concerning and needs to be investigated for further optimization. A possible approach might be an increased thickness, while still treading within the limits set by the electronics components or a change of the backside implant in order to avoid such pronounced diffusion into the bulk.

The evaluation of the change in effective doping concentration N_{eff} and full depletion voltage V_{depl} yielded various insights. First, the methods with which those parameters are extracted from capacitance measurements need to be considered as they may lead to non-negligible discrepancies, especially when dealing with material that exhibits inherently low depletion voltages which are already pushing the evaluation methods to their limits.

Second, results indicate that the higher resistivity material will undergo type inversion at roughly $\Phi_{neq}^{ti} \approx 3 \cdot 10^{13}$ neq/cm^2, while the lower resistivity material seems to be safe in this regard. This is a very satisfying result in two aspects. Since experiments like ILC and CLIC were mentioned as possible instances for application of SiMPl devices for tracking and calorimeter readout, their respective requirements need to be taken into account. As already mentioned, tracking detectors for ILC and CLIC will supposedly experience a total equivalent neutron fluence per year of $\Phi_{neq,\text{ILC}} \approx 1 \cdot 10^{11}$ neq/cm^2 and $\Phi_{neq,\text{CLIC}} \approx 4 \cdot 10^{10}$ neq/cm^2, respectively. Both material batches of SiMPl devices are almost not affected by this fluence at all and type inversion only being an issue for the higher resistivity material after roughly 300 years of ILC or 750 years of CLIC operation. It also needs to be noted that the higher resistivity material is not considered to be deployed this close to the beamline, meaning that the impact of non-ionizing radiation damage will be even less prevalent, while the material which is actually considered for tracking applications is inherently radiation hard in regards to changes in N_{eff} and V_{depl}.

Third, comparison with the simulation showed significant deviations to the measured data pertaining when type inversion will occur. Thus it can be concluded that the model utilized to simulate the change in N_{eff} and V_{depl} still needs to be adapted and optimized in accordance to measured data for further studies.

Lastly, by applying the commonly accepted fit function on the data of the change in N_{eff}, multiple sets of fit parameters were obtained. Since the topic of non-ionizing radiation damage is still not fully cataloged and understood, these parameters can serve future studies dealing with the issue of developing a unified model in order to predict the exact change in N_{eff} for a given material and type of radiation.

9.4.2 Static test devices

Even though the previous section has shown that for both SiMPl4 and SiMPl5 materials, effects like type inversion will not be severely detrimental up to certain higher fluences, it is nonetheless of great importance to determine the impact of radiation damage on various parameters of SiMPl devices. For this purpose, the static test devices were also irradiated alongside the diodes and the following sections will deal with their evaluation.

First, the static test devices of the SiMPl4-2 wafer will be investigated, focusing on parameters like the maximum overbias voltage $V_{ob,max}$ in order to still allow proper quenching and the two recovery times $\tau_{90\%}$ and $\tau_{1/e}$. In the case of SiMPl5 the focus lies mainly in the change of the backside resistance ΔR_{vert} due to the change in effective doping concentration. Both discussions include a comparison to the data obtained from simulation studies.

9.4.2.1 SiMPl4

Quenching

In order to evaluate the impact of non-ionizing radiation damage on the static test devices, the experimental procedures of the non-irradiated situation are repeated. First the changes regarding the potential maximum overbias voltage $\Delta V_{ob,max}$ via the previously mentioned 20 µA rule of thumb were analyzed.

A summary of the results is listed in Table A.3 and visualized in Fig. 9.51. $V_{ob,max}$ is given for all featured pitch/gap combinations and for various equivalent neutron fluences Φ_{neq}. The overall behavior in regards to the geometrical variation can be found to be identical to the case before irradiation (see Sec. 9.2.2.2). Overall the data shows an increase of $\Delta V_{ob,max}$ with increasing fluence, which can be attributed to the decrease

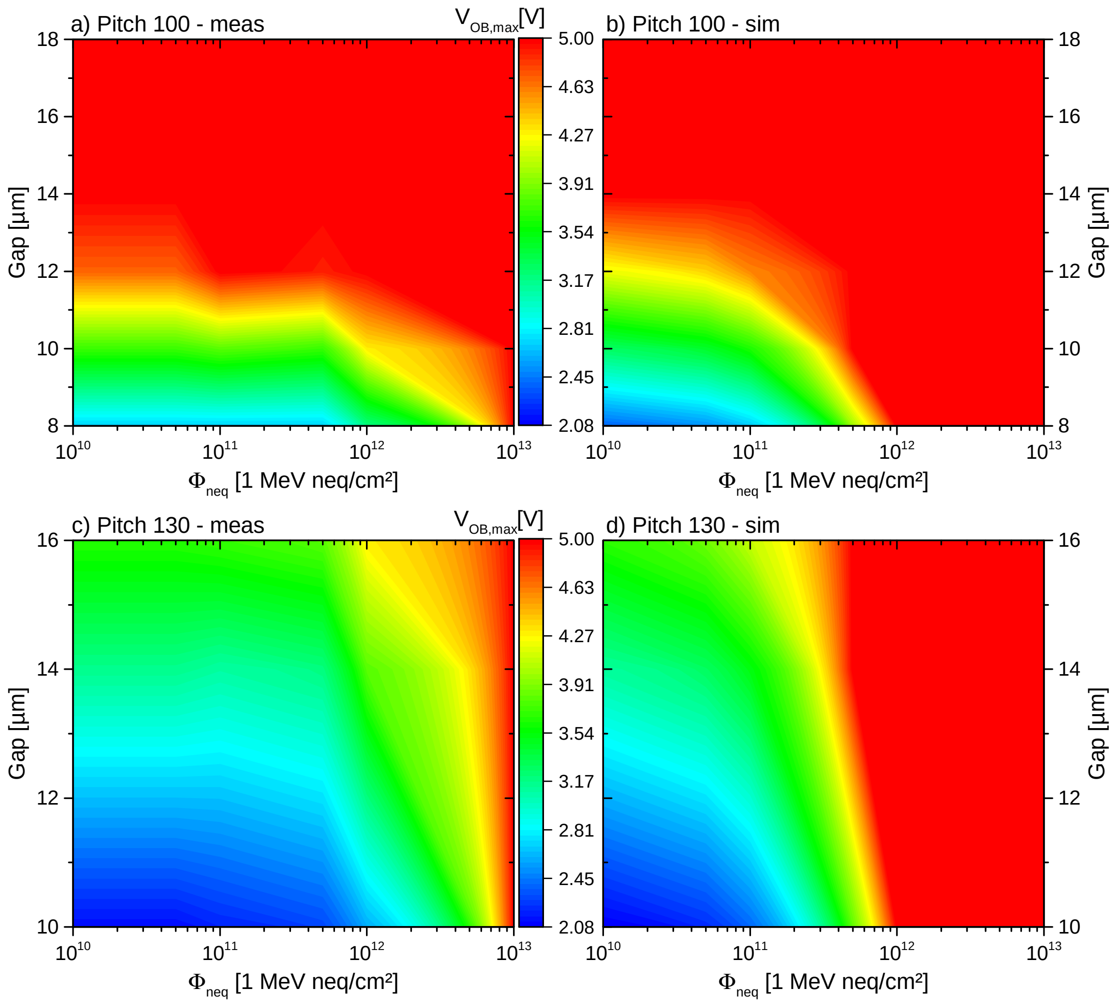

Figure 9.51: $V_{ob,max}$ for different geometries dependent on the experienced equivalent neutron fluence Φ_{neq}. The measured data is shown on the left hand side while the simulation results can be seen on the right. A general increase of $V_{ob,max}$ with increasing Φ_{neq} can be observed due to the decrease in N_{eff}. A full list of all available data can be found in Table A.3.

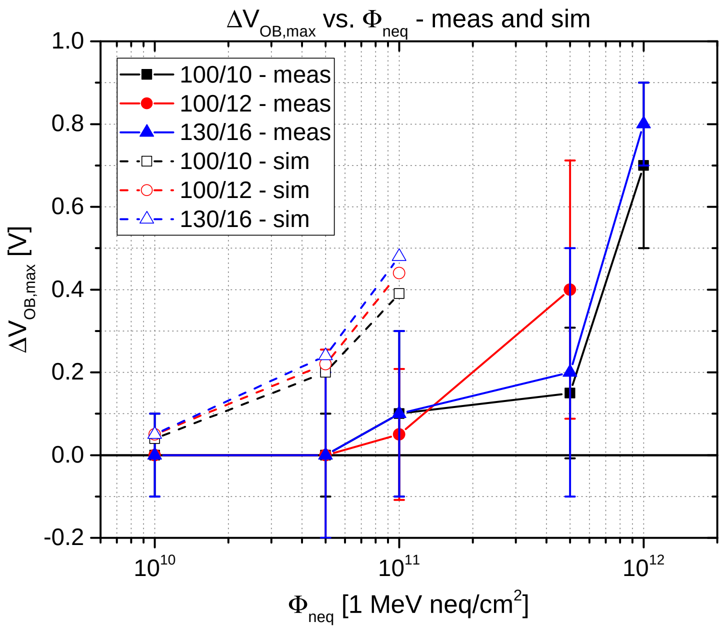

Figure 9.52: Absolute change in maximum overbias voltage $\Delta V_{ob,max}$ for increasing neutron fluences Φ_{neq}. The various colored symbols each represent a different pitch/gap combination with the solid symbols corresponding to experimental and the hollowed ones to simulated results. Only data up to $\Phi_{neq} = 1 \cdot 10^{12}$ neq/cm^2 is displayed, since the final values exceed the maximum considered voltage of 5 V. Initial changes can be observed to be miniscule, however, increasing fluences will result in an increase of $\Delta V_{ob,max}$ with the simulated values being significantly higher compared to the measured ones.

in N_{eff}, thus allowing for an easier depletion of the gap area, as well as the resulting increase of the bulk resistivity ρ. Consequently, R_Q will increase resulting in smaller possible currents and thus a shift of $V_{ob,max}$ to higher values.

In terms of absolute values, the initial difference was already discussed in Sec. 9.2.2.2. The simulated results show a steady increase of $V_{ob,max}$ for even the smaller fluences, in contrast to the measured data. This is illustrated in Fig. 9.52 which depicts $\Delta V_{ob,max}$ for increasing Φ_{neq}. The different symbols each stand for different pitch/gap combination with the solid ones representing the measured and the hollow ones the simulated data. While the initial changes are small, in the case of the simulations $\Delta V_{ob,max}$ increases significantly faster, resulting in higher values than the measured ones for $\Phi_{neq} \geq 5 \cdot 10^{11}$ neq/cm^2 for a pitch of 100 µm and $\Phi_{neq} \geq 5 \cdot 10^{10}$ neq/cm^2 in the case of a 130 µm pitch.

This is contrary to the behavior observed in the previous section and Fig. 9.50a)–d), where a smaller change of N_{eff} due to radiation damage could be observed in the simulated results. Hence, the depletion region should be reduced for the same voltage relations within the bulk area, thus leading to the conclusion that $V_{ob,max}$ should also increase less quickly compared to the measured case. This discrepancy can likely be attributed to the utilized model of non-ionizing radiation damage within Synopsys, further indicating that revisions are necessary to accurately model the removal and introduction of donor and acceptor states, respectively.

Data for $\Phi_{neq} > 1 \cdot 10^{12}$ neq/cm^2 is not included in Fig. 9.52, since the maximum considered $V_{ob,max}$ of 5 V was exceeded after radiation or even beforehand, thus making a determination of $\Delta V_{ob,max}$ not possible. This can also be seen in Table A.3 with many geometrical variation resulting in $V_{ob,max} > 5$ V in cases of even small fluences. For pitch 100 µm, gaps 14 µm, 16 µm and 18 µm, all fluences will lead to $V_{ob,max} > 5$ V. This can also be interpreted as the devices being affected more easily by pinch-off due to the reduced N_{eff} resulting in cases with relative larger gap sizes being more susceptible to this effect, as was seen before.

No data for $\Phi_{neq} > 1 \cdot 10^{13}$ neq/cm^2 is listed, as type inversion was observed to occur at roughly $\Phi_{neq} \approx 3 \cdot 10^{13}$ neq/cm^2. Afterwards, the quenching behavior cannot be extracted any longer with this measurement procedure, since the bulk becomes *p*-type due to donor removal taking place, resulting in the formation of a *n*-*p*-*n*-junction underneath the HF regions of the cells. It is, however, safe to assume that this bulk region will consequently be either fully depleted or, in the case of higher fluences, very high ohmic, thus leading to even higher values of $V_{ob,max}$.

Therefore, it can be concluded that cases previously classified as close to non-quenching will become the most promising variations after experiencing non-ionizing radiation damage, such as 100/8 and 130/10. This can also be considered positive in terms of the sensitive area of the devices, as smaller gaps directly result in larger fill-factors.

Recovery

Following the evaluation of the quenching behavior, the impact of radiation damage on the recovery times $\tau_{90\%}$ and $\tau_{1/e}$ as well as their ratio $\tau_{90\%}/\tau_{1/e}$ was investigated. The procedure is identical to the one utilized before radiation, discussed in Sec. 9.2.2.2.

The results, including a comparison of simulated and measured data are summarized in Table 9.21. The values shown were measured at $V_{ob} = 5$ V and if no values are listed for a specific geometrical variation, the recovery times were considered too large and not feasible and were thereby not included. Similar to the quenching condition, an overall increase of all recovery times with increasing Φ_{neq} is visible with the severity increasing with larger relative gap sizes due to the JFET-like nature of R_Q. The impact of different overbias voltages is not included as the trends observed before radiation are also valid here.

Figure 9.53 depicts the changes in the recovery times $\tau_{90\%}$ in a) and the ratio $\tau_{90\%}/\tau_{1/e}$ in b) for the measured and simulated data. Similar to before, the discrepancy between measured and simulated values shows the simulated ones exhibiting significantly higher changes in recovery times $\Delta\tau$ at smaller fluences. For fluences $\Phi_{neq} < 1 \cdot 10^{12}$ neq/cm^2 the changes in the measured recovery times constitute less than 10% in most cases, which is consistent with the measured changes in $V_{ob,max}$. Cases with larger relative gap sizes exhibit larger $\Delta\tau$ earlier due to the impact of the non-linearity caused by the increased depleted bulk volume.

A similar pattern is visible in the simulated cases, the changes, however, are more pronounced, reaching values > 10% already at $\Phi_{neq} = 1 \cdot 10^{11}$ neq/cm^2, overall exhibiting a linear increase with Φ_{neq}. This, in turn, is consistent with the simulated behavior of $V_{ob,max}$. The discrepancy between simulation and measurement lessens at the highest fluences resulting in recovery times $\tau_{90\%}$ in both cases in the range of tens of µs, with higher gap cases even exhibiting higher measured ones compared to simulations. This can be explained by taking the reduction of N_{eff} into account, resulting in a state close to pinch-off in both cases, in which the volume of bulk depletion becomes similar.

Identical observations regarding the relative changes of $\tau_{90\%}/\tau_{1/e}$ for simulations and measurements can be made. This can be considered evidence that both recovery times are affected equally by the impact of radiation damage and no additional parasitic effect

Table 9.21: Summary of the change in recovery times $\tau_{90\%}$ and $\tau_{1/e}$ as well as the ratio $\tau_{90\%}/\tau_{1/e}$ due to radiation damage. All data was taken at $V_{ob} = 5$ V. Overall, the measured times feature significantly smaller values compared to the simulated ones (see text). Statistical errors could not be obtained due to only one device per fluence being available in some cases. The measurement error can be approximated to result in an error of τ in the range of 10^{-10} s and was therefore omitted.

pitch [µm]	gap [µm]	Φ_{neq} [neq/cm²]	$\Delta\tau_{90\%}$ [10^{-7} s] sim	$\Delta\tau_{90\%}$ [10^{-7} s] meas	$\Delta\tau_{1/e}$ [10^{-7} s] sim	$\Delta\tau_{1/e}$ [10^{-7} s] meas	$\Delta(\tau_{90\%}/\tau_{1/e})$ sim	$\Delta(\tau_{90\%}/\tau_{1/e})$ meas
100	8	$1 \cdot 10^{10}$	0.05	0.05	0.01	0.01	0.01	0.03
		$1 \cdot 10^{11}$	0.53	0.15	0.15	0.04	0.08	0.03
		$5 \cdot 10^{11}$	3.50	0.38	0.98	0.14	0.23	0.07
		$1 \cdot 10^{12}$	8.20	1.02	2.37	0.25	0.22	0.24
		$1 \cdot 10^{13}$	113	80.3	34.6	16.4	0.09	1.76
	10	$1 \cdot 10^{10}$	0.08	0.05	0.02	0.01	0.01	0.02
		$1 \cdot 10^{11}$	0.91	0.32	0.24	0.05	0.08	0.06
		$5 \cdot 10^{11}$	5.99	0.45	1.64	0.16	0.22	0.08
		$1 \cdot 10^{12}$	14.0	2.45	3.92	0.58	0.21	0.33
		$1 \cdot 10^{13}$	193	218	56.8	36.0	0.09	2.69
	12	$1 \cdot 10^{10}$	0.14	0.12	0.04	0.03	0.01	0.05
		$1 \cdot 10^{11}$	1.56	0.62	0.39	0.12	0.09	0.07
		$5 \cdot 10^{11}$	10.1	1.09	2.56	0.28	0.25	0.04
		$1 \cdot 10^{12}$	23.4	3.83	6.10	0.82	0.22	0.36
		$1 \cdot 10^{13}$	324	612	88.3	68.0	0.12	5.31
	14	$1 \cdot 10^{10}$	0.27	0.56	0.06	0.06	0.01	0.06
		$1 \cdot 10^{11}$	2.93	0.85	0.62	0.13	0.12	0.11
		$5 \cdot 10^{11}$	18.7	4.94	4.05	0.49	0.30	0.60
		$1 \cdot 10^{12}$	42.8	12.2	9.60	1.84	0.26	0.92
		$1 \cdot 10^{13}$	597	–	139	125	0.17	–
	16	$1 \cdot 10^{10}$	0.69	2.47	0.10	0.15	0.03	0.30
		$1 \cdot 10^{11}$	7.39	5.50	1.05	0.34	0.22	0.58
		$5 \cdot 10^{11}$	45.3	32.9	6.84	1.33	0.45	3.04
		$1 \cdot 10^{12}$	102	62.5	16.1	4.40	0.34	4.20
		$1 \cdot 10^{13}$	–	–	234	692	–	–
130	10	$1 \cdot 10^{10}$	0.07	0.01	0.02	0.01	0.01	0.01
		$1 \cdot 10^{11}$	0.72	0.11	0.22	0.03	0.06	0.03
		$5 \cdot 10^{11}$	4.78	0.43	1.50	0.06	0.17	0.06
		$1 \cdot 10^{12}$	11.2	1.34	3.60	0.38	0.16	0.15
		$1 \cdot 10^{13}$	153	101	51.4	24.8	0.07	1.33
	14	$1 \cdot 10^{10}$	0.12	0.02	0.04	0.01	0.01	0.01
		$1 \cdot 10^{11}$	1.30	0.19	0.39	0.04	0.06	0.04
		$5 \cdot 10^{11}$	8.51	0.96	2.60	0.27	0.16	0.06
		$1 \cdot 10^{12}$	19.8	2.61	6.19	0.73	0.15	0.20
		$1 \cdot 10^{13}$	271	24.3	88.0	55.8	0.07	1.90
	16	$1 \cdot 10^{10}$	0.16	0.03	0.05	0.01	0.01	0.02
		$1 \cdot 10^{11}$	1.72	0.31	0.50	0.09	0.07	0.03
		$5 \cdot 10^{11}$	11.2	0.58	3.33	0.19	0.17	0.01
		$1 \cdot 10^{12}$	26.0	3.27	7.89	0.86	0.16	0.25
		$1 \cdot 10^{13}$	357	398	112	70.5	0.09	2.46

is thereby occurring. As clearly visible in Fig. 9.53b), the changes in $\tau_{90\%}/\tau_{1/e}$ are small up to $\Phi_{neq} = 1 \cdot 10^{12}$ neq/cm^2 and increase drastically afterwards in the case of the measured data. This discrepancy is likely caused by the devices reaching states closer to type inversion compared to the simulation cases, thus being more heavily affected by the increased bulk depletion and thereby non-linearity. This is also reflected in the increased discrepancies in the case of both recovery times for the highest listed fluence of $\Phi_{neq} = 1 \cdot 10^{13}$ neq/cm^2.

In regards to the discrepancy between simulations and measurements the same argument made above holds true in this analysis, as an overall slower increase should be observed in the simulations according to the results of Fig. 9.50. Thus, it is likely caused by the utilized radiation damage model within Synopsys. In addition, type inversion also prevents proper evaluation of the measurements for higher fluences for the same reasons mentioned above. However, following the same string of arguments, vastly increased recovery times can be expected with further increasing fluences. Equal to the quenching behavior, the most promising device variations can be found in pitch/gap combinations previously exhibiting a non-quenching behavior, since the reduction in N_{eff} will result in comparably normal operation circumstances and thus reasonable recovery times after irradiation.

Analyzing the behavior of $\Delta\tau_{90\%}$(sim) in Fig. 9.53a), a linear increase with Φ_{neq} can be observed. Since the measured increase of $\tau_{90\%}$ was found to be smaller for fluences below type inversion, the simulated results could be utilized as an upper-limit or worst-case estimate in terms of recovery time degradation due to radiation damage. For this purpose, a linear fit was applied to the absolute values of the simulated data of $\Delta\tau_{90\%}$ for all available pitch/gap combinations in order to extract a fluence dependent increase of the recovery time $\tau_{90\%}$ for different geometrical variations ($\Delta\tau_{90\%}/\Phi_{neq}$).

The results can be seen in Fig. 9.54, where $\Delta\tau_{90\%}/\Phi_{neq}$ is plotted for various gap sizes. An overall similar trend to previous investigations regarding parameters related to

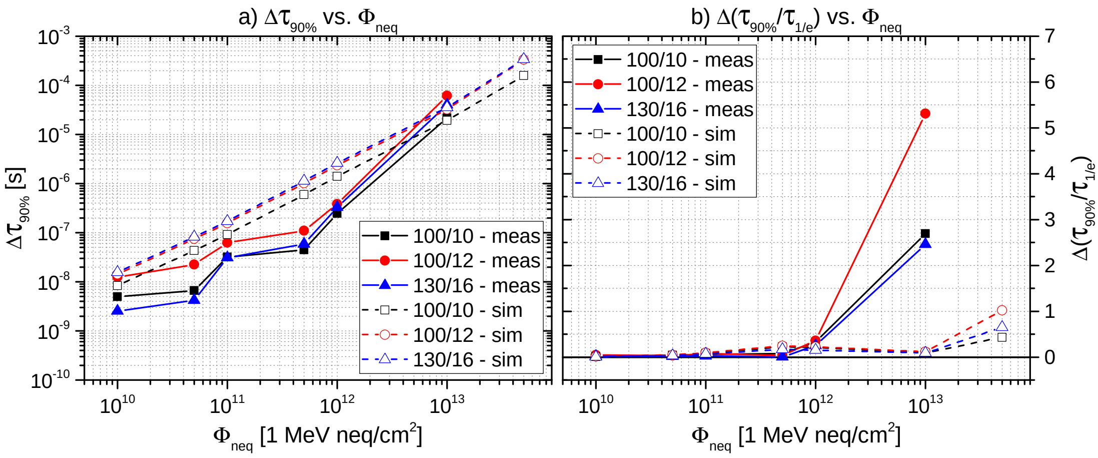

Figure 9.53: Increase of recovery time $\tau_{90\%}$ (a)) and change in $\tau_{90\%}/\tau_{1/e}$ (b)) due to non-ionizing radiation damage. In both plots, the various colored symbols represent different pitch/gap combinations with the solid ones being the measured and the hollow one the simulated data. In a) the simulated data suggest a linear increase of $\Delta\tau_{90\%}$, which can be used to define an upper estimate on the expected increase in $\tau_{90\%}$ (see Fig. 9.54), as the measured values can be seen to be smaller for $\Phi_{neq} < 1 \cdot 10^{13}$ neq/cm^2. The observed changes in the ratios in b) appear to be in good agreement up to $\Phi_{neq} = 1 \cdot 10^{13}$ neq/cm^2, where the experimental data exceeds the simulated results. See Table 9.21 for details.

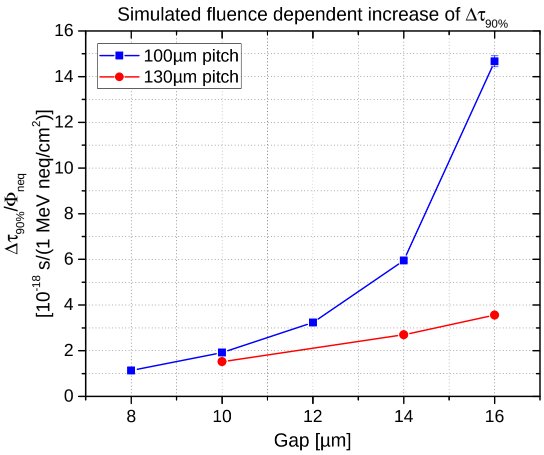

pitch [µm]	gap [µm]	$\Delta\tau_{90\%}/\Phi_{neq}$ [10^{-18}s/(1MeV neq/cm^2)]
100	8	1.13 ± 0.02
	10	1.92 ± 0.03
	12	3.22 ± 0.05
	14	5.95 ± 0.09
	16	14.7 ± 0.24
130	10	1.52 ± 0.02
	14	2.70 ± 0.04
	16	3.56 ± 0.05

Figure 9.54: Increase of $\tau_{90\%}$ due to radiation damage for different pitch/gap combination. The values extracted from linear fitting of the simulated data shown in Fig. 9.53a) can be utilized as a worst case estimate regarding the expected increase of $\tau_{90\%}$ depending on Φ_{neq} up to a fluence of $\Phi_{neq} = 1 \cdot 10^{13}$ neq/cm^2. The non-linear behavior is visible as cases with larger relative gap sizes (thus being closer to pinch-off) exhibit significantly higher increases of $\tau_{90\%}$. The detailed data derived from the linear fitting is listed in the table on the right hand side.

the bulk can be observed, as the non-linearity with increasing relative gap size becomes apparent. A detailed listing of derived values is given in the table on the right hand side of Fig. 9.54. The generally small errors obtained from the linear fitting procedure confirm the linear increase of $\Delta\tau_{90\%}$ up to type inversion. A maximum difference in $\Delta\tau_{90\%}/\Phi_{neq}$ of roughly a factor of 13 and 2 for a pitch size of 100 µm and 130 µm, respectively can be observed. By utilizing the data in this table, an upper limit for the increase of $\tau_{90\%}$ can be estimated for any arbitrary fluence up to $\Phi_{neq} = 1 \cdot 10^{13}$ neq/cm^2. Having a rough understanding of the degree of non-linearity of other geometrical variations also allows for a similar estimate in terms of arbitrary pitch/gap combinations comparable to the ones included in the table.

In summary, the extracted data offers a means to a quick estimation in lieu of sophisticated and time consuming simulation studies as the final experimental result can be expected to be less severe. It should, however, be noted that this estimation is only applicable for similar bulk material, as the depletion characteristics and therefore quenching and recovery are directly connected for SiMPl devices.

Summary

Investigation of the impact of non-ionizing radiation damage on the parameters examinable via the static test devices has yielded various results. The maximum overbias voltage in order to allow proper quenching $V_{ob,max}$ increased with increasing fluence Φ_{neq}, due to the decrease of N_{eff} and the consequent increase of the depletion zone of the gap region. In a similar fashion, an increase of the recovery times $\tau_{90\%}$ and $\tau_{1/e}$ was observed which coincides with the experienced quenching behavior. This, however, only holds true for fluences below the point of type inversion, as the circumstances in the bulk will change drastically, not allowing proper determination of the data any longer.

Even though the data of both parameters in itself is consistent, the comparison to the simulations shows significant discrepancies in the rate of the changes of $V_{ob,max}$ and τ. Simulations suggest increased changes at lower fluences, which is in direct conflict with the results of the previous sections. This can be considered as further prove, that the utilized model for radiation damage within the simulation framework requires further revision.

Overall, cases previously considered not feasible due to potential non-quenching will become the most promising geometrical variations after irradiation as the impact of radiation damage counteracts the non-quenching circumstance. In addition, a means of estimating an upper limit of the increase of $\tau_{90\%}$ for arbitrary fluences was presented and discussed.

9.4.2.2 SiMPl5

The main issue for SiMPl5 in terms of non-ionizing radiation damage is the change in effective doping concentration and subsequent change in the total backside resistance $R_{back} \approx R_{vert}$. Taking the results pertaining to this issue from Sec. 9.4.1.2 into account, an increase will occur, caused by the reduction of N_{eff}, but only very small changes in R_{vert} are to be expected.

This investigation made use of the static test devices, previously utilized in Sec. 9.3.2.2 and the measurement procedure is equivalent to the previous one. All devices were irradiated with their respective doses listed in Sec. 8.4 and underwent the established (80min, 60°C) annealing scenario, while being stored at a temperature of approximately 258 K between measurements. The voltage range was, again, chosen to mimic nominal operation at an overbias voltage of 5 V in order to establish the same depletion conditions in the detector bulk. In addition, simulations with Synopsys, including the introduction of defect states, mirroring the impact of radiation induced damages, were performed for comparison. The model and approach utilized was identical to the ones of the previous sections and adapted for the respective SiMPl5 layouts.

The measured I-V-curves were evaluated and the resulting value for R_{vert} extracted for every available gap size and neutron equivalent fluences Φ_{neq} and finally the change in resistance before and after irradiation ΔR_{vert} was calculated. A summary of all obtained results in shown in Table 9.22. The data is partitioned by gap size and fluence with the upper half containing the results of the hexagonal devices and the simulations for comparison, while the lower half lists the results for the quadratic structures of the chips.

According to simulations, the change in R_{vert} is always positive, which is supported by the theoretical expectations, and negligibly small for $\Phi_{neq} < 1 \cdot 10^{12}$ neq/cm^2. Afterwards ΔR_{vert} increases by one order of magnitude per fluence step and reached values ranging from thousands to tens of thousands of Ohm, depending on the gap size. The simulation also suggests increased ΔR_{vert} values for larger gap sizes, further exhibiting the effect of the JFET-like characteristics, even for very small device thicknesses. A deviation in ΔR_{vert} between gap sizes 8 µm and 30 µm of roughly a factor of 5 can be seen throughout all fluences.

This is in agreement with the simulation results of the SiMPl4 static test devices, but in stark contrast to the results extracted from the simulated data of Sec. 9.4.1.2 as the change in N_{eff} was predicted to be barely visible at all. A ΔR_{vert} of four orders of magnitude would entail N_{eff} decreasing by the same amount, which would have been visible in the previous results. It was already explained that only one method in the evaluation process for N_{eff} and V_{depl} yielded reasonable results while the other was not usable due to the limited thickness and consequent shape of the measured curves. While it is possible that the previous simulations would suggest similar changes in the bulk material but were not correctly identified because of the inadequate nature of the evalu-

Table 9.22: Summary of measured and simulated results for ΔR_{vert} for different gap sizes and geometries depending on the total equivalent neutron fluence Φ_{neq}. The values for the hexagonal devices (measured and simulated) are shown in the upper half, while the lower half lists the quadratic case (only measured data). The simulation suggests an increase in R_{vert} with increasing Φ_{neq}, which is also in concordance to the theory. Measured results, however, exhibit contradictory behavior with lower fluences even showing a decrease in R_{vert} with no systematic pattern visible in regards to gap size. A detailed discussion is presented in the text. No statistical errors are given since data of only one device per case was available. No systematic error could be observed during measurements and the measurement error of the instruments is in the range of roughly 0.001 Ω and was thus considered negligible.

		gap [µm]					
ΔR_{vert}(hex) [Ω]		8	10	12	14	16	30
sim	$1 \cdot 10^{10}$	0.016	0.018	0.020	0.023	0.026	0.081
	$5 \cdot 10^{10}$	0.081	0.091	0.102	0.114	0.129	0.403
	$1 \cdot 10^{11}$	0.161	0.182	0.203	0.228	0.258	0.806
	$5 \cdot 10^{11}$	0.808	0.911	1.022	1.146	1.295	4.045
	$1 \cdot 10^{12}$	1.625	1.833	2.054	2.305	2.605	8.134
	$1 \cdot 10^{13}$	18.01	20.31	22.77	25.55	28.88	90.34
	$5 \cdot 10^{13}$	180.9	204.2	229.1	257.4	290.9	916.3
Φ_{neq} [neq/cm^2]	$1 \cdot 10^{14}$	3609	4088	4583	5140	5791	17535
meas	$1 \cdot 10^{10}$	-6.072	-13.21	-7.631	20.61	11.39	16.06
	$5 \cdot 10^{10}$	-13.91	-12.84	-5.550	-10.40	-4.280	-17.17
	$1 \cdot 10^{11}$	-4.242	-4.858	-77.15	-3.211	-0.534	6.031
	$5 \cdot 10^{11}$	10.95	11.01	11.33	17.91	14.82	9.053
	$1 \cdot 10^{12}$	12.66	5.665	6.491	-1.955	10.26	26.32
	$1 \cdot 10^{13}$	-15.91	-36.13	-7.480	13.50	22.07	27.99
	$5 \cdot 10^{13}$	41.01	50.31	51.73	58.58	60.88	113.2
	$1 \cdot 10^{14}$	33.39	37.73	35.79	46.63	67.98	122.3

		gap [µm]					
ΔR_{vert}(sq) [Ω]		8	10	12	14	16	20
Φ_{neq} [neq/cm^2]	$1 \cdot 10^{10}$	0.386	11.85	7.716	-14.27	-7.738	10.32
	$5 \cdot 10^{10}$	-10.47	-16.27	-23.94	-6.860	-10.12	-18.20
	$1 \cdot 10^{11}$	-5.262	6.069	-27.02	7.634	5.886	-28.54
	$5 \cdot 10^{11}$	15.34	7.463	9.545	16.68	15.72	12.42
	$1 \cdot 10^{12}$	-0.655	-2.737	2.985	7.462	-5.153	8.257
	$1 \cdot 10^{13}$	-49.34	-15.47	-18.79	-22.42	1.235	21.28
	$5 \cdot 10^{13}$	56.34	39.12	53.27	61.34	51.87	82.57
	$1 \cdot 10^{14}$	34.71	55.11	56.27	63.44	70.95	80.84

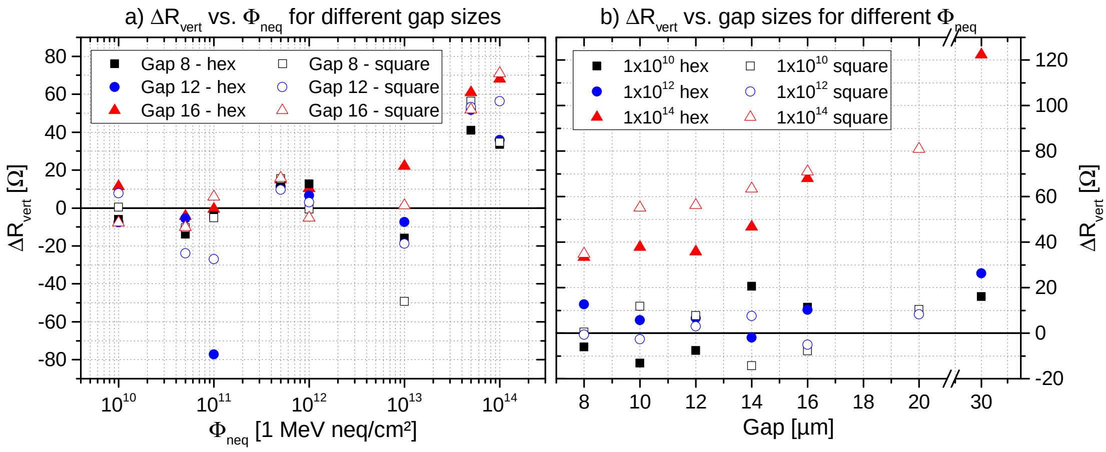

Figure 9.55: Illustration of the change in R_{vert} due to non-ionizing radiation damage. ΔR_{vert} depending on the equivalent neutron fluence Φ_{neq} for different gap sizes and geometries is given in a), while b) presents ΔR_{vert} depending on gap sizes for different geometries and Φ_{neq}. The hexagonal data is given by filled out symbols and the respective quadratic data is represented by identical hollow symbols. A behavior contrary to theoretical expectations can be observed for $\Phi_{neq} < 5 \cdot 10^{13}$ neq/cm^2, exhibiting a decrease in R_{vert} (negative ΔR_{vert}). Besides an increase in ΔR_{vert} with increasing gap size, no clear interpretations can be made from the observations, as explained in the text.

ation method, a more likely cause for this discrepancy is the utilized model for radiation damage in the Synopsys framework. This would also explain the differences between the simulated and measured values, similar to the case of the SiMPl4 static test devices, as was explained in the previous section.

Inspecting the measured data, several observations can be made. The most noticeable one are the randomly scattered negative values obtained for $\Phi_{neq} < 5 \cdot 10^{13}$ neq/cm^2 for both hexagonal and quadratic layouts. This and other observations, discussed in the following, are also depicted in Fig. 9.55 which illustrates ΔR_{vert} for all available fluences for different gap sizes and geometries in a) and ΔR_{vert} for all available gap sizes for different Φ_{neq} in b). In the case of the negative values, no distinct behavior or pattern can be detected, as the range of ΔR_{vert} seems to be random for all gap sizes. Looking at the cases of $\Phi_{neq} > 5 \cdot 10^{13}$ neq/cm^2 no negative values are visible and the previously established trend of increased values of ΔR_{vert} for increasing gap sizes can be observed, albeit with few exceptions. This is in contrast to the theoretically expected behavior as R_{vert} should increase due to the reduction of N_{eff}, therefor only leading to positive values of ΔR_{vert}.

It is unknown, what caused the negative values of ΔR_{vert}. A speculation in regards to contributions from surface currents originating from surface damages like scratches can be made, however no such anomaly was observed. In addition, the measurements from the previous sections should then have been affected in an equal fashion, which was not the case.

Taking only the higher fluences into account, the measured data suggests only small changes in R_{vert} after irradiation, which would amount to 15.8% – 27.8% of the initial values, depending on the gap size and geometry. This is consistent with the measured and simulated diode data in Sec. 9.4.1.2, which both suggest only minimal changes in N_{eff} and thereby the resistivity ρ of the material. In conclusion, a statement in regards to the maximum measured ΔR_{vert} which pertains to the imposed limitations set by the readout electronics, can be made. As already established, a value of $R_{back} < 1$ kΩ is desirable, in order to assure optimal operations of the readout electronics. Considering the largest absolute changes caused by the highest fluences experienced in the measured data, the largest observed resulting backside resistances for the relevant gap sizes for hexagonal and quadratic device are $R_{vert}(\text{hex}) = 427\ \Omega$ and $R_{vert}(\text{sq}) = 562\ \Omega$, respectively. Both of these are far below the tolerance limit, meaning that regarding this aspect, the SiMPl5 devices are safe for use in experimental environments like ILC or CLIC, since the maximum experienced fluence far exceeds the planned initial operation duration of both.

9.4.3 Impact on dynamic measurements with SiMPl4 devices

Ten SiMPl4 chips were chosen for irradiations with neutrons in order to analyze the impact of non-ionizing radiation damage on the device operations of SiMPl arrays. The expected impact was elaborated upon in Sec. 6.5 but only a few aspects can be investigated. Identical to the diodes and static test devices, the SiMPl4 chips were stored at a temperature of 258 K between measurements and underwent the (80min,60°C) annealing scenario.

By performing I-V measurements on 10x10 arrays in a dark box with a probe station at $T \approx 298$ K, the results of Fig. 9.56a) can be obtained. Here every colored line represent a different chip with each one having experienced a different neutron fluence ranging from $\Phi_{neq} = 5 \cdot 10^9$ neq/cm^2 to $\Phi_{neq} = 5 \cdot 10^{14}$ neq/cm^2. The increase of I_{leak} before breakdown with increasing Φ_{neq} can be observed and will be discussed below. For fluences $\Phi_{neq} < 5 \cdot 10^{13}$ neq/cm^2 all measured devices exhibit the same breakdown voltage as before irradiation of roughly 35.3 V, however beyond this fluence V_{bd} appears to increase up to $V_{bd} \approx 65$ V for the highest fluence, almost doubling the initial value.

Taking into account the results of Sec. 9.4.1.2, it is important to realize that the

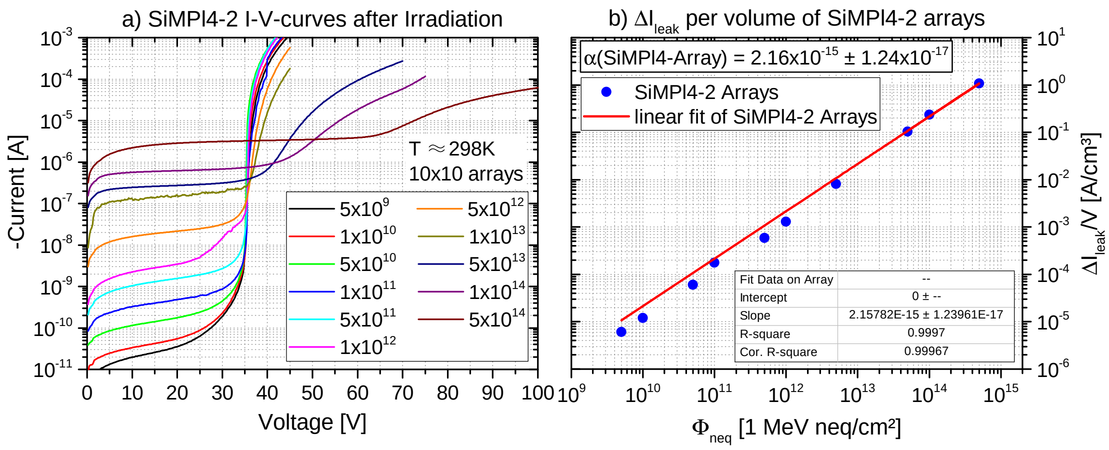

Figure 9.56: a) Breakdown voltage for different neutron fluences of SiMPl4 device and b) the leakage current increase if SiMPl4 devices before breakdown. All measurements were performed at room temperature (≈ 298 K) on 10x10 arrays of hexagonal SiMPl4-2 chips. A shift of V_{bd} for higher fluences can be seen in a), as well as the overall increase of I_{leak} before breakdown proportional to Φ_{neq}. The leakage current increase per volume with Φ_{neq} is depicted in b). While a linear increase is visible, the slope does not coincide with the previously measured ones (see Sec. 9.4.1.2). Further discussion is given in the text.

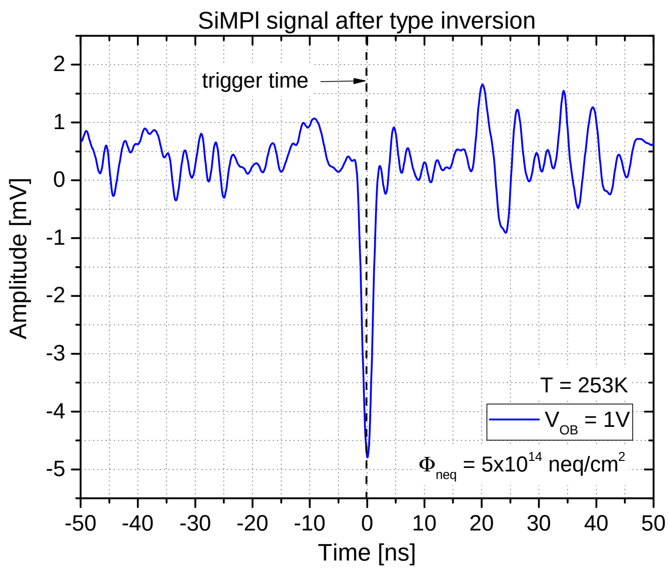

Figure 9.57: Signal of a SiMPl4-2 10x10 array after type inversion ($\Phi_{neq} = 5 \cdot 10^{14}$ neq/cm^2). The signal shape was measured at $T = 253$ K and $V_{ob} \approx 1$ V. While a clear signal peak of a dark count is visible, no apparent recovery can be seen. It is also difficult to interpret the smaller peaks, as they appear to be noise. Increasing the voltage by up to 10 V yields similar results with only small increases in DCR.

shift in V_{bd} starts taking place for fluences at which the material was observed to have undergone type inversion. Therefore, as previously explained, it is possible that a second p-n junction formed between the now p-type bulk and the backside or deep n implant. The subsequent depletion of said volume would lead to a voltage drop over the bulk and to a smaller effective voltage applied to the high-field region of the device. The increased shift of V_{bd} with higher fluences can then be explained with the increase of the potential barrier for the charge carriers establishing the potential in the deep n region, since a higher fluence after type inversion introduces more acceptor state defects in the bulk. Even if no complete depletion in the bulk region is achieved, the increased amount of acceptor defects can have a similar impact. A non-depleted volume would feature the acceptors in their neutral states, thus increasing the overall bulk resistance and thereby resulting in a higher R_Q.

Under these assumptions the decrease in the current after breakdown can also be explained, as only a fraction of the applied voltage will effectively reach the high-field region. This would result in the device being operated at a lower oberbias voltage than intended, thus exhibiting smaller currents. The argument could be made that a series of two p-n junctions was measured and that no breakdown takes place after type inversion, however, Fig. 9.57 shows proof of a Geiger breakdown taking place. The measured pulse shape of a 10x10 array irradiated with $\Phi_{neq} = 5 \cdot 10^{14}$ neq/cm^2 is depicted and a clear peak with a 4.75 mV amplitude attributed to an avalanche process can be seen. Increasing the bias voltage by up to 10 V only slightly affects the observed pulse shape further corroborating the above assumption.

The absence of the longer recovery tail, seen in nominal SiMPl operations could be attributed to the increase of R_Q. The fast signal component visible originates from the generated holes exiting the HF region via the topside while the electrons are effectively being stored due to the low possible current flow. This would, in addition, lead to the cells never properly recovering and the majority of the signals being considered afterpulses, thereby also explaining the low current levels seen after breakdown, as the cells are not firing at their maximum capacity.

Another possibility would be a potential reduction of the mean free path of the charge carriers within the HF region due to the increased amount of trapping states present. Hence, charges would not be able to acquire the same amount of kinetic energy as before, reducing the effective Geiger efficiency. This assumption, however, contradicts the observation of summary studies like [87], where no impact in V_{bd} was found due to non-ionizing radiation damage up to similar fluences. Even thought the working principle in terms of quenching differs between SiMPl and conventional SiPMs, this effect of reducing the mean free path should be equally visible in all devices as it affects the HF region directly. Furthermore, [88] and [89, 90] have shown a shift in V_{bd} from fluences of $\Phi_{neq} = 6 \cdot 10^{12}$ neq/cm^2 and higher with the severity being dependent on the width of the HF region. In [88] the observed shift appeared linear with Φ_{neq} with a maximum of roughly 4 V and in [89] it was only 300 mV after $\Phi_{neq} = 5 \cdot 10^{14}$ neq/cm^2, while the devices in [89] featured a similar HF region width as SiMPl. Operating under the assumption of this shift being width-dependent, a conflict in the results of SiMPl with the data of [89] can be found, as both featured a similar HF width.

Therefore, it is more likely that the observations are caused by a combined impact of a voltage drop within the bulk and the overall increase of R_Q of the non-depleted regions due to the increased acceptor levels. This issue, however, still requires further investigation in future studies.

It was already briefly touched upon that the measured current before breakdown increases with the experienced fluence. Similar to the investigation with the diodes, the current increase per volume was derived for each available fluence, resulting in the data shown in Fig. 9.56b). While the obtained data points can be approximated with a linear fit, the slope can be seen to be roughly a factor 54 larger than the expected current related damage rate $\alpha_R \approx 4 \cdot 10^{-17}$A/cm, implying a higher increase in leakage current than usual. Attributing this discrepancy to surface contributions seems feasible but is ultimately highly unlikely as nothing similar was observed within the diode investigations and those featured the same surface implants and would thus be expected to exhibit the same issue. The exact reason for this behavior is still unknown and requires further in-depth studies.

Currently, the most likely explanation is that due to the SiMPl4 devices already exhibiting issues regarding higher currents and point-like defects, it possible that an uncommonly high concentration of defects is located within the high-field region. It is thereby also plausible for a certain concentration of defects, in addition to those causing said issues, to be present but to not contribute to the thermal current due to their position within the band gap. These defects might act as primary defects allowing for easier formation of secondary defects during neutron irradiation by decreasing the probability of an interstitial-vacancy pair to recombine again. Hence, the rate at which new defects get introduced into the HF region would be higher compared to the rest of the bulk. The current measured there would also be dominant compared to the rest of the device, as the concentration of defects would be higher. This in turn would also explain, why no increase of the slope after type inversion can be observed, even though the formation of a second depletion layer would also lead to a significant increase of the total leakage current. But since not enough data is currently available for more detailed studies, this remains a speculation and further studies will be required in the future.

An investigation of the impact of radiation damage on other parameters like the afterpulsing probability or the optical cross-talk were not carried out as they were deemed unfeasible with the current batch.

9.4.4 Investigation of potential ionizing radiation damage

In MOS-based devices, ionizing radiation damage can lead to effects like a threshold voltage shift of the gate. In the case of DSiMPl (SiMPl5) devices, however, the impact would manifest in a different fashion, as will be explained in the following.

Utilizing Synopsys TCAD, simulations including an increase of the fixed oxide charge in the SiO_2-Si interface caused by ionizing radiation (as explained in Sec. 4.2) can be performed and analyzed. One of the major differences compared to SiMPl4 devices is the structured p^+ topside implant necessary for single pixel readout. Combined with a increase in positive oxide charges at the interface, this can lead to new issues for this approach, as shown in Fig. 9.58.

Figure 9.58 a) and c) illustrate the gap area of the p^+ implant for a situation of no interface charges present, where the electron concentration is given in a) and the resulting electrical field under operational biasing conditions in c). A high-field region can only be detected in the designated area between p^+ and the deep n implant, as intended. The circumstances change, however, by introducing a total fixed charge concentration into the SiO_2-Si interface. The case for a concentration of $1 \cdot 10^{12}$ cm^{-2} is depicted in b) and d). Due to the positive charges in the interface, an accumulation of electrons in the gap area is visible, which in turn will result in an increased electrical field during operations, leading to a very high risk of lateral breakdowns between the boron implant and the detector bulk near the surface.

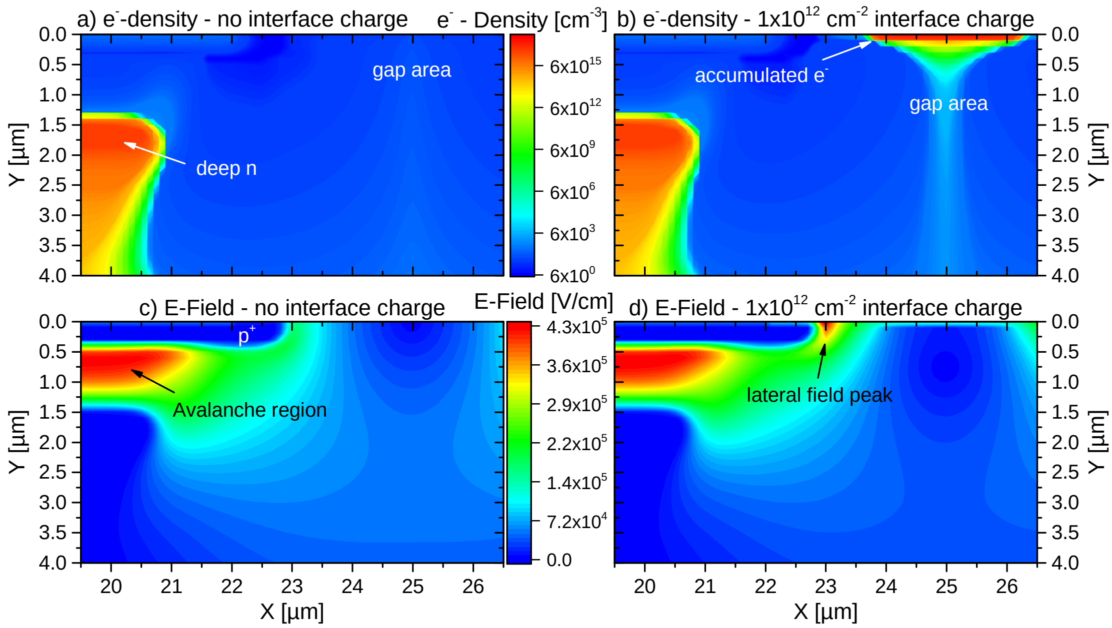

Figure 9.58: Example of the influence of ionizing radiation damage on SiMPl5 devices during operation. The same zoom-in of the simulated gap area around the edge of the p^+ topside implant is shown in all four pictures, with a) and b) depicting the electron concentration and c) and d) the resulting electrical field under nominal bias operations. Fixed interface charges in the SiO_2-Si interface will be created by ionizing radiation. The left hand side shows the case of no fixed interface charges present due to radiation damage (a) and c)) while the right hand side shows the respective case for an interface charge concentration of $1 \cdot 10^{12}$ cm^{-2}. Due to the accumulation of negative charges in b) and d), a sufficiently hight electrical field will be created to support avalanche breakdowns between the topside implant an the gap-bulk region.

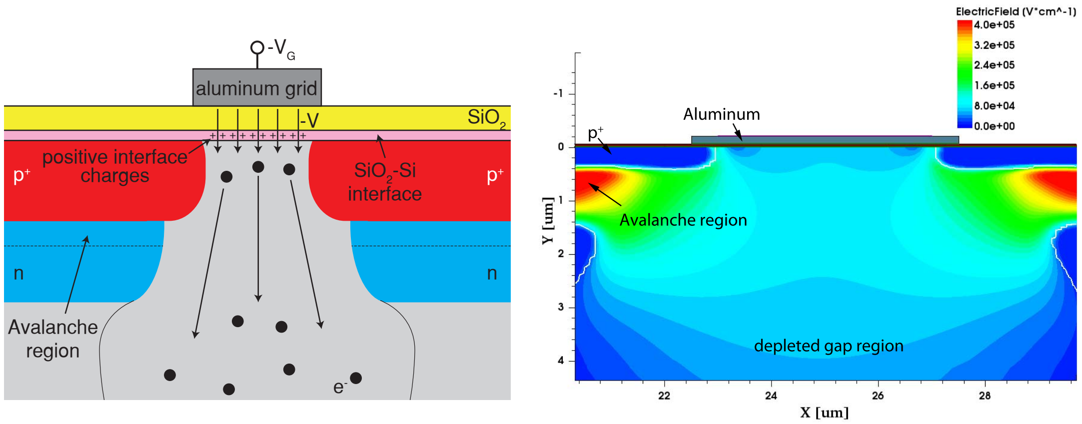

Figure 9.59: Illustration of the working principle of the aluminum grid in the gap region of SiMPl5 device for suppression of the impact of fixed interface charges. The left shows an illustration of the general working principle (not to scale), where the negative charges will be pushed into the bulk region due to the negative potential $-V_G$ applied to the aluminum grid, thus counteracting the electron accumulation. Hence, no lateral electrical field can be established during operation. The right hand side shows the confirmation of this approach via TCAD simulations with a total interface charge concentration of $1 \cdot 10^{12}$ cm^{-2}. The absolute electrical field in the gap region in question is depicted while the potential of 0 V is applied to the aluminum contact (see text) and compared to Fig. 9.58 no lateral field can be seen.

In order to counteract this issue, an aluminum layer deposited on top of the SiO_2 in the gap areas was incorporated in the design of some of the SiMPl5 devices. The gap region would then resemble a gate structure, similar to that of a MOSFET. By applying a sufficiently large negative voltage on the aluminum grid, the accumulated negative charges in the gap region would then be dispersed back into the bulk, thus lowering the lateral electrical fields and the respective risk of an avalanche breakdown. This procedure is depicted in Fig. 9.59, where the left hand side shows the schematic illustration of the working principle and the right hand side the working proof by simulation via Synopsys TCAD. The simulated plot shows the resulting total electrical field in operation mode of a SiMPl device with a fixed charge concentration of $1 \cdot 10^{12}$ cm^{-2}, and as suggested, no lateral field peaks are visible due to the charge carriers being pushed into the bulk.

One benefit of this design lies in the expected low voltage requirements of the aluminum grid. A negative operational voltage at the aluminum grid compared to the bulk will be required, however, due to the bulk being mainly dominated by the positive back-side bias potential, a grid voltage of 0 V already proofs sufficient to achieve the desired effect, according to the simulations. Therefore, simply connecting the aluminum grid to ground should suffice to prevent the impact of ionizing radiation damage in the final designs.

According to TCAD simulation data, the soft threshold in terms of fixed charge concentration in the interface appears to be roughly $5 \cdot 10^{11}$ cm^{-2}. At this concentration, potential lateral avalanche breakdowns will be enabled, assuming no countermeasures like the aluminum grid are in place.

In a next step, the ionizing radiation dose required for the extracted fixed charge concentration needs to be estimated. Various studies like [63] have shown, that the resulting impact on the interface charges depends on many factors concerning the irradiated material and the biasing circumstance during the irradiation process itself. The former includes the thickness and composition of the insulating layers on top of the devices and certain particularities regarding their processing procedure. Hence, in order to properly estimate this subject in simulations, previous studies with equal or similar material are required.

Fortunately, studies of material unrelated to this investigation but similar in composition and processing were provided for reference purposes [117] which allowed rough estimations and follow-up preliminary simulations. Judging from this data, the total ionizing radiation dose required to achieve a total fixed charge concentration of $5 \cdot 10^{11}$ cm^{-2} is approximately 10 kGy − 15 kGy.

Considering the total expected yearly doses for experimental environments like ILC and CLIC, given in Sec. 8.4, the aforementioned critical dose would be reached after 10 years of ILC and 50 years of CLIC operation, respectively. In regards to CLIC, this would mean a safe operation throughout the entirety of its lifetime, while in the case if ILC no issue should arise, considering the usual operating cycles for high energy experiments.

Nevertheless, these conclusion are, at this point in time, mainly derived from estimates and simulations as mentioned above. In order to ascertain the validity of these claims, thorough investigations will be required. Detailed irradiation tests with actual devices have to be performed and in addition sophisticated tests structures allowing the estimation of the fixed charge concentration in the interface also need to be characterized to allow cross-checks with the simulated data.

9.5 Electron detection efficiency measurements

The common application of SiPMs was, up to this point, usually related to the detection of light, either directly originating from a to-be-detected source or as a byproduct of the particles traversing a e.g. scintillator. As described in Sec. 6.4, the aim of DSiMPl is a direct measurement of charged particles with an overarching goal of applying SiMPl devices for particle tracking in high energy physics.

The first steps towards this goal are going to be presented in the following sections. Initial simulations of the potential for the detection of minimum ionizing particles (MIPs) with SiMPl devices were carried out, followed by experimental validations of said simulations with actual SiMPl devices. Afterwards, an outlook for future improvements and iterations of the setups and measurement methods will be discussed.

9.5.1 Theoretical approach & Monte Carlo simulations of the Geiger efficiency

In order to investigate the feasibility of SiMPl devices being utilized as tracking detectors, several issues need to be considered in comparison to the conventional light detection applications. While many technological aspects were already taken care of through the redesign and incorporation of active quenching and readout electronics (see Sec. 6.4), detector inherent matters require additional investigation.

A major advantage of using avalanche devices for the tracking of charged particles in high energy physics mentioned in Sec. 6.4, was the expected inherently high trigger or Geiger efficiency. Conventional SiPMs and SiMPl are commonly utilized for low level light and even single photon detection, hence a single electron-hole-pair (e-h-pair) is capable of initiating an avalanche breakdown leading to a measurable signal (after external amplification). When considering the detection of MIPs, however, the number of created e-h-pairs can be expected to be higher due to the energy loss described by the

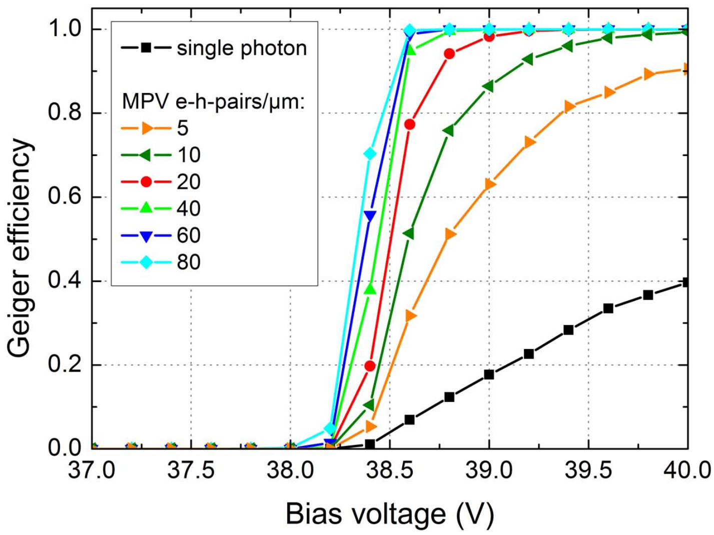

Figure 9.60: Monte Carlo simulation of the Geiger efficiency for MIPs and single photons. The simulations assume normal particle and photon incidence for a doping profile of the HF region of SiMPl2. The black line corresponds to the single photon case while the different colored lines each represent a different most probable value (MPV) for electron-hole-pair generation up to the commonly used rule-of-thumb of 80 pairs/µm. All MIP cases indicate a much steeper increase of the Geiger efficiency compared to the single photon case, leading to a smaller required V_{ob} for reaching approximately 100% efficiency. Simulation data and plot courtesy of Christian Jendrysik [33, 111].

Bethe-Bloch equation (see Eq. (3.34)). Thus, applying the common rule-of-thumb of 80 generated e-h-pairs per micrometer and taking the average thickness of the SiMPl HF regions of roughly 1.0 µm to 1.5 µm into account, it can be expected that roughly 80 e-h-pairs will be created within the HF-region by a MIP. As a consequence, the Geiger efficiency is expected to be significantly higher at the same operational voltage compared to the single photon case, as a larger number of charge carriers will now be able to initiate the avalanche process. This, in turn, would allow operation of SiMPl devices at very low overbias voltages, thus drastically reducing the impact of negative effects like optical cross-talk, afterpulsing and in general the overall dark count rate, without the need to sacrifice the trigger efficiency.

In order to confirm this hypothesis and determine the lowest necessary operational overbias voltage, Monte Carlo simulations of the Geiger efficiency, similar to the ones presented in Sec. 7.3 were performed as a first step. The HF region was based on the extracted data from SiMPl2 simulations. However, instead of varying the initial location of the charge carriers, the number of initial charge carriers was altered to reflect the energy loss of a MIP within the HF region. The results can be seen in Fig. 9.60, where the Geiger efficiency for various bias voltages is presented with the colored lines each representing a different most probable value (MPV) for created e-h-pairs ranging from 5 to the expected 80 and the black line corresponding to the single photon case for comparison.

It becomes apparent that even the lowest scenario of 5 e-h-pairs already results in significantly higher efficiencies compared to the traditional case. In addition for MPVs > 20, the Geiger efficiency can be found to reach 100% at $V_{ob} < 0.5$ V. Hence, even if the number of created charge carriers is lower than expected, the device would exhibit an inherently high Geiger efficiency, due to the nature of the avalanche process.

The impact of this result on the electron detection efficiency of charged particles can be derived by taking the formula for the PDE, given in Eq. (5.11) into account. The quantum efficiency QE is now assumed to be 100% as the particles will always create a track of e-h-pairs traversing through the material, reducing the term of the electron detection efficiency (EDE) to

$$EDE(V_{ob}) = FF \cdot \epsilon_G(V_{ob}) \; . \tag{9.7}$$

With the above results, assuming operation within the plateau region, the Geiger efficiency $\epsilon_G(V_{ob})$ becomes 1, leading to $EDE \approx FF$ and therefore the electron detection efficiency only being limited by the fill factor FF.

9.5.2 First experimental results with SiMPl devices

Following the confirmation of the theoretical predictions via Monte Carlo simulations, an experimental validation with older SiMPl devices (SiMPl2) was carried out. For this purpose, a novel experimental setup was developed during the course of this study. For a sophisticated proof-of-concept approach it was decided to utilize electrons for this iteration, with future improved iterations making use of MIPs in a test beam environment.

An electron beam was obtained through the use of a radioactive source, namely Strontium 90 (^{90}Sr). Its primary radiation is a β-decay to Yttrium 90 (^{90}Y) ($E_{\beta,max}$ = 546 keV) which, in turn, undergoes an additional β-decay ($E_{\beta,max}$ = 2.3 MeV), thus providing a broad electron energy spectrum with two main peaks. It is important to note that electrons cannot be treated identical to MIPs, as their low mass leads to the

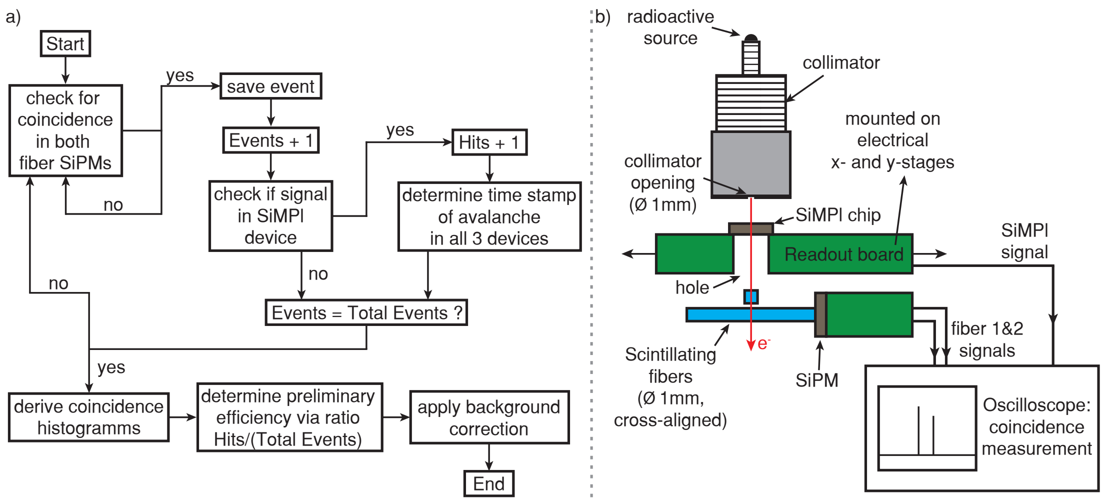

Figure 9.61: Flowchart of the experimental procedure (a) and schematic of the developed experimental setup (b) for determining the EDE. The radioactive electron source is placed in a plastic collimator aimed at the SiMPl chip mounted on a readout board and the two coincidence scintillating fibers, which, in turn, are connected to SiPMs. Manual aim regarding the position of the SiMPl chip is possible due to the readout board being mounted on two electrical stages. The two fibers are arranged in a cross-shape resulting in a total coincidence area of 1 mm^2. The alignment between source and fibers was achieved via a 3D-printed apparatus. The signals of both fiber-SiPMs and the SiMPl device are analyzed with a digital oscilloscope and processed offline. See text for more details.

requirement of additional correction terms in the Bethe-Bloch equation due to scattering with the atomic electrons (see Sec. 3.3). For the purpose of this measurement however, these electrons will be sufficient, as only a small fraction of the lower energy contingent will be lost due to multiple scattering. In the case of higher energy electrons, the charge creation by energy loss can be considered similar to MIPs in order to adhere to the simulated assumptions.

A flowchart of the experimental procedure, as well as a schematic of the developed experimental setup can be seen in Fig. 9.61a) and b), respectively. The ^{90}Sr source was placed in a plastic collimator with an exit diameter of 1 mm aiming downwards at the SiMPl chips, located at a distance of roughly 5 mm on the common readout board. The collimator itself was placed on a 3D-printed mount. In order to ease the requirements on the exact positioning, a 30x30 array (area $\approx 16,4$ mm^2) was utilized rather than a 10x10 array. Even though geometrical considerations of the beam size and opening angle suggest roughly identical sizes of the array area and impinging beam, minimal deviations in positioning already caused a sufficient enough misplacement to result in a severe charge loss. Therefore, an array with a larger active area was favored. The readout board was modified to feature a hole underneath the SiMPl chip, allowing passage of the electrons.

Directly underneath, the coincidence unit is located, consisting of a set of two square shaped scintillating fibers[1] with 1 mm^2 cross-section placed in a 3D-printed construct. They were align on top of each other, forming a cross shape, while also being coated with an opaque material in order to avoid cross-talk between them. Hence, the coincidence area can be expected to be 1 mm^2 in size. The alignment of the collimator exit and fiber cross-section was achieved via the sophisticated design of the aforementioned 3D-printed apparatus, since the source and its collimator were mounted on the same construct holding the fibers. This way, the collimator opening can be designed to be located directly above of the fiber cross-section. The fibers are connected to Hamamatsu MPPCs[2] featuring a peak PDE at the characteristic wavelength of the fibers, mounted on an additional sophisticated readout board.

Aiming the electron beam in relation to the SiMPl array was realized via a common LED laser[3], placed in a special mount allowing an interchange of source holder and laser holder. Finally, the adjustment of the relative position of the SiMPl array to the source/laser and fiber construct could be performed via two electrical stages in x and y-direction[4] which are carrying the latter. The entire setup was placed in a light-tight environmental chamber allowing measurements at a stable temperature. Previous studies with SiMPl2 devices have shown that a lower ambient temperature of 253 K is favorable due the high dark count rate, the electrical stages, however, do not allow temperatures below 273 K. Thus all measurements were performed at $T = 278$ K. The individual signals of the SiMPl array and the two MPPCs coupled to the scintillating fibers are being read out via a LeCroy WaveRunner 610Zi digital oscilloscope (1GHz bandwidth, 20GS/s).

Under normal circumstances, placing the source above the SiMPl array and scintillating fibers would result in the electrons traversing the array, as well as both fibers, thus initiating a signal in the SiMPl device and the MPPCs connected to the fibers. It is, however, also possible for the electron to be absorbed along the way or, in the case of lower energies, change its direction due to multiple scattering. To allow analysis of the

[1] Saint-Gobain scinillating fiber BCF-10, 432 nm emission peak
[2] MPPC S13360, `https://www.hamamatsu.com/resources/pdf/ssd/s13360_series_kapd1052e.pdf`
[3] Laser Components FP-D-635-1P-C-F-GL67 laser module
[4] Physik Instrumente (PI) M112.1 DG Compact Micro-Translation Stage

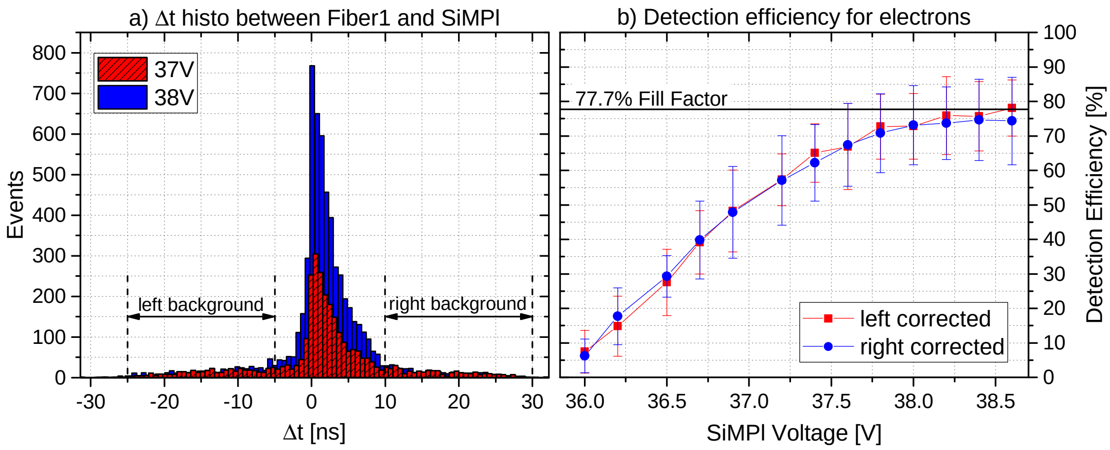

Figure 9.62: Examples of the measured time differences Δt between the signal of the SiMPl device and the first scintillator (a) and the resulting electron detection efficiency of a SiMPl2 device (b). The two histograms in a) correspond to two different bias voltages, exemplifying the difference in efficiency through the number of events. The utilized regions for the background corrections are also illustrated (see text). The resulting electron detection efficiency after the applied background correction for both cases (left and right regions) is given in b). Both cases lead to almost identical efficiency levels within the error margin and reach a plateau region close to the theoretically expected maximum of the fill factor of 77.7%. The plateau can be seen to be reached for $V_{ob} \approx 2$ V (see text).

electron detection efficiency of the SiMPl array, only events in which electrons are able to traverse all three components (array, and both fibers) are of interest. Hence, in order to assure such events, only those were recorded which featured signals in both fiber SiPMs within a small time window. The time window was chosen according to the likelihood of two dark counts occurring in both fiber SiPMs, causing a fake event, and thus depends on the dark count rate of the MPPCs. Thanks to the reduced temperature, the DCR was significantly lowered, allowing for a time window of 60 ns to provide a negligible amount of such fake events. Finally, the detection efficiency for electrons can then be obtained by determining and comparing the fraction of events featuring an avalanche signal in the SiMPl device and those with no signal.

For this purpose, a total of 6500 waveforms per device were recorded under the condition of two contemporary signals in the fibers. This was repeated for various bias voltages of the SiMPl array ranging from $V_{bd} \approx 36.0$ V to 38.6 V. Afterwards, the time difference Δt between each of the signals was analyzed and the number of events with and without a SiMPl signal counted. Δt was determined by deriving the first derivative of the waveform, allowing for a more reliable identification of a signal peak, similar to the method incorporated in the afterpulsing measurements (see Sec. 5.3.7).

Figure 9.62a) depicts two histograms of the Δt values obtained between the upper fiber ("fiber1") and the SiMPl array signal. A positive Δt translates to the fiber signal occurring after the SiMPl one, which is physically expected. The two different colored bar sets represent an applied bias voltage each. An overall higher number of coincident events can be found for the higher voltage depicted, inferring an increase of the detection efficiency with increasing bias voltage. In both cases, the peak coincidence time can be found at $\Delta t \approx 0$ ns with a distribution tail up to roughly $\Delta t \approx 10$ ns. In theory, the peak should be located at $\Delta t > 0$ ns, since the electrons do have a finite traversing time,

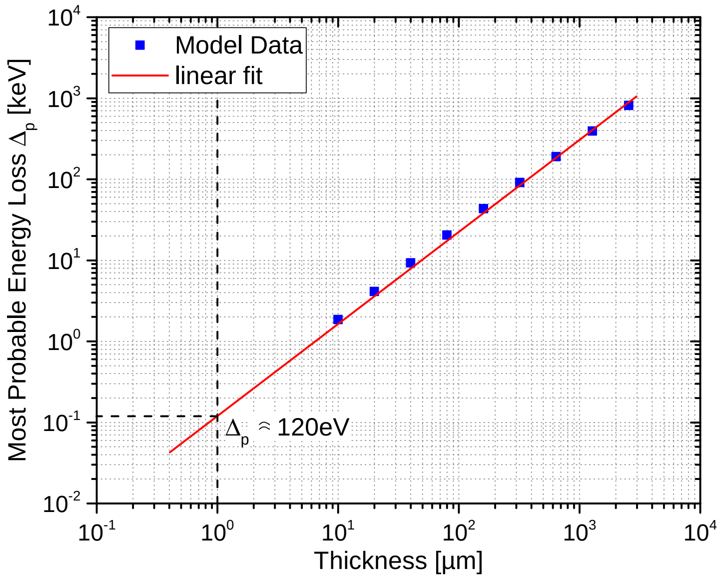

Figure 9.63: Most probable energy loss Δ_p for various thicknesses d. The data was taken from Bichsel [120] and extrapolated via a linear fit (red line). A clear decrease of the energy loss with thinner absorbers can be observed. At $d = 1$ µm a $\Delta_p \approx 120$ eV can be expected according to their model.

in addition to other aspects like the excitation time of the fibers and the general signal processing through the electronics. This discrepancy can be attributed to the signal shape of the SiMPl array, as the ambient temperature during the measurement was not sufficiently low to provide clean signals. As already explained in Sec. 6.3, SiMPl2 was affected by issues leading to a generally increased dark count rate, as well as afterpulsing and cross-talk probability. Therefore, a clear analysis of the waveforms at higher temperatures becomes increasingly difficult, even with the support of the derivative method. Nevertheless, the tail of the distribution being located at positive values of Δt implies an overall physical consistency.

The detection efficiency can then be derived by the ratio of the events with a SiMPl signal to the total recorded events featuring coincidence in both fibers. In order to attribute for coincidence events featuring a dark count within the SiMPl array, the background of the Δt histograms, located on both sides of the peak was utilized. In both cases the mean number over the same range of 32 bins was calculated.

The resulting electron detection efficiency for a 30x30 SiMPl array with a fill factor of 77.7% is shown in Fig. 9.62b). The two different colored data sets represent the background correction with the left and right component of the Δt distribution, respectively. A clear increase up to an efficiency close to the fill factor in both cases can be observed, leading into a plateau region for increasing voltages. This is in very good agreement with the theoretical predictions of the previous section, as it supports the assumption of the Geiger efficiency attaining close to 100% and the overall detection efficiency becoming equal to the fill factor. The steepness of the increase is lower than predicted, as the plateau can be considered reached at $V_{ob} \approx 2$ V in contrast to the predicted $V_{ob,theo} \approx 0.5$ V.

The reason for this discrepancy can be the following. A study by Bichsel [120] found that the most probable energy loss Δ_p of ionizing particles becomes smaller for thinner absorbers due to straggling, thus introducing deviations from the commonly applied Landau model. The data obtained by Bichsel and their model (straggling function) is depicted in Fig. 9.63. Extrapolation of the data via a linear fit leads to an expected $\Delta_p(1\ \mu\text{m}) \approx 120$ eV which translates to roughly 33 generated electron-hole-pairs. While this yield of charge carriers is less than half of the predicted 80 and will lead to decreased efficiencies, Fig. 9.60 still suggests smaller required overbias voltages in this case than the one obtain from measured data. It is, however, unclear if a linear extrapolation of the data can be performed, since the lowest thickness investigated in the study was $d = 10$ µm. Hence, it is unknown if the model is applicable for a thickness one order of magnitude smaller. Deviations and potentially decreased energy losses could thereby be possible.

The results can nevertheless be considered a successful confirmation of the proof-of-concept, as reaching 100% Geiger efficiency at only $V_{ob} \approx 2$ V is unachievable for common light detection applications and thus proves the feasibility of a low overbias operation of SiMPl devices for applications of particle detection.

It should be noted that no SiMPl device of the more recent iterations was utilized in this measurement due to the issues affecting the overall quality of said devices (as discussed in the previous sections). Hence, deploying a SiMPl2 device proved more feasible for this endeavour. As a consequence, the number of functional devices, especially of 30x30 array size was very limited, thus not providing enough chips for a more thorough investigation with varying fill factors.

9.5.3 Outlook

The successful validation of the simulated predictions with the experimental data serves as a first proof-of-concept for particle detection with SiMPl devices. There is, however, ample room for improvement in terms of the measurement procedure and experimental setup utilized, as well as the simulation framework.

The latter exhibited very good agreement to measurements in terms of the breakdown voltage, it is however possible that the avalanche generation procedure requires additional corrections to properly reflect reality. In addition, the model proposed by Bichsel [120] could be incorporated into the simulation framework in order to correct the number of assumed initial charge carriers. The model itself also requires further investigation to assess its validity for thicknesses relevant to the SiMPl case.

In regards to the experimental setup, a momentum selection tool for charged particles was constructed[5], allowing filtering of specific electron energies of a β-source (see Fig. 9.64). Incorporating an electromagnetic coil allows for adjustment of the momentum of the electron exiting the apparatus through a collimator by varying the coil current. In addition, sufficient amounts of tungsten as shielding material have been utilized to avoid bremsstrahlung from the electrons, cropping up if high Z material is used for shielding. Beam size reduction is finally achieved by interchangeable collimator attachments at the exit with 150 µm and 500 µm diameter. If no collimator extension is used, the opening itself offers collimation to a 1 mm diameter.

First measurements investigating the functionality of the device have already been carried out. The aim was to determine the spectrum of a ^{90}Sr source by attaching a plastic scintillator coupled to a Hamamatsu MPPC directly to the exit of the apparatus and measuring the resulting count rate. The data can be seen in the right hand side of Fig. 9.64 with three different collimator sizes utilized. Alternating the coil current allows electrons of different energies to exit the device, thus changing the measured rate. The lower energy peak ($E_{\beta,max} = 546$ keV) can be seen clearly while higher energy one ($E_{\beta,max} = 2.3$ MeV) can only be seen as a more pronounced tail of the distribution.

[5] Blueprints provided by CERN

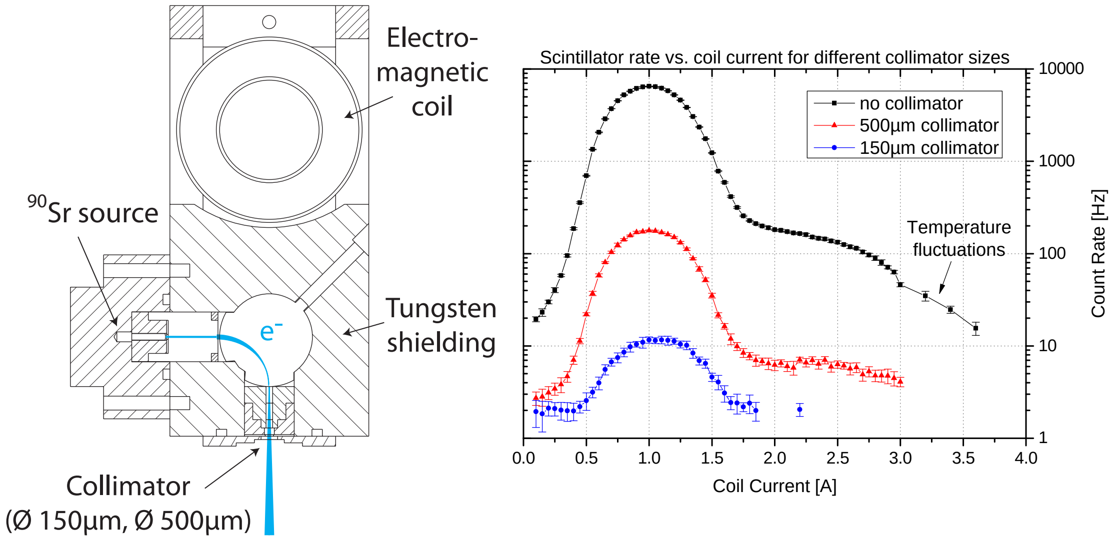

Figure 9.64: Momentum selection tool for electron sources and example of measured ^{90}Sr spectra with different collimator diameters. The left schematic illustrates a top view of the apparatus featuring an electromagnetic coil creating a magnetic field pointing into the drawing plane. As a result, the electrons of the radioactive source are deviated depending on their momentum and can exit the device at the exchangeable collimator opening. The right hand plot shows a measurement of the ^{90}Sr spectrum by varying the coil current and determining the respective count rate with a plastic scintillator coupled to a SiPM for different collimator diameters. A clear decrease of the measured count rate for smaller diameters can be witnessed (see text).

The slight fluctuations at higher coil currents stem from temperature variations due to the increasing heat generation for high currents and the subsequent attempts at cooling down the setup. Since the readout devices are directly connected to the apparatus, significant changes in temperature were also affecting the MPPCs. Nevertheless, the device would allow for a more clean particle source by focusing on the first spectrum peak, however, the inherent problem can already be seen in the count rate measured above. Including proper beam collimation leads to a drastic decrease of the electron rate exiting the device, such that first measurements performed with SiMPl devices placed in a realistic distance yielded no feasible particle rate for any of the above investigations. Hence, a stronger ^{90}Sr source of different radioactive source altogether would be required to allow incorporation into the overall experimental setup.

Finally, the above measurements and more sophisticated studies need to be carried out with newer SiMPl devices, especially SiMPl5 chips and DSiMPl hybrid prototypes as those are the intended devices for such applications. At this point in time, no hybrid devices were ready for such sophisticated measurements and could therefore not be utilized. However, it is possible that due to the issues affecting the most recent SiMPl batches, this will become the subject of a future study after the problems have been identified and taken care of.

9.6 Investigation of early point-like breakdowns

The measurements of SiMPl4 and SiMPl5 devices have shown trends of early point-like breakdowns as well as an unnaturally high dark count rate, making dynamic characterizations impossible. Therefore, the attention of this study shifted towards investigation of said defects in order to allow quantification of the observed effects and to avoid similar issues in future batches of SiMPl. The following section will deal with this investigation, starting with first measurement procedures to identify the issue at hand. Afterwards, one potential explanation for the observed behavior will be illustrated and possible means of its validation will be discussed.

9.6.1 First investigatory measurements

Following the observations from the SiMPl4-1 measurements, the first assumption regarding the reason for the point-like defects was the presence of photoresist residue on the wafer during the implantation of the high-field implants. If present, the resulting doping profile would be shifted towards the surface, resulting in smaller high-field region and thereby larger electric fields at similar bias voltages.

Hence scanning electron microscope (SEM) photographs of the wafer surfaces were taken after every individual step involving the deposition and stripping of photoresist layers during production. An example of such photographs is shown in Fig. 9.65, depicting an array with hexagonal shaped pixel, clearly visible due to the photoresist being deposited in the gap region (brighter structure). The pictures were taken before the implantation of the deep n layer through the darker surface areas shown in the photograph. Both magnifications do not feature any bright spots representing particle residue in the areas affected by the implant. The same is true for every other step involving the photoresists and thus it can be deduced that no clear evidence could be found in favor of particle residues being the reason for the observed behavior.

Another approach in explaining the early point-like defects is stemming from Zener-tunneling. Other than avalanche multiplication, tunneling is also a possible mechanism leading to a breakdown in the high-field region, since a direct band-to-band tunneling process becomes possible for sufficiently high electric fields. The required field, however is smaller compared to the one necessary for impact ionization ($> 3 \cdot 10^5$ V/cm), thus tunneling is expected to set in earlier than the Geiger breakdown, after which a

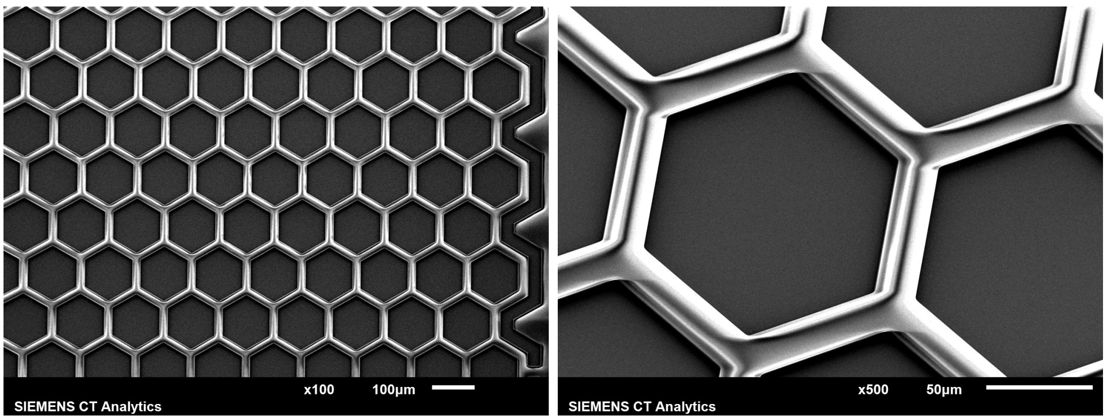

Figure 9.65: Scanning electron microscope photograph of the surface of a SiMPl4 array in-between two processing steps involving the photoresist. A x100 magnification can be seen on the left while the right hand side depicts a x500 magnification. The hexagonal shape of the pixel can be seen clearly due to the photoresist present in the gap area. The previously deposited photoresist in the center of the pixel was removed completely and no traces of particle residue can be found (see text). The measurements were provided by Siemens.

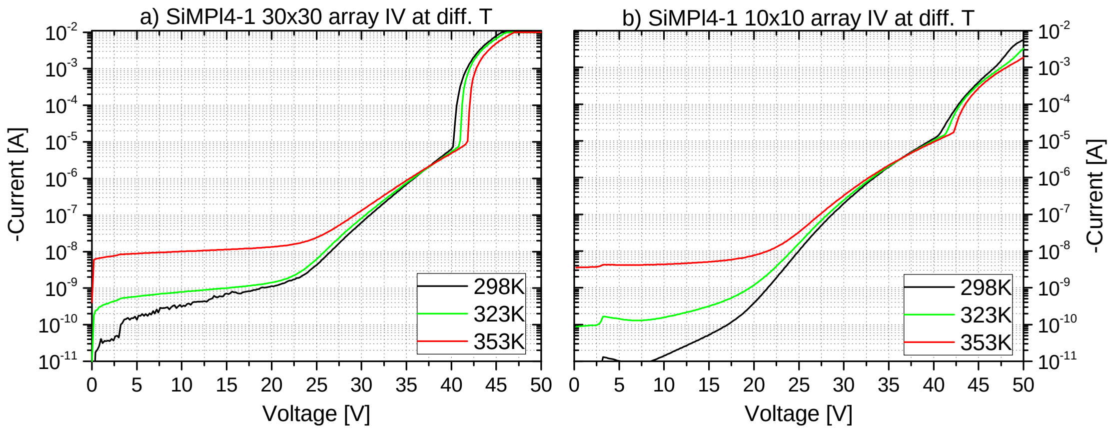

Figure 9.66: Investigation of potential Zener tunneling in SiMPl arrays. I-V measurements on a 30x30 array (a) and a 10x10 array (b) were performed at different temperatures in order to analyze the temperature coefficient of the respective breakdown. Arrays with early point-like defects were chosen. The breakdown located at higher voltages exhibits a positive temperature coefficient, i.e. higher temperatures result in higher breakdown voltages, identifying them as avalanche breakdowns. The same can be observed for the early current increases as the higher temperatures provide a slightly later increase than the lower temperature cases. Thus, Zener tunneling can most likely be dismissed (see text).

combination of both processes will take place, finally culminating in avalanche multiplication dominating for higher electric fields [25]. Zener-tunneling can then occur at very small distances for extreme differences in doping concentration. Avalanche multiplication, in contrast, will still occur if the electric field is sufficient enough. Tunneling would thereby occur at smaller bias voltages and could potentially explain the early breakdown phenomena observed.

In order to differentiate between avalanche breakdown and tunneling the temperature coefficient has to be taken into account. While an avalanche breakdown possesses a positive temperature coefficient, meaning that higher temperatures will result in higher breakdown voltages, tunneling exhibits a negative temperature coefficient, leading to a decrease in the required voltage for tunneling with increasing temperature.

The experimental evaluation of this assumption entails measuring the I-V-curves of various arrays affected by the early breakdown at different temperatures, making identification of the underlying process possible. Examples of such measurements are depicted in Fig. 9.66. Figure 9.66a) shows the result for a 30x30 while b) shows one of a 10x10 array. The different colored lines represent the different temperatures incorporated. In both cases the current starts increasing before the expected breakdown voltage of $V_{bd}(298\text{ K}) \approx 40$ V and the avalanche breakdown at the higher voltage can be seen to exhibit the expected positive temperature coefficient as V_{bd} increases with increasing T.

Determining the behavior at lower voltages is not as straight-forward, since the increased temperatures also result in higher overall dark current levels distorting the observation to a certain degree. In addition, considering the assumption and findings of Sec. 9.2.3.1, the potential impact of increased trap-assisted tunneling also needs to be taken into account. resulting in a temperature independent increased leakage current at higher electrical fields.

However, the slope of the I-V-curve for higher temperatures begins to become more steep at higher voltages compared to the lower temperature equivalents in both cases.

This is most notable when comparing the 298 K data with the 353 K data in a), since the shift to higher voltages at the higher voltage breakdown of roughly 25 V can also be seen in the shift of the slope increase at lower voltages. Thus the assumption can be made that the underlying process responsible for the current increase at lower voltages is also based on avalanche multiplication as opposed to tunneling, as the observed temperature coefficient was positive in both cases.

9.6.2 Potential link to sub-surface damages in SOI material

Sub-surface damages

Of the limited number of SiMPl3 chips tested, none exhibited the early point-like breakdown which is surprising, considering that the technological aspects assumed to be responsible, i.e. photoresist or annealing scenarios, were identical in both batches. However, one major difference lies in the wafers of both batches, as SiMPl3 was processed on standard thickness wafers, while the later batches utilized Silicon-On-Insulator (SOI) material in order to establish the necessary quench resistor within the bulk. The assumption can thereby be made that this issue might be related to the nature of the SOI material.

The SiMPl4 batches also included standard thickness wafers for process-control purposes and these could be utilized to investigate the problem at hand. For this purpose, diodes of 10 mm^2 area on both types of wafers (SOI and non-SOI) were characterized. These diodes feature a high-field implant allowing for avalanche breakdowns to take place at sufficient voltages. Considering the frequency at which the defects were located in 10x10 arrays, the diodes should be affected to an even higher degree due to their area being ten times larger, if said defects are present.

Hence common *I*-*V* measurements of the diodes located in all regions of the wafers, one being standard thickness material and the other SOI material, were performed. The resulting curves are depicted in Fig. 9.67, with a) representing the non-SOI wafer and b) the SOI case of the SiMPl4-2 batch. The previously experienced issues with early breakdowns are apparent in b) with more than 70% of the diodes exhibiting said issue.

The situation is quite different in case of the non-SOI wafer, showing no signs of the

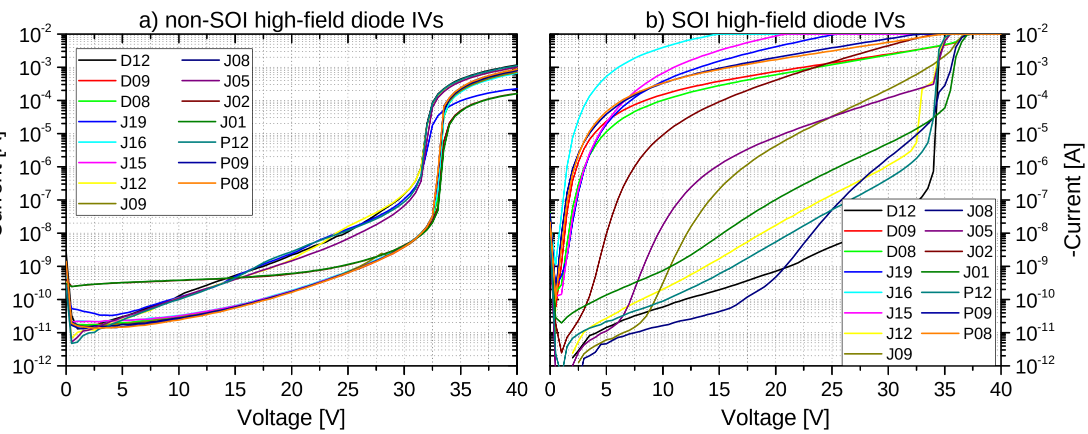

Figure 9.67: Comparison of *I*-*V* measurements of high-field diodes (HFDio) located on a non-SOI and a SOI wafer. Diodes of the non-SOI wafer seen in a) exhibit no early breakdown compared to the ones of a SOI wafer depicted in b). This leads to the assumption of the early point-like breakdowns being related to the SOI material (see text).

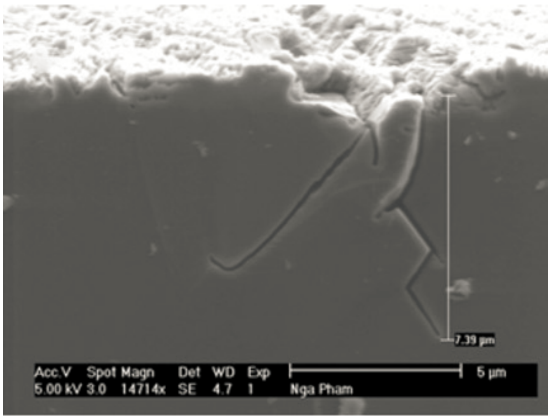

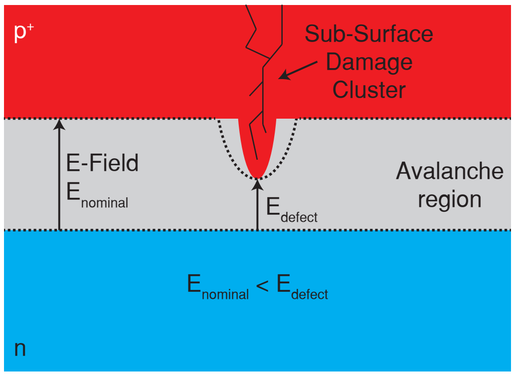

Figure 9.68: Illustration of sub-surface damages in SOI material. The left hand side depicts a cross-sectional SEM image of an SOI wafer after surface grinding and was taken from [121]. The surface cracks can be seen to propagate several µm into the silicon. As a consequence, defect-enhanced diffusion of the high-field implants can occur, as shown in the right hand illustration. This, in turn, can lead to small bumps in the doping profile, causing an highly inhomogeneous electrical field with the avalanche region. The electrical field close to the defect E_{defect} will be larger than the nominal one $E_{nominal}$ for the same bias voltage, resulting in earlier breakdowns at these specific spots (see text).

aforementioned defects in all 15 of the analyzed diodes. It also appears that roughly 50% of these diodes feature an overall higher dark current before breakdown and, in addition, a slightly lower breakdown voltage of $\Delta V_{bd} \approx 1.5$ V. As hot-spots that did not result in early point-like breakdowns also appeared on non-SOI material, it is possible that these two issue might need to be considered as having separate causes. The SOI material might be responsible for the point-like early breakdowns while a different underlying problem can lead to the increased currents also observed on non-SOI material. Nonetheless, the results of Fig. 9.67 give a clear indication that the early breakdowns could likely be connected to the fact that SOI material was utilized.

In order to achieve the desired sensor wafer thicknesses in SOI materials, mechanical grinding, chemical wet etching or a hybrid of both like chemical mechanical polishing (CMP) can be utilized for the thinning process. The most commonly deployed technique due to its high thinning rate and cost-effectiveness is the mechanical grinding [121]. This usually involves a two-step approach consisting of an initial coarse grinding, followed by a subsequent fine grinding with a lower thinning rate. During the grinding surface damages can be created caused by the increased thinning rate and the mechanical stress placed on the wafer surface, which may reach up to roughly 20 µm into the wafer [121]. Hence the second fine grinding step aims to remove said damage layer to a certain degree, since even fine mechanical grinding can always introduce mechanical stress into the surface, albeit less pronounced than in the coarse case. Examples of such damages entail an overall high surface roughness, material extrusions along the grinding grooves and sub-surface cracks due to the mechanical strain propagating into the wafer. The latter is depicted in the left hand side of Fig. 9.68, where a cross-sectional SEM image of an SOI wafer after coarse surface grinding can be seen. The created crack propagates several µm into the wafer.

The removal of the surface and sub-surface defects, however, hinges on the application of an additional CMP or wet etching step as well as the total thickness removed within the fine grinding step. If the latter is insufficient or not adequately fine, the presence of remaining sub-surface damages like the cracks seen in Fig. 9.68 cannot be ruled out. The issue arising in regards to the most recent SiMPl batches is that all were, in terms of wafer thinning, processed at the same time and this task was outsourced to an external supplier due to the lack of required lab equipment on site.

One assumption incorporates the potential sub-surface damages or cracks, as illustrated in the right side of Fig. 9.68. Assuming an insufficiently fine polishing, it is possible for cracks to be present several µm deep within the wafer. Since the high-field region is shallow by virtue of aiming to be sensitive to short wavelengths, it is therefore also feasible to assume that these damage clusters can protrude close to or even into the high-field region. Taking defect-enhanced diffusion of e.g. boron in silicon into account [122], it is now plausible for small bumps of boron at the locations of the defects to be created during annealing, as the diffusion rate will be increased thanks to the defect cluster. This in turn will result in an inhomogeneous avalanche region in terms of its thickness, with the aforementioned defect regions featuring significantly smaller thicknesses and spikes in the profile. By applying an external bias voltage, the resulting electric field at these respective spots (E_{defect}) will be much higher therefore be able to reach V_{bd} much earlier compared to the rest of the avalanche region ($E_{nominal}$), thus causing early point-like breakdowns visible within the arrays.

Sub-surface damages would also explain the different yields observed for the SiMPl4 batches SiMPl4-1 and SiMPl4-2. An overall higher yield was obtained for SiMPl4-2 devices, meaning less arrays were affected by the early point-like breakdowns compared to SiMPl4-1. The main difference in both batches was the topside p^+-implant, namely its depth with SiMPl4-1 featuring a more shallow implant for entrance window engineering. If sub-surface damages are responsible for the irregular behavior of the devices, it is valid to assume that the high-field region located closer to the surface would be affected more severely, which in turn would coincide with the experimental observations. It should also be noted, that the observed issues are similar to the ones exhibited by SiMPl2, whereas SiMPl2 was produced in an earlier different batch with an even deeper high-field region, thus showing less pronounced issues.

The assumption of the presence of sub-surface damages would also be consistent with the hypothesis of trap-assisted tunneling as an attempt to explain the increased dark count rate of the measured arrays and their deviating behavior from expected SRH statistics, as discussed in Sec. 9.2.3.1. Sub-surface damages would result in a damaged silicon lattice, thus leading to additional defects like vacancies within the affected regions. These defects can then either directly or by formation of more stable defects increase the contributions of trap-assisted tunneling, resulting in the observed deterioration of the characteristics of the devices. While mainly the most severe cases will lead to early point-like breakdowns, the less severe instances will still be able to increase trap-assisted tunneling contributions and lead to the observed hot-spots without early breakdowns.

Attempt at experimental validation

According to [123–125] there exist various methods for verification of sub surface damage. The majority of these methods was not readily available in the short time-frame required and could thus not be attempted. In the course of this study only one method could be utilized for investigation of the potential sub-surface damage issue and the results will be presented in the following.

The method at hand is called the Time-of-Flight Secondary Ion Mass Spectroscopy (ToF-SIMS) procedure [126, 127]. By shooting a pulsed ion beam at the surface of the sample, particles (secondary ions) will be removed in this sputtering process. The

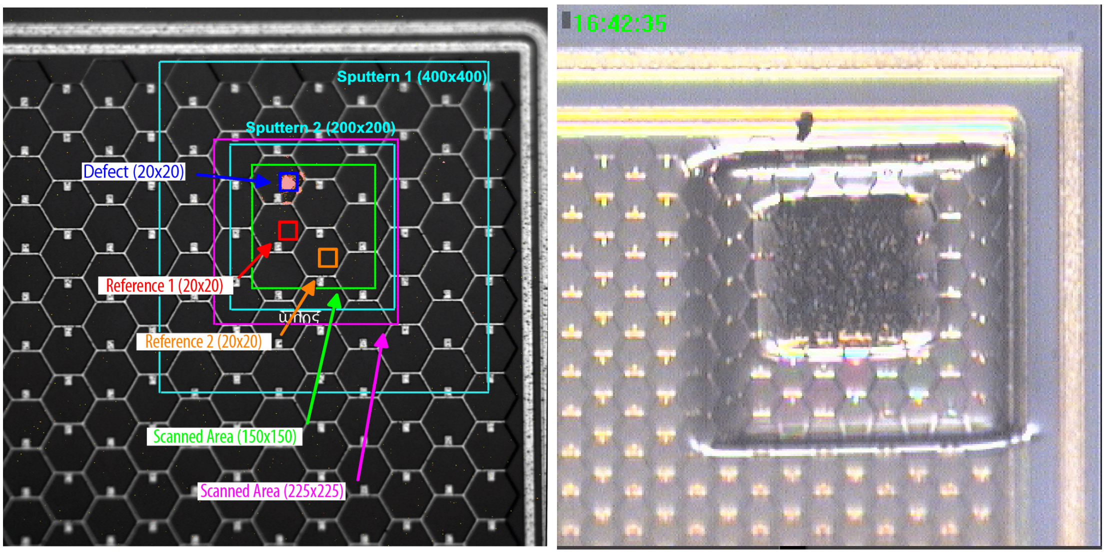

Figure 9.69: Illustration of the various regions scanned during the Time-of-Flight Secondary Ion Mass Spectroscopy (ToF-SIMS) procedure in order to investigate a potential defect enhanced diffusion of boron in the high-field region. The underlying photon emission photograph on the left hand side depicts a hot spot and the respective scan region is marked blue. Two additional reference regions of the same size of proper working pixels (red and orange) were also included for comparison. The larger green region was also measured as reference and can be seen as the darker rectangle on the right hand photograph after sputtering. The largest outline (cyan) was sputtered to estimate the required sputter rate.

secondary ions then enter an acceleration stage where their flight time is dependent on their mass. Thus, by measuring the time-of-flight, the ion mass and subsequently the type of particle can be identified. The measurement was performed externally by Siemens [127], which were debriefed in detail regarding the applied methodology and the results were provided upon completion.

The goal of this investigation was to identify possible differences in the boron profile within the region affected by the defect due to the assumed defect-enhanced diffusion. If compared to a nominal high-field region boron implant, it is expected to encounter a potentially less pronounced boron peak with a tail reaching deeper into the wafer. Conventional SIMS measurements provide less spatial resolution compared to the ToF-SIMS approach, thus not being capable of detecting profile discrepancies on such a small scale.

In order to make use of this procedure, a SiMPl5 array, heavily affected by the early breakdown phenomenon ($V_{bd,defect} \approx 8$ V) was chosen. The experimental plan for the ToF-SIMS measurement is illustrated in Fig. 9.69, with the photon emission microscopy photograph as underlying layer, depicting the affected region in question as red dot within one pixel. On this basis, multiple areas for sputtering and scanning were chosen. First, a rough macro-area was defined to establish an estimated sputter rate for the sample, seen as the 400 µm x 400 µm rectangle in cyan (left) and as the corresponding sputtered outline on the right hand microscope photograph of Fig. 9.69. Next a 150 µm x 150 µm area was defined for a complete scan, given by the green rectangle on the left and visible as darker, completely sputtered area on the right, entailing several sub-section which were scanned in more detail. These were defined as 20 µm x 20 µm regions, one containing the defect (blue) and two reference spots without defects (red and orange,

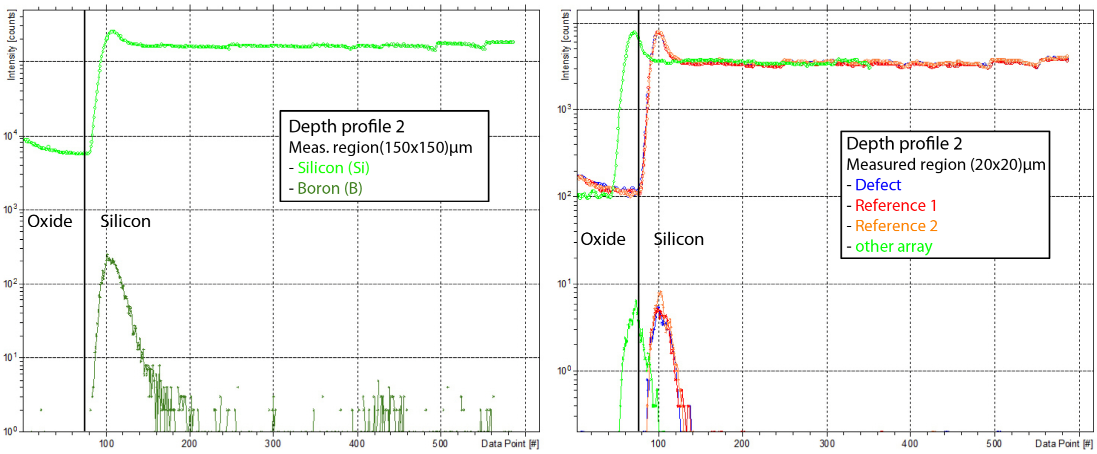

Figure 9.70: Resulting profiles of the ToF-SIMS measurements for the a) 150 µm x 150 µm and b) the individual 20 µm x 20 µm spots. The boron profile is is given in the lower part of the plots while the upper one represents the silicon concentration. In a) a clear boron profile is visible but still almost three orders of magnitude smaller than the measured equivalent for silicon. For smaller scanning regions (b)) the boron profile becomes difficult to interpret due to the low statistics. Nonetheless, no apparent discrepancy between the region including the defect (blue) and the three "clean" reference regions (red, orange and green) can be observed. The absolute shift of the green datasets is stemming from a different sputter rate for the respective measurement. See text for more details. The measurement and resulting data were provided by Siemens [127].

labeled "Reference 1" and "Reference 1", respectively) for comparison. In addition, a third reference spot of the same size in a different array was measured which did not suffer from any point-like defects.

The results of the ToF-SIMS are summarized in Fig. 9.70. In both cases the relative intensity of the measured secondary ions versus the sputter depth can be seen. The depth is only given in units of Data Points as the exact sputter rate is not known, however depth-profiling measurements were utilized to determine the amount of material removed in order to affirm that the total high field region was successfully removed during sputtering. In the left plot, the measured boron profile (lower, dark green) and the measured concentration of silicon (upper, light green) can be seen for the 150 µm x 150 µm sputter area. The sudden increase of the silicon concentration can be used to identify the transition from SiO_2 to Si. At the same depth, boron can be seen to increase, as expected but no tail can be eluded to as the scanned area is too large. The method makes use of all measured data points in x and y-direction to evaluated the profile by taking the mean data of all data points. Since the defect areas are expected to be smaller in comparison, the data of all other "healthy" points would dominate the resulting profile.

Hence the additional 20 µm spots were measured in order to increase the spatial sensitivity of the procedure and the results are depicted in the right hand side plot. Again, both silicon and boron are shown and the different colored lines represent the various scanned spots with blue corresponding to the spot containing the defect, red and orange the reference spots of the same array and green the reference spot of the other array. Due to required readjustments of the measurement procedure for the second array, the sputter rate changed, leading to the absolute shift in depth compared to the rest of the measured profiles. It is easy to see that compared to the larger region profiles, the overall intensity of the measured boron dropped by two orders of magnitude because of the reduced spacial size. Even now, no difference between the spot containing the defect and the reference spots can be seen as all profiles exhibit the identical peak height and no tail is visible for the blue graph. It can thus be assumed that the spacial expansion of the defect is still comparatively small, leading to the impact of the defect being lost during the process of evaluating the mean of all data points.

A reasonable next step would be to further reduce the spacial size of the analyzed regions, since the setup has a minimum spacial resolution of 2 µm, thereby allowing a minimum spot size of 2 µm x 2 µm. Even though the resolution would increase the chances of detecting any anomaly in the boron profile since data like the one seen in Fig. 9.68 has shown the defects to potentially be in the dimension of few µm, the experimental confirmation was not possible.

The observed particle intensity decreases drastically with decreasing spot size. As a result, no feasible information could be obtained from the 2 µm x 2 µm spot data, as the boron peak consisted of merely one data point. Considering a boron peak concentration in the range of 10^{19} cm^{-3} the tail in question can be expected to feature at least two orders of magnitude smaller boron concentrations. A threshold for a sufficient amount of measured boron intensity to identify differences in the tail can be given by $> 10^1$ or preferably $> 10^2$ particles. However, even the data obtained from the 150 µm x 150 µm spots would barely satisfy this threshold criteria for boron and 20 µm x 20 µm spots cannot be expected to yield feasible results, as their peak boron count amounts to < 10.

It must therefore be summarized that the results of the ToF-SIMS method are inconclusive as the required spacial resolution cannot provide the needed intensity resolution at the same time. Considering the above estimates, it is also unlikely that this method will be able provide the means necessary to identify discrepancies in the boron profile.

9.6.3 Summary and outlook

In order to investigate the observed issues of all SiMPl4 and SiMPl5 batches, several measurements were performed, each being able to identify different potential causes. First, SEM photographs were taken after every processing step involving the photoresists used on the wafers with the suspicion of particle residue of said photoresist being responsible for the irregularities in the high-field region. However, no indication of particle residues could be found. The notion of the early breakdown being caused by band-to-band tunneling (Zener-Tunneling) could also be dismissed as *I*-*V* characteristics at different temperatures exhibited a positive temperature coefficient for both early and late breakdowns, associated with a common avalanche multiplication process.

Inspecting the data of SiMPl3 and the non-SOI wafers of SIMPl4 led to the assumption of the SOI material being involved in the issue, as all available data of non-SOI avalanche structures did not exhibit any early breakdown phenomenon. It was hence deduced that the potential presence of sub-surface damages in the uppermost layers of the wafer could be responsible for the issues at hand. Due to defect-enhanced diffusion at these defect clusters, the high-field region would become inhomogeneous, leading to higher electric field peaks in close proximity to the defects, thus requiring smaller external voltage for breakdowns. An attempt at confirming this theory by measuring the boron profile at one of the measured hot-spots was made with the goal of identifying irregularities in the profile like a smaller peak height or tail, however the results remain inconclusive, as the required resolution of the ToF-SIMS measurement deployed was not sufficient.

There are, however, multiple other methods which allow identification of sub surface damages in silicon wafers as explained by e.g. Haapalinna [125]. The majority of the available techniques aim at analysis of the entire wafer or large spot sizes, most likely lacking the resolution required to identify the damages at hand. However methods like X-ray diffraction, utilizing Bragg diffraction and the fact that sub-surface damages impact the lattice constant in silicon are also capable of investigating smaller areas. In this technique the diffraction angles change because of the impact on the lattice constant which can be observed as a broadening of the Gaussian-shaped diffraction angle distribution.

A different approach is given in the form of chemical surface etching [128]. Specific etch solution allow for identification of damages by means of SEM measurements after the etching process. Due to the disturbance of the crystal lattice by sub-surface damages, the atomic bonds are significantly weakened. The selective etching agent is thus capable of exhibiting higher etching rates in these areas compared to the nominal lattice regions. The resulting surface dislocations can then be utilized in SEM measurements to identify areas of higher defect concentration.

As already stated, it was not possible to arrange for such procedures within the time-frame of this study. However, both techniques mentioned above and several other ones are currently being investigated and will be subject of future studies. It was therefore not possible to clearly identify the cause of the high leakage currents and subsequent dark count rates, as well as the early point-like breakdowns within the scope of this study.

10 Summary and Outlook

The initial goal of this study was the improvement of technological as well as device specific aspects of the SiMPl concept, based on the data obtained from the previous prototype batches, in order to optimize the performance of the classic design for low light level detection and in addition develop a novel design for application in high energy particle tracking.

The first step in this endeavor was the patching of issues present in the previous prototype batches, leading to the execution of dedicated TCAD simulations analyzing the different relevant technological parameters during manufacturing. These were afterwards supplemented with device and Monte Carlo simulations, investigating the direct impact on the device performance, so that effects like the edge breakdown could be identified.

The resulting batch, labeled SiMPl3 and processed on standard wafer material, was then characterized allowing for confirmation of the simulated data while also providing parameter sets for the lowest current levels and a homogeneous breakdown behavior without edge breakdown.

At the same time, a novel type of device was developed that would allow direct contacting and characterization of the bulk-integrated quench resistor and in addition direct comparison to the simulations for the first time. Technology and device simulations of these static test devices provided the necessary parameters and yielded promising results, thus leading to the inclusion of several chips containing a multitude of said devices on each subsequently produced wafer.

In regards to the classic approach, the findings of SiMPl3 were incorporated in addition to the engineering of a dedicated entrance window in order to reduce surface reflections for the pertinent wavelengths. Simulations in this topic provided the necessary technological data for implementation in the manufacturing process and suggested an optical transmittance for the peak wavelength interval around 400 nm above 90%.

Simulations for the follow-up batch, labeled SiMPl4, offered first estimates on various characteristics, such as breakdown voltage, recovery time, and maximum overbias voltage, dependent on the pitch/gap combination of the device, thus enabling an educated selection of feasible size variations for the final placement on the wafers. While the simulations still suggested recovery times $\tau_{90\%}$ in the order of several hundred ns due to the JFET-like nature of the quench resistor, utilization in applications with requirements for fast trigger timings and high fill factors would still prove feasible.

First wafer-level characterization of the processed SiMPl4 batch, however, have revealed a major issue, present on all available wafers. Even though roughly 40% - 70% of the arrays show normal operation in static measurements, the remaining ones exhibit drastically increased currents at lower voltages, stemming from early point-like breakdowns occurring within the array, as confirmed by photon emission microscopy measurements. If present, this early breakdown would dominate the behavior of the affected array. Since the static test devices do not rely on an avalanche breakdown, their full characterization was possible and carried out. The results enabled an in-depth analysis of the impact of various technological parameters on the maximum breakdown voltage and recovery time and were found to be in very good agreement with the simulated data. This, in turn, allowed for identification of preferable geometrical variations depending on the applications and their specific requirements.

Due to the aforementioned issue, dynamic characterizations of SiMPl4 arrays proved challenging. Devices unaffected by the early breakdowns still exhibited uncharacteristically high DCRs complicating the measurement procedures even for operation at $T = 233$ K. As a consequence, the majority of the tested device could not provide any data pertaining to the device characteristics. Hence, the main goal in regards to SiMPl4 shifted to the identification of the observed issue, in order to single out its exact cause.

The analysis of the temperature scaling of the dark current before breakdown and the resulting DCR indicated a deviation of the expected thermal generation according to SRH. Considering cases in which saturation was not reached, an increased deviation from the expected DCR-ratios for specific temperature steps could be observed for higher operating voltages and thus electric fields. This lends credence to the assumption that an increased amount of trap-assisted tunneling is taking place.

In addition, comparison of SOI data of SiMPl4 and standard wafer thickness material of SiMPl3 and SiMPl4 revealed only the SOI material to be affected by the issue. The assumption can therefore be made that it is related to the thinning procedure employed during the manufacturing of SOI material. The general idea is the occurrence of sub-surface damages caused by a insufficiently fine polishing step, resulting in an abundance of defect states close to the surface. The effect can thus be two-fold: First, sub-surface damage clusters can cause defect-enhanced diffusion of the topside p^+-implant, leading to smaller local avalanche regions and thereby higher electric fields compared to the rest of the high-field region. This could then result in the early point-like breakdowns observed. Second, the generally increased concentration of defects would also support the previous assumption of a higher rate of trap-assisted tunneling, thus explaining the increased DCR and overall sub-par performance of the devices.

First attempts at experimental validation of this theory have not been able to yield any tangible evidence, as the utilized method lacked the required sensitivity, hence no definitive statement in regards to the issue can be made. Nonetheless, various other methods are available and are currently being investigated. However, taking all findings into consideration, the above assumption appears to be the most likely explanation for the experienced problems.

Consequently, any evaluation on the potential of future SiMPl batches and their competitiveness with commercially available devices is difficult to make. However, even after eliminating the above problem, commercial devices have profited from various technological improvements in the last years, resulting in improved overall performance and cost of production. For SiMPl to achieve performances on a par with such devices, multiple technological improvements would be required, such as the implementation of optical trenches. Furthermore, in order to avoid surface damages, epitaxial technology could be utilized. However, this implementation would also remove one its major advantages, namely the fast and simplified production. Assuming an optimistic case outcome in these regards, SiMPl could still be expected to compete with conventional SiPMs by virtue of featuring an inherently higher fill factor and bulk diffusion barrier.

The second application of SiMPl and major focus of this thesis was particle tracking in high energy particle physics. The basic premise is to make use of the inherently high Geiger efficiency found in SiPMs for the detection of charged particles compared to single photons. This hypothesis was first confirmed via Monte Carlo simulations of the Geiger efficiency with varying numbers of initially generated charge carriers, showing efficiencies close to 100% for only 0.5 V overbias voltages. For experimental validation, a novel setup was developed which allowed the determination of the electron detection efficiency of electrons from a Strontium 90 source via a sophisticated coincidence unit made up of crossed fiber scintillators, coupled to readout SiPMs. The results, obtained with a SiMPl2 device, were in good agreement with the simulated predictions, exhibiting a plateaued detection efficiency around the level of the fill factor. By achieving plateaued Geiger efficiencies more quickly, the devices can be operated at lower voltages and thereby with lower contributions from effects like OCT, afterpulsing or generally lower levels of DCRs, without loosing efficiency.

Based on these results the venture was carried out, to develop a new SiMPl design to allow coupling via bump-bonding to dedicated readout, quenching and recharge electronics in order to obtain a hybrid device (DSiMPl), capable of being deployed as tracking detector. The main focus now was the adaptation towards low sensor thicknesses below 20 µm and towards the requirements of the ASIC to ensure proper ASIC-sensor interaction. One of the major aspects in this regard was an upper limit on the total resulting backside thickness of the device, which needed to be small (< 1 kΩ) as well as determining the various electronics parameters of the device so that the ASIC can be design accordingly.

TCAD simulations were carried out and were able to provide the required parameters, such as the vertical resistor capacitance and thickness and pitch/gap combinations could be determined which were within the limitations regarding the backside resistance. Additional technological simulations were also needed before manufacturing was possible due to the change in sensor design. The respective batch of wafers for this application, labeled SiMPl5, was then manufactured according to the findings of the simulations and wafer level measurements were carried out. However, SiMPl5 was also affected by the issues mentioned above, thus the quality and yield can be assumed to be below expectations. Direct measurement of the total backside resistance was in good agreement with the simulated data and small deviations can be attributed to total thickness variations over the entirety of the waver, as simulations showed a heavy dependence of the resistance on the device thickness. Overall, all relevant size combinations exhibited values below the imposed limit of 1 kΩ.

Since the actual sensor devices are design for single pixel readout via electronics, wafer level tests were not feasible at this stage. In order to ascertain the sensor quality, first working DSiMPl hybrids will be required. Currently first bump-bonding attempts with ASICs and interposers proved successful, enabling the next step with actual sensors, followed by signal transmission measurements. Afterwards, sophisticated test beam campaigns are planed to evaluated the hybrid performance.

The final point of focus of this thesis was the radiation hardness of the SiMPl4 and SiMPl5 designs. The need for a radiation hard sensor in the case of SiMPl5 is apparent due to the intended utilization as a potential vertex tracking detector, while it would also be desired for implementation of SiMPl4 for calorimeter readout. Due to a possible application in one of the upcoming linear collider experiments, namely ILC and CLIC, the expected levels of radiation damage for the innermost layer of detectors were used as baseline for this study.

In terms of ionizing radiation damage, no measurements could be carried out in the timeframe of this thesis, however TCAD simulations suggest potential lateral breakdowns in the SiMPl5 design due to the now structured topside implant and the accumulation of negative charges within the bulk-gap area. This issue was remedied, however, by the introduction of an aluminum grid in the gap area, acting as a quasi-gate structure and counteracting the charge accumulation by application of negative voltages to the grid. Simulations have shown the feasibility of this approach and predict very low voltage requirements in the order of ground level to stop the accumulation.

Regarding non-ionizing radiation damage, several impacts on the SiMPl design can be expected, such as an increased DCR and the subsequent increased OCT as well as an increase of R_Q due to changes in the bulk doping thereby directly affecting the recovery time and breakdown voltage. In extreme cases, the formation of a second junction within the bulk is expected, resulting in a voltage drop, further increasing V_{bd}. In the case of SiMPl5, this also will affect the total backside resistance, thus the rate of the increase needs to be obtained.

Various array structures and test devices were irradiated with thermal neutrons to achieve the desired fluence levels and, in addition, TCAD simulations, including a model with radiation damage were carried out. The leakage current increase given by the current related damage rate α was in accordance to previously established studies. In regards to the change in effective doping concentration, the SiMPl5 material was found to be exceptionally radiation hard and practically unaffected by prolonged exposure to radiation damage equal to multiple life cycles of the aforementioned collider experiments. The change in the total backside resistance, obtained via the static test devices was also found to be non-threatening to the device operations, even though clear discrepancies to the simulations were observed. This was most likely caused by the limited model implemented and requires further improvements. In regards to SiMPl4 the diode measurements suggest the material undergoing type inversion at around $\Phi_{neq}^{ti} \approx 3 \cdot 10^{13}$ neq/cm^2 which is roughly one order of magnitude lower than the simulations, while nevertheless being completely safe for the intended calorimeter operation. Finally, by applying a fit function to the diode depletion voltage data, the corresponding fit parameters b (acceptor state creation probability) and c (donor removal cross-section), necessary for the formation of a general model for the impact of non-ionizing radiation damage could be extracted and compared to previous studies, further adding data towards this endeavor.

Static test devices of SiMPl4 material allowed determination of the change in the maximum overbias voltage and recovery time up to the point of type inversion, showing an increase in both $V_{ob,max}$ and τ_{rec} due to the decrease in N_{eff}. These changes are generally heavily dependent on the pitch/gap combination and can thus be minimized by a proper choice of said combination. Dynamic measurements of arrays indicated a shift in the breakdown voltage and the analysis of the waveforms obtained after type inversion suggests a heavy increase of R_Q and formation of a second junction within the bulk. Nonetheless, operation after type inversion was possible, thus proving at least limited utilization potential beyond.

Overall, both SiMPl batches and their materials were found to be sufficiently radiation hard for their respective applications.

In summary, first simulation studies and subsequent prototype productions yielded positive results and allowed for the manufacturing of the sophisticated device batches. While both were affected by technological issues, distinct discoveries could be made. Even though the initial question pertaining to the quality improvements of SiMPl4 could not be answered, a better understanding of the devices in general could be achieved and it was possible to narrow down the cause of the issue, thus allowing future productions to avoid a similar fate. The first prototypes of SiMPl devices for particle tracking proved adequate for further hybrid testing and will be used for full characterizations of the first DSiMPl hybrids, thus paving the way for the next iteration towards a possible vertex tracking detector.

A Appendix

Table A.1: Extracted parameters from first static simulations of SiMPl4 for feasibility purposes (annealing #4). The fill factor FF, as well as the recovery times $\tau_{90\%}$ and $\tau_{1/e}$ and the ratio $\tau_{90\%}/\tau_{1/e}$ are given for each pitch-gap-combination, simulated at $V_{OB} =$ 5 V. $V_{OB,max}$ denotes the theoretical maximum overbias voltage according to 20 µA rule of thumb. For increasing gap sizes, pinch-off can be witnessed, while too small gaps result in insufficient quench resistors and thus may cause non-quenching to occur (see text). The trade-off between potential maximum overbias voltage and recovery time can be seen clearly. Note that the panels without recovery times translate to times in order seconds and minutes and were therefore omitted.

pitch [µm]	gap [µm]	FF [%]	Quenching $V_{OB,max}$ [V]	Recovery $\tau_{90\%}$ [10^{-7} s]	Recovery $\tau_{1/e}$ [10^{-7} s]	Recovery $\tau_{90\%}/\tau_{1/e}$	comment
100	6	88.4	2.2	2.13	0.67	3.17	non-quenching
	8	84.6	3.0	3.45	1.06	3.25	
	10	81.0	3.9	5.63	1.62	3.47	
	12	77.4	4.8	9.97	2.54	3.93	
	14	74.0	>5.0	22.5	4.27	5.27	
	16	70.6	>5.0	149	8.37	17.8	pinch-off
	18	67.2	>5.0	–	24.5	–	pinch-off
	20	64.0	>5.0	–	619	–	pinch-off
	30	49.0	>5.0	–	–	–	pinch-off
110	10	82.6	3.3	4.58	1.44	3.19	
	12	79.4	4.0	6.90	2.04	3.37	
	14	76.2	4.9	11.1	2.97	3.72	
	16	73.0	>5.0	20.5	4.52	4.54	
120	10	84.0	2.8	3.98	1.31	3.03	
	12	81.0	3.4	5.49	1.76	3.13	
	14	78.0	4.0	7.71	2.36	3.27	
	16	75.1	4.8	11.3	3.20	3.52	
130	10	85.2	2.3	3.59	1.23	2.93	non-quenching
	12	82.4	2.8	4.69	1.57	2.98	
	14	79.6	3.4	6.22	2.00	3.05	
	16	76.9	3.9	8.09	2.55	3.17	
	20	71.6	>5.0	15.5	4.27	3.63	

Table A.2: Values for the vertical bulk resistor R_{vert} for SiMPl5 devices, extracted from TCAD simulations. The results for various geometrical variations for two specific annealing scenarios are given, including thicknesses ranging from d_{min} to d_5 and gap sizes from 8 µm to 16 µm. The deviation stemming from a 10 % bulk doping variation (ΔR_{vert}), as well as the goodness-of-fit parameter R^2 of the linear fit applied in order to extract R_{vert} are also listed. A general trend of R_{vert} according to Eq. (9.2) can be observed, leading to an increase with gap size and thickness (see text). The impact of ΔR_{vert} can be seen to be negligible in comparison. Values of R^2 closer to 1 translate to a more linear behavior of the fitted I-V-curves, indicating that the non-linear behavior of the thick SiMPl devices is also present here for increased thicknesses.

		annealing #4			annealing #11		
thick	gap [µm]	R_{vert} [Ω]	ΔR_{vert} [Ω]	R^2	R_{vert} [Ω]	ΔR_{vert} [Ω]	R^2
	8	13.446	0.005	0.999	11.911	0.003	0.999
	10	14.926	0.005	0.999	13.121	0.004	0.999
d_{min}	12	16.668	0.006	0.999	14.788	0.004	0.999
	14	18.769	0.006	0.999	16.675	0.005	0.999
	16	21.256	0.007	0.999	18.902	0.005	0.999
	8	73.72	0.15	0.996	73.56	0.15	0.994
	10	81.41	0.16	0.996	81.16	0.17	0.994
d_1	12	90.33	0.18	0.996	89.95	0.19	0.994
	14	100.96	0.20	0.996	100.42	0.21	0.994
	16	113.64	0.23	0.995	112.88	0.24	0.994
	8	160.13	0.61	0.990	163.98	0.66	0.987
	10	177.02	0.68	0.990	181.16	0.74	0.988
d_2	12	196.23	0.77	0.988	200.56	0.83	0.988
	14	218.98	0.87	0.989	223.51	0.94	0.988
	16	246.26	0.99	0.989	250.97	1.07	0.988
	8	324.83	2.15	0.982	333.17	2.31	0.982
	10	360.50	2.43	0.982	369.69	2.61	0.982
d_3	12	400.00	2.74	0.982	409.73	2.94	0.981
	14	446.32	3.11	0.981	456.52	3.32	0.981
	16	501.94	3.56	0.980	512.63	3.80	0.980
	8	606.84	6.39	0.976	617.28	6.69	0.976
	10	677.87	7.27	0.975	689.73	7.61	0.975
d_4	12	754.31	8.25	0.974	766.80	8.62	0.975
	14	842.75	9.41	0.974	855.53	9.81	0.974
	16	948.69	10.82	0.973	961.39	11.27	0.973
	8	1034.8	15.9	0.971	1042.7	16.3	0.972
	10	1165.5	18.3	0.970	1175.3	18.8	0.971
d_5	12	1302.6	20.9	0.969	1312.6	21.4	0.970
	14	1459.0	24.0	0.968	1467.9	24.5	0.969
	16	1645.5	27.7	0.967	1652.4	28.3	0.968

Table A.3: Summary of the change in $V_{ob,max}$ with increasing Φ_{neq} for various pitch/gap combinations. Generally, an increase of $V_{ob,max}$ with increasing fluence can be observed. Pinch-off will take place faster with increasing fluence due to the reduced donor concentration in the bulk.

pitch [µm]	gap [µm]	Φ_{neq} [neq/cm^2]	$V_{ob,max}$ [V] Synopsys	$V_{ob,max}$ [V] measured
100	8	0	2.35	2.70 ± 0.09
		$1 \cdot 10^{10}$	2.39	2.70 ± 0.01
		$5 \cdot 10^{10}$	2.52	2.70 ± 0.07
		$1 \cdot 10^{11}$	2.68	2.70 ± 0.14
		$5 \cdot 10^{11}$	3.99	2.85 ± 0.14
		$1 \cdot 10^{12}$	>5	3.20 ± 0.14
		$1 \cdot 10^{13}$	>5	>5
	10	0	3.24	3.71 ± 0.10
		$1 \cdot 10^{10}$	3.28	3.71 ± 0.07
		$5 \cdot 10^{10}$	3.44	3.71 ± 0.07
		$1 \cdot 10^{11}$	3.63	3.80 ± 0.14
		$5 \cdot 10^{11}$	>5	3.85 ± 0.14
		$1 \cdot 10^{12}$	>5	4.30 ± 0.14
		$1 \cdot 10^{13}$	>5	>5
	12	0	4.16	4.69 ± 0.15
		$1 \cdot 10^{10}$	4.21	4.70 ± 0.07
		$5 \cdot 10^{10}$	4.38	4.70 ± 0.14
		$1 \cdot 10^{11}$	4.60	4.95 ± 0.14
		$\geq 5 \cdot 10^{11}$	>5	>5
	14, 16, 18	all	>5	>5
130	10	0	2.05	2.13 ± 0.10
		$1 \cdot 10^{10}$	2.08	2.13 ± 0.07
		$5 \cdot 10^{10}$	2.22	2.13 ± 0.07
		$1 \cdot 10^{11}$	2.40	2.20 ± 0.07
		$5 \cdot 10^{11}$	3.82	2.40 ± 0.14
		$1 \cdot 10^{12}$	>5	2.65 ± 0.14
		$1 \cdot 10^{13}$	>5	>5
	14	0	3.08	3.16 ± 0.14
		$1 \cdot 10^{10}$	3.12	3.16 ± 0.07
		$5 \cdot 10^{10}$	3.29	3.16 ± 0.07
		$1 \cdot 10^{11}$	3.52	3.16 ± 0.07
		$5 \cdot 10^{11}$	>5	3.25 ± 0.28
		$1 \cdot 10^{12}$	>5	3.85 ± 0.14
		$1 \cdot 10^{13}$	>5	>5
	16	0	3.62	3.66 ± 0.13
		$1 \cdot 10^{10}$	3.67	3.66 ± 0.07
		$5 \cdot 10^{10}$	3.86	3.66 ± 0.14
		$1 \cdot 10^{11}$	4.10	3.70 ± 0.14
		$5 \cdot 10^{11}$	>5	3.85 ± 0.21
		$1 \cdot 10^{12}$	>5	4.35 ± 0.14
		$1 \cdot 10^{13}$	>5	>5

Bibliography

[1] J. E. Brau *et al.*, 2012. LC-REP-2012-071; ILC ESD-2012/4; CLIC-Note-949: The Physics Case for an e+e- Linear Collider, arXiv:1210.0202 [hep-ex].

[2] H. Baer *et al.*, “The International Linear Collider Technical Design Report - Volume 2: Physics,” 2013. arXiv:1306.6352 [hep-ph].

[3] L. Linssen *et al.*, “Physics and Detectors at CLIC: CLIC Conceptual Design Report,” 2012. arXiv:1202.5940v1 [physics.ins-det].

[4] P. W. Higgs, “Broken Symmetries and the Masses of Gauge Bosons,” *Physical Review Letters*, vol. 13, pp. 508–509, Oct 1964.

[5] ATLAS Collaboration, “Observation of a new particle in the search for the Standard Model Higgs boson with the ATLAS detector at the LHC,” *Physics Letters B*, vol. 716, no. 1, pp. 1 – 29, 2012.

[6] C. Adolphsen *et al.*, “The International Linear Collider Technical Design Report - Volume 3.I: Accelerator R&D in the Technical Design Phase,” 2013. arXiv:1306.6353v1 [physics.acc-ph].

[7] C. Adolphsen *et al.*, “The International Linear Collider Technical Design Report - Volume 3.II: Accelerator Baseline Design,” 2013. arXiv:1306.6328v1 [physics.acc-ph].

[8] T. Behnke *et al.*, “The International Linear Collider Technical Design Report - Volume 1: Executive Summary,” 2013. arXiv:1306.6327v1 [physics.acc-ph].

[9] H. Abramowicz *et al.*, “The International Linear Collider Technical Design Report - Volume 4: Detectors,” 2013. arXiv:1306.6329v1 [physics.ins-det].

[10] Linear Collider Collaboration Webpage. `http://www.linearcollider.org/content/images-and-graphics`.

[11] H. Spieler, *Semiconductor Detector Systems*. USA: Oxford University Press, 2005.

[12] E. Graugés *et al.*, “Study of geiger avalanche photo-diodes (gapds) applications to pixel tracking detectors,” *Nuclear Instruments and Methods in Physics Research Section A: Accelerators, Spectrometers, Detectors and Associated Equipment*, vol. 617, no. 1, pp. 541 – 542, 2010. 11th Pisa Meeting on Advanced Detectors.

[13] The CALICE collaboration and C Adloff and others, “Construction and commissioning of the CALICE analog hadron calorimeter prototype,” *Journal of Instrumentation*, vol. 5, May 2010.

[14] NASA Goddard Space Flight Center. Goddard Media Studios, `https://svs.gsfc.nasa.gov/12969`.

[15] J.A. Hinton and W. Hofmann, “Teraelectronvolt Astronomy,” *Annual Review of Astronomy and Astrophysics*, vol. 47, no. 1, pp. 523–565, 2009.

[16] The CTA Consortium, “Design concepts for the cherenkov telescope array cta: an advanced facility for ground-based high-energy gamma-ray astronomy,” *Experimental Astronomy*, vol. 32, pp. 193–316, Dec 2011.

[17] Cherenkov Telescope Array Consortium, “Science with the Cherenkov Telescope Array,” Feb 2018. arXiv:1709.07997v2 [astro-ph.IM].

[18] Berrie Giebels and H. E. S. S. Collaboration, “Status and recent results from H.E.S.S,” 2013. arXiv:1303.2850v1 [astro-ph.HE].

[19] A. D. Angelis, “Status of MAGIC and recent results,” *Advances in Space Research*, vol. 51, no. 2, pp. 280 – 285, 2013. The Origins of Cosmic Rays: Resolving Hess’s Century-Old Puzzle.

[20] Nicola Galante and the VERITAS Collaboration, “Status And Highlights Of VERITAS,” 2012. arXiv:1210.5480v1 [astro-ph.HE].

[21] CTA Collaboration. CTA Observatory webpage, `https://www.cta-observatory.org/`.

[22] G. F. Knoll, *Radiation Detection and Measurement.* Wiley, New York, 3rd ed., 2000.

[23] A. Bouvier and others, “Photosensor characterization for the Cherenkov Telescope Array: silicon photomultiplier versus multi-anode photomultiplier tube,” *Hard X-Ray, Gamma-Ray, and Neutron Detector Physics XV*, Sep 2013.

[24] A. Biland and others., “Calibration and performance of the photon sensor response of FACT — the first G-APD Cherenkov telescope,” *Journal of Instrumentation*, vol. 9, Oct 2014.

[25] S. M. Sze, *Semiconductor Devices: Physics and Technology.* New York: John Wiley & Sons, 2nd ed. ed., 2001.

[26] S. M. Sze and K. K. Ng, *Physics of Semiconductor Devices.* John Wiley & Sons, 3rd ed. ed., 2006.

[27] M. Levinshtein, J. Kostamovaara, and S. Vainshtein, *Breakdown Phenomena in Semiconductors and Semiconductor Devices.* World Scientific, 2005.

[28] W. R. Leo, *Techniques for Nuclear and Particle Physics Experiments.* Springer-Verlag, 2nd ed., 1994.

[29] F. Hartmann, *Evolution of Silicon Sensor Technology in Particle Physics.* Berlin, Heidelberg: Springer, 1st ed. ed., 2009.

[30] C. Grupen and B. Shwartz, *Particle Detectors.* Cambridge University Press, 2nd ed., 2008.

[31] G. Lutz, *Semiconductor Radiation Detectors - Device Physics.* Berlin, Heidelberg: Springer, 1st ed. 1999. 2nd printing ed., 1999.

[32] F. Thuselt, *Physik der Halbleiterbauelemente.* Springer-Verlag, 2nd ed., 2011.

[33] C. Jendrysik, *Development and characterisation of silicon photomultipliers with bulk-integrated quench resistors for future applications in particle and astroparticle physics.* PhD thesis, Technical University of Munich, 2014.

[34] W. Shockley and W. T. Read, "Statistics of the Recombinations of Holes and Electrons," *Physical Review*, vol. 87, pp. 835–842, Sep 1952.

[35] R. N. Hall, "Electron-hole recombination in germanium," *Physical Review*, vol. 87, pp. 387–387, Jul 1952.

[36] R. V. Overstraeten and H. D. Man, "Measurement of the ionization rates in diffused silicon p-n junctions," *Solid-State Electronics*, vol. 13, no. 5, pp. 583 – 608, 1970.

[37] NIST, 2019. XCOM: Photon Cross Sections Database, `https://www.nist.gov/pml/xcom-photon-cross-sections-database`.

[38] H. Bethe, "Zur Theorie des Durchgangs schneller Korpuskularstrahlen durch Materie," *Annalen der Physik*, vol. 397, no. 3, pp. 325–400, 1930.

[39] F. Bloch, "Bremsvermögen von Atomen mit mehreren Elektronen," *Zeitschrift für Physik*, vol. 81, no. 5-6, pp. 363–376, 1933.

[40] L. Landau, "On the energy loss of fast particles by ionization," *Journal of Physics (USSR)*, vol. 8, pp. 201–205, 1944.

[41] M. Tanabashi (Particle Data Group) *et al.*, "Review of Particle Physics," *Physical Review D*, vol. 98, Aug 2018.

[42] S. Cova *et al.*, "Avalanche photodiodes and quenching circuits for single-photon detection," *Applied Optics*, vol. 35, pp. 1956–1976, Apr 1996.

[43] B. Dolgoshein *et al.*, "Status report on silicon photomultiplier development and its applications," *Nuclear Instruments and Methods in Physics Research Section A: Accelerators, Spectrometers, Detectors and Associated Equipment*, vol. 563, no. 2, pp. 368 – 376, 2006.

[44] S. Seifert *et al.*, "Simulation of Silicon Photomultiplier Signals," *IEEE Transactions on Nuclear Science*, vol. 56, pp. 3726–3733, Dec 2009.

[45] P. Eckert *et al.*, "Characterisation studies of silicon photomultipliers," *Nuclear Instruments and Methods in Physics Research Section A: Accelerators, Spectrometers, Detectors and Associated Equipment*, vol. 620, no. 2, pp. 217 – 226, 2010.

[46] A. J. van Lint *et al.*, "Mechanisms of radiation effects in electronic materials. Vol. 1," *NASA STI/Recon Technical Report A*, vol. 81, 1980.

[47] M. Moll, *Radiation Damage in Silicon Particle Detectors - microscopic defects and macroscopic properties.* PhD thesis, University of Hamburg, 1999.

[48] J. Lindhard and V. Nielsen, "Nuclear collisions and ionisation fluctuations in charged particle detectors," *Physics Letters*, vol. 2, no. 5, pp. 209 – 211, 1962.

[49] M. Frey, *Developement of highly radiation hard silicon strip sensors for application at the super large hadron collider.* PhD thesis, University of Karlsruhe, 2009.

[50] B. MacEvoy, G. Hall, and K. Gill, "Defect evolution in irradiated silicon detector material," *Nuclear Instruments and Methods in Physics Research Section A: Accelerators, Spectrometers, Detectors and Associated Equipment*, vol. 374, no. 1, pp. 12 – 26, 1996.

[51] R. Wunstorf *et al.*, "Results on radiation hardness of silicon detectors up to neutron fluences of 10^{15} n/cm^2," *Nuclear Instruments and Methods in Physics Research Section A: Accelerators, Spectrometers, Detectors and Associated Equipment*, vol. 315, no. 1–3, pp. 149 – 155, 1992.

[52] R. Wunstorf, *Systematische Untersuchungen zur Strahlenresistenz von Silizium-Detektoren für die Verwendung in Hochenergiephysik-Experimenten.* PhD thesis, University of Hamburg, 1992.

[53] D. Pitzl *et al.*, "Type inversion in silicon detectors," *Nuclear Instruments and Methods in Physics Research Section A: Accelerators, Spectrometers, Detectors and Associated Equipment*, vol. 311, pp. 98 – 104, 1992.

[54] E. Fretwurst *et al.*, "Radiation hardness of silicon detectors for future colliders," *Nuclear Instruments and Methods in Physics Research Section A: Accelerators, Spectrometers, Detectors and Associated Equipment*, vol. 326, no. 1–2, pp. 357 – 364, 1993.

[55] E. Fretwurst *et al.*, "Recent advancements in the development of radiation hard semiconductor detectors for S-LHC," *Nuclear Instruments and Methods in Physics Research Section A: Accelerators, Spectrometers, Detectors and Associated Equipment*, vol. 552, no. 1–2, pp. 7 – 19, 2005.

[56] G. Lindström *et al.*, "Radiation hard silicon detectors—developments by the RD48 (ROSE) collaboration," *Nuclear Instruments and Methods in Physics Research Section A: Accelerators, Spectrometers, Detectors and Associated Equipment*, vol. 466, no. 2, pp. 308 – 326, 2001.

[57] G. Lindström, "Radiation damage in silicon detectors," *Nuclear Instruments and Methods in Physics Research Section A: Accelerators, Spectrometers, Detectors and Associated Equipment*, vol. 512, pp. 30 – 43, 2003.

[58] G. Lindström *et al.*, "Towards super radiation tolerant semiconductor detectors for future elementary particle research," *Journal of Optoelectronics and Advanced Materials*, vol. 6, pp. 23 – 38, 2004.

[59] S. Rummel, *Investigation of DEPFET as Vertex Detector at ILC - Intrinsic properties, radiation hardness and alternative readout schemes.* PhD thesis, Technical University of Munich, 2009.

[60] A. Chilingarov, "Generation current temperature scaling," Tech. Rep. PH-EP-Tech-Note-2013-001, CERN, Geneva, Jan 2013.

[61] J. Matheson, M. Robbins, and S. Watts, "The effect of radiation induced defects on the performance of high resistivity silicon diodes," *Nuclear Instruments and Methods in Physics Research Section A: Accelerators, Spectrometers, Detectors and Associated Equipment*, vol. 377, no. 2–3, pp. 224 – 227, 1996.

[62] S. Rashkeev *et al.*, "Defect Generation by Hydrogen at the Si SiO2 Interface," *Physical Review Letters*, vol. 87, 10 2001.

[63] A. Ritter, *Radiation Hardness Studies for DEPFETs in Belle II.* PhD thesis, Technical University of Munich, 2013.

[64] J. R. Cricchi and D. F. Barbe, "Compensation of Radiation Effects by Charge Transport in Metal-Nitride-Oxide-Semiconductor Structures," *Applied Physics Letters*, vol. 19, no. 3, pp. 49 – 51, 1971.

[65] Y. Takahashi *et al.*, "Radiation-induced trapped charge in metal-nitride-oxide-semiconductor structure," *IEEE Transactions on Nuclear Science*, vol. 46, pp. 1578 –1585, December 1999.

[66] V. Raparla *et al.*, "A model of radiation effects in nitride–oxide films for power MOSFET applications," *Solid-State Electronics*, vol. 47, no. 5, pp. 775 – 783, 2003.

[67] Q. Wei, *Studies of Radiation Hardness of MOS Devices for Application in a Linear Collider Vertex Detector.* PhD thesis, Technical University of Munich, 2008.

[68] S. Petrovics, "*Neutron Irradiations and Punch-Through Biasing Studies with DEPFETs for BELLE II*," Master's thesis, Ludwig-Maximilians-University Munich, 2012.

[69] C. R. Crowell and S. M. Sze, "Temperature dependence of avalanche multiplication in semiconductors," *Applied Physics Letters*, vol. 9, no. 6, pp. 242–244, 1966.

[70] D. K. Schroder, *Semiconductor Material and Device Characterization.* Chichester, West Sussex, New York: John Wiley & Sons, 3rd ed. ed., 2006.

[71] P. Buzhan *et al.*, "The cross-talk problem in sipms and their use as light sensors for imaging atmospheric cherenkov telescopes," *Nuclear Instruments and Methods in Physics Research Section A: Accelerators, Spectrometers, Detectors and Associated Equipment*, vol. 610, no. 1, pp. 131 – 134, 2009. New Developments In Photodetection NDIP08.

[72] Y. Du and F. Retière, "After-pulsing and cross-talk in multi-pixel photon counters," *Nuclear Instruments and Methods in Physics Research Section A: Accelerators, Spectrometers, Detectors and Associated Equipment*, vol. 596, no. 3, pp. 396 – 401, 2008.

[73] P. Eckert, R. Stamen, and H. C. Schultz-Coulon, "Study of the response and photon-counting resolution of silicon photomultipliers using a generic simulation framework," *Journal of Instrumentation*, vol. 7, Aug 2012.

[74] C. Jendrysik *et al.*, "New method for the determination of non-quenching regime for silicon photomultipliers: A comparative study," *Nuclear Instruments and Methods in Physics Research Section A: Accelerators, Spectrometers, Detectors and Associated Equipment*, vol. 695, pp. 226 – 228, 2012. New Developments in Photodetection NDIP11.

[75] P. Buzhan *et al.*, "The advanced study of silicon photomultiplier," *Advanced Technology and Particle Physics*, pp. 717–728, 2002.

[76] K. Iniewski, *Semiconductor Radiation Detection Systems.* CRC Press, 2010.

[77] R. Newman, "Visible Light from a Silicon $p-n$ Junction," *Physical Review*, vol. 100, pp. 700–703, Oct 1955.

[78] M. Pavesi *et al.*, "Spontaneous hot-carrier photon emission rates in silicon: Improved modeling and applications to metal oxide semiconductor devices," *Physical Review B*, vol. 65, May 2002.

[79] J. Bude, N. Sano, and A. Yoshii, "Hot-carrier luminescence in Si," *Physical Review B*, vol. 45, pp. 5848–5856, Mar 1992.

[80] R. Mirzoyan, R. Kosyra, and H.-G. Moser, "Light emission in si avalanches," *Nuclear Instruments and Methods in Physics Research Section A: Accelerators, Spectrometers, Detectors and Associated Equipment*, vol. 610, no. 1, pp. 98 – 100, 2009.

[81] A. L. Lacaita *et al.*, "On the bremsstrahlung origin of hot-carrier-induced photons in silicon devices," *IEEE Transactions on Electron Devices*, vol. 40, pp. 577–582, March 1993.

[82] L. Andriček, G. Lutz, and R. Richter, "Avalanche photodiode for use in avalanche radiation detector, has electrode arranged lateral to diode layer so that it depletes substrate laterally adjacent to layer, when resistance layer is shielded from diode layer opposite to electrode." Patent, DE 102007037020 B3.

[83] J. Ninković *et al.*, "Simpl—novel high qe photosensor," *Nuclear Instruments and Methods in Physics Research Section A: Accelerators, Spectrometers, Detectors and Associated Equipment*, vol. 610, no. 1, pp. 142 – 144, 2009.

[84] J. Ninković *et al.*, "Simpl—an avalanche diode array with bulk integrated quench resistors for single photon detection," *Nuclear Instruments and Methods in Physics Research Section A: Accelerators, Spectrometers, Detectors and Associated Equipment*, vol. 617, no. 1, pp. 407 – 410, 2010.

[85] J. Ninković *et al.*, "The first measurements on sipms with bulk integrated quench resistors," *Nuclear Instruments and Methods in Physics Research Section A: Accelerators, Spectrometers, Detectors and Associated Equipment*, vol. 628, no. 1, pp. 407 – 410, 2011.

[86] I. Diehl *et al.*, "Readout ASIC for fast digital imaging using SiPM sensors: Concept study," in *2015 IEEE Nuclear Science Symposium and Medical Imaging Conference (NSS/MIC)*, Oct 2015.

[87] E. Garutti and Y. Musienko, "Radiation damage of SiPMs," *Nuclear Instruments and Methods in Physics Research Section A: Accelerators, Spectrometers, Detectors and Associated Equipment*, vol. 926, pp. 69 – 84, 2019.

[88] A. Heering *et al.*, "Effects of very high radiation on sipms," *Nuclear Instruments and Methods in Physics Research Section A: Accelerators, Spectrometers, Detectors and Associated Equipment*, vol. 824, pp. 111 – 114, 2016.

[89] R. Klanner *et al.*, "Characterisation of radiation-damaged SiPMs," International Conference on the Advancement of Silicon Photomultipliers, ICASiPM 2018.

[90] M. C. Vignali *et al.*, "Neutron irradiation effect on SiPMs up to $\Phi_{neq} = 5 \cdot 10^{14}$ cm^{-2}," *Nuclear Instruments and Methods in Physics Research Section A: Accelerators, Spectrometers, Detectors and Associated Equipment*, vol. 912, pp. 137 – 139, 2018.

[91] T. Tsang *et al.*, "Neutron radiation damage and recovery studies of SiPMs," *Journal of Instrumentation*, vol. 11, no. 12, 2016.

[92] C. Xu *et al.*, "Influence of x-ray irradiation on the properties of the hamamatsu silicon photomultiplier s10362-11-050c," *Nuclear Instruments and Methods in Physics Research Section A: Accelerators, Spectrometers, Detectors and Associated Equipment*, vol. 762, pp. 149 – 161, 2014.

[93] M. Andreotti *et al.*, "Silicon photo-multiplier radiation hardness tests with a white neutron beam," in *2013 3rd International Conference on Advancements in Nuclear Instrumentation, Measurement Methods and their Applications (ANIMMA)*, pp. 1–4, June 2013.

[94] P. Cattaneo *et al.*, "Radiation hardness tests with neutron flux on different silicon photomultiplier devices," *Journal of Instrumentation*, vol. 12, jul 2017.

[95] Y. Musienko *et al.*, "Radiation damage in silicon photomultipliers exposed to neutron radiation," *Journal of Instrumentation*, vol. 12, jul 2017.

[96] E. Pilicer, F. Kocak, and I. Tapan, "Excess noise factor of neutron-irradiated silicon avalanche photodiodes," *Nuclear Instruments and Methods in Physics Research Section A: Accelerators, Spectrometers, Detectors and Associated Equipment*, vol. 552, no. 1, pp. 146 – 151, 2005. Proceedings of the 5th International Conference on Radiation Effects on Semiconductor Materials, Detectors and Devices.

[97] Synopsys, 2013. Sentaurus Process User Guide: Version H-2013.03.

[98] Synopsys, 2013. Sentaurus Device User Guide: Version H-2013.03.

[99] Synopsys, 2013. Sentaurus Structure Editor User Guide: Version H-2013.03.

[100] A. Spinelli and A. L. Lacaita, "Physics and numerical simulation of single photon avalanche diodes," *IEEE Transactions on Electron Devices*, vol. 44, pp. 1931–1943, Nov 1997.

[101] D. Passeri *et al.*, "TCAD-based analysis of radiation-hardness in silicon detectors," *IEEE Transactions on Nuclear Science*, vol. 45, pp. 602–608, June 1998.

[102] V. Eremin, E. Verbitskaya, and Z. Li, "The origin of double peak electric field distribution in heavily irradiated silicon detectors," *Nuclear Instruments and Methods in Physics Research Section A: Accelerators, Spectrometers, Detectors and Associated Equipment*, vol. 476, no. 3, pp. 556 – 564, 2002.

[103] F. Moscatelli *et al.*, "Effects of Interface Donor Trap States on Isolation Properties of Detectors Operating at High-Luminosity LHC," *IEEE Transactions on Nuclear Science*, vol. 64, pp. 2259–2267, Aug 2017.

[104] D. Pennicard *et al.*, "Simulations of radiation-damaged 3D detectors for the Super-LHC," *Nuclear Instruments and Methods in Physics Research Section A: Accelerators, Spectrometers, Detectors and Associated Equipment*, vol. 592, no. 1, pp. 16 – 25, 2008.

[105] M. Petasecca *et al.*, "Numerical Simulation of Radiation Damage Effects in p-Type and n-Type FZ Silicon Detectors," *IEEE Transactions on Nuclear Science*, vol. 53, pp. 2971–2976, Oct 2006.

[106] Å. Folkestad *et al.*, "Development of a silicon bulk radiation damage model for sentaurus tcad," *Nuclear Instruments and Methods in Physics Research Section A: Accelerators, Spectrometers, Detectors and Associated Equipment*, vol. 874, pp. 94 – 102, 2017.

[107] F. Moscatelli *et al.*, "An enhanced approach to numerical modeling of heavily irradiated silicon devices," *Nuclear Instruments and Methods in Physics Research Section B: Beam Interactions with Materials and Atoms*, vol. 186, no. 1, pp. 171 – 175, 2002.

[108] W. G. Oldham, R. R. Samuelson, and P. Antognetti, "Triggering phenomena in avalanche diodes," *IEEE Transactions on Electron Devices*, vol. 19, pp. 1056–1060, Sep. 1972.

[109] R. J. McIntyre, "On the avalanche initiation probability of avalanche diodes above the breakdown voltage," *IEEE Transactions on Electron Devices*, vol. 20, pp. 637–641, July 1973.

[110] S. Ramo, "Currents Induced by Electron Motion," *Proceedings of the IRE*, vol. 27, pp. 584–585, Sep. 1939.

[111] C. Jendrysik, 2013. HLL, Munich. Private communications.

[112] D. Žontar *et al.*, "Time development and flux dependence of neutron-irradiation induced defects in silicon pad detectors," *Nuclear Instruments and Methods in Physics Research Section A: Accelerators, Spectrometers, Detectors and Associated Equipment*, vol. 426, no. 1, pp. 51 – 55, 1999.

[113] L. Snoj, G. Žerovnik, and A. Trkov, "Computational analysis of irradiation facilities at the JSI TRIGA reactor," *Applied Radiation and Isotopes*, vol. 70, no. 3, pp. 483 – 488, 2012.

[114] I. Mandić, 2012. Jožef Stefan Instute, Ljubljana. Private communications.

[115] S. Larouche and L. Martinu, "Openfilters: open-source software for the design, optimization, and synthesis of optical filters," *Applied Optics*, vol. 47, no. 13, pp. C219–C230, 2008.

[116] G. A. M. Hurkx *et al.*, "A new analytical diode model including tunneling and avalanche breakdown," *IEEE Transactions on Electron Devices*, vol. 39, pp. 2090–2098, Sep. 1992.

[117] R. Richter, 2019. Semiconductor Laboratory of the Max-Planck Society, Munich. Private communications.

[118] I. Diehl, 2017. DESY, Hamburg. Private communications.

[119] E. Fretwurst *et al.*, "The influence of edge effects on the determination of the doping profile of silicon pad diodes," *Nuclear Instruments and Methods in Physics Research Section A: Accelerators, Spectrometers, Detectors and Associated Equipment*, vol. 867, pp. 231 – 236, 2017.

[120] H. Bichsel, "Straggling in thin silicon detectors," *Review of Modern Physics*, vol. 60, pp. 663–699, Jul 1988.

[121] Y. Yang *et al.*, "Process induced sub-surface damage in mechanically ground silicon wafers," *Semiconductor Science and Technology*, vol. 23, no. 7, 2008.

[122] P. M. Fahey, P. B. Griffin, and J. D. Plummer, "Point defects and dopant diffusion in silicon," *Review of Modern Physics*, vol. 61, pp. 289–384, 1989.

[123] S. Rein, *Lifetime Spectroscopy - A Method of Defect Characterization in Silicon for Photovoltaic Applications.* Berlin Heidelberg: Springer-Verlag, 1st ed., 2005.

[124] M. Wilson *et al.*, "QSS-μPCD measurement of lifetime in silicon wafers: advantages and new applications," *Energy Procedia*, vol. 8, pp. 128 – 134, 2011.

[125] A. Haapalinna, S. Nevas, and D. Pähler, "Rotational grinding of silicon wafers - sub-surface damage inspection," *Materials Science and Engineering: B*, vol. 107, no. 3, pp. 321 – 331, 2004.

[126] A. Benninghoven, "Chemical Analysis of Inorganic and Organic Surfaces and Thin Films by Static Time-of-Flight Secondary Ion Mass Spectrometry (TOF-SIMS)," *Angewandte Chemie International Edition in English*, vol. 33, no. 10, pp. 1023–1043, 1994.

[127] W. Holzapfel, 2017. Siemens AG, Munich. Private communications.

[128] M. Fathi, "Delineation of crystalline extended defects on multicrystalline silicon wafers," *International Journal of Photoenergy*, vol. 2007, 2007.

List of Figures

List of Tables

List of Publications

Journals and proceedings

- I. Diehl, et al., "Readout of digital SiPMs", *IEEE Nuclear Science Symposium and Medical Imaging Conference Proceedings (NSS/MIC)*, 2018.
- S.Petrovics, et al., "A novel Silicon Photomultiplier with bulk integrated quench resistors: utilization in optical detection and tracking applications for particle physics", *Nuclear Instruments and Methods in Physics Research Section A: Accelerators, Spectrometers, Detectors and Associated Equipment*, Vol. 845, pp. 150 - 153, 2017.
- I. Diehl, et al., "Readout ASIC for fast digital imaging using SiPM sensors: Concept study", *IEEE Nuclear Science Symposium and Medical Imaging Conference (NSS/MIC)*, 2015.
- T. Ostermayr, et al., "Laser plasma accelerator driven by a super-Gaussian pulse", *Journal of Plasma Physics*, Vol. 78, pp. 447–453, 2012.
- K. Nakajima, et al., "Operating plasma density issues on large-scale laser-plasma accelerators toward high-energy frontier", *Physical Review Special Topics: Accelerators and Beams*, Vol. 14, 2011.

Conference and workshop contributions

- Poster: "DSiMPl - utilization of the SiMPl concept for tracking applications in particle physics" (Presented by J. Ninković), *11th International "Hiroshima" Symposium on the Development and Application of Semiconductor Tracking Detectors (HSTD11) in conjunction with 2nd Workshop on SOI Pixel Detectors (SOIPIX2017)*, Okinawa, Japan, 2017.
- Oral: "The DSiMPl Detector Concept", *LC Vertex Detector Workshop 2017*, Castle Ringberg, Germany, 2017
- Oral: "A novel Silicon Photomultiplier with bulk integrated quench resistors - utilization in optical detection and tracking applications for particle physics", *VCI2016 - The 14th Vienna Conference on Instrumentation*, Vienna, Austria, 2016.
- Oral: "A novel Silicon Photomultiplier with bulk integrated quench resistors", *LIGHT 14 - Workshop on the Latest Developments of Photon Detectors*, Castle Ringberg, Germany, 2014.
- Oral: "Utilization of novel Silicon Photomultipliers with bulk integrated quench resistors in tracking applications for particle physics", *Tipp 2014 - Third International Conference on Technology and Instrumentation in Particle Physics*, Amsterdam, Netherlands, 2014.

Acknowledgments

I would like to take this opportunity to thank everyone who made this thesis possible. Many special thanks to the following people:

- **Prof. Dr. Jochen Schieck** for supervising this thesis even after switching universities and being busy with many new responsibilities - I really appreciate it.
- **Prof. Dr. Christian Kiesling** for being the second supervisor of this thesis.
- **Dr. Jelena Ninković** for giving me the opportunity to work on the SiMPl project at the HLL, the day-to-day supervision and many helpful discussions and for keeping the project (and myself) on track in difficult times. Also many thanks for proofreading this thesis.
- **Rainer Richter** for sharing his vast knowledge in the fields semiconductors and electronics with me, for the many helpful discussions which always helped giving my work a push in the right direction and for proofreading critical parts of this thesis.
- **Dr. Christian Jendrysik** for introducing me to the basics of silicon photomultipliers and the entire simulation framework of this thesis and for taking out time of his schedule in the final steps of his PhD to do so. Also many thanks for the great office atmosphere and numerous discussions during the years.
- my colleagues at the MPP, in particular **Dr. Frank Simon** and **Dr. Marco Szalay** for their help with the experimental setups and the many fruitful discussions. Also many thanks to the engineering department for manufacturing several parts of the experimental setups.
- **Danilo Mießner** for bonding and other lab work of the SiMPl devices and the helpful suggestions.
- **Dr. Andreas Wassatsch** for introducing me to 3D-printing.
- **The entire staff of the HLL**, especially those working on the SiMPl project, but also the IT-crowd (in particular **Jorma Jakowitsch** and **Vladimir Travalja**).
- **All the many colleagues** and friends in my office for many interesting but also entertaining discussions about physics and life in general. Also special thanks for the great atmosphere over the years. In particular many thanks to **Dr. Christian Jendrysik**, **Dr. Stephan Schlee** and **Dr. Paola Avella** and later on **Martin Hensel**, **Daniel Klose** and **Mitja Predikaka**.
- **My friends** that helped me keep my already dwindling level of sanity during this taxing phase. Special thanks go to **Dr. Lutz Girgenrath**, **Dr. Tobias Ostermayr**, **Markus Seigfried**, **Dr. Felix Müller** and **Christian Schirmer**.
- last, but not least, **my whole family** for their never ending support in all situations.

Finally, I would like to dedicate this thesis to my late grandfather **Gruja Amidzić**.